博士論文

Inversion Domain Boundaries in ZnO: Atomic-Scale Structural and Elemental Analysis, Electronic Structure Calculations and Thermoelectric Properties

(酸化亜鉛における反転ドメイン境界の原子・電子構造および熱電特性に関する研究)

Hoemke, Joshua Patrick

（ヘムキ ジョシュア パトリック）

Submitted in partial fulfillment of the requirements for Doctor of Philosophy in Engineering

Department of Materials Science and Engineering, University of Tokyo

December 2017

Abstract

ZnO is a functional material that has been extensively investigated for use in a number of applications including transparent conducting oxides (TCO), light-emitting diodes (LED), magnetic semiconductors, piezoelectrics, photovoltaics, thermoelectrics, gas sensors and varistors. Several characteristics of ZnO make it well-suited for use in practical applications. These include a large band gap (3.3-3.44 eV), allowing for optical transparency, the ability to achieve a high carrier density through doping, a large exciton binding energy (~60 meV), a non-centrosymmetric crystal structure, a low cost and abundant and non-toxic constituent elements, its resistance to degradation in air at high temperatures and the potential for the modification of its properties through nanostructuring and nanoscale defect formation.

Currently, ZnO is primarily used as a varistor material. However, investigations of ZnO for applications in new areas such as magnetic semiconductors, piezoelectrics, LEDs and thermoelectics have increased significantly over the last two decades. In addition, the emergence of the field of nanomaterials has resulted in an intense focus on expanding the range of applications and improving the properties of ZnO through nanostructuring. A number of ZnO nanostructures (e.g. nanoparticles, nanohelices, nanowires, nanobelts and nanorings) have been synthesized and represent interesting potential avenues for achieving advances in various practical areas of application. Nanoscale defects are another area that has become the subject of increasing research interest, particularly with the improvement of high-resolution imaging methods such as scanning transmission electron microscopy (STEM).

Inversion domain boundaries (IDBs) are one type of nanoscale defect that has been studied in AlN, GaN and ZnO-based systems. IDBs are defects at which an inversion of the ZnO *c*-axis polarity occurs. They form via the addition of specific dopants to ZnO once the solubility limit of these dopants has been exceeded. IDB formation is often accompanied by the formation of inversion domain networks, which can be described as homologous phases

with the chemical formula: $RMO_3(ZnO)_n$, where *R* and *M* represent the dopants occupying the basal-plane and pyramidal-plane IDBs (b-IDB and p-IDB) respectively. Although it has been shown that the formation of homologous phase compound members results in the modification of the structural and functional properties of ZnO, only a few systems (e.g. $In_2O_3(ZnO)_n$, $Ga_2O_3(ZnO)_n$ and $Fe_2O_3(ZnO)_n$) have been investigated extensively thus far. Thus, the identification of new $RMO_3(ZnO)_n$ systems, with b-IDB and p-IDB sites each occupied by either one or by multiple dopants, is crucial for obtaining new ZnO-based materials with properties that can be tuned based on the synthesis conditions and the concentrations and types of dopants occupying the b-IDB and p-IDB sites.

Preface

In this thesis, atomic-scale observations of IDBs and ID networks in several previously uninvestigated ZnO-based systems are described. The results of electronic structure calculations of model IDB structures and thermoelectric property measurements of ZnO-based materials, which have been studied in terms of the influence of both the dopant concentration and IDB formation on the thermoelectric properties, are also described.

Chapter 1 provides an introduction to the crystal structures and properties of ZnO, the $RMO_3(ZnO)_n$ homologous phase compounds and ZnO-based spinel phases. The thermoelectric properties of ZnO-based ceramics, in particular those containing inversion boundaries, are also described.

In Chapter 2, the synthesis methods used to prepare $Zn_{1-x-y}Mn_xAl_yO$ and $Zn_{1-x-y}Sn_xAl_yO$ ceramic samples, the experimental methods used to characterize the chemical and microstructural features of these materials, in particular the atomic structure of the IDBs, the theoretical methods used to model the IDB atomistic and electronic structures and the measurement techniques utilized to characterize the thermoelectric properties of the $Zn_{1-x-y}Mn_xAl_yO$ and $Zn_{1-x-y}Sn_xAl_yO$ ceramics are described.

Chapter 3 focuses on the phase and microstructural analysis of Mn-Al dual-doped ZnO using XRD, SEM, and BF/DF-TEM. The atomic structure of the b-IDBs in $Zn_{0.89}Mn_{0.10}Al_{0.01}O$ was studied in detail using HAADF/ABF-STEM and EDS/EELS. This chapter is based on results published in J. Am. Ceram. Soc. 100, 4252 (2017) Joshua Hoemke, Eita Tochigi, Tetsuya Tohei, Hidehiro Yoshida, Naoya Shibata, Yuichi Ikuhara and Yoshio Sakka, “Inversion Domain Boundaries in Mn and Al Dual-Doped ZnO: Atomic Structure and Electronic Properties” and

in J. Ceram. Soc. Jpn. 124, 515 (2016) Joshua Hoemke, Atta Ullah Khan, Hidehiro Yoshida, Takao Mori, Eita Tochigi, Naoya Shibata, Yuichi Ikuhara and Yoshio Sakka, "Sintering Characteristics and Thermoelectric Proprties of Mn-Al Co-Doped ZnO Ceramics". Several images within this chapter were originally published in the articles listed above and have been reprinted with permission from the Wiley Publishing Group and the Ceramic Society of Japan.

In chapter 4, ID network stabilization in Sn-Al dual-doped ZnO due to the localization of Sn and Al at the respective sites of the b-IDBs and p-IDBs, which also results in spinel phase suppression, is described. Phase and microstructural analysis of the Sn-Al dual-doped ZnO samples was carried out using XRD, SEM and BF/DF-TEM. The atomic structures of the b-IDBs and p-IBDs in $Zn_{0.98}Sn_{0.01}Al_{0.01}O$ were characterized in detail using HAADF/ABF-STEM and EDS/EELS. The results of this chapter are to be published as: Joshua Hoemke, Eita Tochigi, Tetsuya Tohei, Hidehiro Yoshida, Naoya Shibata, Yuichi Ikuhara and Yoshio Sakka, "Inversion Domain Network Stabilization and Spinel Phase Suppression in ZnO".

In chapter 5, the results of first principles calculations of the structural and electronic properties obtained for models based on the Mn-rich and Sn-rich b-IDBs observed experimentally are described. This chapter is partially based on results published in J. Am. Ceram. Soc. 100, 4252 (2017) Joshua Hoemke, Eita Tochigi, Tetsuya Tohei, Hidehiro Yoshida, Naoya Shibata, Yuichi Ikuhara and Yoshio Sakka, "Inversion Domain Boundaries in Mn and Al Dual-Doped ZnO: Atomic Structure and Electronic Properties".

In chapter 6, the thermoelectric properties of the Mn-Al and Sn-Al dual-doped ZnO ceramics are described and discussed. Comparisons are made with previous studies of the thermoelectric properties of ZnO ceramics containing IDBs. This chapter is based on results published in J.

Ceram. Soc. Jpn. 124, 515 (2016) Joshua Hoemke, Atta Ullah Khan, Hidehiro Yoshida, Takao Mori, Eita Tochigi, Naoya Shibata, Yuichi Ikuhara and Yoshio Sakka, “Sintering Characteristics and Thermoelectric Proprties of Mn-Al Co-Doped ZnO Ceramics” and AIP Conf. Proc. 1763, 050004 (2016) Joshua Hoemke, Atta Ullah Khan, Hidehiro Yoshida, Takao Mori, Eita Tochigi, Naoya Shibata, Yuichi Ikuhara and Yoshio Sakka, “Microstructural Analysis and Thermoelectric Properties of Sn-Al Co-Doped ZnO Ceramics”. Data described in this chapter were originally published in these articles and have been replotted in the figures included in this chapter.

The thesis is concluded by a summary of the results and an outlook toward future studies.

Contents

List of Abbreviations and Symbols

Annular Bright Field (ABF)

Atomic Number (Z)

Band Gap (E_g)

Basal-Plane Inversion Domain Boundary (b-IDB)

Bright-Field Transmission Electron Microscopy (BF-TEM)

Carrier Concentration (n)

Conduction Band Minimum (CBM)

Dark-Field Transmission Electron Microscopy (DF-TEM)

Density (ρ)

Density Functional Theory (DFT)

Density of States (DOS)

Effective Hubbard Parameter (U_{eff})

Electrical Conductivity (σ)

Electron Diffraction Pattern (EDP)

Electronegativity (U)

Electron Energy-Loss Spectroscopy (EELS)

Energy-Dispersive X-Ray Spectroscopy (EDS)

Fermi Level (E_f)

Generalized Gradient Approximation (GGA)

Head-to-Head (H-H)

High-Angle Annular Dark-Field (HAADF)

High Temperature (HT)

Inversion Domain (ID)

Inversion Domain Boundary (IDB)

Local Density of States (LDOS)

Partial Density of States (PDOS)

Projector Augmented-Wave (PAW)

Pyramidal-Plane Inversion Domain Boundary (p-IDB)

Room Temperature (RT)

Scanning Electron Microscopy (SEM)

Scanning Transmission Electron Microscopy (STEM)

Seebeck Coefficient (S)

Selected Area Electron Diffraction (SAED)

Specific Heat (C_p)

Stacking Fault (SF)

Tail-to-Tail (T-T)

Thermal Conductivity (κ)

Thermal Diffusivity (α)

Thermoelectric Figure of Merit (ZT)

Thermoelectric Power Factor (PF)

Transmission Electron Microscopy (TEM)

Valence Band Maximum (VBM)

Vienna Ab Initio Simulation Package (VASP)

X-Ray Diffraction (XRD)

Zinc Oxide (ZnO)

Zinc Vacancy (V_{Zn})

List of Figures

Appendix

List of Tables

Chapter 1. Introduction

1.1 Zinc Oxide

1.1.1 Crystal Structure and Functional Applications

ZnO is a wide-bandgap semiconductor that is stable in the hexagonal wurtzite phase (space group #186, $P_6 3mc$) at room temperature under atmospheric pressure [1]. An inclined view of the unit cell of ZnO is shown in Fig. 1.1 (a). The Zn and O atoms are colored grey and red respectively. The unit cell consists of two ZnO formula units and both Zn and O atoms occupy tetrahedral sites. Views of the ZnO crystal structure along the $[1\bar{2}10]$ (*a*-axis), $[1\bar{1}00]$ (*m*-axis) and $[0001]$ (*c*-axis) directions are shown in Fig. 1 (b), (c) and (d) respectively. The lattice constants and bond lengths of ZnO are listed in Table 1.1. The ZnO lattice consists of alternating cation (Zn) and anion (O) layers along the *c*-axis and exhibits an αβαβ *c*-axis cation stacking sequence. When viewed along the $[1\bar{2}10]$ direction, the Zn and O atoms can be imaged as individual cation and anion columns that appear as dumbbell pairs. As shown in Fig. 1 (c), the $[1\bar{1}00]$ direction exhibits a rectangular symmetry.

ZnO is a non-centrosymmetric crystal and thus lacks inversion symmetry and possesses a polar axis, which is aligned with the *c*-axis. [1]. The exposed Zn-rich face along the +*c* direction corresponds to a $\{0002\}$ plane, while the exposed O-rich face along the -*c* direction corresponds to a $\{000\bar{2}\}$ plane. The non-centrosymmetric character is attributed to the cation-anion stacking sequence along the *c*-axis. Zn atoms have a four-fold, tetrahedral coordination with nearest neighbor oxygen atoms. An observation of the Zn atom, labeled Zn in Fig. 1 (a), shows that it is shifted upward along the [0001] direction toward the O4 oxygen atom and out of the plane of the O1, O2 and O3 oxygen atoms. This shift along the positive [0001] direction results in the loss of inversion symmetry and induces a piezoelectric character

in the ZnO crystal [1]. A downward shift of the Zn atom along the $[000\bar{1}]$ direction, while keeping the oxygen sublattice fixed, would result in an inversion of the cation-anion stacking sequence along the [0001] direction and, hence, in an inversion of polarity of the crystal lattice. The different polarities, +*c* and –*c*, that occur in ZnO result in different functional properties for the Zn (+*c*) and O (-*c*) terminated surfaces [1].

Table 1.1. Lattice Constants and Bond Lengths of Undoped ZnO [1]	
Lattice Constant, *a*	**3.25 Å**
Lattice Constant, *c*	**5.21 Å**
***c*/*a* Ratio**	**1.602**
Zn-O Bond Length	**1.95 Å**

The wide bandgap (E_g) of ZnO (E_g: 3.3-3.44 eV [2]) makes it suitable for use in applications as a transparent conducting oxide (TCO) semiconductor, for which an optical bandgap $\geq$ 3.1 eV is necessary for use in the visible range. There are a number of other advantages inherent to ZnO including a low cost, abundant and non-toxic constituent elements, n-type (as well as limited reports of p-type [1]) dopability and a non-centrosymmetric crystal structure, which imparts a piezoelectric character [1-3]. ZnO is currently being investigated for use in a wide range of device applications including TCOs [4], spintronic devices [5], piezoelectrics [6], light-emitting diodes (LEDs) [6], high mobility 2D electron gas systems [7] and oxide thermoelectrics [8-16]. Intrinsic defects such as oxygen vacancies, V_o, and zinc interstitials, Zn_i, are typically found in ZnO; these defects may be the source of the n-type semiconducting character often observed in nominally undoped ZnO [1].

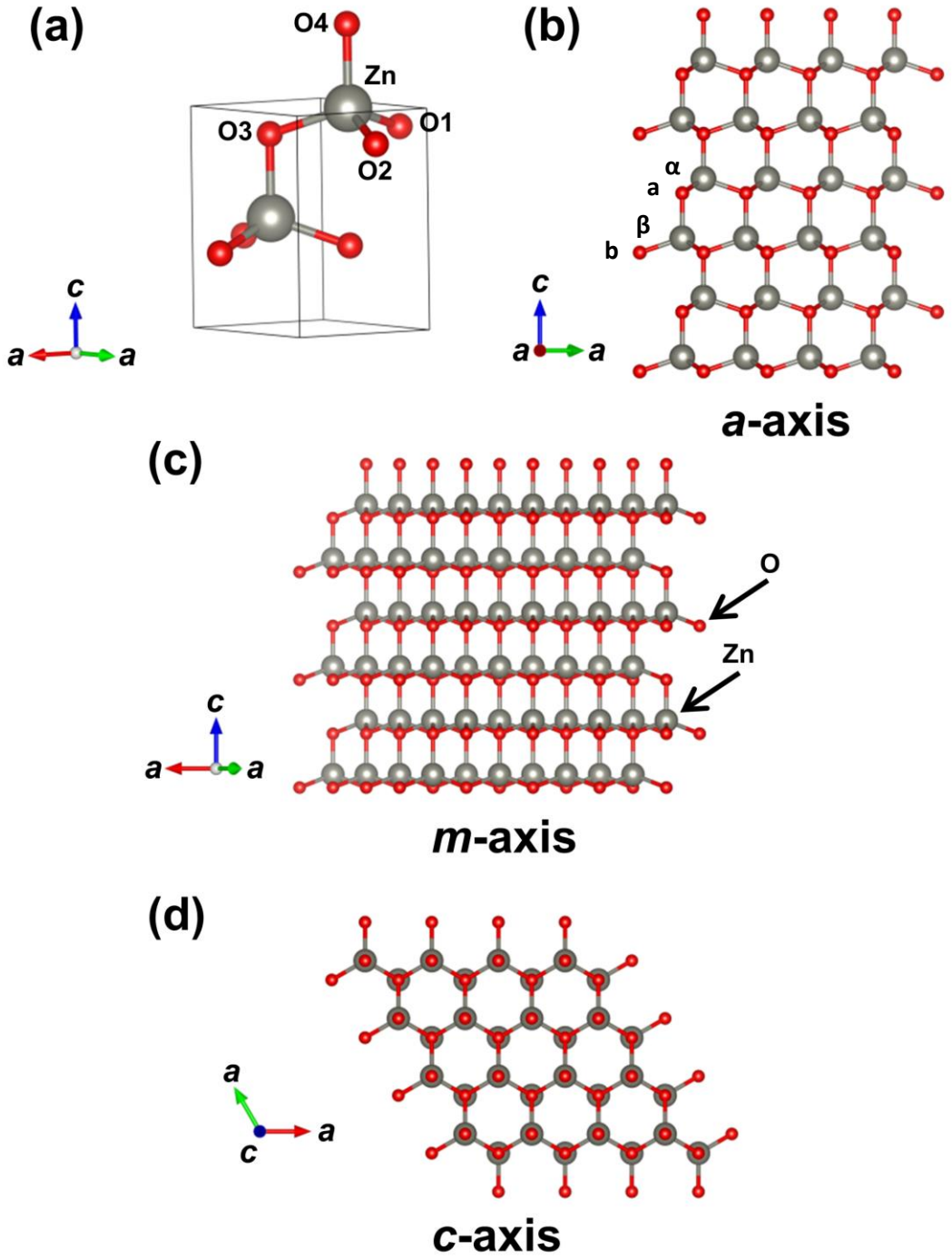

Figure 1.1. (a) Inclined view of the ZnO unit cell. Zn and O atoms are colored grey and red respectively. **(b)** *a*-axis view of the crystal structure of ZnO. The cation-anion stacking sequence along the *c*-axis, b-β-a-α, can be observed at the *a*-axis. **(c)** *m*-axis and **(d)** *c*-axis views of the crystal structure of ZnO. By observing the cation-anion stacking sequence along the *c*-axis, at either the *m*- or *a*-axis, the polarity of the crystal can be determined. The crystal structures were visualized using VESTA [17].

1.1.2 Effects of Doping on the Electronic and Microstructural Properties of ZnO

Through the addition of dopants to ZnO, it is possible to significantly increase the carrier density (from ~ 10^{15} cm^{-3} for undoped ZnO to ~ 10^{18} cm^{-3} in 0.25 at. % Al-doped ZnO [13]). n-type dopants used in ZnO typically have a a 3+ valence (e.g. Al^{3+} [9], Ga^{3+} [16], In^{3+} [8] and Fe^{3+} [15]) or 4+ valence (e.g. Ti^{4+} [11] and Sn^{4+} [12]). In contrast, p-type doping of ZnO has been more difficult to achieve, although a number of dopants (e.g. N, P, As and Sb [1]) and synthesis methods [1] have been reported to result in p-type semiconducting character in ZnO. The solubility limit of most dopants in ZnO is low (Ti^{4+}: $\leq$ 1 at. % [11], Al^{3+}: 0.3 at. % [18], Sn^{4+}: < 0.1 at. % [19], Fe^{3+}: 0.05-0.4 at. % [20], In^{3+}: $\leq$ 0.1 at. % [21]), with the exception of several dopants that have a 2+ valence (e.g. Mg^{2+}: > 10 at. % [1,10,22], Mn^{2+}: 3-8 at. % [23-25] and Co^{2+}: 12-19.5 at. % [26]). The addition of dopants with a high solubility limit in ZnO (e.g. Cd^{2+} and Mg^{2+}) has proven to be effective for modifying the band structure of ZnO [1].

In the case of the addition of dopants with high valences ($\geq$ 3+) and low solubility limits, when the solubility limit is exceeded changes occur in the microstructure of ZnO. Typically, spinel secondary phases (e.g. $ZnAl_2O_4$ [9,18], $ZnGa_2O_4$ [16,27], $ZnFe_2O_4$ [15,20], Zn_2SnO_4 [12,19] and Zn_2TiO_4 [11]) form at dopant concentrations exceeding the solubility limit. Spinel phases often appear as precipitates that are found within ZnO grains or at grain boundaries. Alternatively, homologous phase compounds with the chemical formula: $RMO_3(ZnO)_n$, where *R* and *M* are the dopants which occupy the basal and pyramidal inversion domain boundaries (b-IDB and p-IBD) in the defect networks that form the homologous phases, can form under specific sintering conditions when trivalent dopants such as Ga^{3+} [16], In^{3+} [8,14,28] and Fe^{3+} [20] are added to ZnO. Higher-valence dopants (e.g. Sn^{4+} [29], Ti^{4+} [30] or Sb^{5+} [31]) have not been found to cause homologous phase formation in ZnO, although they can induce the formation of a microstructure with a single b-IDB in each grain [29-31].

1.2 Inversion Domain Boundaries (IDB) in the $RMO_3(ZnO)_n$ Homologous Phase Compounds

1.2.1 Structure and Properties of the $RMO_3(ZnO)_n$ Phases

Schematics of the microstructure observed in the $RMO_3(ZnO)_n$ homologous phases are shown in Fig. 1.2 and Fig. 1.3. The basal-plane IDBs (b-IDB) and pyramidal-plane IDBs (p-IDB) are labeled. b-IDBs are composed of monolayers of edge-sharing octahedra containing cation dopants. b-IDBs form via two operations resulting in a shift of the ZnO lattice. These operations include: 1) an inversion of the ZnO *c*-axis polarity and 2) a shift of the inverted section of the crystal lattice along the *m*-axis, producing a *c*-axis stacking fault and a local cubic cation stacking sequence, at the b-IDB interface [31]. A head-to-head, HH $(\rightarrow|\leftarrow)$, configuration of the *c*-axis is observed at the b-IDB and Zn tetrahedra in the bulk-like domain regions above and below the b-IDB share corners with the b-IDB octahedra [20,31,32]. p-IDBs form at planes diagonal to the ZnO *c*-axis with indices of $\{11\bar{2}l\}$ and p-IDB sites accommodate dopants in a five-fold, or trigonal bipyramidal, coordination [33]. p-IDBs can vary in width from an atomic monolayer to several atomic layers, depending on the ionic radius of the dopant(s) occupying the p-IDB sites [33]. In inversion domain (ID) networks consisting of both b-IDBs and p-IDBs, the *c*-axis must undergo a second inversion, between neighboring b-IDBs, at the p-IDB, which results in a tail-to-tail $(\leftarrow|\rightarrow)$ configuration of the *c*-axis at the p-IDB interface [20,31-33].

1.2.2 IDB Formation Mechanism

The formation of planar two-dimensional (2D) defects such as IDBs can occur when the dopant solubility limit is exceeded in ZnO [34]. The formation of IDBs becomes energetically favorable in order to relieve strain within the ZnO lattice and maintain charge balance by incorporating excess dopants at the b-IDB and p-IDB sites [35]. It has been shown

that large dopants (e.g. In) prefer to occupy the b-IDB, while smaller dopants (e.g. Al) prefer to occupy the p-IDB [35]. IDB nucleation is controlled by two specific diffusion mechanisms, depending on the type of dopant. These include internal diffusion, which is characteristic of dopants with a 3+ valence (e.g. In^{3+} and Fe^{3+}), and surface diffusion, the primary mechanism by which higher-valence dopants (e.g. Sn^{4+} and Sb^{5+}) induce IDB formation [32]. The internal diffusion mechanism results in homologous phase development, as dopants with a 3+ valence are mobile and can stabilize the formation of both b-IDBs and p-IDBs [32]. IDBs may nucleate preferentially at octahedral sites near surface clusters of zinc-vacancies (V_{Zn}) [32]. Dopant diffusion occurs by a V_{Zn}-mediated mechanism and b-IDBs can nucleate either at surfaces and propagate into the ZnO grain interior or nucleate within grains and propagate to the grain surface [20,32,33]. Thus, because dopants such as In^{3+} or Fe^{3+} can diffuse to and occupy both b-IDBs and p-IDBs, doping with only In^{3+} or Fe^{3+} is sufficient to acheive complete homologous phase formation in ZnO, with networks of IDs developing throughout entire ZnO grains [20,32].

Higher-valence dopants (e.g. Sn^{4+} and Sb^{5+}) are likely to be less mobile and cannot readily diffuse within the crystal lattice of ZnO [32]. This results in the growth of b-IDBs via the recrystallization of neighboring normal ZnO grains onto grains containing b-IDBs [29,36,37]. Grains with IDBs are more stable than normal ZnO grains and grow anisotropically along the direction parallel to the basal plane by consuming normal ZnO grains until the IDB-containing grains eventually impinge upon each other, inhibiting further grain growth [29,36,37]. After this occurs, grain growth proceeds considerably more slowly, primarily by Ostwald ripening in the direction orthogonal to the basal plane [29,36,37]. Because higher-valence dopants such as Sn^{4+} or Sb^{5+} cannot stabilize the formation of p-IDBs, only a single b-IDB develops in each grain in ZnO doped with only Sn^{4+} [29,32,36] or Sb^{5+} [30-32,37].

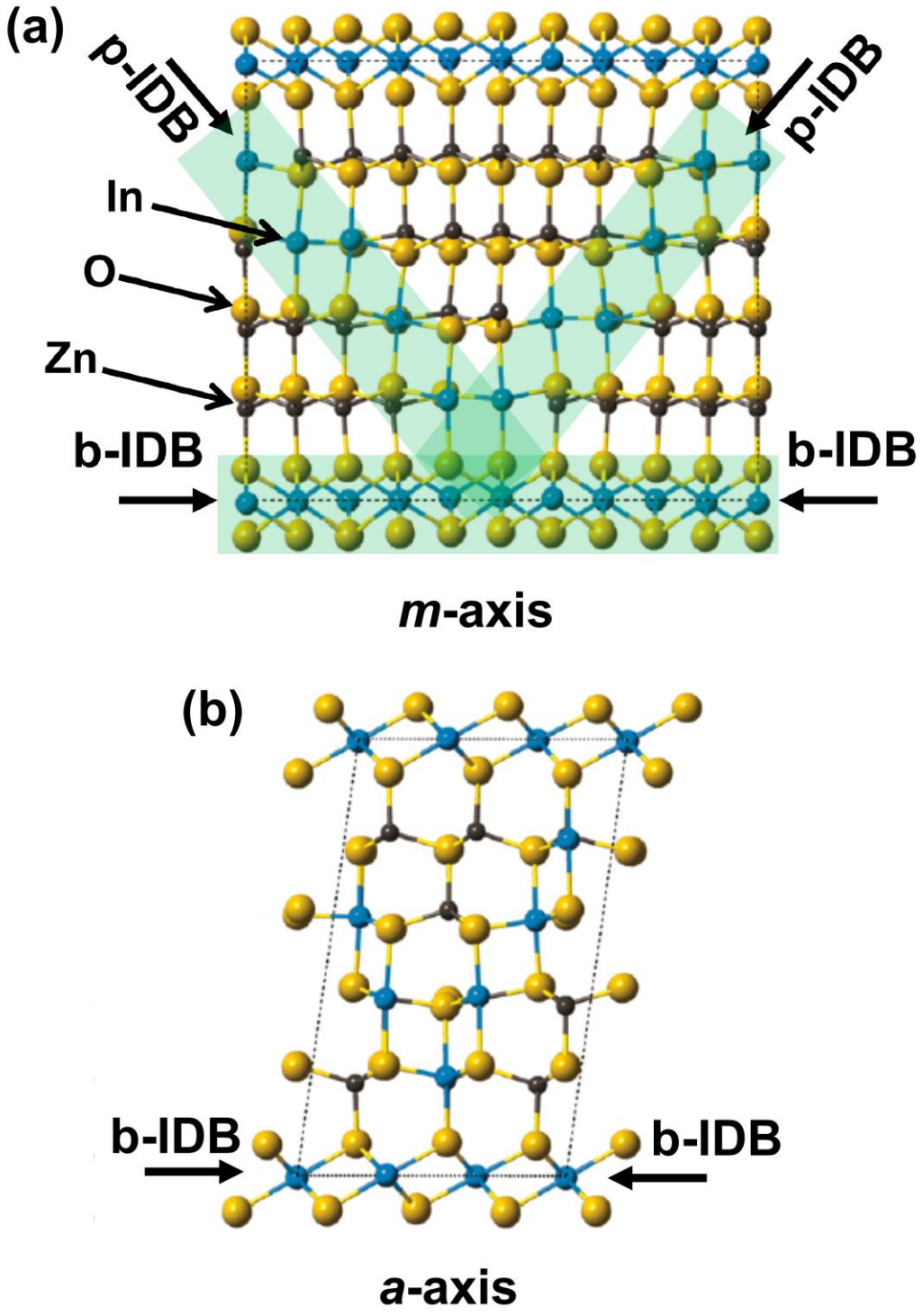

Figure 1.2. Models of the atomic structure of the zigzag-like inversion domain networks that form in the $RMO_3(ZnO)_n$ homologous phase compounds. **(a)** The model proposed by Goldstein et al. [33], which consists of b-IDBs and p-IDBs that can be simultaneously viewed edge-on at one of the *m*-axes of ZnO. **(b)** The model proposed by Da Silva et al. [35], in which both b-IDBs and p-IDBs can be simultaneously viewed edge-on at one of the *a*-axes. The model shown in (a) has been observed experimentally [33]. The images are adapted from [33] and reprinted with permission from the American Chemical Society.

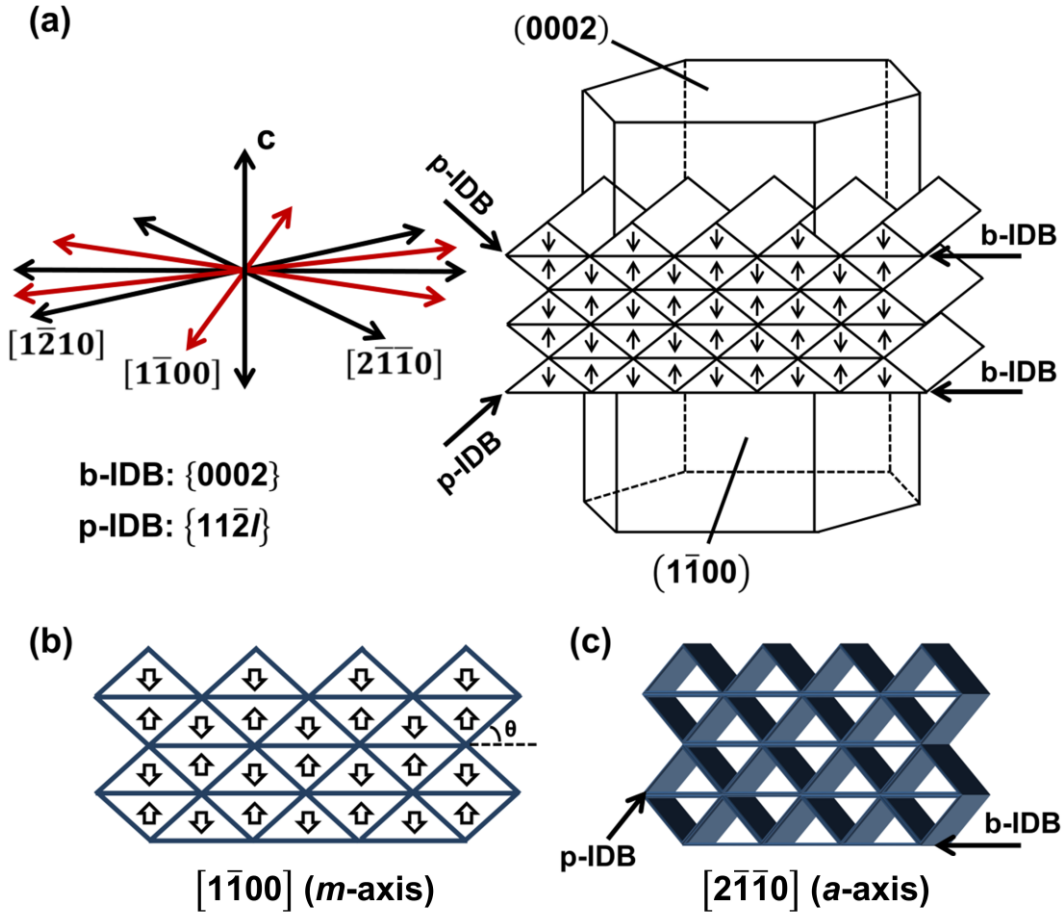

Figure 1.3. Schematics of the inversion domain microstructure. In **(a)** the inversion domain microstructure is shown with respect to the crystallographic zone-axes and hexagonal crystal structure of ZnO. b-IDBs form at {0002} planes, while p-IDBs form at {11$\bar{2}l$} planes. **(b)/(c)** Views of the inversion domain networks at the (b) [1$\bar{1}$00] and (c) [2$\bar{1}\bar{1}$0] zone-axes. The vertical arrows in (a) and (b) represent the polarity of the *c*-axis in individual inversion domains. Both b-IDBs and p-IDBs can be viewed edge-on at only one of the *m*-axes (e.g. [1$\bar{1}$00]). The angle, θ, that forms between the b-IDBs and p-IDBs is shown in (b).

1.2.3 Control of the Electronic and Microstructural Properties of the $RMO_3(ZnO)_n$ Phases Through Dopant Selection

A number of experimental studies have been carried out to investigate the influence of the varying the dopant concentration on the properties of the $RMO_3(ZnO)_n$ homologous

phases. The $In_2O_3(ZnO)_n$ system has been investigated most extensively and it was found that optimal properties (e.g. electrical conductivity and optical transparency) are achieved at specific values of *n* [14,28,38]. As the value of *n* decreases, the electrical conductivity increases, due to increasing carrier transport isotropy [38]. For larger values of *n*, carrier transport anisotropy increases due to increasing conducting electron localization within the In_2O_3 b-IDB layers [14,28,38]. It has been determined that the electronic structure of $In_2O_3(ZnO)_n$ is dependent on the characteristic features of the electronic structures of the end members (i.e. In_2O_3 and ZnO) [38], indicating the possibility to modify the electronic properties of the $RMO_3(ZnO)_n$ homologous through the selection of the specific *R* and *M* dopants substituting at the b-IDB and p-IDB sites respectively.

In addition to the electronic properties, it has also been shown that the microstructure of the $RMO_3(ZnO)_n$ phases can be modified by changing the dopant type and controlling the dopant concentration. The b-IDB spacing along the *c*-axis can be modified based on the dopant concentration and the angle formed between the p-IDB and b-IDB is dependent on the specific type of dopant occupying the p-IDB. As the size of the dopant occupying the p-IDB increases (e.g. in the case of In), the p-IDB angle increases in order to reduce strain within the ZnO lattice by minimizing the number of dopants in each basal-plane segment composing the p-IDB; in contrast, smaller dopants (e.g. Fe) induce less strain within the ZnO lattice and can thus be incorporated at higher concentrations, resulting in p-IDBs composed of basal-plane segments several atomic planes thick [33]. A general relationship between the *l* value of the p-IDB plane, $\{11\bar{2}l\}$, and the average number of cation columns in each basal-plane segment composing the p-IDB is: *l*/2 (e.g. in In-doped ZnO *l* ~2-3, resulting in p-IDBs with basal-plane segments ~1-1.5 atomic columns wide on average) [33]. Co-occupation of the p-IDB by several different dopants could enable the modification of the p-IDB angle between the characteristic values for the case of single dopant occupation. The *c*-axis stacking sequence of cation planes across the b-IDB, which can be determined when the b-IDB is viewed along the *a*-axis, is also affected

by the type of cation occupying the b-IDB. A cation stacking sequence of αβαβ|α|γαγα has been found to be stable in In [21], Sn [39] and Fe-doped ZnO [40], while Sb-doped ZnO exhibits a stacking sequence of αβαβ|α|γβγβ [31]. The stable cation stacking sequence may be correlated with the ionic radius or valence state of the dopant occupying the b-IDB.

A number of studies have also been carried out to analyze the influence of the concentration of grains containing IDBs on grain growth in ZnO ceramics doped with higher-valence IDB-forming dopants such as Sn^{4+} [29,36] and Sb^{5+} [37]. Although these dopants do not cause complete homologous phase formation, they result in a microstructure with a single b-IDB in each grain [29-32,36,37]. As described in Section 1.2.2, ZnO grains containing IDBs grow preferentially in the direction parallel to the basal plane while consuming the surrounding normal ZnO grains in the process. This results in a high rate of grain growth, producing anisotropically-shaped IDB-containing grains, that is only halted when the IDB-containing grains impinge on each other. A higher initial concentration of IDB-containing grains results in a smaller mean free path to impingement, which produces a final microstructure with a reduced grain size [29,36,37].

1.3 Spinel Phase Formation in ZnO

1.3.1 Structure and Properties of the Spinel Phases

The $RMO_3(ZnO)_n$ homologous phases only form when ZnO is doped with specific elements (e.g. Ga^{3+}, In^{3+} and Fe^{3+}) and sintered under specific conditions (e.g. at high temperatures for long times [28,41]). In contrast, spinel secondary phase formation has been observed more frequently and occurs when ZnO is doped with a broad range of dopants and sintered under a wide range of conditions. The properties of some of the spinel phases which form when specific dopants are added to ZnO are listed in Table 1.2. The spinel phases can display a wide range of lattice constants that are largely dependent on the type of dopant M, in

the specific $Zn_xM_{3-x}O_4$ spinel compound. The spinel compounds usually have a cubic lattice structure, as shown in Fig. 1.4 for the case of $ZnAl_2O_4$, although tetragonal phases can also form (e.g. the $Zn_xMn_{3-x}O_4$ compounds, where a Jahn-Teller distortion of the Mn^{3+} occupied octahedral sites occurs [42]). Zn typically occupies the tetrahedral site, while the M dopant occupies the octahedral site. However, in the case of dopants with higher valences (e.g. Sn^{4+} [43], Ti^{4+} [44] and Sb^{5+} [45]), Zn can also occupy the octahedral site. The spinel phases form as precipitates and are observed within ZnO grains and at grain boundaries. IDBs form as 2D planar defects which may be precursors to spinel phase formation [34]. This is supported by the shared structural features (e.g. edge-sharing octahedra containing dopant atoms) present in both IDBs and the ZnO-based spinel phases and also by the fact that IDBs form at lower temperatures than the Zn_2SnO_4 spinel phases in Sn-doped ZnO [29,32]. However, this relationship has not been established conclusively.

Table 1.2. ZnO-Based Spinel Compounds

Compound	Lattice Constant	Band Gap
Zn_2SnO_4	*a*:8.657 Å [43]	3.25-4.1 eV [43]
$ZnAl_2O_4$	*a*:8.085 Å [46]	3.8-6.6 eV [47-49]
$ZnGa_2O_4$	*a*:8.33 Å [48]	4.4-5.0 eV [47,48]
$Zn_7Sb_2O_{12}$	*a*:8.595 Å [50]	2.6 eV [50]
$ZnMn_2O_4$	*a*: 8.087 Å [51] *c*: 9.245 Å [51]	1.28 eV [52]
$ZnFe_2O_4$	*a*:8.443 Å [53]	2.43-2.61 eV [54]
Zn_2TiO_4	*a*: 8.48 Å [55]	3.1 eV [55]

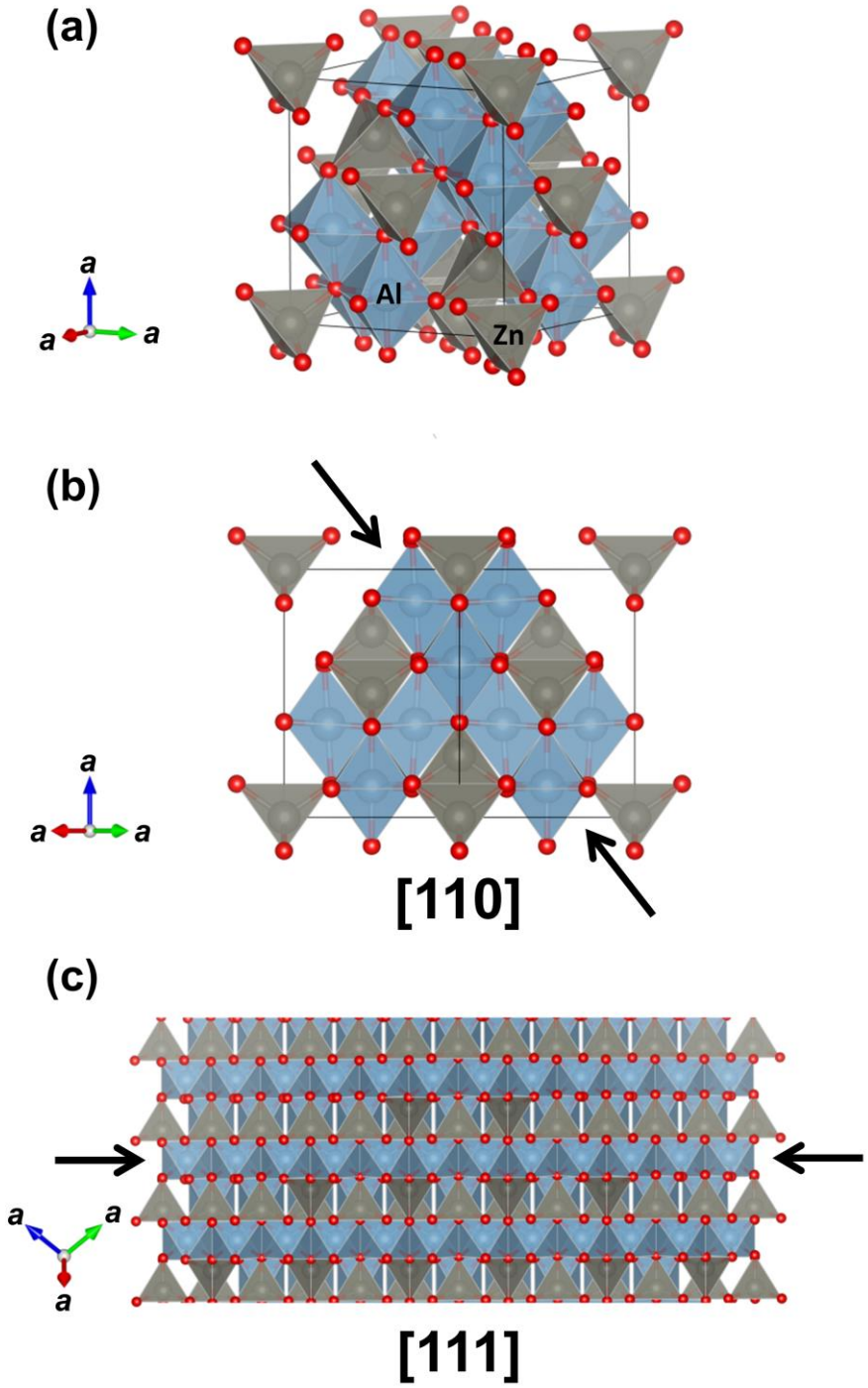

Figure 1.4. (a) Inclined view of the unit cell of $ZnAl_2O_4$. Red spheres represent oxygen and Zn tetrahedra and Al octahedra are colored grey and blue respectively. **(b)** [110] zone-axis view of the $ZnAl_2O_4$ unit cell. The layer of Al octahedra indicated by the black arrows resembles the ID network b-IDB cation layer as viewed along the *a*-axis. **(c)** Extended view of the crystal structure of the $ZnAl_2O_4$ spinel, viewed at the [111] zone-axis. The layer of Al octahedra indicated by the arrows resembles the ID network b-IDB cation layer as viewed at the *m*-axis. The crystal structures were visualized using VESTA [17].

1.3.2 Influence of Spinel Secondary Phases on the Properties of ZnO

At high dopant concentrations, the influence of the spinel phases on the properties of ZnO can become significant and effects that are detrimental to device functionality may be observed. Spinel phase formation often negatively impacts the electrical conductivity (σ) of ZnO, which begins to drop sharply when the n-type dopant solubility limit is exceeded and the concentration of the spinel phases increases in Al [9], Sn [12,19], Ga [27] and Sb [56] doped ZnO. This is due to the low electrical conductivity of the spinel phases, which may be related to their large band gap, E_g, values ($ZnAl_2O_4$: 3.8-6.6 eV [47-49], Zn_2SnO_4: 3.25-4.1 eV [43] and $ZnGa_2O_4$: 4.4-5.0 eV [47,48], values listed are ranges). This effect is in stark contrast to homologous phase development in systems such as $In_2O_3(ZnO)_n$, in which the formation of secondary phases (e.g. spinels) does not occur, as the homologous phases display optimal thermoelectric and optoelectric properties at specific values of n and do not exhibit σ degradation due to secondary phase formation until large In_2O_3:ZnO ratios are reached [14,28,38].

1.4 Thermoelectric Properties of ZnO

1.4.1 Thermoelectric Materials

Thermoelectric materials are receiving increasing attention due to their potential application in the conversion of waste heat to electricity [57-59]. Similar to photovoltaics, wind energy, hydroelectricity, geothermal energy and biomass-fueled energy generation, thermoelectrics represent a source of renewable energy and an alternative to fossil fuels and coal as a means of energy production. Thermoelectric energy conversion offers a number of advantages including being completely solid state and not producing any waste products [57-59], unlike nuclear energy generation or energy production methods that result in the emission of CO_2 or other greenhouse gases, and also being scalable for a wide range of applications [57].

Thermoelectric energy conversion is based on the Seebeck effect, discovered by Thomas Johann Seebeck in 1821. According to the Seebeck effect, when a thermal gradient is applied to a thermoelectric material, an electrical voltage is generated due to the transport of electrons from the hot to the cold side of the material. Related to the Seebeck effect is the Seebeck coefficient, which is defined as: $S = -\frac{\Delta V}{\Delta T}$, i.e. the ratio of the voltage drop, ΔV, to the temperature difference applied to a material, ΔT, under which ΔV develops. The converse of the Seebeck effect is the Peltier effect, which describes the generation of a thermal gradient in response to the application of an electrical potential to a material. A schematic of a typical thermoelectric energy conversion module is shown in Fig. 1.5 (a) [57]. It consists of two primary components, usually an n-type and p-type semiconductor, and also a positive and negative electrical lead. Thermoelectric modules are electrically connected in series and arranged so that a thermal gradient can develop between the top and bottom faces of the complete device and electricity can flow between neighboring modules and ultimately through the positive and negative leads connected to the complete device.

Thermoelectric performance is evaluated based on the figure of merit: $ZT = (\sigma S^2)T/\kappa$, where σ, S, κ and T are the electrical conductivity, Seebeck coefficient, thermal conductivity and temperature respectively. ZT is maximized when the electrical conductivity and Seebeck coefficient are high and the thermal conductivity is low. In practice, this proves difficult to achieve because these parameters have an interdependency. The electrical conductivity is expressed as $\sigma = e*n*\mu$, where e, n and μ are the electron charge, carrier concentration and electronic mobility respectively. The Seebeck coefficient for a degenerate semiconductor, which many of the best thermoelectric materials are, or a metal can be expressed as: $S = \frac{\left(8\pi^2 k_B^2\right)}{\left(3eh^2\right)} m^* T \left(\frac{\pi}{3n}\right)^{\frac{2}{3}}$, where k_B is Boltzmann's constant, h is Planck's constant and m^* is the electron mass [57]. The electrical conductivity has a direct relationship with the carrier

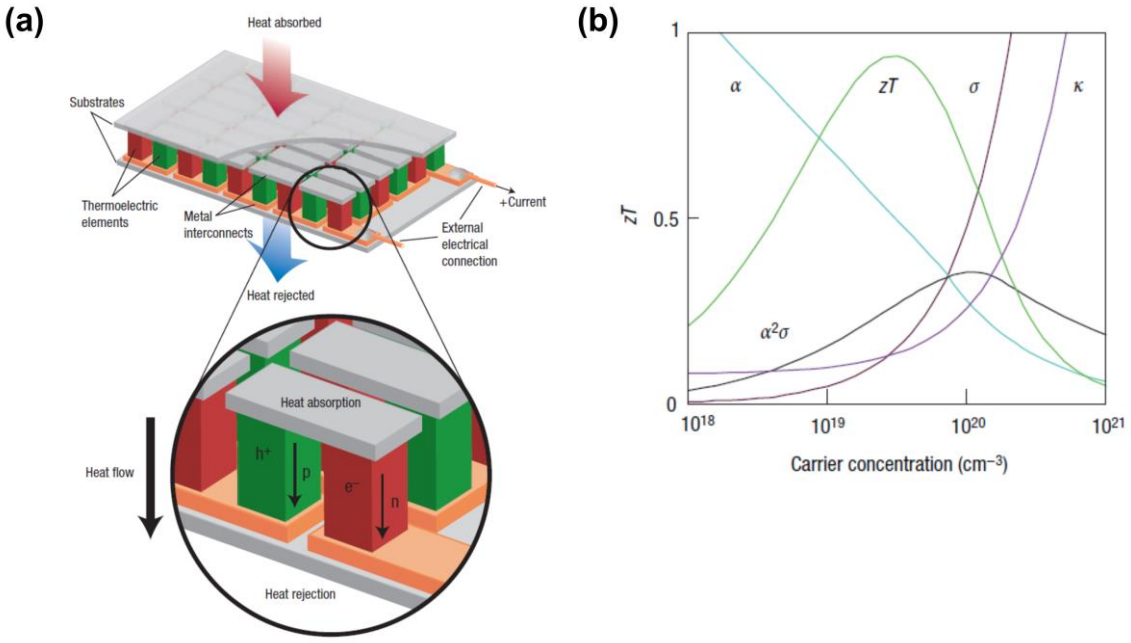

Figure 1.5. (a) Schematic of a typical thermoelectric module. n-type and p-type elements are connected electrically in series, but stacked within a single layer in order to allow a thermal gradient to develop across the faces of the module. The thermal gradient results in electron and hole countercurrents, which produce a net electric current through the complete module. **(b)** Graph showing the dependence of the thermoelectric parameters on the carrier density (n) for a typical thermoelectric material. The Seebeck coefficient (α in the graph shown) and electrical conductivity respectively exhibit an inverse and a direct dependence on n. Thus, values of n exist for which both ZT and the power factor, $\alpha^2\sigma$, are maximized. The images are adapted from [57] and reprinted with permission from the Nature Publishing Group.

concentration, while the Seebeck coefficient has an inverse relationship. Thus, the power factor, defined as σS^2, attains a maximum value at a specific carrier density, as shown in Fig. 1.5 (b). In addition, the thermal conductivity consists of two components, being defined as $\kappa = \kappa_l + \kappa_e$, where κ_l and κ_e are the lattice and electronic components of the thermal conductivity. κ_e is defined as $L\sigma T$, where L is the Lorenz factor, which is a constant for free electrons [57]. Often, the lattice component of the thermal conductivity is significantly larger than the electronic component. However, when the lattice component is low and the carrier density is high, the electronic component can become significant, resulting in an increase of the thermal

conductivity as the electrical conductivity increases. These issues have led to great difficulties in achieving high ZT values over the last 70 years. However, recently a number of new strategies including nanostructuring and the investigation of new, more complex thermoelectric materials have created new avenues to realizing improvements in the maximum ZT values attainable [13-16,57-60,65].

1.4.2 ZnO Ceramics for Thermoelectric Energy Conversion

In recent years, oxide thermoelectric materials have begun to receive attention. In comparison to conventional high performance thermoelectrics such as Bi_2Te_3, PbTe, $CoSb_3$, Mg_2Si and SiGe, oxide thermoelectrics have a number of advantages, including low material cost, abundant constituent elements, non-toxicity and resistance to degradation in air during use at high temperatures [58,59]. As shown in Table 1.3, several p-type oxide thermoelectric materials with high ZTs approaching or even exceeding 1 [61,62], often considered the threshold ZT value for commercial implementation [57-59], have been identified. In contrast, as shown in Table 1.3, the maximum ZTs identified for n-type thermoelectrics thus far are lower [9,13-16,58,60,63-65]. The construction of thermoelectric modules, as shown in Fig. 1.5 (a), ideally requires both n-type and p-type components. Thus, the development of new n-type oxides that exhibit high ZT values is critical for the advancement of the usage of oxide materials in practical thermoelectric energy generation applications.

ZnO is among the n-type oxide thermoelectrics that have been studied most extensively over the last two decades [58]. In terms of potential for use in thermoelectric energy conversion, ZnO has a number of advantages, including low material cost, abundant constituent elements, non-toxicity and stability in air at temperatures in excess of 1000°C [3,58]. However, the highest ZTs identified for ZnO thus far (~0.3-0.44 [9,13]) are still too low for usage in practical applications. In comparison to undoped ZnO [9,10], the thermoelectric

Table 1.3. Properties of Conventional Thermoelectrics and Oxide Thermoelectrics					
Stoichiometry	**Transport: n-type or p-type**	**Figure of Merit, ZT**	**Measurement Temperature**	**Description of Material**	**Ref.**
$Zn_{0.98}Al_{0.02}O$	n-type	0.30	1000°C	Bulk Polycrystal	[9]
Nano-AZO	n-type	0.44	730°C	Nanostructured Bulk Polycrystal	[13]
$In_2O_3(ZnO)_4$	n-type	0.09	800°C	Bulk Polycrystal IDB Formation	[14]
$Zn_{0.82}Fe_{0.18}O$	n-type	0.02	800°C	Bulk Polycrystal IDB Formation?	[15]
$Zn_{0.96}Ga_{0.04}O_{1.02}$	n-type	0.09	750°C	Bulk Polycrystal IDB Formation	[16]
$Zn_{1-2x}Ga_xIn_xO$[(a)]	n-type	0.19	500°C	Bulk Polycrystal IDB Formation	[60]
$Na_xCoO_{2-\delta}$	p-type	1.20	530°C	Single Crystal	[61]
$Ca_3Co_4O_{9+\delta}$	p-type	0.60	850°C	Bulk Polycrystal	[62]
La-$SrTiO_3$	n-type	0.27	800°C	Single Crystal	[63]
$SrTi_{0.8}Nb_{0.2}O_3$	n-type	0.35	730°C	Bulk Polycrystal	[64]
$SrTiO_3$/ $SrTi_{0.8}Nb_{0.2}O_3$	n-type	0.24	20°C	Thin-Film Superlattice	[65]
$Bi_2Te_{3-x}Se_x$	n-type	1.15	100°C	Bulk Ingot Nanostructured	[59]
PbTe-Ag_2Te	n-type	1.60	500°C	Nanocomposite	[59]
SiGe	n-type	1.30	900°C	Nanocomposite	[59]
$Mg_2Si_{1-x}Sn_x$	n-type	1.30	430°C	Bulk Alloy	[59]
Fe,Te-$CoSb_3$	n-type	1.30	550°C	Nanocomposite	[59]

[(a)] $x = 0.004$

properties of bulk ZnO ceramics are improved considerably by doping with donor elements such as Al^{3+} [9], Ti^{4+} [11], Sn^{4+} [12], In^{3+} [14], Fe^{3+} [15], Ga^{3+} [16] and Sb^{5+} [56]. However, when the solubility limit of these elements in ZnO is exceeded, spinel phases begin to form and

the thermoelectric performance may be degraded as the content of the spinel phases increases. Thus, it is necessary to find new strategies by which to circumvent the bottlenecks associated with conventional dopant addition in order to improve the functional performance of bulk ZnO ceramics for electronic device applications such as thermoelectric energy conversion.

1.4.3 IDBs in ZnO Thermoelectrics

In contrast to conventionally-doped bulk ZnO thermoelectric ceramics, the thermoelectric properties of the $In_2O_3(ZnO)_n$ homologous phase compounds exhibit different behavior due to the formation of nanoscale defects, specifically b-IDBs and p-IDBs. 2D planar defects such as IDBs have been demonstrated to influence the thermoelectric properties of ZnO significantly, with IDBs acting as nanoscale defects which scatter phonons, resulting in the reduction of the thermal conductivity [14,16,60]. In addition, electronic potential barriers or quantum wells may form at interfaces such as IDBs, resulting in the modification of the electronic transport properties, i.e. the electrical conductivity and Seebeck coefficient [65-67]. The ZnO-In_2O_3 phase diagram indicates that spinel phase formation does not occur and, consequently, no electrical conductivity reduction due to spinel phase formation occurs over the entire range of In_2O_3:ZnO stoichiometries [14,28]. As shown in Fig. 1.6, for the $In_2O_3(ZnO)_n$ homologous phase compounds, a maximum power factor is achieved for a specific value of n at which the carrier transport isotropy is high (i.e. at a low value of n), while the thermal conductivity can simultaneously be significantly reduced due to the formation of ID networks with a high density of interfaces [14,38]. Thus, the study of the thermoelectric properties of new $RMO_3(ZnO)_n$ systems and the influence of IDB formation on the thermoelectric properties of ZnO is useful for the design of new nanostructured ZnO thermoelectrics with properties that can be maximized based on the overall concentration and type of the R and M dopants, which occupy the b-IDB and p-IDB sites respectively, and also based on the fractional occupancy of specific IDB sites by these dopants. It should be noted

that in the case of very low values of n, i.e. $n \leq 3$, in the $In_2O_3(ZnO)_n$ homologous phase compounds, the thermoelectric performance begins to decline as In_2O_3 secondary phases appear, due to the difficulty of achieving structural equilibrium even at high temperatures in homologous phase compounds with very small IDB interface periodicities [14], indicating that the improvements in the thermoelectric performance of these compounds do not occur monotonically over all compositions.

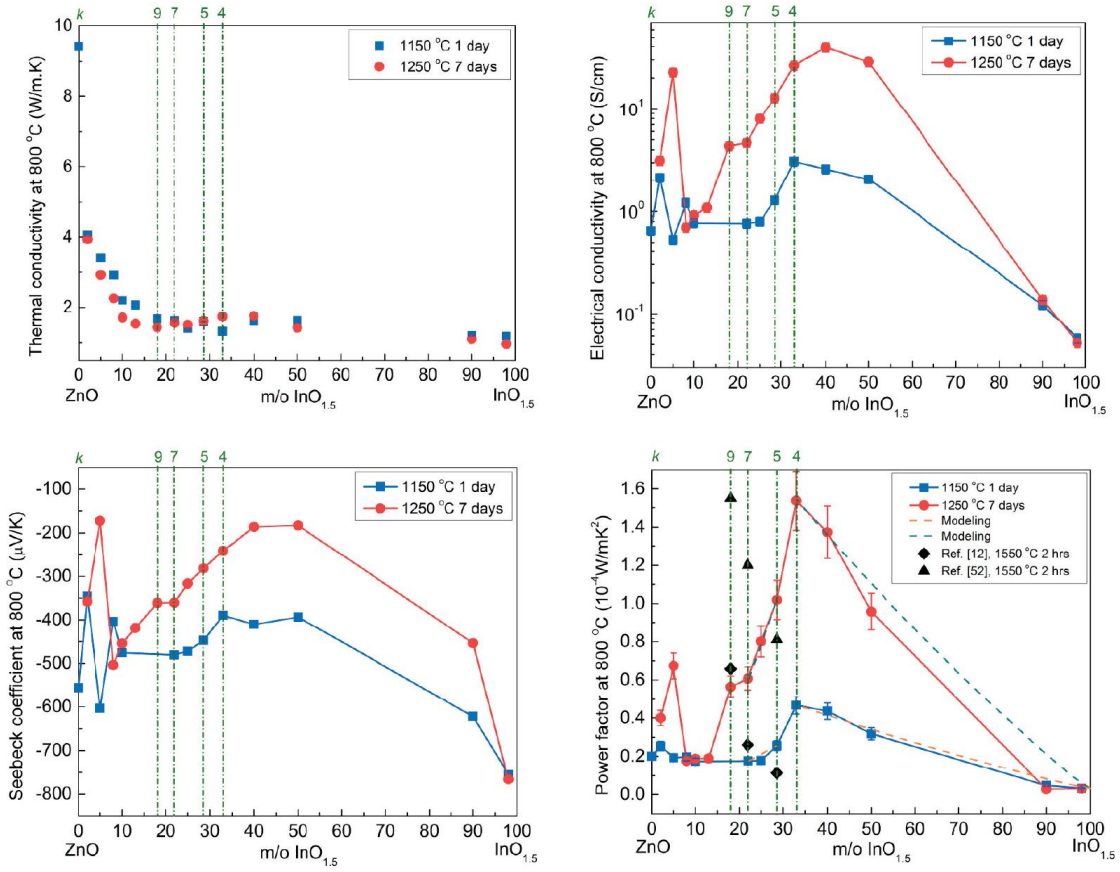

Figure 1.6. Graphs showing the dependence of the thermoelectric properties on the value of k (analogous to n) in the $In_2O_3(ZnO)_k$ homologous phase compounds, measured at 800°C. While the thermal conductivity generally exhibits a monotonic decrease as the value of k decreases, the power factor exhibits a maximum at $k = 4$. This is attributed to increasing carrier transport isotropy, which occurs as k decreases, leading to increased electrical conductivity values, and also to increased Seebeck coefficient values at intermediate values of k, possibly due to significant carrier filtering at the IDB interfaces. The images shown are adapted from ref. 14 and reprinted with persmission from the Elsevier Publishing Group.

1.5 Motivation for Research and Thesis Outline

In order to study the effects of dopant-controlled inversion domain boundary formation on the microstructural and functional properties of ZnO, several new material systems have been investigated. The Mn-Al and Sn-Al dual-doped ZnO systems have been studied in detail. The Mn and Sn dopants were initially co-doped with Al to investigate the influence on the thermoelectric properties. Al is known to act as a donor dopant in ZnO, increasing the electrical conductivity by several orders of magnitude [9,13]. Varying concentrations of Mn were co-doped with Al to investigate the influence of Mn doping on thermal conductivity reduction, due to the fact that Mn has a rather high solubility limit in ZnO [23-25]. Thus, Mn dopants may substitute on the Zn sublattice, acting as point defects and causing phonon scattering, potentially resulting in an improvement of the thermoelectric properties. Alternatively, Sn was co-doped with Al due to the fact that Sn has previously been found to introduce resonant states in Bi_2Te_3 upon doping [68]. Similarly, there exists the possibility that Sn doping may induce the formation of resonant states within the conduction band of ZnO. The formation of hybridizing resonant levels can result in local increases in the density of states, causing an increase of the Seebeck coefficient and potentially leading to an improvement of the thermoelectric performance [69,70]. In the process of analyzing the microstructural features of the Mn-Al and Sn-Al dual-doped ZnO systems, in order to explain the observed thermoelectric properties, the formation of interesting microstructural features was found to occur. The analysis of these microstructural features forms the bulk of the results reported in this thesis.

Via microstructural observation, it was found that the addition of Mn can induce the formation of inversion domain networks. At high Mn concentrations, ID networks develop in Mn-Al dual-doped ZnO. The unique microstructural features that develop in $Zn_{0.99-x}Mn_xAl_{0.01}O$ ($x \leq 0.1$) materials have been characterized and atomic-scale observations have revealed new

features not previously observed in $RMO_3(ZnO)_n$ homologous phase compounds, indicating the potential to tailor the microstructural properties of the homologous phase compounds through dopant selection. The Sn-Al dual-doped ZnO system was also investigated and the development of ID networks, which do not form in ZnO doped with either Sn or Al only, has been confirmed. Thus, it was found that dual-dopant addition of Sn and Al results in the stabilization of ID network formation, via the localization of Sn and Al at the respective sites of the b-IDBs and p-IDBs, the preferred sites for dopants with large and small ionic radii respectively. The development of ID networks in Sn-Al dual-doped ZnO also results in the suppression of spinel phase formation. These results demonstrate that the stabilization of ID networks and the simultaneous suppression of the spinel phases can be achieved through multi-dopant addition. The local electronic properties at the Mn-doped and Sn-doped b-IDBs have also been investigated by first principles calculations and the bulk thermoelectric properties of the $Zn_{0.99-x}Mn_xAl_{0.01}O$ and $Zn_{1-x-y}Sn_xAl_yO$ systems have been measured and analyzed, to study the effects of IDB formation on the properties of ZnO, both at the nanoscale and bulk levels. The results of these studies demonstrate that the local properties at IDB interfaces can be tuned by changing the specific type of dopant which localizes at the b-IDB sites, while the bulk properties of ZnO (e.g. the electrical and thermal conductivity) can also be modified via the selection of specific IDB-forming dopants.

The structure of this thesis is as follows. In Chapter 2, the experimental and theoretical methods used are described in detail. Chapter 3 provides a description of the phase and microstructural analysis, including atomic-scale observations and elemental analysis by HAADF/ABF-STEM, EDS and EELS, of Mn-Al co-doped ZnO, with a particular focus on the atomic structure of the b-IDBs. In Chapter 4, the results of phase and microstructural analysis of the Sn-Al co-doped ZnO system are described and the atomic-scale structure of the ID networks that form in $Zn_{0.98}Sn_{0.01}Al_{0.01}O$, determined by HAADF/ABF-STEM, EDS and EELS analysis, is characterized. Extensive analysis of both the b-IDB and p-IDB interfaces that

constitute the ID networks is included. The factors contributing to the stabilization of the ID networks and the suppression of the spinel phases in $Zn_{0.98}Sn_{0.01}Al_{0.01}O$ are considered and discussed in detail. In addition, the possibility of the occupation of the b-IDB and p-IDB sites by other types of dopants which have not yet been studied experimentally is discussed, based on dopant ionic radius and valence state considerations. In Chapter 5, the results of first principles investigations of Mn-doped and Sn-doped b-IDB models are described and the local changes in the electronic structure at the b-IDB interfaces due to the localization of the specific dopants are discussed. Chapter 6 focuses on the analysis of the effects of varying the Mn concentration in the $Zn_{0.99-x}Mn_xAl_{0.01}O$ ($x \leq 0.1$) materials and also of the influence of IDB development in the Mn-Al and Sn-Al dual-doped ZnO materials ($Zn_{0.89}Mn_{0.1}Al_{0.01}O$ and $Zn_{0.98}Sn_{0.01}Al_{0.01}O$) on the thermoelectric properties. The specific influences of substitutional dopants and interfaces (i.e. IDBs) on the electrical conductivity, Seebeck coefficient, power factor, thermal conductivity and thermoelectric figure of merit are analyzed. Strategies for further improving the thermoelectric properties of bulk ZnO ceramics containing IDBs are also described. Finally, in Chapter 7 the results of the thesis are summarized and a discussion of potential future studies focusing on the formation and characterization of IDBs in ZnO and on the synthesis and functional properties of compounds in the $RMO_3(ZnO)_n$ homologous phase systems is included.

1.6 References

[1] Ü. Özgur, Y.I. Alivov, C. Liu, A. Teke, M.A. Reschikov, S. Doğan, V. Avrutin, S.J. Cho, and H. Morkoç, J. Appl. Phys., **98**, 041301 (2005)

[2] X. Ma, Y. Wu, Y. Lu, and Y. Zhu, J. Phys. Chem. C., **117**, 26029 (2013)

[3] K.P. Ong, D.J. Singh, and P. Wu, Phys. Rev. B, **83**, 115110 (2011)

[4] K. Nomura, H. Ohta, K. Ueda, T. Kamiya, M. Hirano, and H. Hosono, Science, **300**, 1269 (2003)

[5] P. Sharma, A. Gupta, K.V. Rao, F.J. Owens, R. Sharma, R. Ahuja, J.M. Osorio Guillen, B. Johansson, and G.A. Gehring, Nat Mater., **2**, 673 (2003)

[6] C. Pan, L. Dong, G. Zhu, S. Niu, R. Yu, Q. Yang, Y. Liu, and Z.L. Wang, Nat. Photon., **7**, 752 (2013)

[7] A. Tsukazaki, A. Ohtomo, T. Kita, Y. Ohno, H. Ohno, and M. Kawasaki, Science, **315**, 1388 (2007)

[8] H. Ohta, W.S. Seo, and K. Koumoto, J. Am. Ceram. Soc., **79**, 2193 (1996)

[9] T. Tsubota, M. Ohtaki, K. Eguchi, and H. Arai, J. Mater. Chem., **7**, 8590 (1997)

[10] T. Tsubota, M. Ohtaki, K. Eguchi, and H. Arai, J. Mater. Chem., **8**, 409 (1998)

[11] K. Park, and K.Y. Ko, J. Alloys and Comp., **430**, 200 (2007)

[12] K. Park, J.K. Seong, Y. Kwon, S. Nahm, and W.S. Cho, Mater. Res. Bull., **43**, 54 (2008)

[13] P. Jood, R. Mehta, Y. Zhang, G. Peleckis, X. Wang, R. Siegel, T. Borca-Tasciuc, S. X. Dou, and G. Ramanath, Nano Lett., **11**, 4337 (2011)

[14] X. Liang, and D.R. Clarke, Acta Mater., **63**, 191 (2014)

[15] X. Liang, ACS Appl. Mater. Interfaces, **7**, 7927 (2015)

[16] E. Guilmeau, P. Díaz-Chao, O.I. Lebedev, A. Rečnik, M.C. Schäfer, F. Delorme, F. Giovanelli, M. Košir, and S. Bernik, Inorg. Chem., **56**, 480 (2017)

[17] K. Momma, and F. Izumi, J. Appl. Crystallogr., **44**, 1272 (2011)

[18] K. Shirouzu, T. Ohkusa, M. Hotta, N. Enomoto and J. Hojo, J. Ceram. Soc. Jpn., **115**, 254 (2007)

[19] M. Peiteado, Y. Iglesias, J.F. Fernández, J. De Frutos, and A.C. Caballero, Mater. Chem. Phys., **101**, 1 (2007)

[20] O. Köster-Scherger, H. Schmid, N. Vanderschaeghe, F. Wolf, and W. Mader, J. Am. Ceram. Soc., **90**, 3984 (2007)

[21] H. Schmid, E. Okunishi, T. Oikawa, and W. Mader, Micron, **43**, 49 (2012)

[22] E.R. Segnit, and A.E. Holland, J. Am. Ceram. Soc., **48**, 409, (1965)

[23] M. Kakazey, M. Vlasova, M. Dominguez-Patiño, J. Kliava, and T. Tomila, J. Am. Ceram. Soc., **89**, 1458 (2006)

[24] L. Nádherný, O. Jankovský, Z. Sofer, J. Leitner, C. Martin, and D. Sedmidubský, J. Eur. Ceram. Soc., **35**, 555 (2015)

[25] F.C.M. Driessens, and G.D. Rieck, J. Inorg. Nucl. Chem., **28,** 1593 (1966)

[26] N.H. Perry, and T.O. Mason, J. Am. Ceram. Soc., **96**, 966 (2013)

[27] G.B. Palmer, and K.R. Poeppelmeier, Solid State Sciences, **4**, 317 (2002)

[28] T. Moriga, D.D. Edwards, T.O. Mason, G.B. Palmer, K.R. Poeppelmeier, J.L. Schindler, C.R. Kannewurf, and I. Nakabayashi, J. Am. Ceram. Soc., **81**, 1310 (1998)

[29] N. Daneu, A. Rečnik, S. Bernik, and D. Kolar, J. Am. Ceram. Soc., **83**, 3165 (2000)

[30] S. Bernik, N. Daneu, and A. Recnik, J. Eur. Ceram. Soc., **24**, 3703 (2004)

[31] A. Rečnik, N. Daneu, T. Walther, and W. Mader, J. Am. Ceram. Soc., **84**, 2657 (2001)

[32] A. Rečnik, N. Daneu, and S. Bernik, J. Eur. Ceram. Soc., **27**, 1999 (2007)

[33] A.P. Goldstein, S.C. Andrews, R.F. Berger, V.R. Radmilovic, J.B. Neaton, and P. Yang, ACS Nano, **7**, 10747 (2013)

[34] A. Rečnik, M. Čeh, and D. Kolar, J Eur Ceram Soc., **21**, 2117 (2001)

[35] J.L.F. Da Silva, Y. Yan, and S.H. Wei, Phys. Rev. Lett., **100**, 255501 (2008)

[36] N. Daneu, A. Rečnik, and S. Bernik, J. Am. Ceram. Soc., **94**, 1619 (2011)

[37] S. Bernik, J. Bernard, N. Daneu, and A. Recnik, J. Am. Ceram. Soc., **90**, 3239 (2007)

[38] A. Walsh, J.L.F. Da Silva, Y. Yan, M.M. Al-Jassim, and S.H. Wei, Phys. Rev. B., **79**, 073105 (2009)

[39] S. Eichhorn, H. Schmid, W. Assenmacher, and W. Mader, J. Solid State Chem., **246**, 214 (2017)

[40] F. Wolf, B.H. Freitag, and W. Mader, Micron, **38**, 549 (2007)

[41] T. Hörlin, G. Svensson, and E. Olsson, J. Mater. Chem., **8**, 2465 (1998)

[42] M. Peiteado, S. Sturm, A.C. Caballero, and D. Makovec, Acta Mater., **56**, 4028 (2008)

[43] M.A. Alpuche-Aviles, and Y. Wu, J. Am. Chem. Soc., **131**, 3216 (2009)

[44] H.T. Kim, Y. Kim, M. Valant and D. Surovov, J. Am. Ceram. Soc., **84**, 1081 (2001)

[45] K.G. Vasantha Kumari, P. Divya Vasu, V. Kumar, and T. Asokan, J. Am. Ceram. Soc., **85**, 703 (2002)

[46] S. Mathur, M. Veith, M. Haas, H. Shen, N. Lecerf, V. Huch, S. Hüfner, R. Haberkorn, H.P. Beck, and M. Jilavi, J. Am. Ceram. Soc., **84**, 1921 (2001)

[47] S. K. Sampath, and J. F. Cordaro, J. Am. Ceram. Soc., **81**, 649 (1998)

[48] H. Dixit, N. Tandon, S. Cottenier, R. Saniz, D. Lamoen, B. Partoens, V. Van Speybroeck, and M. Waroquier, New. J. Phys., **13**, 063002 (2011)

[49] H. Dixit, N. Tandon, S. Cottenier, R. Saniz, D. Lamoen, and B. Partoens, Phys. Rev. B, **87**, 174101 (2013)

[50] D.S. Gouveia, L.E.B. Soledade, C.A. Paskocimas, E. Longo, A.G. Souza, and I.M.G. Santos, Mater. Res. Bull., **41**, 2049 (2006)

[51] S. Åsbrink, A. Waśkowska, L. Gerward, J. Staun Olsen, and E. Talik, Phys. Rev. B, **60**, 651 (1999)

[52] R. Gherbi, Y. Bessekhouad, and M. Trari, J. Alloys Compd., **655**, 188 (2016)

[53] C. Yao, W. Zeng, G.F. Goya, T. Torres, J. Liu, H. Wu, M. Ge, Y. Zeng, Y. Wang, and J.Z. Jiang, J. Phys. Chem. C, **111**, 12274 (2007)

[54] M. Sultan, and R. Singh, J. Phys. D: Appl. Phys., **42**, 115306 (2009)

[55] P.H. Borse, C.R. Cho, K.T. Lim, T.E. Hong, E.D. Jong, J.H. Yoon, S.M. Yu, and H.G. Kim, J. Ceram. Proc. Res., **13**, 42 (2012)

[56] K. Park, J.K. Seong, and S. Nahm, J. Alloys Compd., **455**, 331 (2008)

[57] G. J. Snyder, and E. S. Toberer, Nat. Mater., **7**, 105114 (2008)

[58] S. Walia, S. Balendhran, H. Nili Ahmadabadi, S. Zhuiykov, G. Rosengarten, Q. Wang, M. Bhaskaran, S. Sriram, M. Strano, and K. Kalantar Zadeh, Prog. Mater. Sci., **58**, 1443 (2013)

[59] M. Rull-Bravo, A. Moure, J.F. Fernandez, and M. Martin-Gonzalez, RSC Adv., **5**, 41653 (2015)

[60] H. Takemoto, K. Fugane, P. Yan, J. Drennan, M. Saito, T. Mori, and H. Yamamura, RSC Adv., **4**, 2661 (2014)

[61] K. Fujita, T. Mochida and K. Nakamura, Jpn. J. Appl. Phys., **40**, 4644 (2001)

[62] N.V. Nong, N. Pryds, S. Linderoth, and M. Ohtaki, Adv. Mater., **23**, 2484 (2011)

[63] S. Ohta, T. Nomura, H. Ohta and K. Koumoto, J. Appl. Phys., **97**, 034106 (2005)

[64] S. Ohta, H. Ohta and K. Koumoto, J. Ceram. Soc. Jpn, **114**, 102105 (2006)

[65] H. Ohta, S. Kim, Y. Mune, T. Mizoguchi, K. Nomura, S. Ohta, T. Nomura, Y. Nakanishi, Y. Ikuhara, M. Hirano, H. Hosono, and K. Koumoto, Nat. Mater., **6**, 129 (2007)

[66] X. Liang, Phys. Chem. Chem. Phys., **17**, 29655 (2015)

[67] Y. Yan, G.M. Dalpian, M.M. Al-Jassim, and S.H. Wei, Phys. Rev. B, **70**, 193206 (2004)

[68] C.M. Jaworski, V. Kulbachinskii, and J.P. Heremans, Phys. Rev. B, **80**, 233201 (2009)

[69] J.P. Heremans, V. Jovovic, E.S. Toberer, A. Saramat, K. Kurosaki, A. Charoenphakdee, S. Yamanaka, and G.J. Snyder, Science, **321**, 544 (2008)

[70] J.P. Heremans, B. Wiendlocha, and A.M. Chamoire, Energy Environ. Sci., **5**, 5510 (2012)

Chapter 2. Methods

2.1 Synthesis Methods

In this thesis, the samples studied were polycrystalline ceramics prepared using solid-state reaction methods. Nanometric oxide powders, listed in Table 2.1, were used in the synthesis of the samples studied. In order to obtain bulk samples having the stoichiometric ratios listed in Table 2.2, mixtures of the oxide powders were prepared by first weighing the powders together and then adding ethanol. The resulting solutions were mixed at 2000 rpm for 3 hr using the Planetary Centrifugal Mixer AR-250 (Thinky). The $Zn_{0.99}Sn_{0.01}O$ sample was prepared by mixing in ethanol using yttria-stabilized zirconia (YSZ) balls for 24 hr inside a polyethylene bottle. After a homogeneous solution was obtained, the powder mixtures were dried at 60°C-70°C in a drying oven until the ethanol solvent evaporated. $Zn_{0.99}Sn_{0.01}O$ was dried at 180°C in a beaker on a hot plate. After drying, the mixtures were crushed using alumina balls ($Zn_{0.99}Sn_{0.01}O$: YSZ balls), sifted with a mesh of size 250 μm and stored in dry environment at ~20°C. In order to prepare ceramic pellets, the powders were uniaxially pressed at a pressure of 20 MPa ($Zn_{0.99}Sn_{0.01}O$: 10 MPa). The ceramic compacts were then loaded into an alumina crucible and sintered in air at 1400°C for 12 hr with heating and cooling rates of 5°C/min and 10°C/min respectively. The preparation process resulted in dense ceramic pellets with high relative densities. The densities were determined using either Archimedes' method or using the sample weight and dimensions. The densities of the bulk samples are listed in Table 2.2.

Table 2.1. Oxide Powders Used in Sample Synthesis			
Oxide	**Purity**	**Manufacturer**	**Particle Size**
ZnO	99.9 %	Nanotek	34 nm
Al_2O_3	99.99 %	Taimicron (TM-DAR)	100 nm
Mn_3O_4	99.5 %	Nanotek	56 nm
SnO_2	99.9 %	Nanotek	21 nm

Table 2.2. Stoichiometry of Samples Studied and Density of Sintered Bodies		
Sample Stoichiometry	**Density (g/cm^3)**	**Relative Density (%)[(a)]**
$Zn_{0.99}Al_{0.01}O$	5.66	99.8
$Zn_{0.99}Sn_{0.01}O$	5.44	96.0
$Zn_{0.98}Sn_{0.01}Al_{0.01}O$	5.48	96.6
$Zn_{0.98}Mn_{0.01}Al_{0.01}O$	5.46	96.3
$Zn_{0.97}Mn_{0.02}Al_{0.01}O$	5.24	92.4
$Zn_{0.94}Mn_{0.05}Al_{0.01}O$	5.33	94.0
$Zn_{0.89}Mn_{0.10}Al_{0.01}O$	5.28	93.1

(a) Theoretical Density of ZnO: 5.67 g/cm^3

2.2 Phase and Microstructure Analysis

2.2.1 X-Ray Diffraction, XRD

X-ray diffraction (XRD) was used for phase analysis of the samples prepared. XRD is useful for analyzing the crystalline structure of materials, due to its ability to determine the lattice spacing of crystallographic planes based on the constructive interference of X-rays satisfying the condition for Bragg diffraction. The Bragg equation, which describes the condition for the constructive interference of diffracted X-rays with a specific wavelength, λ, is described by the following expression:

$$2dsin\theta_B = n\lambda, \qquad \text{eqn. 2.1}$$

where d, θ and n represent the lattice spacing, diffraction angle and the order of the reflection respectively [1]. A schematic of the Bragg diffraction of an incident X-ray beam by a crystalline lattice is shown in Fig. 2.1.

XRD analysis typically involves heating a filament to produce electrons which are then used to bombard a target, in order to produce characteristic X-rays. The X-rays are then monochromated using a filter and focused onto the sample to be studied. The angle θ between the incident beam and the sample plane is varied while keeping the wavelength constant. In this experimental configuration, a 1D XRD pattern is obtained, with high intensity peaks appearing at values of θ which satisfy the condition for Bragg diffraction. The intensity of the diffracted X-rays is typically plotted as a function of 2θ.

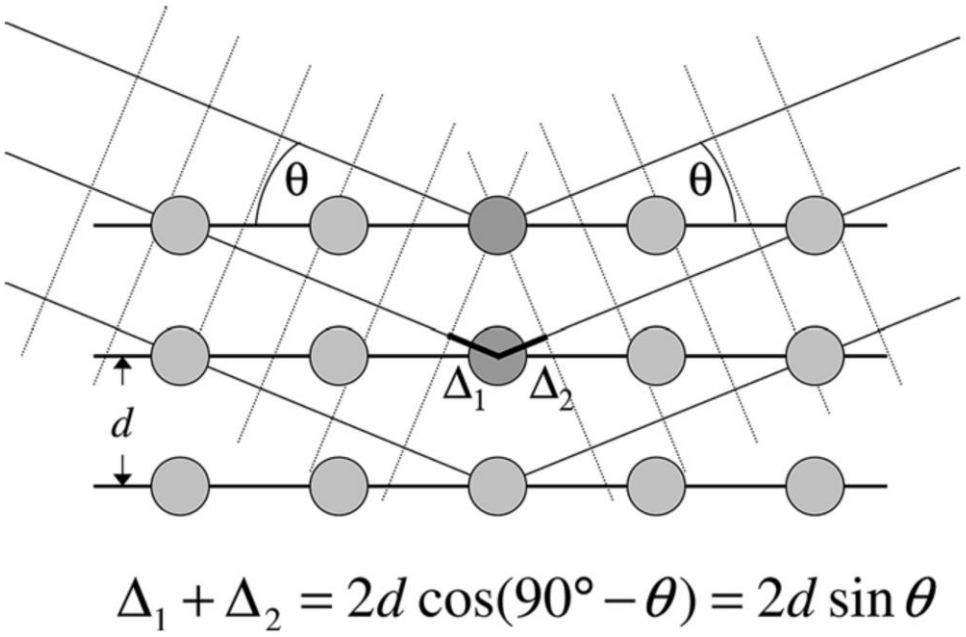

$$\Delta_1 + \Delta_2 = 2d\cos(90° - \theta) = 2d\sin\theta$$

Figure 2.1. Schematic showing the diffraction of X-rays by the atomic planes in a crystal. [1]. X-rays incident at an angle θ on the sample surface are diffracted by atomic planes with a spacing of d. At specific values of θ, corresponding to the condition for Bragg diffraction, the diffracted X-rays, phase-shifted by a total amount of $\Delta_1+\Delta_2$, will constructively interfere, resulting in peaks in the XRD pattern corresponding to the specific planes with indices of hkl representative of the crystal structure being analyzed. Image reprinted from [1], with permission from the Wiley Publishing Group.

The type of constituent elements in a crystal will influence the intensity of the reflections in the XRD pattern due to the atomic form factor [1]. The symmetry of the crystal will also determine the presence or absence of, as well as relative intensity of, the XRD peaks according to the atomic structure factor. Temperature effects (e.g. thermal vibrations), the multiplicity of the diffracting planes, the polarity of the diffracted beam, the spreading of the diffracted beam, beam absorption by the sample and instrumental settings will also have an influence on the XRD peak intensities [1].

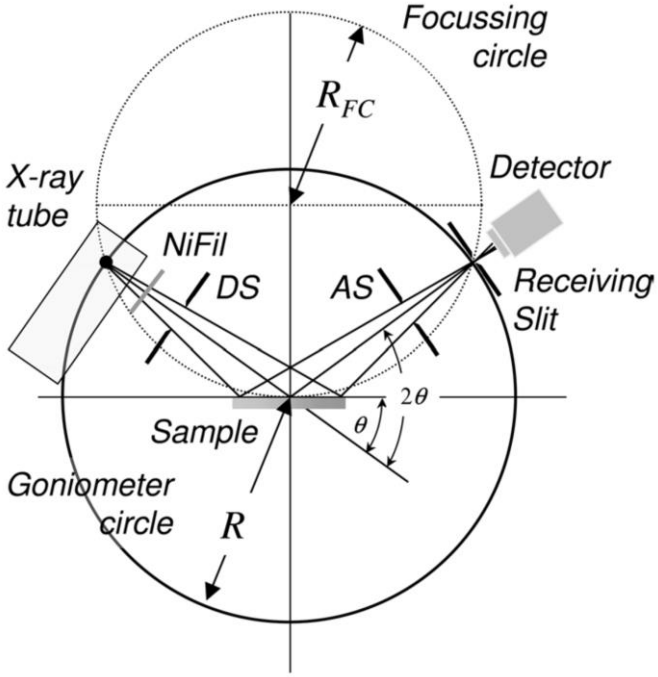

Figure 2.2. Diagram of the experimental setup for θ/2θ XRD analysis using the Bragg-Brentano detector geometry. X-rays of a specific wavelength are focused on the sample surface using a series of slits. The angle, θ, formed between the incident X-ray beam and the sample and also between the sample and the detector is varied by rotating the position of the X-ray tube and detector simultaneously, while keeping the position of the sample fixed. Thus, an X-ray diffraction pattern with values of intensity, I, that vary as a function of θ can be obtained. Image adapted from [1] and reprinted with permission from the Wiley Publishing Group.

In addition, microstructural features can influence the observed intensity of the peaks. Such features include the sample texture, degree of crystalline disorder (e.g. amorphization) and sample thickness [1]. Broadening of the peaks may also be observed, due to structural defects such as strain, stresses, dislocations, stacking faults, twinning, precipitates and inclusions, a reduction in grain or particle size or lattice modulations (e.g. superlattice or intergrowth formation) [2,3].

In this study, XRD patterns were collected with the Rigaku SmartLab X-Ray Diffractometer using Cu-K_α radiation (λ = 1.54 Å). Before data collection, samples were crushed using a mortar and pestle to produce powders. These were then uniformly spread on a glass slide to obtain a flat sample surface. The Bragg-Brentano experimental setup was used for collecting experimental data. A diagram of the setup is shown in Fig. 2.2.

2.2.2 Scanning Electron Microscopy, SEM

Observation of the microstructure of the samples produced was carried out using scanning electron microscopy (SEM). A schematic showing the interaction of the electron beam with the sample surface in a scanning electron microscope is shown in Fig. 2.3. A filament is heated to produce an electron beam which is then focused at the sample surface using a system of electromagnetic lenses within the microscope. The electron beam is scanned across the sample surface using a pair of deflector lenses and an image is produced by using separate electron detectors to collect either the secondary electrons (SE), which are useful for imaging surface features, or back-scattered electrons (BSE), which are useful for phase analysis due to the dependence of the BSE intensity on the atomic number (Z). Elemental analysis using SEM-EDS can also be carried out with an X-ray detector, which can be used to obtain an elemental map by collecting the characteristic X-rays produced by the excitation of core shell electrons and subsequent relaxation of outer shell electrons at the sample surface.

In this study, SEM imaging combined with elemental analysis using EDS was carried out using the JEOL 6510 (LA) SEM with an accelerating voltage of 10-20 keV. Samples were polished with a diamond slurry with particle sizes of 9, 3 and 0.5 µm until a mirror surface was obtained. In order to obtain images with clearly defined grain boundaries, thermal etching of the mirror-polished samples was carried out in air inside an alumina crucible at 1300-1350^{o}C for 30 min with a heating and cooling rate of 5^{o}C/min and 10^{o}C/min respectively. In order to minimize surface charging during imaging, a carbon coating of ~10 nm was deposited on the sample surface using a sputter coating system (Gatan).

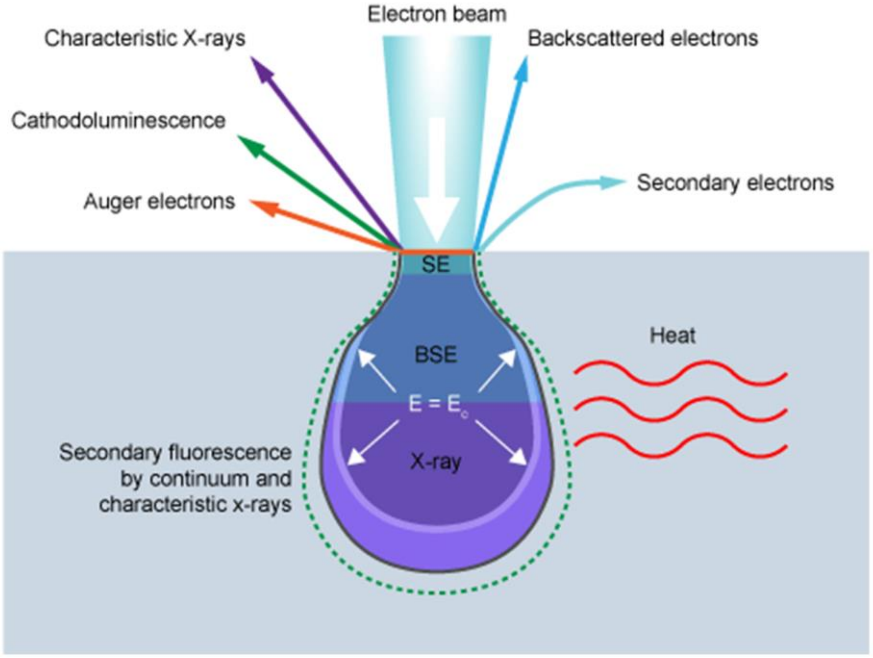

Figure 2.3. Schematic of the interaction of the electron beam used in SEM imaging with the sample surface. The scanned electron beam interacts with a volume of the sample surface, producing backscattered electrons and secondary electrons, which are useful for phase and topographical analysis respectively. The characterisitic X-rays that are produced can be used for elemental analysis. Image adapted from [4].

2.2.3 Transmission Electron Microscopy, TEM

Images of the sample microstructure were also obtained using the JEOL 2010-HC TEM. A diagram of the imaging system used in a transmission electron microscope is shown in Fig. 2.4. In a transmission electron microscope, a current is passed through a filament which becomes heated. In the process, an electron beam is produced due to the thermionic emission of electrons at the cathode-vacuum interface [5]. The electrons gain energy due to the applied accelerating voltage. The electron beam is focused using a series of electromagnetic coils which allow for beam alignment by manipulating the magnetic field strength in the microscope [5]. The sample is shifted along the z-axis to align it with the eucentric height of the microscope and the objective lens strength is adjusted to control the image focus at the phosphor viewing screen.

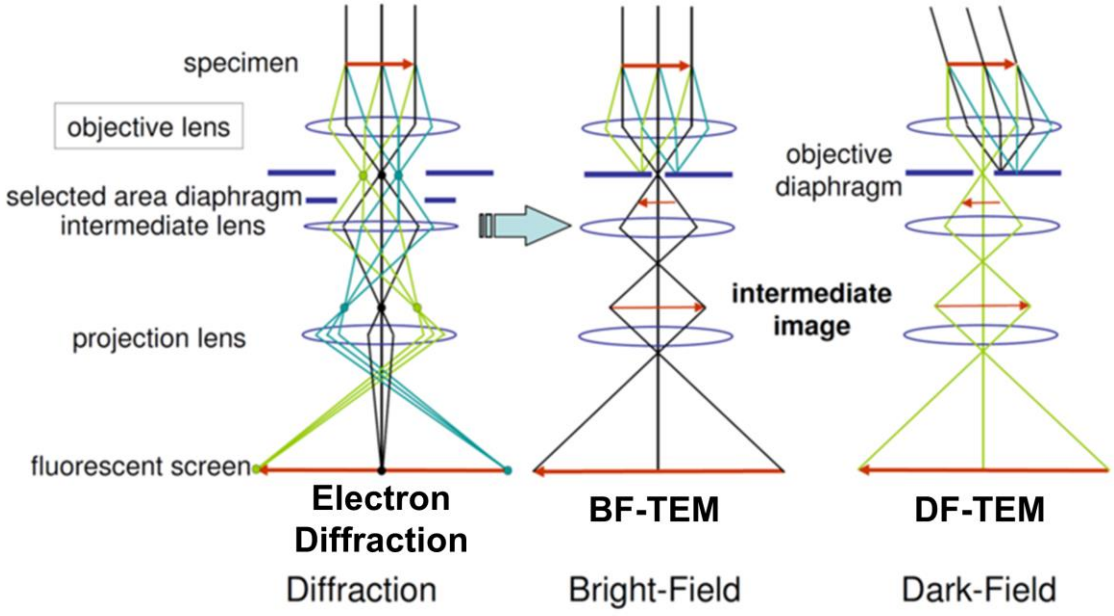

Figure 2.4. Diagram showing the imaging conditions used for SAED, BF-TEM and DF-TEM. By selecting a specific imaging mode, it is possible to obtain both SAED and BF/DF-TEM images. Once either the central beam or a diffracted beam has been selected using the objective aperture in SAED mode, either BF or DF-TEM images can be respectively recorded while in normal imaging mode. Conversely, in SAED mode, EDPs can be recorded once an area of the sample has been selected using the selected area aperture while in normal imaging mode. Image adapted from [6].

The electron beam can pass through samples which are sufficiently thin, typically < 100 nm [5]. The electrons interact with the sample and produce an image at the phosphor viewing screen. The image contrast reflects structural features of the sample, such as the local thickness, local average mass, sample bending and defects (e.g. dislocations, stacking faults, grain boundaries etc.) [5]. When imaging a crystalline sample, the transmitted electrons either pass directly through the sample, forming a central beam, or are diffracted by crystallographic planes with a specific periodicity, resulting in Bragg reflections. When one of the principle crystallographic directions is aligned with the incident electron beam, the crystal is said to be at the zone-axis. Under this condition, an electron diffraction pattern (EDP) can be obtained by placing the selected area electron diffraction (SAED) aperture over the strongly diffracting region of the image plane. By shifting to diffraction mode, an EDP reflecting the crystallographic symmetry of the area of the sample imaged can be observed. In diffraction mode, an objective aperture can be inserted at the back focal plane of the microscope and shifted to select specific reflections in the EDP. Bright-field (BF) images, which exhibit increased contrast, can be obtained by selecting the central beam. Dark-field (DF) images, which are obtained by placing the objective aperture over one of the Bragg reflections or features other than the central beam in the EDP, can also be obtained and exhibit increased image intensity due to the crystallographic features which produce the diffracted beam selected in the back focal plane [5].

Samples for TEM observation were prepared by the cutting, grinding, polishing and dimpling of bulk polycrystalline samples. Polishing was done using an alumina slurry with particle sizes of 9, 3 and 1 μm. After samples were sufficiently thinned to a thickness of ~20-50 μm, Ar^+ ion milling was carried out using the Precision Ion Polishing System (PIPS, Gatan). Initial milling was carried out at 4 kV with an incident beam angle of 6°-7°. After a hole formed in the sample, a final milling step was carried out at 5° for 15, 10 and 5 min at voltages of 1.5, 1.0 and 0.5 kV respectively, in order to obtain a clean sample surface by removing redeposition.

For TEM analysis, samples were placed in a double-tilt holder (Gatan), loaded into the microscope and BF/DF-TEM images and EDPs were collected using the JEOL 2010-HC TEM operating at 200 kV. Images were recorded on film, developed and converted into digital data using a scanner.

2.3 Scanning Transmission Electron Microscopy, STEM

Atomic-resolution observations were carried out using STEM imaging methods. STEM is similar to conventional TEM in that both use scattered electrons to produce images. However, there are several key differences. A schematic of the detector configuration used for STEM imaging is shown in Fig. 2.5. In STEM, the condenser lens strength is controlled in order to converge the electron beam at the sample, forming an electron beam probe [5]. The angle of the convergent beam at the sample surface is referred to as the semi-convergence angle, α. Unlike TEM, which uses a static electron beam, in STEM the electron beam probe is rastered across the sample using a pair of pre-sample scanning coils. The incident beam propagates through the sample and is scattered over a range of angles at the exit surface of the sample. By making use of an annular detector in the post-sample field, the electrons scattered to a specific range of angles by the sample can be collected in order to produce an image. Several important types of STEM images that can be recorded by making use of different types of detectors include ABF, LAADF, MAADF, ADF and HAADF-STEM [5]. In this study, primarily ABF and HAADF-STEM images were collected.

A JEOL ARM-200F scanning transmission electron microscope operating at 200 keV was used for data collection in this study. This microscope uses a cold emission gun. An aberration-corrected optics system is also used in order to reduce the lens aberrations. The ARM-200F can also be operated in TEM mode.

2.3.1 High-Angle Annular Dark-Field (HAADF) STEM

An imaging method extensively used in this study is HAADF-STEM, shown schematically in Fig. 2.5. In HAADF-STEM imaging, lattice images can be formed by collecting the electrons that are elastically scattered to high angles (~50-370 mrad) due to Rutherford scattering caused by the Coulombic interaction of the electrons with the atomic nuclei [5,7,8]. Thermal diffuse scattering (TDS) also makes a contribution to the electrons scattered to this angular range; in contrast, the scattered electrons due to Bragg diffraction generally contribute to the intensity in STEM images collected at lower angles (e.g. in MAADF or ADF-STEM) [9]. HAADF-STEM imaging is particularly useful for observing high atomic number elements, which exhibit increased contrast in HAADF images due to increased high-angle electron scattering. HAADF-STEM image intensity is proportional to the average atomic number of the atoms in the column imaged, resulting in the following expression:

$$I \propto Z^n \ (1.6 < n < 1.9), \qquad \text{eqn. 2.2}$$

where I is the image intensity and Z is the atomic number [11]. Generally, this makes interpretation of HAADF-STEM images straightforward; however, low average atomic number (Z < ~13) atomic columns typically cannot be imaged using HAADF-STEM [12-14]. Another advantage of HAADF-STEM in comparison to high-resolution TEM (HRTEM) is the weak dependence of the HAADF-STEM image contrast on the sample thickness and defocus value [7]. However, the observed intensity of defect structures (e.g. interfaces) imaged by HAADF-STEM may be significantly influenced by additional factors including misorientation tilt, sample thickness, defocus value and local strain or lattice distortion [9,13].

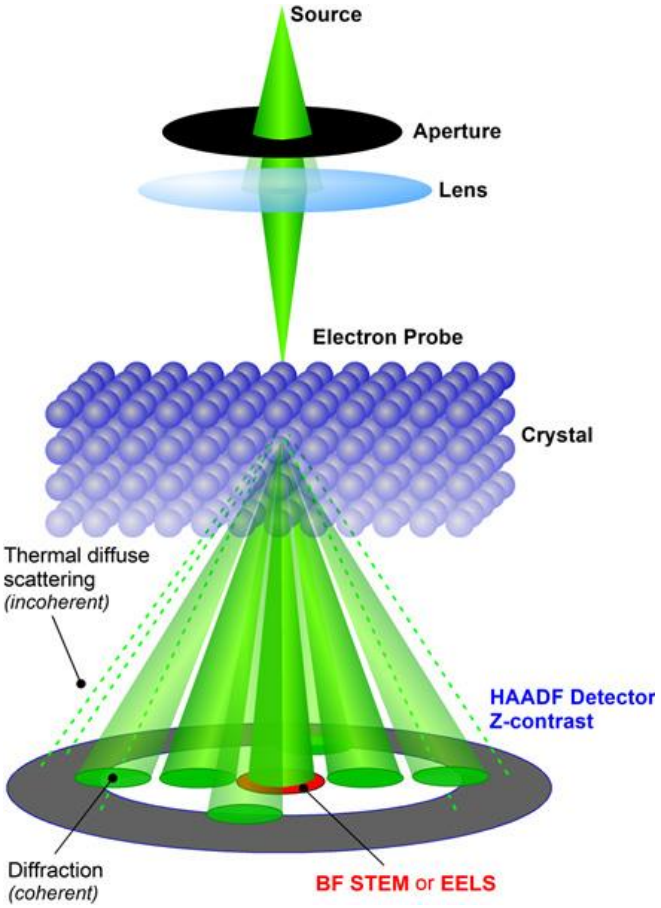

Figure 2.5. Schematic of the imaging of a crystal lattice by STEM. In STEM imaging, the electron beam is focused to converge approximately at the surface of the thin crystal specimen and is then scanned across the area of the sample to be imaged. Electrons scattered to low angles (~10-20 mrad) can be collected by a BF (or ABF) detector. STEM-EELS analysis is also accomplished using the electrons scattered within low angular ranges. Electrons scattered to intermediate and high angles can be used in ADF and HAADF imaging respectively. As shown in the above image, coherent diffraction of the electron beam resulting in Bragg diffraction spots occurs primarily at intermediate angular ranges (18-48 mrad) [9]. HAADF-STEM images are formed by collecting the electrons scattered to higher angular ranges (~50-370 mrad). The scattering of electrons to high angles is the result of Rutherford scattering due to the electrostatic interactions of the electrons with the positively charged atomic nuclei of the crystal. This results in the Z^n dependence of the atomic column intensity observed in HAADF images. Image adapted from [10].

2.3.2 Annular Bright-Field (ABF) STEM

Another STEM imaging technique that has gained attention in recent years is ABF-STEM [12-14]. A schematic of the detector system used in ABF-STEM imaging is shown in Fig. 2.5. In contrast to HAADF-STEM, ABF imaging uses an annular detector with a much smaller angular range and upper limit to the detector collection angle, due to the dependence of the ABF detector collection angle on the probe semi-convergence angle, α, with the ABF angle typically taking a value of α/2~α. For the ARM-200F, the value of α is ~24 mrad; thus, the range of angles used for ABF-STEM imaging is ~12-24 mrad. ABF is effective for imaging both low and high atomic number elements, with ABF-STEM contrast approximately scaling with Z according to the following expression: $I \propto Z^{1/3}$ [14]. A dark contrast is produced in ABF images due to the absence of intensity resulting from high-angle scattering of electrons at the positions of high atomic number elements [15]. The great advantage of ABF imaging, however, is that low atomic number elements can also be imaged as dark contrasts which appear due to an "electron lensing" effect that occurs at the positions of low atomic number columns [15]. Using ABF-STEM, low atomic number elements such as lithium and oxygen have been successfully imaged [12-14]. Like HAADF-STEM, ABF-STEM images also have the advantage of exhibiting only a weak dependence of contrast on the sample thickness and defocus value [12].

2.3.3 Energy-Dispersive X-Ray Spectroscopy, EDS

Elemental analysis of the sample microstructure was carried out using SEM-EDS and STEM-EDS. EDS enables the mapping of the elemental composition of the sample by collecting the characteristic X-rays that are produced by the interaction of the electron beam with the sample. The characteristic X-rays correspond to the specific transitions between the energy levels of the electron shells that are unique to each element [5]. A schematic of the X-

ray emission process due to the interaction of the electron beam with the sample is shown in Fig. 2.6. By collecting the characteristic X-rays associated with specific transitions, the elemental mapping of the sample is possible. This is typically achieved by using a detector placed near the sample inside the SEM, TEM or STEM column. The ARM-200F is equipped with a silicon drift detector (JEOL).

2.3.4 Electron Energy-Loss Spectroscopy, EELS

EELS is an effective method for obtaining valuable information about sample characteristics such as the local elemental composition, valence states and coordination environment [5,17]. This is achieved by using a detector to record the energy losses associated with the inelastic interactions of the incident electron beam with the sample. The energy losses are due to the emission of electrons from the characteristic electron levels in different elements [5]. Fig. 2.7 shows the relationship between the core-shell levels in an oxide and the corresponding edges in the associated EEL spectrum [5]. In addition to elemental fingerprinting, the strength of the beam-sample interactions can also be affected by the bonding environment, allowing for the determination of the valence state by analysis of the spectral shape and features [5]. EELS data can be acquired by placing a post-specimen detector inside the STEM column [17]. A small collection angle is used to collect the inelastically scattered electrons. A detector with a dispersion of up to ~0.05 eV/channel is used to collect EELS data, which can be acquired by scanning the electron beam across the sample, to obtain spatially mapped data. Previous studies have determined the local valence state of specific atomic sites using atomic column-resolved EELS [18]. A Gatan Enfinium detector was used to acquire EELS data reported in this thesis.

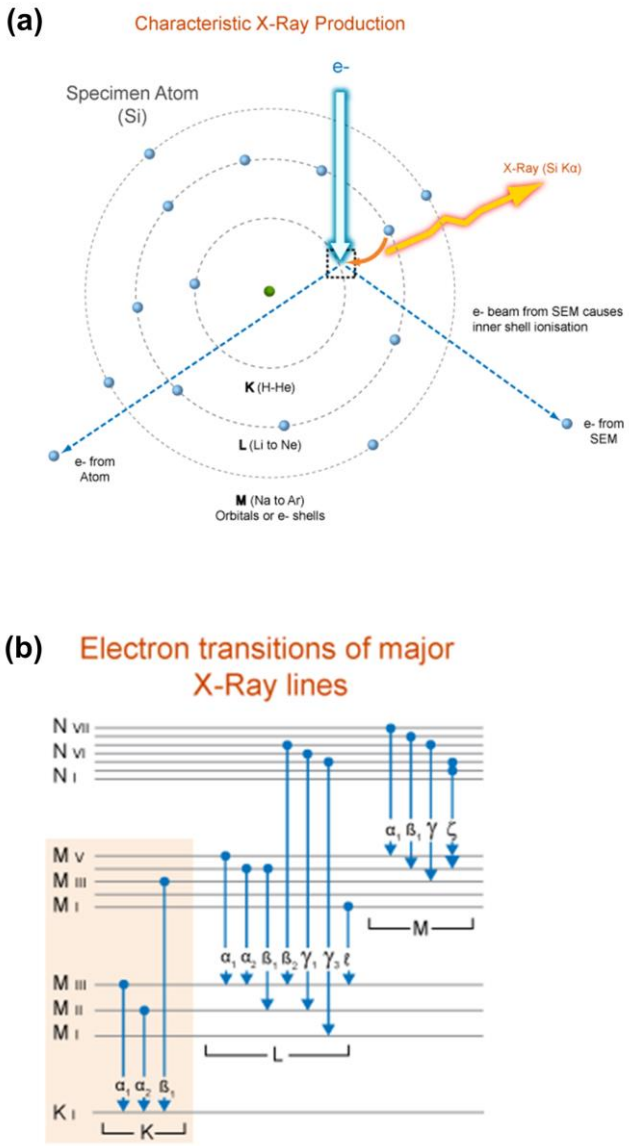

Figure 2.6. (a) Schematic of characteristic X-ray emission due to the interaction of the electron beam with the sample in SEM, TEM or STEM imaging. The electron beam imparts energy to the electrons bound to the atoms in the crystal. This transfer of energy causes the excitation of inner shell electrons. Characteristic X-rays are produced by the relaxation of electrons from the outer to the inner electronic shells, corresponding to states of high and low electronic energy respectively. **(b)** Electron energy level diagram showing the specific transitions producing characteristic X-rays. The transitions corresponding to the *K*, *L* and *M* edges in EDS profiles are shown. The *K* edge transitions (highlighted) were used extensively for EDS elemental analysis in this thesis. Images adapted from [16]

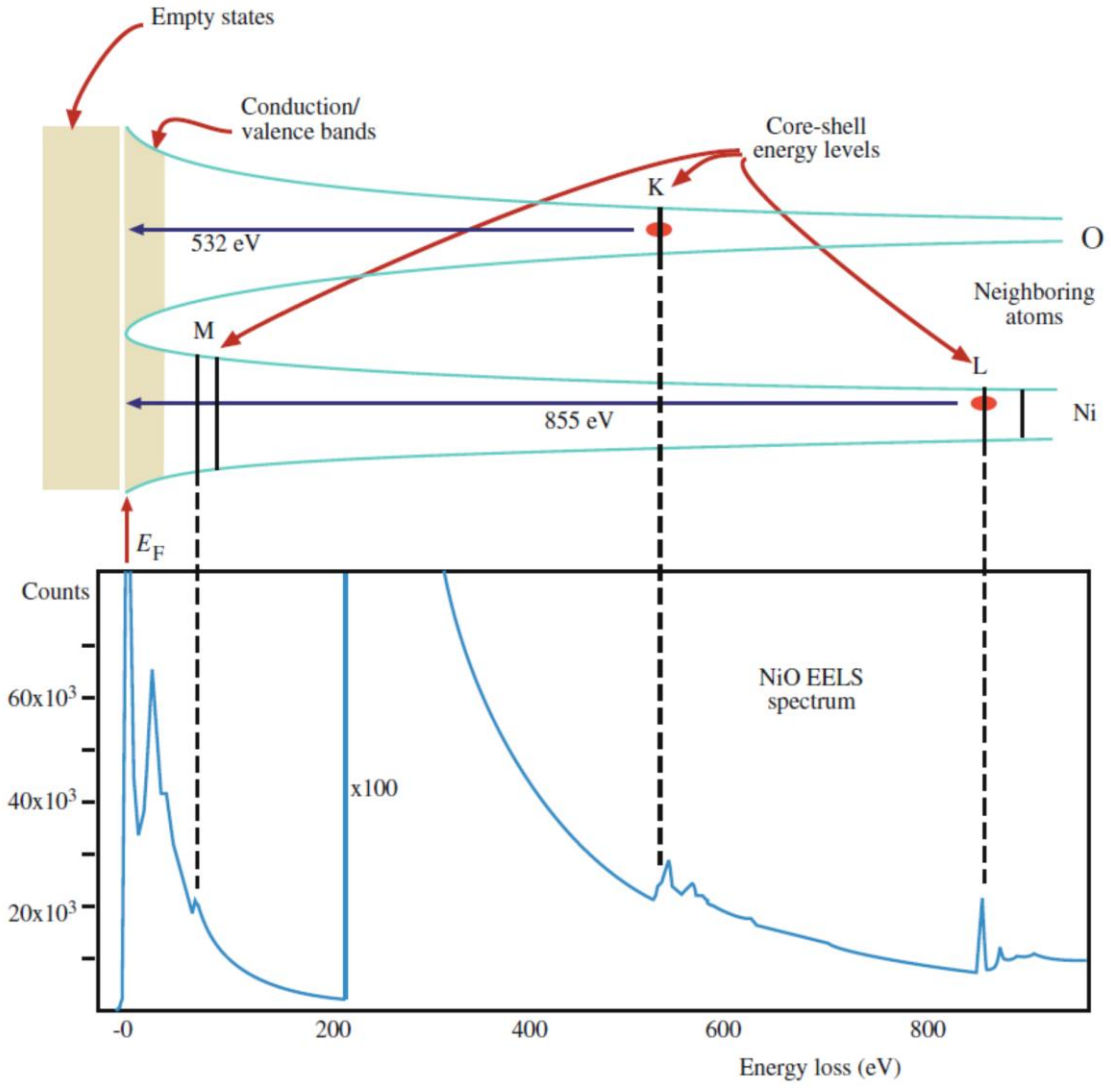

Figure 2.7. The interaction of the STEM electron beam probe with the sample results in inelastic interactions of the electron beam with the atoms in the crystal. As shown in the schematic above, characteristic edges are observed in EEL spectra due to the inelastic scattering of electrons, which causes the ionization of atoms in the crystal. Ionization results in the promotion of inner shell electrons to the empty states in the valence or conduction band. The transition of electrons from the inner-shell electron orbitals to the unoccupied energy levels results in the appearance of different characteristic edges in the EEL spectrum, at energy-loss values corresponding to the energies of transition between specific electron shells and the unoccupied energy levels of the valence or conduction band. Image adapted from [5] and reprinted with permission from the Springer Publishing Group.

2.4 First Principles Calculations

The structural and electronic properties of IDBs were investigated using the density functional theory (DFT) [19,20] as implemented in the Vienna Ab Initio Simulation Package (VASP) [21]. The nature of the chemical bonds between atoms within materials is largely determined by the electronic structure, which is in turn due to the crystalline environment. The ground state electronic configuration of a specific material system can be determined by solving the corresponding Schrödinger equation. The Schrödinger equation for an electron can be expressed as:

$$\hat{H}\Psi = \epsilon_i \Psi, \qquad \text{eqn. 2.3}$$

where Ψ and ϵ_i are the electron wave function and eigenenergy respectively. $\hat{H}$ is the Hamiltonian, which, for an electron in a crystal, can be written as:

$$\hat{H} = \left[\hat{T}_e + \hat{T}_n + \hat{V}_{ee} + \hat{V}_{nn} + \hat{V}_{ne}\right], \qquad \text{eqn. 2.4}$$

where $\hat{T}_e$ and $\hat{T}_n$ are the kinetic energy of the electrons and atomic nuclei, respectively, and $\hat{V}_{ee}$, $\hat{V}_{nn}$ and $\hat{V}_{ne}$ represent the electron-electron Coulombic repulsion, nucleus-nucleus Coulombic repulsion and the electron-nucleus Coulombic attraction respectively. DFT calculations rely on several approximations to calculate the quantum mechanical ground state of a specific material system. Based on the Born-Oppenheimer approximation, commonly implemented in DFT calculations, which states that due to the large difference in the masses of the nuclei and electrons the portions of the wave function due to the electrons and the nuclei can be separated [22], and the $\hat{T}_n$ term can be ignored as a result of the negligible kinetic energy of the nuclei in comparison to the electrons. The $\hat{V}_{nn}$ and $\hat{V}_{ne}$ terms can also be combined into a single term, $\hat{V}_{ext}$, which represents an external potential that the electrons experience. Eqn 2.4 then reduces to:

$$\hat{H} = \left[\hat{T}_e + \hat{V}_{ee} + \hat{V}_{ext}\right] \qquad \text{eqn. 2.5}$$

However, the determination of the $\hat{V}_{ee}$ term, representing the electron-electron interaction, is

not straightforward and requires additional assumptions.

In order to determine the $\hat{V}_{ee}$ term and calculate the ground-state of the system being studied, several assumptions must be made. First, it is assumed that the total free energy of the system can be expressed as a function of the charge density, $n(\vec{r})$ [19]. Second, the ground-state electronic density configuration is defined as that for which the total free energy of the system is minimized [19]. DFT calculations approach this problem by defining a ground-state energy, E_0, which can be expressed as:

$$E_0 = E[n_0] = \langle \Psi[n_0] | \hat{T}_e + \hat{V}_{ee} + \hat{V}_{ext} | \Psi[n_0] \rangle, \qquad \text{eqn. 2.6}$$

where n_0 is the ground-state charge density. The external potential can be written as a function of $n(\vec{r})$, as:

$$V_{ext}[n] = \int V(\vec{r}) n(\vec{r})\, d^3r \qquad \text{eqn. 2.7}$$

The total energy can then be written as a function of $n(\vec{r})$ according to the following equation:

$$E[n] = \hat{T}_e[n] + \hat{V}_{ee}[n] + \int V(\vec{r}) n(\vec{r})\, d^3r \qquad \text{eqn. 2.8}$$

The determination of the ground-state electronic configuration then becomes a problem of minimizing $E[n]$ with respect to n [19]. The DFT calculation is generally carried out by first assuming a trial charge density and then back-calculating the corresponding potential and electronic wave function [20]. The calculation then uses the obtained solutions to the Schrödinger equation in order to calculate a new charge density [19]. This process contintues iteratively, updating the trial charge density in order to find the ground-state solution which minimizes the difference between the input and output charge densities subject to a predefined convergence criterion. The effective potential calculated during this process is defined as:

$$V_{eff}[\vec{r}] = V_{ext}[\vec{r}] + V_{Hart}[n] + V_{xc}[n], \qquad \text{eqn. 2.9}$$

where $V_{Hart}[n]$ and $V_{xc}[n]$ are terms due to the electron-electron Coulombic repulsive interaction and the exchange-correlation interaction respectively. A determination of the best form of the equation to use in modeling $V_{xc}[n]$ is a central problem associated with DFT

calculations [20].

In this thesis, the generalized gradient approximation (GGA) [23-25] was implemented in the DFT calculations in order to model the density functional. GGA is a scheme for determining the exchange-correlation interaction by approximating it as an equation including terms that depend on both the charge density, $n(\vec{r})$, and its local gradient. GGA has been found to have improved accuracy compared to methods introduced earlier, such as the local density approximation (LDA) and local spin density approximation (LSDA), which do not include higher-order terms due to the charge density gradient in the expression for the density functional [20,21,26]. The effective electronic on-site Coulombic interaction parameter, U_{eff}, also known as the Hubbard parameter [27], was also included in the calculations. The inclusion of U_{eff} has been found to result in improved agreement of the calculated bandgap of ZnO, and a number of other materials, with the experimental bandgap [28].

Various schemes have been devised to represent the potentials that the valence electrons experience. These include the augmented plane wave (APW) [29], pseudopotential [30,31], linear augmented plane wave (LAPW) [32] and projector augmented-wave (PAW) methods [33,34]. The use of augmented plane waves is effective in that it allows the wave functions to be modeled by considering the regions near the ionic cores separately from the interstitital regions between the nuclei when carrying out the self-consistent quantum mechanical calculation. The use of pseudopotentials allows the inner-shell electrons to be included with the ionic cores as part of a background potential experienced by the valence electrons [30,31]. The PAW method as implemented in the VASP code was used to determine the stable configuration of the IDB interfaces. The PAW method combines aspects of the augmented plane wave and psuedopotential methods [33,34], and can deal with the rapid oscillations of the electronic wave function that occur near the ionic cores [33]. Within the framework of the PAW method, pseudo wave functions are created which match exactly with the valence or “all-electron” wave functions outside a specific augmentation region. Within the

augmentation region, the pseudo wave functions introduce a smooth continuation of the all-electron wave functions. This is achieved by creating a set of projector functions to transform the pseudo wave function into the all-electron electon wave functions to assure their matching outside the augmentation region [33].

Slab model calculations were carried out to determine the stable atomic configurations of the IDB interfaces, modeled based on experimentally observed structures. DFT calculations which implement slab models have been found to be effective for determining the structural and electronic properties of isolated interfaces [35]. Interface calculations relying on the slab model approach generally consist of a single interface separated from the surface planes by a specific number of bulk-like atomic planes sufficient in total thickness to avoid interactions between the interface and the surface layers. The b-IDB interface was modeled as a monolayer of edge-sharing cation octahedra, separated from each surface in the slab model by 11 bulk-like Zn-O cation-anion layers. A vacuum layer of ~12-15 Å is typically included between surfaces in order to minimize interactions between periodic images of the slab model [35]. In this study, the surfaces were terminated by oxygen-rich planes. Thus, to maintain charge balance and avoid dangling bonds, which can result in the formation of spurious mid-gap electronic states, at the surfaces, the surface oxygen atoms were passivated with pseudo hydrogen atoms, each having a charge of 0.5 e. The slab model shape, dimensions and atomic coordinates were all relaxed in order to determine the stable IDB configuration, subject to a convergence criterion of $\leq$ 0.02 eV/Å for all ionic forces.

2.5 Thermoelectric Property Measurements

2.5.1 Electrical Conductivity and Seebeck Coefficient

The thermoelectric properties of the samples produced were measured from room temperature (RT) to ~730-750°C. For electrical conductivity and Seebeck coefficient meaurements, bar-shaped samples were produced by cutting the sintered polycrystalline ceramic samples using a diamond isometric cutter. The samples produced had a length of ~8-11 mm and a cross-section of ~2x3 mm^2 and the sides were polished to obtain flat surfaces. The Seebeck coefficient and electrical conductivity were measured simultaneously using the ZEM-2 (Ulvac-Riko), which enables electronic transport property measurement within an inert He atmosphere. Measurements were carried out using a four-probe voltage measurement scheme as shown in Fig. 2.8. In this configuration, the temperature is increased from 50°C to 730°C in

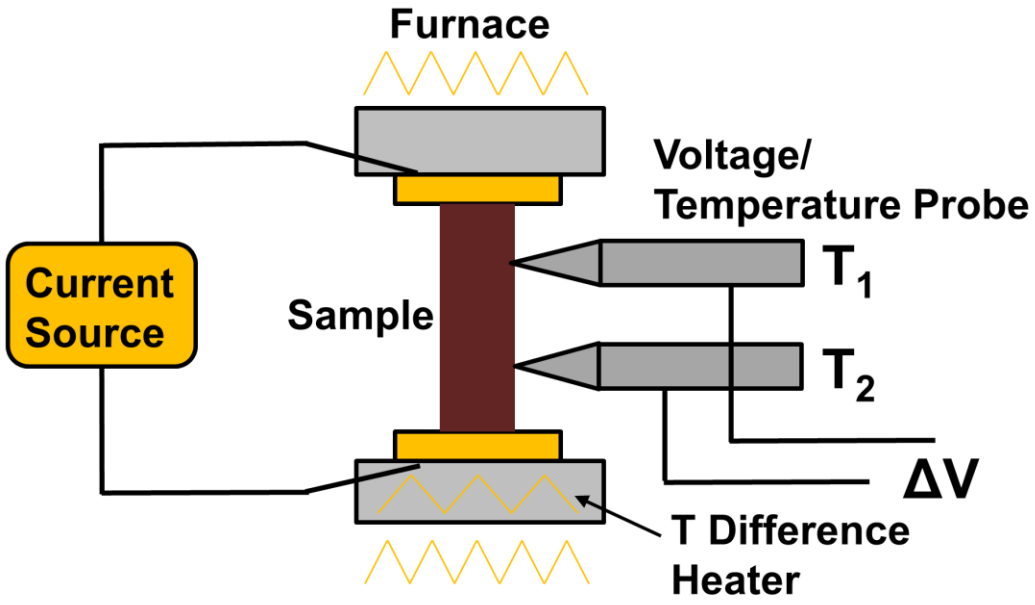

Figure 2.8. Schematic of the experimental setup used by the ZEM-2 for electrical conductivity and Seebeck coefficient measurement. A bar-shaped sample is placed between two pressure contacts. The furnace temperature is increased in increments corresponding to the preset measurement temperatures. At each measurement temperature, the electrical conductivity is determined by passing a current through the sample, while the Seebeck coefficient is measured by applying a thermal gradient to the sample and measuring the resulting voltage difference across the probe contacts at the sample surface.

increments of 100°C (50 °C increment at HT). For electrical conductivity measurements, a current is applied to the sample and the resulting voltage drop is measured at each measurement temperature. The Seebeck coefficient is then determined by using a heater at one end of the sample to produce temperature gradients of 10, 20 and 30 K across the sample. These temperature gradients are applied in sequence and the resulting voltage difference for each temperature gradient is measured across two central probes at the sample surface. The Seebeck coefficient is determined from the slope of the plot of the ΔV and ΔT values. The measurements were acquired along the direction perpendicular to the pressing direction of the ceramic pellet.

2.5.2 Thermal Conductivity

The thermal conductivity was measured using the laser flash method (Ulvac-Riko, TC-7000) from RT to 750°C. Samples were prepared by polishing the sintered ceramic pellets to obtain cylindrical samples with a diameter of ~10-11 mm and thickness of ~1-2 mm. The samples were sprayed with a black carbon coating to reduce thermal emissivity losses from the sample surface at high measurement temperatures. A schematic of the experimental setup for the laser flash method is shown in Fig. 2.9. The pellet is placed in the sample chamber and a laser pulse is applied at one side of the sample. The resulting temperature rise at the opposite face of the sample is recorded by an IR detector and the thermal diffusivity is determined by a fitting procedure applied to the measured temperature profile. The temperature within the sample chamber is then increased, in increments of 100°C (50°C increment at HT), and the measurement procedure is repeated. The thermal conductivity can be calculated according to the expression: $\kappa = \alpha * C_p * \rho$, where α, C_p and ρ are the thermal diffusivity, specific heat and density respectively. The C_p values used in the calculation of the thermal conductivity represent literature values for undoped ZnO [36]. Laser flash measurements were carried out parallel to the pressing direction of the sintered ceramic pellet.

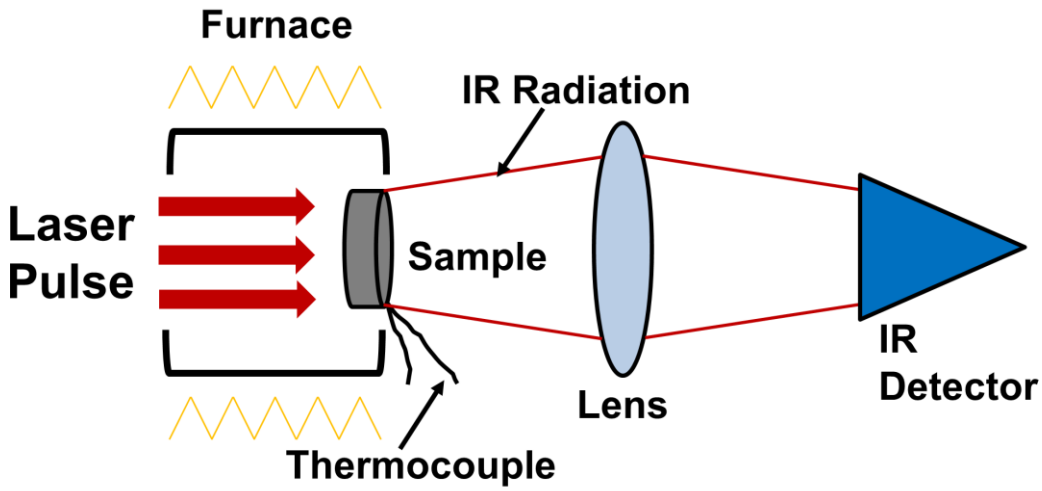

Figure 2.9. Schematic of the experimental setup for the laser flash method in the TC-7000. The furnace temperature is increased incrementally and, at each measurement temperature, a laser pulse is applied to one side of the sample pellet and the resulting increase in temperature at the other side of the pellet is measured using an IR detector. The thermal diffusivity is determined via a fitting procedure applied to the temperature increase profile. C_p values can also be measured simultaneously using a thermocouple attached to the sample surface; however, in this thesis, κ values were determined using C_p values from the literature.

2.6 References

[1] M. Birkholz, "Chapter 1: Principles of X-Ray Diffraction." *Thin Film Analysis by X-Ray Scattering*. John Wiley & Sons, (2006)

[2] T. Ungár, Scr. Mater., **51**, 777 (2004)

[3] T. Moriga, D.D. Edwards, T.O. Mason, G.B. Palmer, K.R. Poeppelmeier, J.L. Schindler, C.R. Kannewurf, and I. Nakabayashi, J. Am. Ceram. Soc., **81**, 1310 (1998)

[4] http://www.ammrf.org.au/myscope/sem/background/concepts/interactions.php

[5] C.B. Carter and D.B. Williams, *Transmission Electron Microscopy*. Springer-Verlag US, (2009)

[6] https://physik.uni-paderborn.de/lindner/forschung/temstem/

[7] S.J. Pennycook, and L.A. Boatner, Nature, **336**, 565 (1988)

[8] S.J. Pennycook, and D.E. Jesson, Phys. Rev. Lett., **64**, 938 (1990)

[9] T. Yamazaki, N. Nakanishi, A. Rečnik, M. Kawasaki, K. Watanabe, M. Čeh, and M. Shiojiri, Ultramicroscopy, **98**, 305 (2004)

[10] https://microscopy.empa.ch/bin/view/Main/STEM

[11] A.B. Yankovich, B. Puchala, F. Wang, J.H. Seo, D. Morgan, X. Wang, and P.M. Voyles, Nano Lett., **12**, 1311 (2012)

[12] S.D. Findlay, N. Shibuta, H. Sawada, E. Okunishi, Y. Kondo, and Y. Ikuhara, Ultramicroscopy, **110**, 903 (2010)

[13] S.D. Findlay, S. Azuma, N. Shibata, N. Okunishi, and Y. Ikuhara, Ultramicroscopy, **111**, 285 (2011)

[14] X. Lu, Y. Sun, Z. Jian, X. He, L. Gu, Y.S. Hu, H. Li, Z. Wang, W. Chen, X. Duan, L. Chen, J. Maier, S. Tsukimoto, and Y. Ikuhara, Nano Lett., **12**, 6192 (2012)

[15] D. Batuk, M. Batuk, A.M. Abakumov, and J. Hadermann, Acta Crystal. Sec. B, **71**, 127 (2015)

[16] http://www.ammrf.org.au/myscope/analysis/eds/xrayintensity/

[17] N.D. Browning, M.F. Chisholm, and S.J. Pennycook, Nature, **366**, 143 (1993)

[18] M. Varela, M.P. Oxley, W. Luo, J. Tao, M. Watanabe, A.R. Lupini, S.T. Pantelides, and S.J. Pennycook, Phys. Rev. B., **79**, 085117 (2009)

[19] P. Hohenberg, and W. Kohn, Phys. Rev., **136**, B864 (1964)

[20] W. Kohn, and L.J. Sham, Phys. Rev., **140**, A1133 (1965)

[21] G. Kresse, and J. Furthmüller, Phys. Rev. B, **54**, 11169 (1996)

[22] M. Born, and R. Oppenheimer, Annalen der Physik, **20**, 30 (1927)

[23] D.C. Langreth, and J.P. Perdew, Phys. Rev. B, **21**, 5469 (1980)

[24] J.P. Perdew, Phys. Rev. B, **33**, 8822 (1986)

[25] J.P. Perdew, K. Burke, and M. Ernzerhof, Phys. Rev. Lett., **77**, 3865 (1996)

[26] U. von Barth, and L. Hedin, J. Phys. C: Solid State Phys., **5**, 1629 (1972)

[27] V.I. Anisimov, J. Zaanen, and O.K. Andersen, Phys. Rev. B, **44**, 943 (1991)

[28] X. Ma, Y. Wu, Y. Lu, and Y. Zhu, J. Phys. Chem. C, **117**, 26029 (2013)

[29] J.C. Slater, Phys. Rev., **51**, 846 (1937).

[30] D.R. Hamann, M. Schlueter, and C. Chiang, Phys. Rev. Lett., **43**, 1494 (1979)

[31] G.B. Bachelet, D.R. Hamann, and M. Schlueter, Phys. Rev. B, **26**, 4199 (1982)

[32] O.K. Andersen, Phys. Rev. B, **12**, 3060 (1975)

[33] P.E. Blöchl, Phys. Rev. B, **50**, 17953 (1994)

[34] G. Kresse, and D. Joubert, Phys. Rev. B, **59**, 1758 (1999)

[35] R. Puthenkovilakam, E.A. Carter, and J.P. Chang, Phys. Rev. B, **69**, 155329 (2004)

[36] A. Seko, F. Oba, A. Kuwabara, and I. Tanaka, Phys. Rev. B, **72**, 024107 (2005)

Chapter 3. Inversion Domain Boundaries in Mn-Al Dual-Doped ZnO: Atomic-Scale Observations

3.1 Introduction

The microstructural properties of IDBs have been characterized in ZnO systems containing a number of dopants, including Sb [1,2], Fe [3,4], Ga [5], In [6-9], and Sn [10,11]. However, the study of additional systems is important for identifiying unique or previously unidentified microstructural features. In this chapter, the results of phase and microstructure analysis of ZnO co-doped with Al and varying concentrations of Mn by XRD, SEM and TEM are discussed. It is found that IDBs develop at a high Mn concentration of 10 at. %. Further characterization of the atomic-scale structure and chemical composition of the basal-plane IDB by HAADF/ABF-STEM and STEM-EDS/EELS has been carried out and the findings are also discussed and analyzed. Comparisons are made with the microstructural features previously observed by atomic-scale analysis of b-IDBs in ZnO doped with other elements and the formation mechanisms of the IDBs observed in the Mn-Al co-doped ZnO system are discussed in detail.

3.2 Methods

Synthesis

Samples were prepared by weighing powders of ZnO (CIK NanoTek, 99.9 % purity, 34 nm), Al_2O_3 (Taimei Chemicals, Taimicron TM-DAR, 99.99 % purity, 100 nm) and Mn_3O_4 (CIK NanoTek, 99.5 % purity, 56 nm) together and then mixing them in an ethanol solution using the AR-250 Planetary Centrifugal Mixer (Thinky) at 2000 rpm for 3 hr. Samples having the following stoichiometries were prepared: $Zn_{1-x-y}Mn_xAl_yO$, x = 0.0, 0.01, 0.02, 0.05 and 0.1

and y = 0.01. The mixtures were dried at 60°C-70°C until the ethanol solvent evaporated and the resulting powders were crushed using alumina balls and sifted with a mesh of size 250 μm. Dense ceramic compacts were obtained by pressing the powders into pellets at 20 MPa using a uniaxial press and then sintering them in an alumina crucible at 1400°C for 12 hr in air. Heating and cooling rates of 5°C/min and 10°C/min respectively were used.

Characterization

Phase analysis was carried out by XRD (Rigaku, SmartLab, Cu-K_α, 2θ = 10°-80°) and microstructure observation was done using SEM (JEOL, JSM-6510 LA, 20 kV). SEM-EDS elemental mapping was also carried out. Samples for TEM and STEM analysis were prepared by cutting, grinding, polishing, dimpling and finally Ar^+ ion milling using the Precision Ion Polishing System (PIPS, Gatan). TEM observation was done using the JEOL 2010-HC operating at 200 kV. STEM analysis was done using the JEOL ARM-200F operating at 200 kV with a probe-forming semiangle of 24 mrad. Two separate detectors were used for HAADF and ABF-STEM imaging. The HAADF and ABF detector collection ranges were 90-370 mrad and 12-24 mrad respectively. Elemental mapping by EDS was carried out using a silicon drift detector (JEOL) and EELS data were acquired with the Enfinium spectrometer (Gatan). STEM-EDS and EELS data were analyzed with the Digital Micrograph software (Gatan). ABF-STEM images were smoothed using a spatial filter. EELS data were analyzed by first subtracting the background, modeled by an exponential function, and then applying a low pass filter with a window of 15 eV twice to reduce noise. To determine Mn-$L_{2,3}$ edge maxima, fitting was done using Gaussian functions.

3.3 Results and Discussion

3.3.1 Phase and Microstructure Analysis by XRD and SEM

The XRD patterns of ZnO doped with 1 at. % Al and 0, 1, 2, 5 and 10 at. % Mn are shown in Fig. 3.1. Primary phase peaks are indexed according to the ZnO wurtzite phase. As the concentration of Mn increases, a shift of the ZnO wurtzite phase peaks to lower 2θ values is observed. Fig. 3.1 (b) shows an enlarged view of the 103 ZnO peak. The shift to lower 2θ values as the Mn concentration increases is evident. The bulk solubility limit of Mn in ZnO is rather high, ~3-8 at. % at 1400°C [12,13], and increases with temperature. Thus, this shift can be attributed to the substitution of Mn on the Zn sublattice of ZnO, which causes lattice constant expansion due to the larger ionic radius of Mn^{2+} in comparison to Zn^{2+} [14]. Fig. 3.2 and Table 3.1 show the ZnO *a* and *c* lattice constant values vs. the Mn concentration. A linear increase of the lattice constants with increasing Mn concentration is observed. A fit of the data with a Vegard's law calculation for the ZnO [15] and MnO [16] wurtzite end member compounds is also shown. The experimental values show a minor deviation (0.0-0.12 %) from the theoretical values, suggesting that Mn substitution for Zn has occurred.

Table 3.1. Lattice Constants of $Zn_{0.99-x}Mn_xAl_{0.01}O$ Samples

	ZnO, *a* (Å)	ZnO, *c* (Å)	Spinel, *a* (Å)
$Zn_{0.99}Al_{0.01}O$	3.248	5.204	8.095
$Zn_{0.98}Mn_{0.01}Al_{0.01}O$	3.253	5.206	8.105
$Zn_{0.97}Mn_{0.02}Al_{0.01}O$	3.253	5.206	8.118
$Zn_{0.94}Mn_{0.05}Al_{0.01}O$	3.256	5.217	8.150
$Zn_{0.89}Mn_{0.10}Al_{0.01}O$	3.559	5.219	-

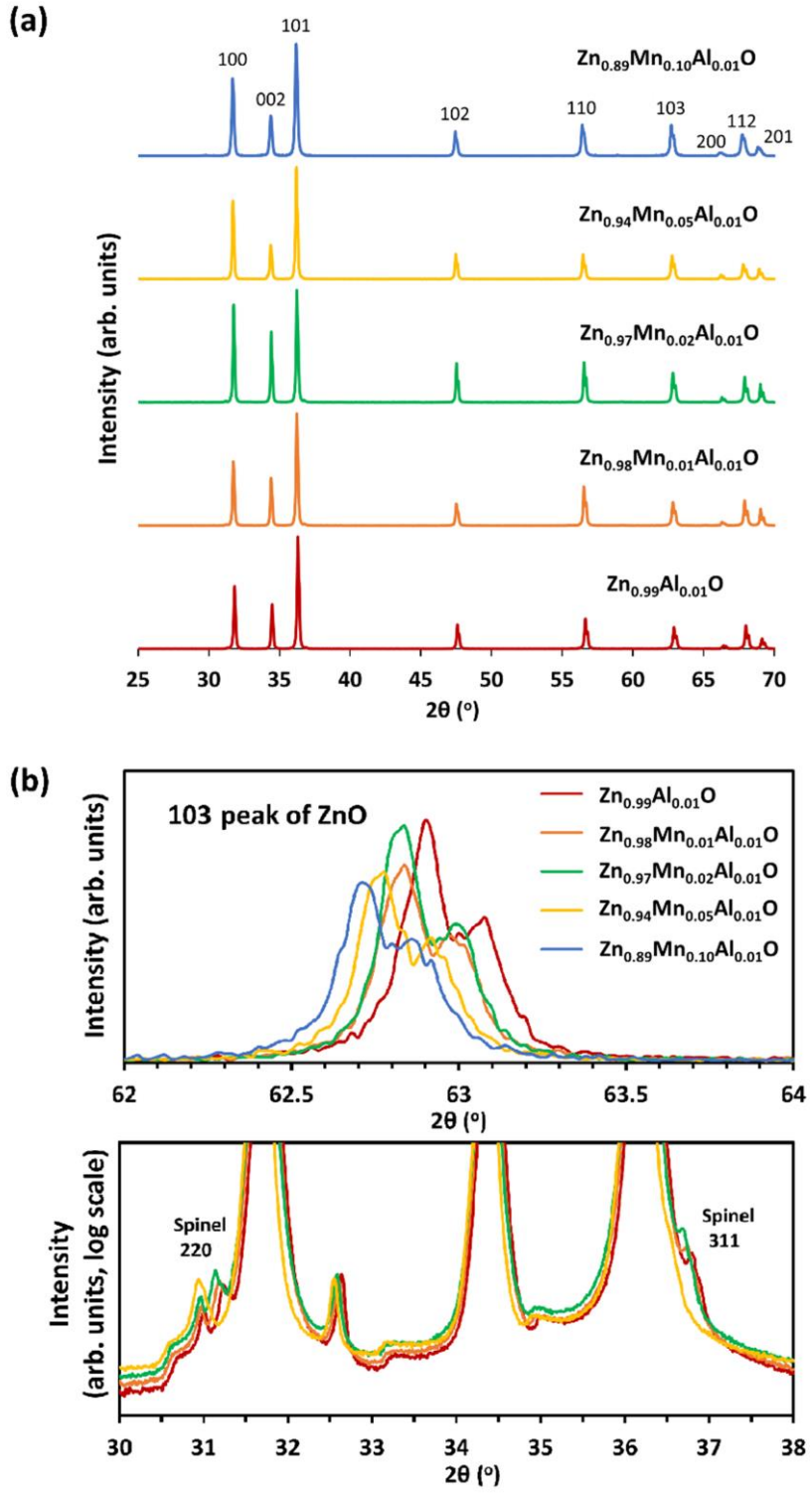

Figure 3.1. (a) XRD patterns for $Zn_{0.99-x}Mn_xAl_{0.01}O$ samples. Peaks due to the ZnO wurtzite phase are indexed. **(b)** (top) Enlarged view of the ZnO wurtzite 103 peak, showing the shift to lower 2θ values as the Mn concentration increases. (bottom) Enlarged view of the 2θ range of 30°-38°, showing the spinel secondary phase peaks, which also exhibit a shift to lower 2θ values with increasing Mn concentration.

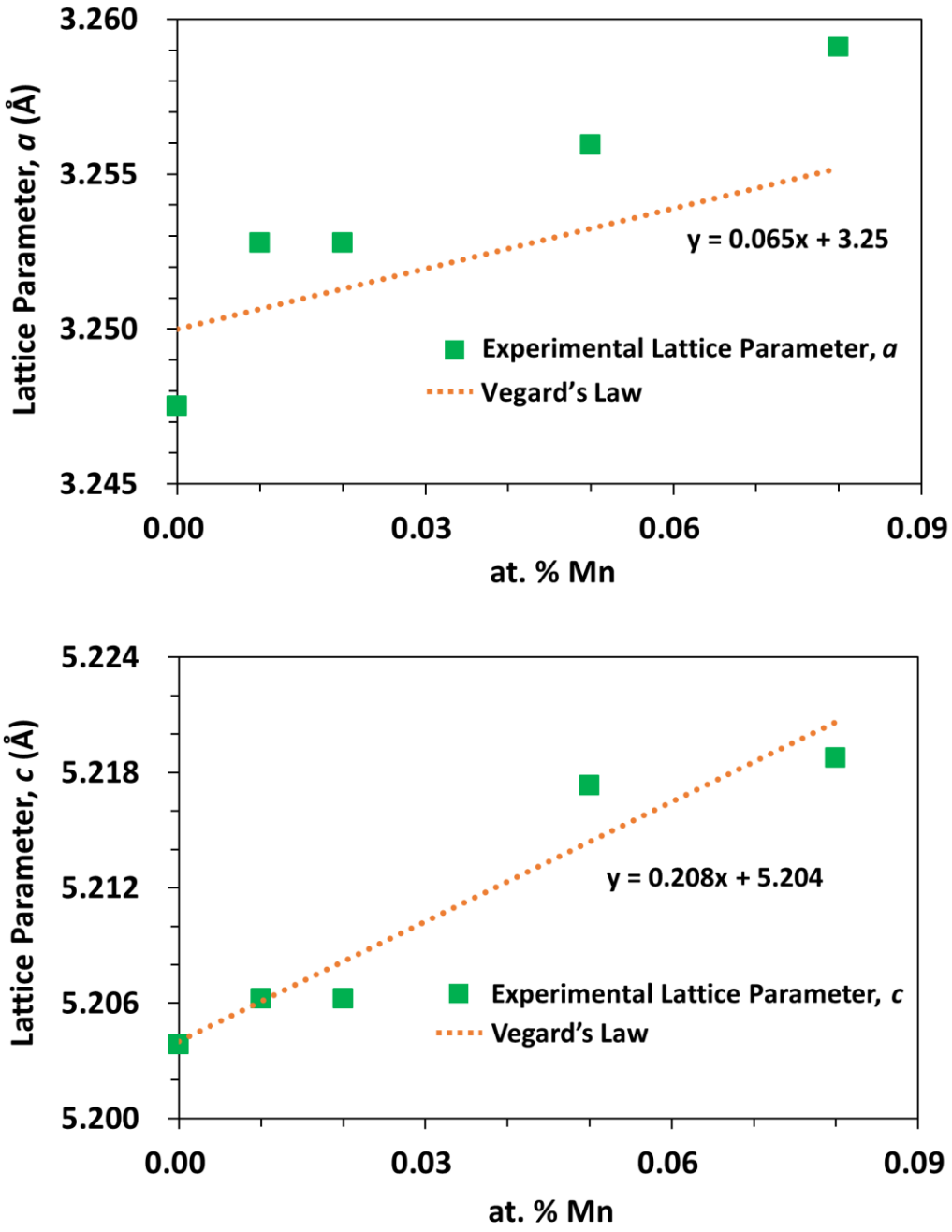

Figure 3.2. Graphs showing the dependence of the ZnO wurtzite *a* and *c* lattice parameters on the concentration of the Mn dopant. An increase of both *a* and *c* is observed as the Mn concentration increases, indicating the substitution of the larger Mn^{2+} for Zn^{2+} on the Zn sublattice. A general agreement of the experimental values with a Vegard's law calculation of the lattice parameters using *a* and *c* values for the wurtzite ZnO [15] and MnO [16] end members is observed. The nominally 10 at. % Mn-doped sample is plotted as 8 at. % Mn to reflect the reported solubility limit of 8 at. % for Mn in ZnO at 1400°C in air [13].

The 2θ region of 28°-38° is shown enlarged in Fig. 3.3. In addition to the ZnO wurtzite primary phase, low-intensity secondary phase peaks are also observed. The secondary phase peaks observed at 31.2° and 36.8° in $Zn_{0.97}Mn_{0.02}Al_{0.01}O$ are in agreement with the (220) and (311) peaks of the $ZnAl_2O_4$ spinel phase [17]. As the Mn concentration increases, the position of these peaks shifts to lower 2θ values. This can be attributed to Mn substitution in the $ZnAl_2O_4$ phase, since Mn^{3+} and Mn^{2+} both have larger respective ionic radii than Al^{3+} and Zn^{2+} at their respective sites in $ZnAl_2O_4$ [14]. At a Mn doping level of 10 at. %, a broad low-intensity spinel phase peak appears in the 2θ range of 29.2°-30.2°. The location of this peak is in agreement with that of the $Zn_xMn_{3-x}O_4$ (220) peak, previously observed in Mn-doped ZnO [18].

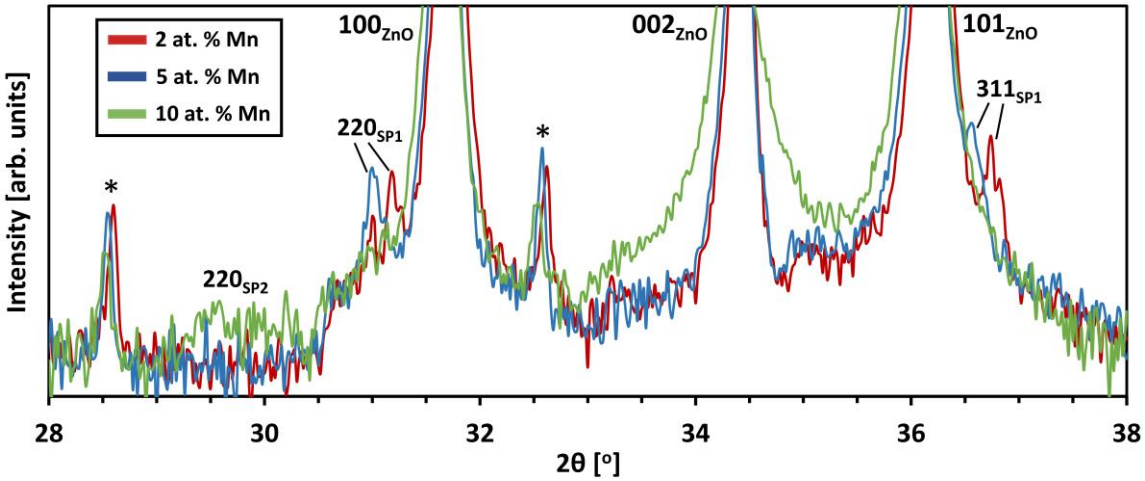

Figure 3.3. Enlarged view of the region 2θ = 28°-38° showing the XRD patterns of $Zn_{0.97}Mn_{0.02}Al_{0.01}O$, $Zn_{0.94}Mn_{0.05}Al_{0.01}O$ and $Zn_{0.89}Mn_{0.10}Al_{0.01}O$. Peaks are indexed as follows: wurtzite ZnO Cu-K_α (ZnO), wurtzite ZnO Cu-K_β (*), Mn-substituted $ZnAl_2O_4$ spinel (SP1) and $Zn_xMn_{3-x-y}Al_yO_4$ spinel (SP2). A clear broadening of the 002 ZnO peak in the XRD pattern of $Zn_{0.89}Mn_{0.10}Al_{0.01}O$ is observed, indicating defect formation.

In addition, as shown in Fig. 3.3, the XRD profile for $Zn_{0.89}Mn_{0.1}Al_{0.01}O$ exhibits a significant broadening of the ZnO 002 peak in comparison to the samples containing lower concentrations of Mn. Broadening of XRD peaks is indicative of defect formation [19] and has been previously observed in the $In_2O_3(ZnO)_n$ homologous phase compounds when the In:Zn ratio is low [7]. The broadening itself is due to the distribution of spacings between neighboring

b-IDBs along the *c*-axis in $RMO_3(ZnO)_n$ homologous phase compounds with large values of *n* [20].

SEM micrographs of Mn-Al co-doped ZnO samples are shown in Fig. 3.4. The densities, grain sizes and precipitate sizes for each these samples are also listed in Table 3.2. $Zn_{0.99}Al_{0.01}O$ exhibits a grain size of 11.1 μm and a high theoretical density (99.8 %), in agreement with previous reports [21]. As the Mn concentration increases, the grain size increases and the density decreases. The increase in grain size can be attributed to increased grain boundary diffusion in ZnO due to Mn doping [22]. However, in $Zn_{0.89}Mn_{0.1}Al_{0.01}O$ a reduction in grain size occurs. Precipitates are observed in all $Zn_{0.99-x}Mn_xAl_{0.01}O$ samples, with precipitate size increasing as the Mn concentration increases. The results of SEM-EDS

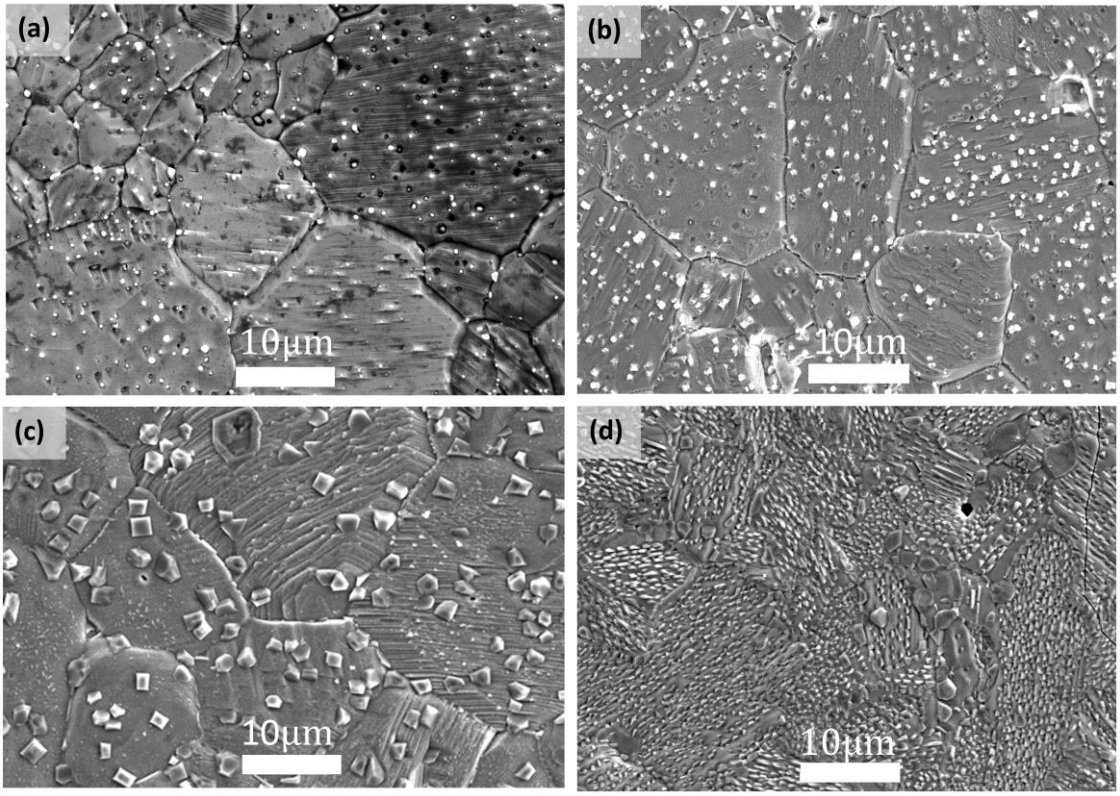

Figure 3.4. SEM images of the microstructure of **(a)** $Zn_{0.99}Al_{0.01}O$ **(b)** $Zn_{0.97}Mn_{0.02}Al_{0.01}O$ **(c)** $Zn_{0.94}Mn_{0.05}Al_{0.01}O$ and **(d)** $Zn_{0.89}Mn_{0.10}Al_{0.01}O$. Samples surfaces were polished and thermally etched at 1300-1350°C in air. Nanometric precipitates are observed within grains and at grain boundaries in all samples. The microstructure of $Zn_{0.89}Mn_{0.10}Al_{0.01}O$ also exhibits lamellar or intergrowth-like structures at grain surfaces.

elemental mapping are shown in Fig. 3.5 and Fig. 3.6. Increased concentrations of Mn and Al are detected at the positions of precipitates in $Zn_{0.94}Mn_{0.05}Al_{0.01}O$, while some precipitates rich in Mn are observed in $Zn_{0.89}Mn_{0.1}Al_{0.01}O$, in agreement with the Mn-substituted $ZnAl_2O_4$ and $Zn_xMn_{3-x}O_4$ phases respectively, as detected by XRD. $Zn_{0.89}Mn_{0.1}Al_{0.01}O$ also shows an increased Mn concentration at grain boundaries, indicating that Mn-rich spinel precipitates may preferentially form at grain boundaries. In addition, the $Zn_{0.89}Mn_{0.1}Al_{0.01}O$ sample exhibits a texture on the surface of each grain which is not observed in the samples doped with lower concentrations of Mn.

Table 3.2. Density, Average Grain Size and Average Precipitate Size

Sample Stoichiometry	Density (g/cm^3)	Relative Density (%)[(a)]	Avg. Grain Size (µm)	Avg. Precipitate Size (µm)
$Zn_{0.99}Al_{0.01}O$	5.66	99.8	11.1	0.48
$Zn_{0.98}Mn_{0.01}Al_{0.01}O$	5.46	96.3	-	-
$Zn_{0.97}Mn_{0.02}Al_{0.01}O$	5.24	92.4	22.8	0.95
$Zn_{0.94}Mn_{0.05}Al_{0.01}O$	5.33	94.0	22.8	1.7
$Zn_{0.89}Mn_{0.10}Al_{0.01}O$	5.28	93.1	12.0	2.0

[(a)] Theoretical Density of ZnO: 5.67 g/cm^3

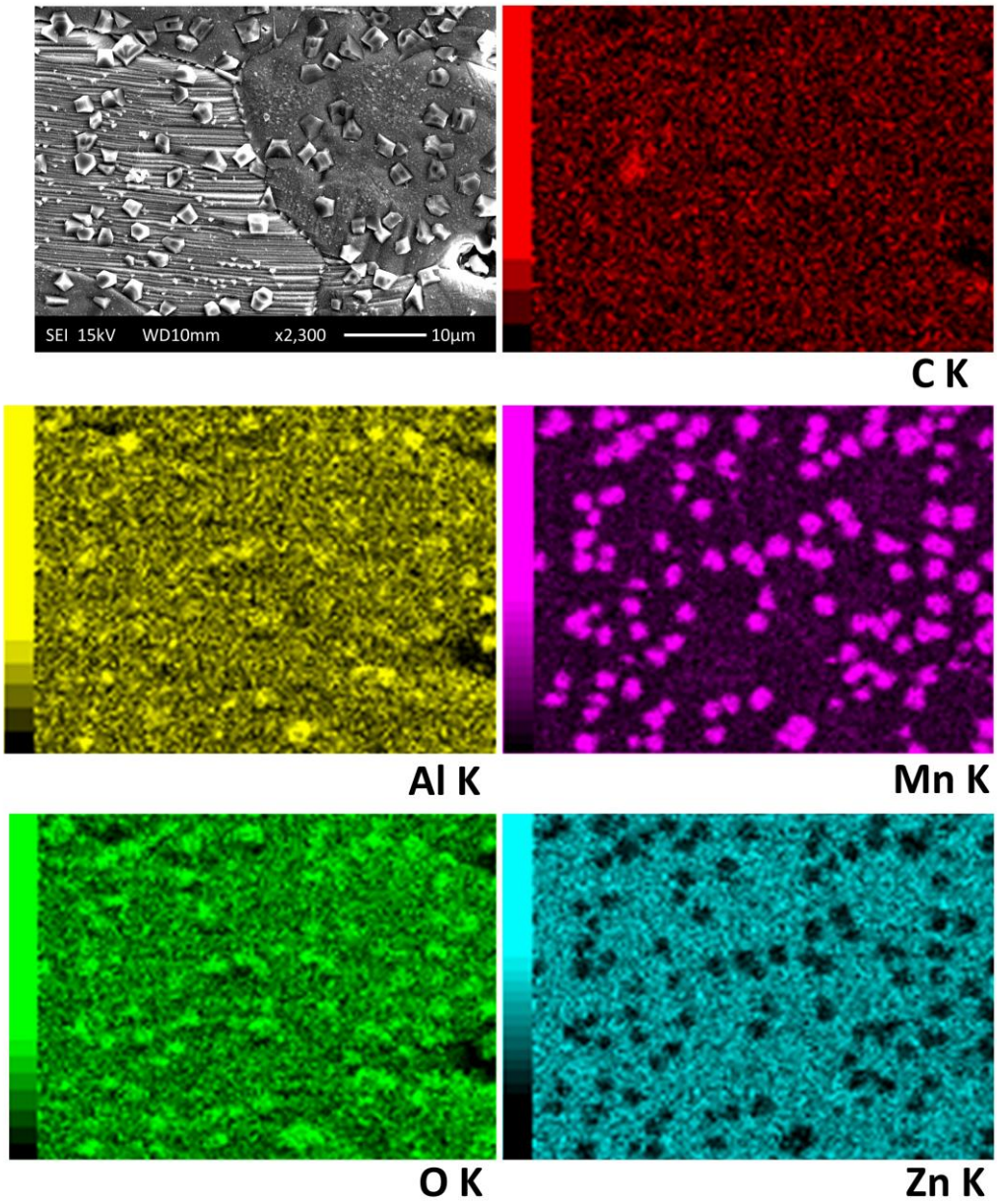

Figure 3.5. SEM-EDS elemental mapping of $Zn_{0.94}Mn_{0.05}Al_{0.01}O$. Precipitates rich in Mn, Al and O are observed, in agreement with the Mn-substituted $ZnAl_2O_4$ phase detected by XRD.

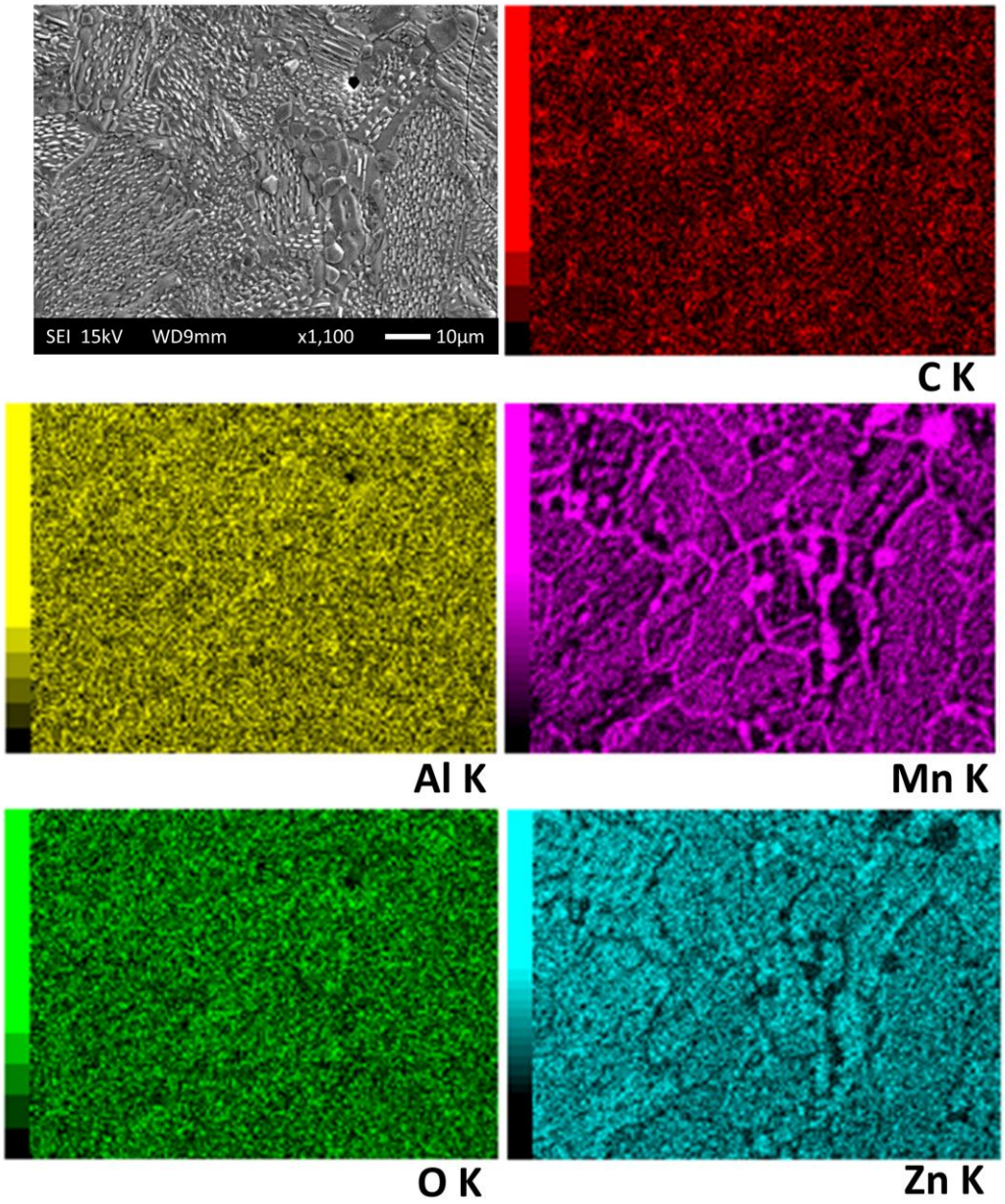

Figure 3.6. SEM-EDS elemental mapping of $Zn_{0.89}Mn_{0.10}Al_{0.01}O$. In addition to Mn-rich precipitates, the segregation of Mn and corresponding depletion of Zn is observed at the grain boundaries.

3.3.2 Microstructure Observation by TEM

In order to determine the source of the 002 peak broadening in the XRD pattern of $Zn_{0.89}Mn_{0.1}Al_{0.01}O$ and the texture observed at the grain surfaces by SEM in $Zn_{0.89}Mn_{0.1}Al_{0.01}O$, microstructure observation was carried out using TEM. For comparison, TEM microstructure observations of the $Zn_{0.99}Al_{0.01}O$ and $Zn_{0.94}Mn_{0.05}Al_{0.01}O$ samples were also carried out. Bright-field (BF) TEM images of the microstructures of $Zn_{0.99}Al_{0.01}O$ and $Zn_{0.94}Mn_{0.05}Al_{0.01}O$ are shown in Fig. 3.7. Spinel precipitates were observed in both samples, at grain boundaries and also within grains. In $Zn_{0.94}Mn_{0.05}Al_{0.01}O$, some precipitates exhibited no particular orientation relationship (OR) with respect to the ZnO grains; however, precipitates with ORs were also observed. Two distinct orientation relationships, OR1: $[10\bar{1}0]_{ZnO}//[0\bar{1}1]_{SP}$, $(0002)_{ZnO}//(111)_{SP}$ (Fig. 3.7) and OR2: $[\bar{1}2\bar{1}0]_{ZnO}//[1\bar{1}\bar{2}]_{SP}$, $(0002)_{ZnO}//(220)_{SP}$ (Fig. A1), were identified by obtaining EDPs near the common zone-axes of the spinel precipitates and the ZnO grains.

As shown in Fig. 3.7, at 5 at. % Mn doping, spinel precipitates with a uniform contrast are observed. In contrast to the 5 at. % Mn-doped sample, the 10 at. % Mn-doped sample contained spinel precipitates with bands indicative of twinning, as shown in Fig. 3.8. Twinning may occur in the spinel phases at high Mn concentrations due to an increasing content of Jahn-Teller active Mn^{3+} octahedra, which induce a tetragonal distortion of the $Zn_xMn_{3-x}O_4$ unit cell [23]. A large tetragonal distortion can stabilize the formation of twinned domains [24]. Based on the indexing of the EDP, shown in Fig. 3.8 (d), which corresponds to the spinel precipitate in Fig. 3.8 (a)-(c), the twins are determined to form approximately at $\{221\}$ cubic planes. The formation of ferroelastic domains, resembling those shown in Fig. 3.8, has been previously observed in other manganite spinels [24] as well as in ZrO_2 ceramics [25-30]. In both cases, the twinned domains are considered to form in order to accommodate the lattice strain associated with a phase transition [24-30]. In the case of manganite spinels, the phase transition can be characterized as a cubic→tetragonal transformation that occurs as the concentration of

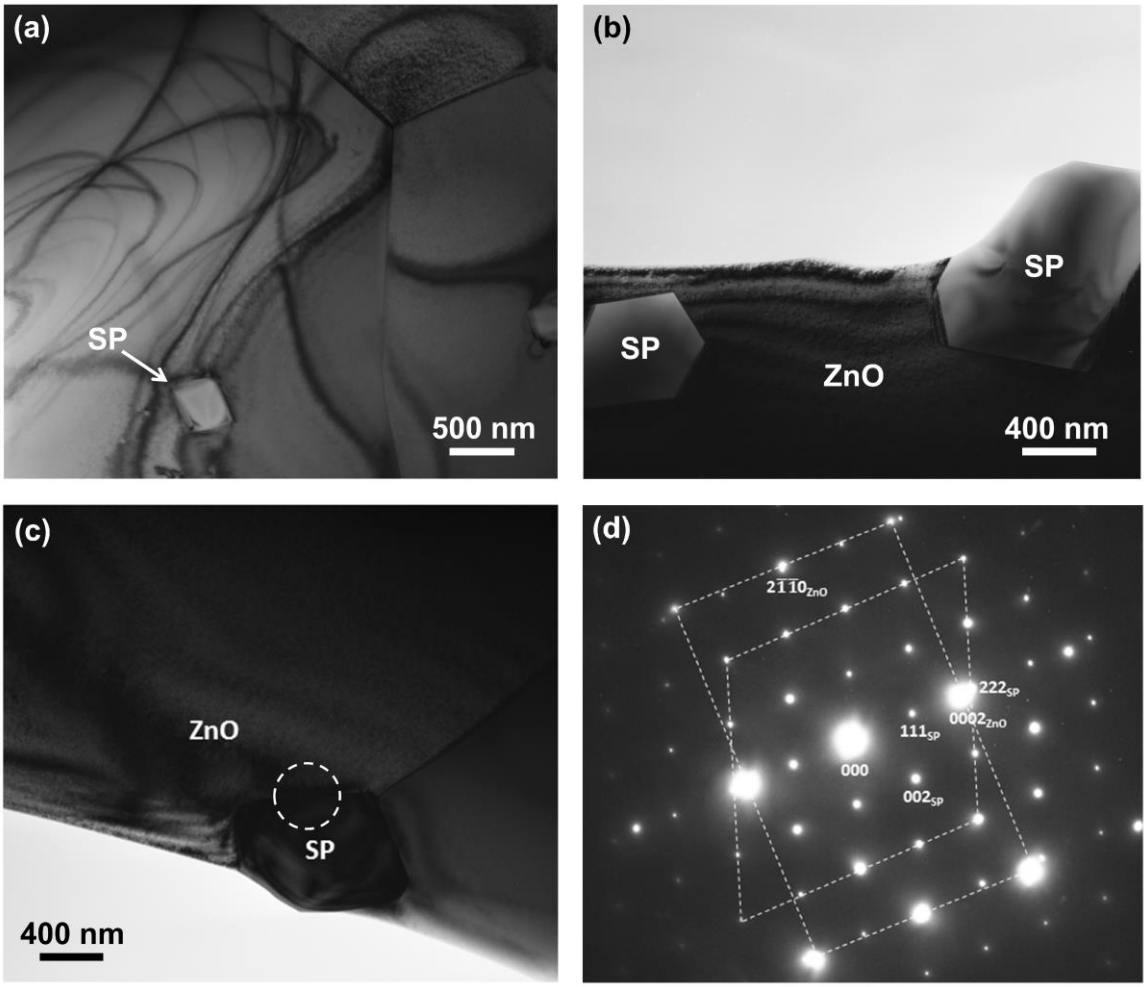

Figure 3.7. (a) BF-TEM image of $Zn_{0.99}Al_{0.01}O$. Nanometric spinel precipitates (SP) are observed. **(b)** BF-TEM image of $Zn_{0.94}Mn_{0.05}Al_{0.01}O$. Spinel precipitates without a specific orientation relationship (OR) with the surrounding ZnO grain (ZnO) are observed. **(c)** BF-TEM image of $Zn_{0.94}Mn_{0.05}Al_{0.01}O$. A spinel precipitate possessing an OR with the ZnO grain is observed. **(d)** EDP corresponding to the dashed circle in (c). A specific orientation relationship (OR1) is observed between the ZnO grain and the spinel precipitate. The spinel [111] direction and ZnO [0002] direction are approximately parallel, with a misorientation angle of ~1.2º along the [0002] direction. The zone-axes, ZnO: $[10\bar{1}0]$ and SP: $[0\bar{1}1]$, are also aligned, resulting in the following crystallographic orientation relationship (OR1): $[10\bar{1}0]_{ZnO}//[0\bar{1}1]_{SP}$, $(0002)_{ZnO}//(111)_{SP}$.

Jahn-Teller distorted Mn^{3+} octahedra increases [23,24], while two phase transformations can occur in ZrO_2 ceramics, namely the high temperature cubic→tetragonal and low temperature tetragonal→monoclinic transitions [28]. In the case of ZrO_2 ceramics, it is the combination of the formation of ferroelastic tetragonal twin domains [29], which can undergo domain

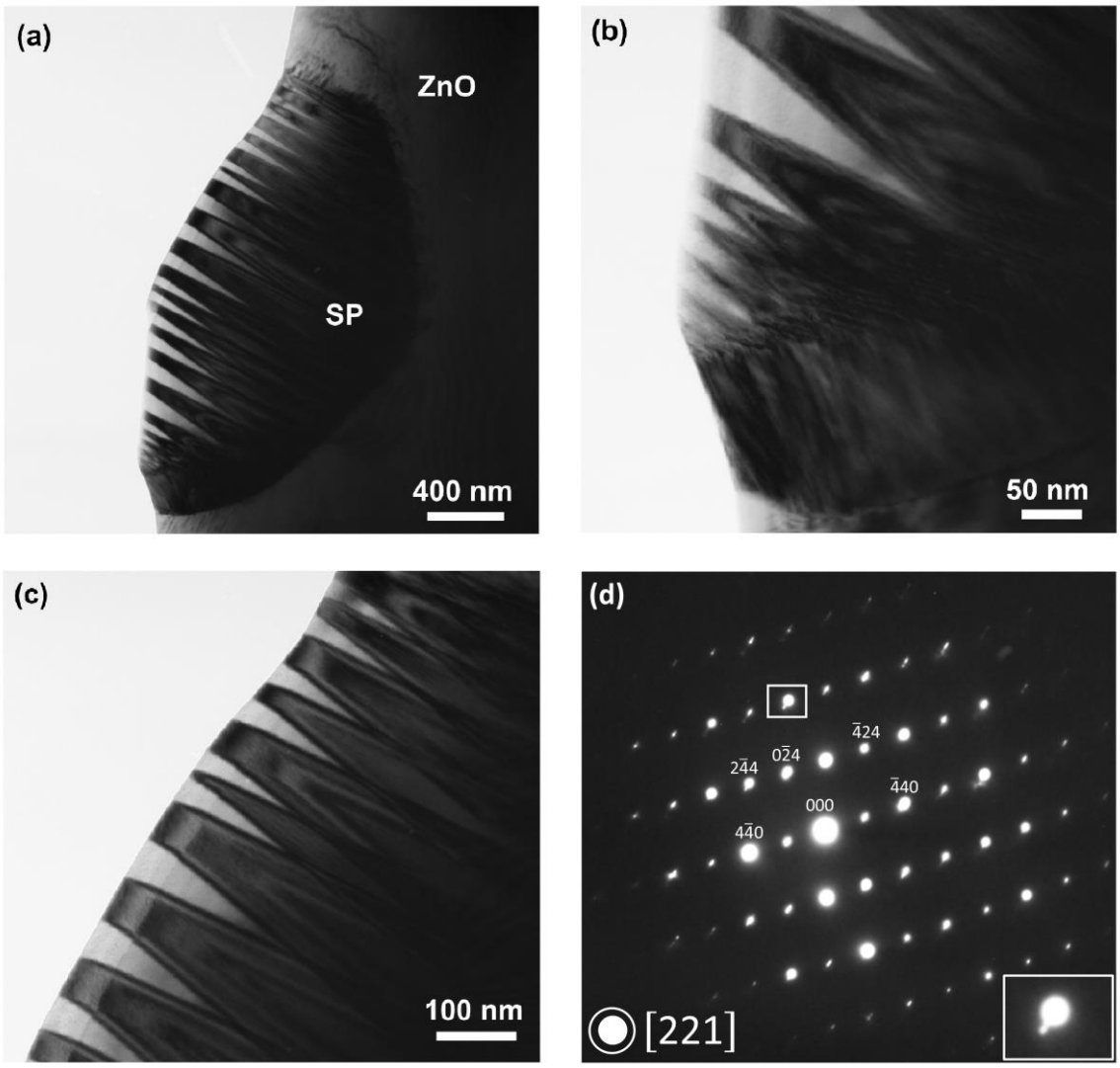

Figure 3.8. (a) BF-TEM image of a spinel precipitate (SP) in $Zn_{0.89}Mn_{0.10}Al_{0.01}O$. A twinned microstructure not observed in the spinel precipitates that form in $Zn_{0.99-x}Mn_xAl_{0.01}O$ samples with $x \leq 0.05$ is observed. **(b)** High-magnification BF-TEM image of the region near the interface between the spinel precipitate and the ZnO grain. A region that appears to be representative of the early stages of nucleation of the twinned microstructure is observed at the interface. **(c)** High-magnification BF-TEM image of the well-developed twinned bands in the precipitate. Twin domains resembling those observed in ferroelastic materials [24-28] are observed. **(d)** [221] zone-axis image of the EDP corresponding to the spinel precipitate shown in (a)-(c), indexed according to the fcc spinel crystal structure. The twin boundaries within the precipitates appear to form approximately parallel to the cubic {221} planes. The rectangular outlined area within the EDP, shown as an enlarged inset at the bottom right corner in (d), clearly shows the splitting of the Bragg reflections, indicative of crystallographic twinning.

switching to accommodate an applied stress, during quenching from the cubic phase as well as the formation of twinned monoclinic domains within a tetragonal ZrO_2 matrix [30], which can occur under an applied stress, both of which are considered to contribute to transformation toughening, which leads to ultrahigh toughness values in ZrO_2-based materials [25-30].

In $Zn_{0.89}Mn_{0.1}Al_{0.01}O$, the volume content of the spinel phases is low. In contrast to $Zn_{0.99-x}Mn_xAl_{0.01}O$ samples with $x \leq 0.05$, intergrowth-like features are present throughout most grains. Thus, they will likely have a significant influence on the bulk properties of $Zn_{0.89}Mn_{0.1}Al_{0.01}O$. To determine the nature of the intergrowth-like defects, dark-field (DF) TEM images were acquired. Fig. 3.9 (a) and (b) show DF-TEM images of $Zn_{0.89}Mn_{0.1}Al_{0.01}O$ obtained at the $[1\bar{2}10]$ zone-axis using the $\mathbf{g} = 0002$ and $\mathbf{g} = 000\bar{2}$ reflections respectively. When the imaging reflection is changed from $\mathbf{g} = 0002$ to $\mathbf{g} = 000\bar{2}$, the contrast inverts across two sets of planes, one parallel to and one diagonal to the ZnO basal plane. A similar type of microstructure composed of domains which form a network of zigzag-like features has been reported for studies on In-doped ZnO and Fe-doped ZnO [3,8]. Because the contrast inverts when the DF imaging reflection is changed from $\mathbf{g} = 0002$ to $\mathbf{g} = 000\bar{2}$, it can be concluded that the defects observed are inversion domain boundaries. The inversion occurs due to the difference in the scattering factors of the $\mathbf{g} = 0002$ and $\mathbf{g} = 000\bar{2}$ reflections in thin crystals, which is a result of the violation of Friedel's law that may be observed in non-centrosymmetric crystals [1,31]. DF-TEM imaging can be used to identify planar defects as IDBs. However, the determination of the polarity of the *c*-axis at the IDB interfaces, which may assume either a H-H or T-T configuration, cannot be determined by DF-TEM imaging alone. Electron microdiffraction has been used in previous studies to determine the *c*-axis configuration at IDB interfaces [1]. As will be discussed in Section 3.3.3, we have used the ABF-STEM method to determine the *c*-axis polarity at the b-IDB interfaces in $Zn_{0.89}Mn_{0.1}Al_{0.01}O$.

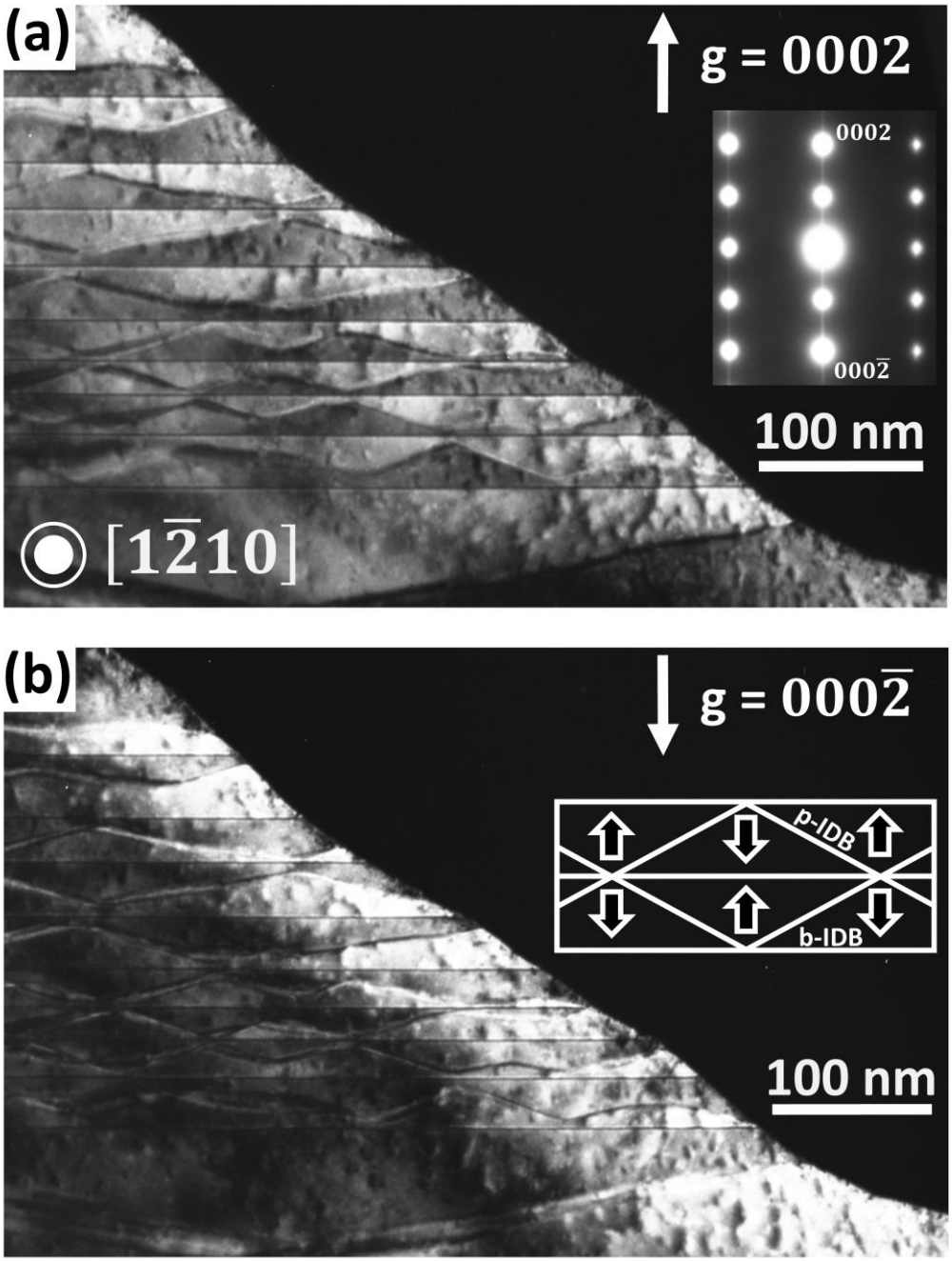

Figure 3.9. DF-TEM images of the IDs in $Zn_{0.89}Mn_{0.10}Al_{0.01}O$, acquired using the **(a) g** = 0002 and **(b) g** = 000$\bar{2}$ DF imaging reflections. When the DF imaging reflection is changed from **g** = 0002 to **g** = 000$\bar{2}$, the ID contrast inverts across planes parallel to and diagonal to the basal plane, corresponding to the basal-plane IDBs and pyramidal-plane IDBs respectively. The DF imaging reflections used correspond to the 0002 and 000$\bar{2}$ reflections in the EDP in (a) (inset). The streaks observed between peaks along the *c*-axis in the EDP are due to the stacking faults that form at the b-IDBs. A schematic of the ID network microstructure is shown in (b) (inset).

The formation of IDBs in $Zn_{0.89}Mn_{0.1}A\ l_{0.01}O$ is due to the high concentration of Mn, which exceeds the solubility limit of ~3-8 at. % that has been reported for Mn in ZnO at 1400°C in air [12,13]. 2D nanoscale planar defects such as IDBs may form as precursors to secondary phase formation when the dopant solubility limit is exceeded [32]. Significant IDB formation results in the formation of polytypes or homologous phase compound members. Below the solubility limit of Mn in ZnO (i.e. at $\leq$ 3-8 at. % Mn), Mn can substitute for Zn and act as a point defect. Above the solubility limit (e.g. at 10 at. % Mn), the formation of IDBs becomes favorable in order to reduce strain within the ZnO lattice by incorporating excess dopant atoms at specific crystallographic sites, while also maintaining electroneutrality [33]. According to Pauling's rule of electrostatic neutrality, the cation dopants occupying the octahedral b-IDB sites should have an average valence of 3+ [1,34]. Al^{3+} and Mn^{3+} are both stable at the sintering temperature of 1400°C [17,23]. Thus, the stabilization of the formation of b-IDBs due to occupation by these dopants, when their solubility limits are exceeded, is understandable based on electroneutrality requirements. Additionally, high sintering temperatures and long sintering times are favorable for achieving structural equilibrium leading to IDB or homologous phase formation, due to the increased kinetic driving force for dopant diffusion [7,8]. Thus, the sintering conditions (1400°C, 12 hr) may also assist in stabilizing the formation of the ID networks observed in $Zn_{0.89}Mn_{0.1}Al_{0.01}O$. As in the case of the $In_2O_3(ZnO)_n$ homologous phase compounds, increasing the sintering time, sintering temperature or Mn concentration could result in an improvement of the microstructural homogeneity by facilitating the diffusion of the IDB-forming element in order to achieve structural equilibrium [7,8].

3.3.3 Atomic-Scale Analysis of b-IDBs by HAADF and ABF-STEM

To characterize the atomic structure of IDBs in $Zn_{0.89}Mn_{0.1}Al_{0.01}O$, observations using atomic-resolution STEM were carried out. The b-IDB was chosen for STEM analysis because it is the most clearly defined defect within the ID networks. Fig. 3.10 (a) and (b) respectively show HAADF and ABF images of the ID network microstructure in $Zn_{0.89}Mn_{0.1}Al_{0.01}O$. Decreased contrast is observed at b-IDB interfaces and there is a variation in the spacing between the b-IDBs along the *c*-axis. An atomic-resolution image of the b-IDB viewed at the $[\bar{1}2\bar{1}0]$ zone-axis is shown in Fig. 3.11 (a). HAADF intensity is related to the average atomic number, Z, of the atomic column imaged according to the following equation: $I \propto Z^n$ ($1.6 \leq n \leq 1.9$) [2]. Thus, the bright contrasts within the domain interior in Fig. 3.11 (a) correspond to cation columns primarily composed of Zn (Z = 30). Oxygen columns are not imaged due to their lower average atomic number (Z = 8). A dispersion of reduced contrast is

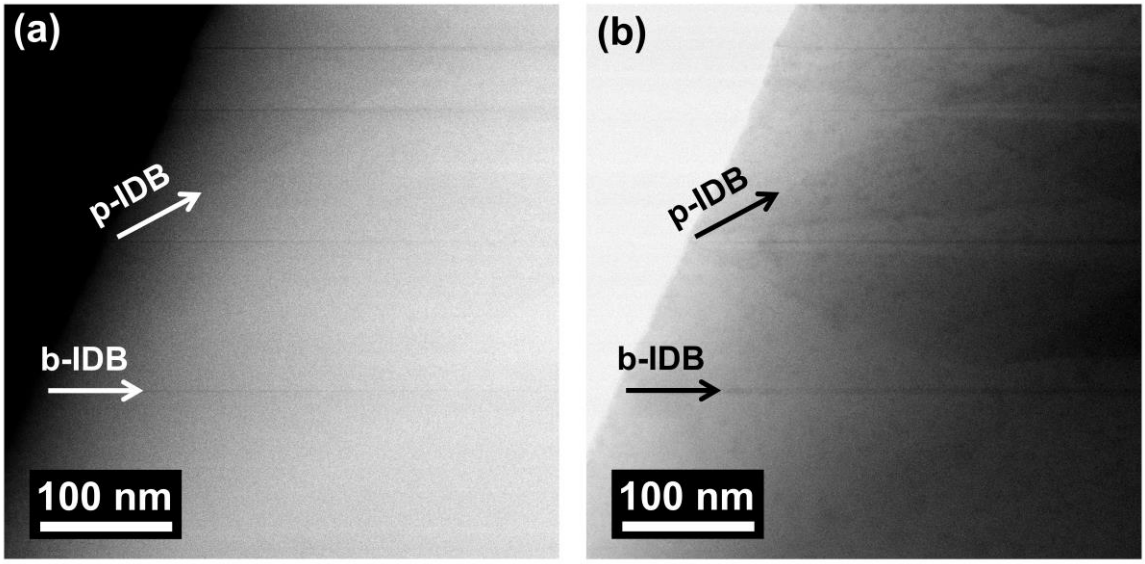

Figure 3.10. (a) HAADF and **(b)** ABF-STEM images of the IDs, viewed at the $[\bar{1}2\bar{1}0]$ zone-axis. The b-IDBs are viewed edge-on, while the p-IDBs are inclined with respect to the zone-axis. Both b-IDB and p-IDB interfaces exhibit reduced intensity relative to the bulk-like domain interior regions in the images. The reduced intensity may be due to the localization of the low atomic number dopants (Mn and Al), in the case of the HAADF image, and/or local strain or lattice distortion, which can cause a reduction in the image intensity at defect structures such as interfaces in HAADF and ABF-STEM images [35].

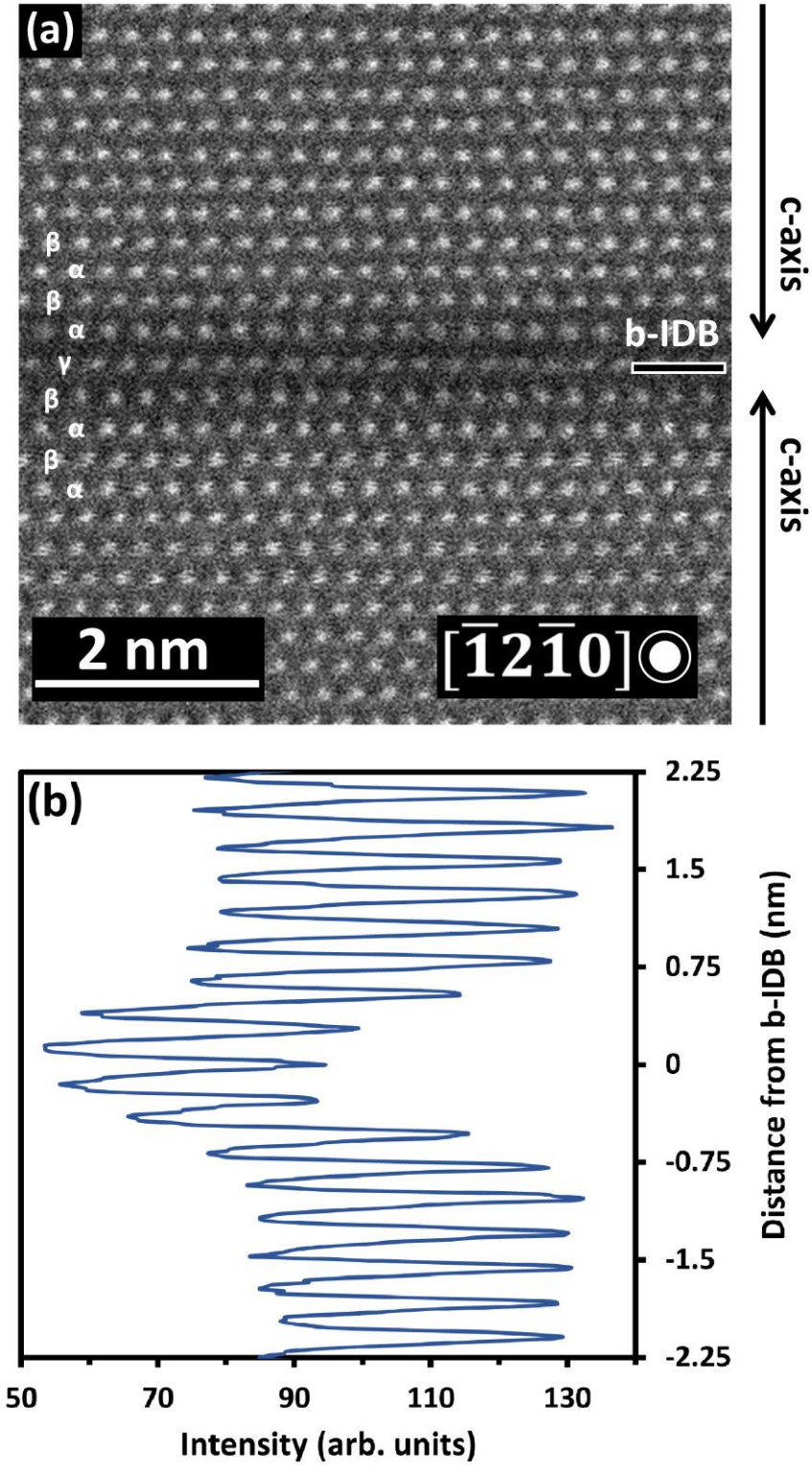

Figure 3.11. (a) Atomic-resolution HAADF-STEM image of a b-IDB viewed at the [$\bar{1}2\bar{1}0$] zone-axis. **(b)** Average intensity line profile along the *c*-axis. As shown in (b), the HAADF intensity of the cation columns is significantly reduced at the b-IDB and in the two cation layers directly neighboring the b-IDB. The *c*-axis cation stacking sequence at the b-IDB (αβαβ|γ|αβαβ) is shown in (a).

observed at the b-IDB cation plane. Fig. 3.11 (b) shows an average intensity line profile across the b-IDB in Fig. 3.11 (a). There is a sharp reduction in the HAADF intensity exactly at the b-IDB cation plane. The reduction in intensity could be due to occupation of the b-IDB cation layer by Mn (Z = 25) or Al (Z = 13).

The intensity of the cation columns directly neighboring the b-IDB is reduced to a level between that of the b-IDB plane and the bulk-like domain interior. This could be caused by strain, which occurs at the b-IDB due to an expansion of the $\{0002\}$ cation interplanar spacing by 8.5 % relative to the domain interior. Strain or lattice distortion at defect structures such as interfaces can result in a reduction of the HAADF intensity [35]. Similar effects have been observed at b-IDBs in Fe-doped ZnO, with the reduction in HAADF intensity attributed to a local increase in the strain around the b-IDB, resulting in a reduction in electron channeling [4]. Other potential sources for the dispersion of reduced contrast around the b-IDB interface include factors related to the imaging conditions (e.g. misorientation tilt, defocus etc. [36]), sample thickness variation [36] or the increased substitution of Mn^{2+} or Al^{3+} for Zn^{2+}, relative to the domain interior, at the tetrahedral sites directly neighboring the b-IDB, possibly accommodated by the strain at the interface. The *c*-axis cation stacking sequence across the b-IDB is determined to be αβαβ|γ|αβαβ. This is different from the *c*-axis cation stacking sequence of αβαβ|α|γαγα, previously reported for Fe [4], Sn [10] and In [37] doped ZnO, and the sequence of αβαβ|α|γβγβ, reported for Sb-doped ZnO [1].

ABF-STEM imaging of the b-IDB was also carried out. In contrast to HAADF-STEM, ABF-STEM has the advantage of imaging elements with both high and low atomic numbers, since the intensity observed in ABF-STEM images approximately scales with Z according to the following expression: $I \propto Z^{1/3}$ [38]. Thus, the imaging of elements such as Li and O can be achieved by ABF-STEM [38]. An ABF-STEM image of the b-IDB is shown in Fig. 3.12. Smaller dark contrasts correspond to the positions of oxygen anion columns, while larger dark contrasts correspond to the positions of cation columns. By observing the stacking sequence

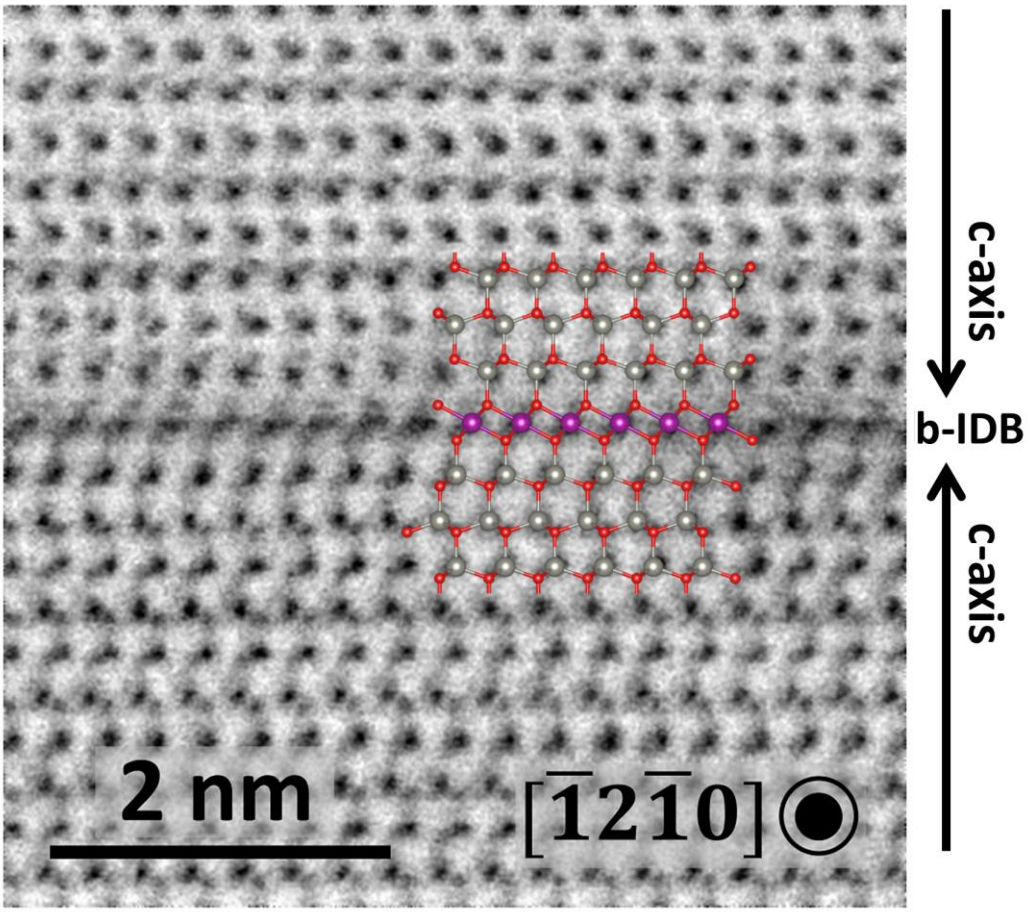

Figure 3.12. Atomic-resolution ABF-STEM image of a b-IDB viewed at the $[\bar{1}2\bar{1}0]$ zone-axis. Cation and anion columns are both imaged, as large darker and small less dark contrasts respectively. Based on the cation-anion stacking sequence along the *c*-axis, the H-H *c*-axis configuration at the b-IDB is confirmed. The cation-anion coordination also changes from tetrahedral within the ZnO bulk-like domain interior to octahedral at the b-IDB. A section of a b-IDB slab model, which includes a Mn-doped monolayer of edge-sharing octahedra as the b-IDB interface, that was refined by first principles calculations (discussed in Chapter 5) is shown superimposed. Mn, Zn and O atoms are colored purple, grey and red respectively. A general agreement between the ABF-STEM image and the model is observed.

along the *c*-axis of both anion and cation $\{0002\}$ planes at either side of the b-IDB, it can be determined that a H-H configuration of the *c*-axis forms at the b-IDB. In addition, in contrast to the tetrahedral oxygen coordination of the cations in the domain interior, the cations within the b-IDB plane exhibit an octahedral oxygen coordination. By careful observation of the cation and anion positions, it can be determined that the Zn tetrahedra directly neighboring the

b-IDB share corners with the b-IDB octahedra. Sharing of corners between b-IDB octahedra and the Zn tetrahedra occurs in order to reduce the Coulombic repulsion associated with unfavorable face-sharing of b-IDB octahedra with neighboring Zn tetrahedra [1,3,34]. A model of the Mn-doped b-IDB, obtained by DFT calculations (discussed in detail in Chapter 5), is shown superimposed in Fig. 3.12. The ABF-STEM image and the model, which assumes a full occupancy of the b-IDB cation plane by Mn, are in general agreement. The assumption of a b-IDB cation plane occupied primarily by Mn is supported by the results of STEM-EDS and EELS, discussed in the following section.

3.3.4 Elemental Analysis of b-IDBs by EDS and EELS

To determine whether or not the localization of Mn or Al at the b-IDB interface occurs, elemental analysis was carried out using STEM-EDS and EELS. STEM-EDS net counts maps acquired at a b-IDB are shown in Fig. 3.13. There is a significant increase in the Mn *K* signal intensity at the b-IDB, indicating that Mn localizes at the b-IDB. A weaker increase of the Al *K* signal intensity is also observed at the b-IDB. Thus, Al also localizes at the b-IDB, at a lower concentration. This is expected, given that the concentration of Mn (10 at. %) significantly exceeds that of Al (1 at. %), and also due to the fact that the respective solubility limits of Mn and Al are approximately 3-8 at. % [12,13] and 0.3 at. % [39] at 1400ºC in air. The occupation of the b-IDB by Mn and Al is further confirmed based on the STEM-EDS net counts map corresponding to the Zn *K* signal, which is significantly reduced at the b-IDB. Co-occupation of the b-IDB cation plane by Mn^{3+} and Al^{3+} is understandable considering the fact that an average cation valence of 3+ is necessary in order to maintain electroneutrality at the b-IDB octahedral site [1,34]. Mn^{3+} and Al^{3+} also prefer to occupy the octahedral site in the $ZnMn_2O_4$ [23] and $ZnAl_2O_4$ [17] compounds.

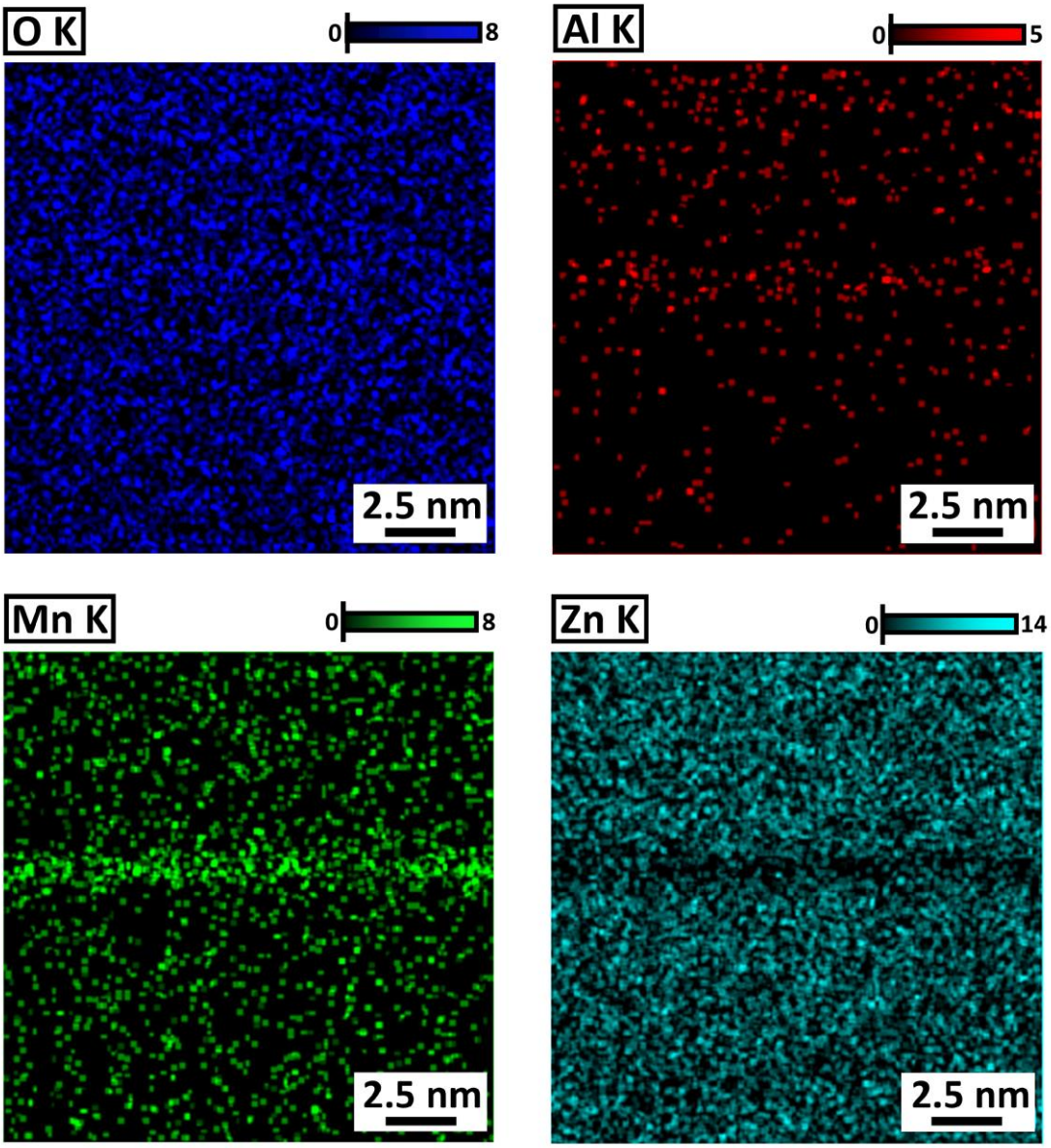

Figure 3.13. STEM-EDS net counts elemental maps acquired at a b-IDB. At the b-IDB, a significant increase of the Mn *K* signal and a minor increase of the Al *K* signal is observed, indicating the localization of Mn and Al at the b-IDB. The Zn *K* signal is also reduced at the b-IDB, indicating the depletion of Zn.

To analyze dopant localization at the b-IDB at a higher resolution, an EELS line scan was also acquired across the b-IDB interface. Fig. 3.14 (b) shows the EELS data corresponding to the line scan shown in the ADF-STEM image in Fig. 3.14 (a). The Mn-$L_{2,3}$ signal is low within the domain interior and increases in intensity at the b-IDB cation plane, indicating that significant Mn localization occurs at the b-IDB. Several measurements of the energy-loss

difference between the Mn L_2 and L_3 edge maxima, $\Delta E(L_2\text{-}L_3)$, at the b-IDB were also made and the average value was determined to be 11.13 eV, in agreement with the value for a mixed Mn valence of 3+/2+ ($\Delta E(L_2{-}L_3)$ = 11.2 ± 0.1 eV [40]). A mixed valence of 3+/2+ may be observed due to the combined contributions to the EELS signal from both the domain interior and the b-IDB cation plane, where the stable Mn valence should be 2+ [40] and 3+ [34] respectively.

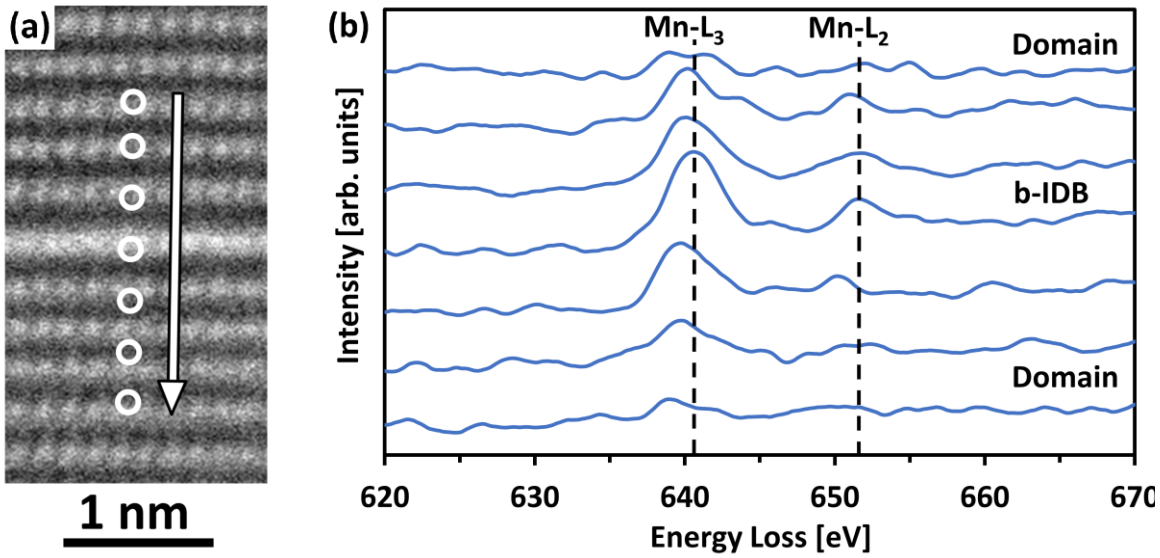

Figure 3.14. (a) ADF-STEM image of a b-IDB showing the line scan corresponding to the EEL spectra in **(b)**. In (b), the Mn-$L_{2,3}$ edges exhibit a significant increase in intensity at the b-IDB interface, indicating Mn localization. The Mn-L_3 peak also exhibits a shift to higher energy-loss values at the b-IDB relative to the domain interior, suggesting a local increase of the Mn valence state [40].

3.3.5 IDB Formation Mechanism in $Zn_{0.89}Mn_{0.1}Al_{0.01}O$

IDB formation occurs when the concentration of Mn reaches 10 at. % in ZnO. At lower Mn concentrations (≤ 5 at. %), IDB formation is not observed at the same sintering conditions (1400°C, 12 hr). Thus, a high Mn concentration appears to be the crucial factor determining whether ID network formation occurs in Mn-Al co-doped ZnO. Previous studies have found that larger dopants prefer to occupy the b-IDB, while smaller dopants prefer to occupy the p-

IDB [9,33]. This occurs in order to reduce strain within the ZnO lattice by allowing larger dopants (e.g. In) to occupy the larger octahedral b-IDB site. Smaller dopants (e.g. Fe) have been found to preferentially occupy the p-IDB when ZnO is doped with multiple dopants (e.g. in In-Fe co-doped ZnO [9]). Thus, in Mn-Al co-doped ZnO, Mn and Al may prefer to occupy the b-IDBs and p-IDBs respectively, due to the difference in the size of their ionic radii (octahedral ionic radius: Mn^{3+}: 65 pm (HS), Al^{3+}: 54 pm; five-fold ionic radius: Mn^{3+}: 58 pm, Al^{3+}: 48 pm [14]). Al doping alone has never been found to stabilize ID network formation in ZnO [21,39], possibly as a result of the small ionic radius of Al^{3+}, which prevents the formation of a stable monolayer of edge-sharing cation octahedra (i.e. a b-IDB) due to significant electrostatic repulsion between neighboring octahedra. It is likely that Mn doping alone can stabilize ID network formation in ZnO, since Fe^{3+} can stably occupy both p-IDBs and b-IDBs [3] and the ionic radius of Fe^{3+} and Mn^{3+} is nearly the same (octahedral site, HS: 65 pm, five-fold site: 58 pm [14]).

IDB nucleation may occur when dopants are adsorbed at the surface of ZnO grains, with surface octahedral sites near zinc vacancy (V_{Zn}) clusters potentially acting as preferential sites for b-IDB nucleation [9,34]. The presence of amorphous and semicrystalline spinel phases at the surfaces of ZnO grains in Sb-doped ZnO has been directly confirmed by TEM [41]. Similar highly-defected $Zn_xMn_{3-x}O_4$ spinel phases could form at grain surfaces in Mn-doped ZnO [12]. At the sintering temperature of 1400°C, Mn^{3+} and Al^{3+} are stable at the octahedral site in $ZnMn_2O_4$ [23] and $ZnAl_2O_4$ [17] respectively. Thus, defected spinel surface phases could provide a source of Mn^{3+}, which can diffuse into the interior of ZnO grains. Al^{3+} may also be present in these phases and could, therefore, diffuse together with Mn^{3+}.

The formation of IDBs likely occurs by the internal diffusion of Mn^{3+} and Al^{3+}, since IDB development has been found to occur by an internal diffusion mechanism in ZnO doped with elements having a valence of 3+ (e.g. In^{3+} and Fe^{3+} [34]). When IDB formation is controlled by internal diffusion, b-IDBs can both nucleate at grain surfaces and propagate into

the grain interior and can also form within grains and propagate to the grain surfaces [3,34]. b-IDBs likely propagate by the diffusion of Mn^{3+}, and possibly Al^{3+}, with dopant diffusion primarily occurring by a V_{Zn}-mediated mechanism for dopants with a 3+ valence in ZnO [9,34,42,43]. Zinc vacancies have a low formation energy in n-type ZnO [44]. Thus, at the high sintering temperature of 1400°C, a significant V_{Zn} concentration should be present in ZnO, facilitating a high rate of dopant diffusion [42-44]. When b-IDBs form, the Zn sublattice either above or below the b-IDB cation plane gradually shifts away from the b-IDB, to occupy Zn tetrahedral sites that share corners with the b-IDB octahedra [3,34]. This prevents energetically unfavorable face-sharing between the b-IDB octahedra and the neighboring Zn tetrahedra. p-IDBs form and propagate together with b-IDBs in order to facilitate the inversion of the *c*-axis between neighboring b-IDBs [9]. As observed in $Zn_{0.89}Mn_{0.1}Al_{0.01}O$, the internal diffusion mechanism ultimately results in the formation of ID networks with multiple H-H b-IDBs and T-T p-IDBs in each ZnO grain [34].

The observed range of angles that form between b-IDBs and p-IDBs is 8.8°-2.3°, corresponding to $\{11\bar{2}l\}$ p-IDB planes with a range of l values of 8-21 (average: 13). These l values are considerably larger than those previously reported for In-doped ZnO (l ~2-3 [9]) and Fe-doped ZnO (l ~5 [3]). Larger p-IDB angles and smaller l values are observed when the p-IDB is occupied by large dopants (e.g. In) which induce significant strain within the ZnO lattice, resulting in high-angle p-IDBs that accommodate fewer dopants per basal plane segment [9]. The smaller ionic radii of Mn and Al relative to other known IDB-forming dopants (e.g. In and Fe) likely contribute to the formation of smaller-angle p-IDBs that can accommodate significantly more dopants per basal-plane segment [9]. The substitution of Al at the p-IDB in the $InMO_3(ZnO)_n$ homologous phase compounds has been determined by DFT calculations to result in similar energetic stability for both flat p-IDBs, which can be described as basal-plane monolayers of five-fold coordinated cations (i.e. T-T b-IDBs), and zigzag-shaped p-IDBs [33], which are observed in $Zn_{0.89}Mn_{0.1}Al_{0.01}O$. Thus, Al doping should be particularly effective for

stabilizing p-IDBs with small angles. It should be noted, however, that in $RMO_3(ZnO)_n$ compounds with high concentrations of ZnO, i.e. large values of n, as in the case of $Zn_{0.89}Mn_{0.1}Al_{0.01}O$, the formation of zigzag-shaped p-IDBs should be more favorable than flat p-IDBs, due to the need to distribute the cation dopants efficiently within the $(MZn_n)O_{n+1}$ layers between neighboring b-IDBs, in order to reduce the built-in strain within these layers [33].

3.4 Conclusion

Inversion domain boundaries have been observed in ZnO doped with 10 at. % Mn and 1 at. % Al ($Zn_{0.89}Mn_{0.1}Al_{0.01}O$). At lower Mn concentrations ($\leq$ 5 at. %), inversion domain boundary formation does not occur, suggesting that at a high Mn concentration, exceeding the solubility limit, inversion domain boundary formation becomes energetically favorable. Two types of inversion domain boundaries, basal-plane and pyramidal-plane inversion domain boundaries, have been observed. The atomic structure of the basal-plane inversion domain boundaries has been investigated by scanning transmission electron microscopy. A *c*-axis cation stacking sequence of αβαβ|γ|αβαβ and a head-to-head configuration of the *c*-axis have been observed at the basal-plane inversion domain boundary interface. Elemental analysis of the basal-plane inversion domain boundary by energy-dispersive X-ray spectroscopy and electron energy-loss spectroscopy revealed significant Mn localization, as well as minor Al localization, at the basal-plane inversion domain boundary interface. Electron energy-loss spectroscopic analysis indicated a valence state of 3+ for the Mn occupying the octahedral site of the basal-plane inversion domain boundary, as expected based on Pauling's rule of electroneutrality.

The formation of a network of inversion domains in $Zn_{0.89}Mn_{0.1}Al_{0.01}O$ suggests that the development of the inversion domain boundaries occurs by an internal diffusion mechanism, characteristic of dopants with a 3+ valence. It is likely that Mn^{3+} alone can stabilize the

formation of both b-IDBs and p-IDBs, as the ionic radii of both Mn^{3+} and Fe^{3+}, a dopant known to induce the formation of $Fe_2O_3(ZnO)_n$ homologous phases [3], are nearly identical [14]. The Al^{3+} dopant should, on the other hand, primarily contribute to the stabilization of the p-IDB, which is considered to be the more favorable IDB site for Al to occupy [33]; although, based on the results of STEM-EDS analysis, Al^{3+} appears to also be able to co-occupy the b-IDB with Mn^{3+} to some extent. The observation of IDBs in the Mn-Al co-doped ZnO system demonstrates that new co-doping strategies are effective for synthesizing yet unidentified $RMO_3(ZnO)_n$ compounds with microstructural features not previously observed in other systems (e.g. $In_2O_3(ZnO)_n$, $InFeO_3(ZnO)_n$ and $Fe_2O_3(ZnO)_n$). The study of additional $RMO_3(ZnO)_n$ systems containing two or more dopants should enable the systematic modification of microstructural properties such as the b-IDB spacing along the *c*-axis, the p-IDB angle and the fractional occupancy of the b-IDB and p-IDB sites by multiple dopants. This may assist in the optimization of functional properties such as the electrical conductivity, optical transmission and thermal conductivity at the bulk level in a diverse range of $RMO_3(ZnO)_n$ homologous phase systems.

3.5 References

[1] A. Rečnik, N. Daneu, T. Walther, and W. Mader, J. Am. Ceram. Soc., **84**, 2657 (2001)

[2] A.B. Yankovich, B. Puchala, F. Wang, J.H. Seo, D. Morgan, X. Wang, and P.M. Voyles, Nano Lett., **12**, 1311 (2012)

[3] O. Köster-Scherger, H. Schmid, N. Vanderschaeghe, F. Wolf, and W. Mader, J. Am. Ceram. Soc., **90**, 3984 (2007)

[4] F. Wolf, B.H. Freitag, and W. Mader, Micron, **38**, 549 (2007)

[5] E. Guilmeau, P. Díaz-Chao, O.I. Lebedev, A. Rečnik, M.C. Schäfer, F. Delorme, F. Giovanelli, M. Košir, and S. Bernik, Inorg. Chem., **56**, 480 (2017)

[6] Y. Yan, S.J. Pennycook, S.J. Dai, R.P. Chang, A. Wang, and T.J. Marks, Appl. Phys. Lett., **73**, 2585 (1998)

[7] T. Moriga, D.D. Edwards, T.O. Mason, G.B. Palmer, K.R. Poeppelmeier, J.L. Schindler, C.R. Kannewurf, and I. Nakabayashi, J. Am. Ceram. Soc., **81**, 1310 (1998)

[8] T. Hörlin, G. Svensson, and E. Olsson, J. Mater. Chem., **8**, 2465 (1998)

[9] A.P. Goldstein, S.C. Andrews, R.F. Berger, V.R. Radmilovic, J.B. Neaton, and P. Yang, ACS Nano, **7**, 10747 (2013)

[10] S. Eichhorn, H. Schmid, W. Assenmacher, and W. Mader, J. Solid State Chem., **246**, 214 (2017)

[11] N. Daneu, A. Rečnik, S. Bernik, and D. Kolar, J. Am. Ceram. Soc., **83**, 3165 (2000)

[12] M. Kakazey, M. Vlasova, M. Dominguez-Patiño, J. Kliava, and T. Tomila, J. Am. Ceram. Soc., **89**, 1458 (2006)

[13] L. Nádherný, O. Jankovský, Z. Sofer, J. Leitner, C. Martin, and D. Sedmidubský, J. Eur. Ceram. Soc., **35**, 555 (2015)

[14] R.D. Shannon, Acta Cryst. Sec. A, **32**, 751 (1976)

[15] Ü. Özgur, Y.I. Alivov, C. Liu, A. Teke, M.A. Reschikov, S. Doğan, V. Avrutin, S.J. Cho,

and H. Morkoç, J. Appl. Phys., **98**, 041301 (2005)

[16] A. Schrön, C. Rödl, and F. Bechstedt, Phys. Rev. B, **82**, 165109 (2010)

[17] S. Mathur, M. Veith, M. Haas, H. Shen, N. Lecerf, V. Huch, S. Hüfner, R. Haberkorn, H.P. Beck, and M. Jilavi, J. Am. Ceram. Soc., **84**, 1921 (2001)

[18] A.V. Deshmukh, S.I. Patil, S.M. Yusuf, A.K. Rajarajan, and N.P. Lalla, J. Magn. Magn. Mater., **322**, 536 (2010)

[19] T. Ungár, Scr. Mater., **51**, 777 (2004)

[20] X. Liang, Phys. Chem. Chem. Phys., **17**, 29655 (2015)

[21] J.P. Han, P.Q. Mantas, and A.M.R. Senos, J. Mater. Res., **16**, 459 (2001)

[22] J. Han, P. Q. Mantas, and A. M. R. Senos, J. Eur. Ceram. Soc., **20**, 2753 (2000)

[23] M. Peiteado, S. Sturm, A.C. Caballero, and D. Makovec, Acta Mater., **56**, 4028 (2008)

[24] N. El Horr, S. Guillemet-Fritsch, A. Rousset, H. Bordeneuve, and C. Tenailleau, J. Eur. Ceram. Soc., **34**, 317 (2014)

[25] D. Baither, B. Baufeld, U. Messerschmidt, A.H. Foitzik, and M. Rühle, J. Am. Ceram. Soc., **80**, 1691 (1997)

[26] D. Baither, M. Bartsch, B. Baufeld, A. Tikhonovsky, A. Foitzik, M. Rühle, and U. Messerschmidt, J. Am. Ceram. Soc., **84**, 1755 (2001)

[27] C.J. Chan, F.F. Lange, M. Rühle, J.F. Jue, and A.V. Virkar, J. Am. Ceram. Soc., **74**, 807 (1991)

[28] R.A. Cutler, J.R. Reynolds, and A. Jones, J. Am. Ceram. Soc., **75**, 2173 (1992)

[29] V. Lanteri, R. Chaim, and A.H. Heuer, J. Am. Ceram. Soc., **69**, C-258 (1986)

[30] S.T. Buljan, H.A. McKinstry, and V.S. Stubican, J. Am. Ceram. Soc., **59**, 351 (1976)

[31] J.C. Kim, and E. Goo, J. Am. Ceram. Soc., **73**, 877 (1990)

[32] A. Rečnik, M. Čeh, and D. Kolar, J. Eur. Ceram. Soc., **21**, 2117 (2001)

[33] J.L.F. Da Silva, Y. Yan, and S.H. Wei, Phys. Rev. Lett., **100**, 255501 (2008)

[34] A. Rečnik, N. Daneu, and S. Bernik, J. Eur. Ceram. Soc., **27**, 1999 (2007)

[35] S.D. Findlay, S. Azuma, N. Shibata, N. Okunishi, and Y. Ikuhara, Ultramicroscopy, **111**, 285 (2011)

[36] T. Yamazaki, N. Nakanishi, A. Rečnik, M. Kawasaki, K. Watanabe, M. Čeh, and M. Shiojiri, Ultramicroscopy, **98**, 205 (2004)

[37] H. Schmid, E. Okunishi, T. Oikawa, and W. Mader, Micron, **43**, 49 (2012).

[38] X. Lu, Z. Liang, X. He, R. Xiao, L. Gu, Y.S. Hu, H. Li, Z. Wang, X. Duan, L. Chen, J. Maier, and Y. Ikuhara, Adv. Mater., **24**, 3233 (2012)

[39] K. Shirouzu, T. Ohkusa, M. Hotta, N. Enomoto, and J. Hojo, J. Ceram. Soc. Jpn., **115**, 254 (2007)

[40] H.K. Schmid, and W. Mader, Micron, **37**, 426 (2006)

[41] V. Kraševec, M. Trontelj, and L. Golič, J. Am. Ceram. Soc., **74**, 760 (1991)

[42] K.M. Johansen, L. Vines, T.S. Bjørheim, R. Schifano, and B.G. Svensson, Phys. Rev. Appl., **3**, 024003 (2015)

[43] D. Steiauf, J.L. Lyons, A. Janotti, and C.G. Van de Walle, APL Materials, **2**, 096101 (2014)

[44] A. Janotti, and C.G. Van de Walle, Phys. Rev. B, **76**, 165202 (2007)

Chapter 4. Inversion Domain Network Stabilization and Spinel Phase Suppression in Sn-Al Dual-Doped ZnO

4.1 Introduction

In some ZnO-based material systems, incomplete ID network formation is observed. This occurs when ZnO is doped with higher-valence elements such as Sn^{4+} [1,2] or Sb^{5+} [3-5], which induce IDB formation primarily by the surface diffusion mechanism [6]. These dopants can stabilize the formation of b-IDBs but not p-IDBs, with the formation of a microstructure consisting of only a single b-IDB in each grain and spinel precipitates dispersed within grains and at grain boundaries observed in the Sn [1,2] or Sb-doped ZnO [3-5] systems. p-IDB formation is necessary for the inversion of the *c*-axis between neighboring b-IDBs and, consequently, for the stabilization of ID network formation. Thus, in order to facilitate the formation of ID networks in these systems, the addition of a dopant which can stably occupy the p-IDB site is necessary.

In this chapter, the results of phase and microstructural analysis of Sn-Al co-doped ZnO by XRD, SEM and TEM are described. By co-doping ZnO with Sn and Al, the stabilization of ID network formation has been acheived. In addition to ID network formation, Sn-Al co-doping of ZnO also results in the suppression of the Zn_2SnO_4 and $ZnAl_2O_4$ spinel phases, which form when ZnO is doped with either Sn or Al only. Thus, a monophasic material is obtained, with the formation of the spinel secondary phases suppressed. Atomic-resolution HAADF and ABF-STEM observations of both b-IDBs and p-IDBs have been carried out and the results are analyzed in detail. Elemental analysis was also carried out using STEM-EDS and EELS to analyze dopant localization at the b-IDBs and p-IDBs and the findings are described. It is found that Sn and Al primarily localize at the distinct sites of the b-IDBs and p-

IDBs respectively. Based on experimental observations, the formation mechanism of the ID networks as well as the factors contributing to the stabilization of ID network development and spinel phase suppression in Sn-Al co-doped ZnO are discussed in terms of the distinct characteristics of the Sn and Al dopants. Finally, the factors that determine the potential for different types of dopants to occupy specific IDB sites and induce IDB formation are described generally, with an eye toward future studies focusing on the stabilization of yet unidentified types of $RMO_3(ZnO)_n$ compounds with b-IDB and p-IDB sites intentionally doped with specific types of dopants in unique configurations.

4.2 Methods

Synthesis

Mixtures with stoichiometries of $Zn_{0.99}Al_{0.01}O$, $Zn_{0.99}Sn_{0.01}O$ and $Zn_{0.98}Sn_{0.01}Al_{0.01}O$ were prepared by weighing ZnO (CIK NanoTek, 99.9 % purity, 34 nm), SnO_2 (CIK NanoTek, 99.9 % purity, 21 nm) and Al_2O_3 (Taimei Chemicals, Tamicron TM-DAR, 99.99 % purity, 100 nm) powders together and mixing them in ethanol. Mixing of $Zn_{0.99}Al_{0.01}O$ and $Zn_{0.98}Sn_{0.01}Al_{0.01}O$ was done using the AR-250 Planetary Centrifugal Mixer (Thinky) at 2000 rpm for 3 hr. $Zn_{0.99}Sn_{0.01}O$ was prepared by milling in ethanol inside a PE bottle for 24 hr using YSZ balls. The mixtures were dried in air at 60°C-70°C ($Zn_{0.99}Sn_{0.01}O$: 180°C) to evaporate the ethanol solvent, crushed using alumina balls ($Zn_{0.99}Sn_{0.01}O$: YSZ balls) and sifted with a mesh of size 250 μm. Dense ceramic compacts were obtained by pelletizing powders using a uniaxial press at 20 MPa ($Zn_{0.99}Sn_{0.01}O$: 10 MPa) and sintering the pellets in an alumina crucible in air at 1400°C for 12 hr with heating and cooling rates of 5°C/min and 10°C/min respectively.

Characterization

The methods used for sample characterization include XRD, SEM, TEM and STEM-EDS/EELS, and are essentially the same as described in Chapter 3. Image analysis methods are also the same as described in Chapeter 3. EEL spectra corresponding to the b-IDB interface and domain region represent the average of several spectra, collected at the b-IDB and within the domain interior respectively. For the analysis of EELS data, a low pass filter of 5 eV was applied once to reduce noise in the raw EEL spectra.

4.3 Results and Discussion

4.3.1 Phase and Microstructural Analysis by XRD, SEM, and TEM

The XRD patterns of $Zn_{0.98}Sn_{0.01}Al_{0.01}O$, $Zn_{0.99}Sn_{0.01}O$ and $Zn_{0.99}Al_{0.01}O$ are shown in Fig. 4.1. Primary phase peaks which can be indexed according to the ZnO wurtzite phase are

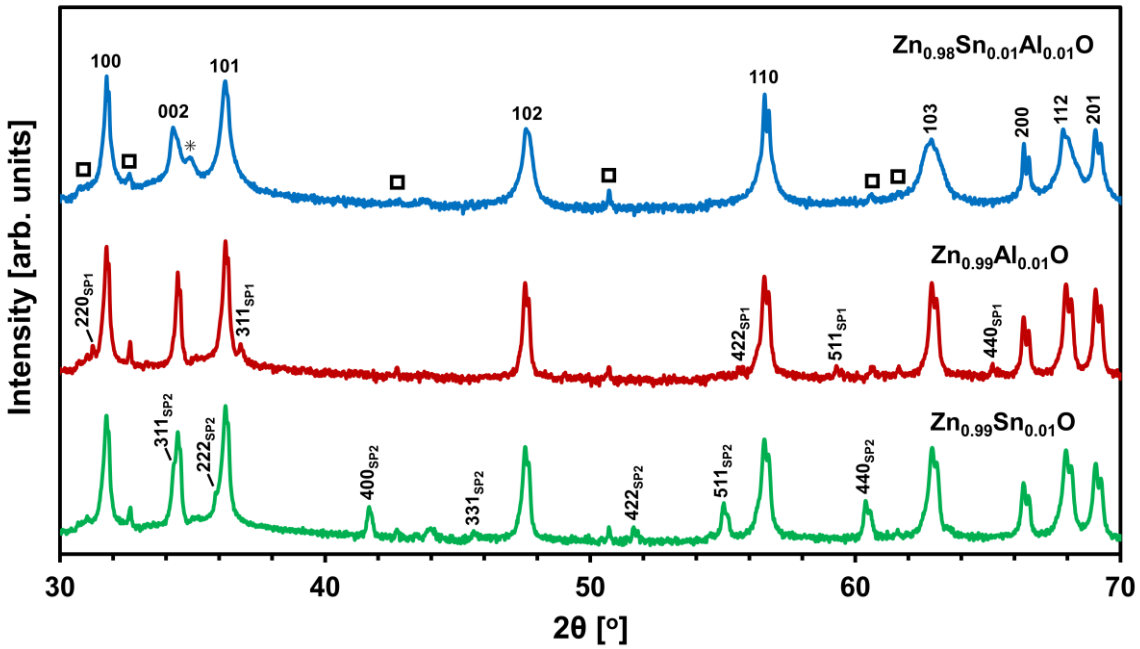

Figure 4.1. XRD patterns for $Zn_{0.98}Sn_{0.01}Al_{0.01}O$, $Zn_{0.99}Al_{0.01}O$ and $Zn_{0.99}Sn_{0.01}O$. Peaks are labelled as follows: ZnO Cu-K_α (indices only), ZnO Cu-K_β (□), $ZnAl_2O_4$ (SP1), Zn_2SnO_4 (SP2) and additional peak in $Zn_{0.98}Sn_{0.01}Al_{0.01}O$ (∗).

observed in all samples. The XRD pattern of $Zn_{0.98}Sn_{0.01}Al_{0.01}O$ contains an additional low-intensity peak at 34.94° and exhibits broadening of the 002, 102, 103 and 112 peaks. As described in Chapter 3, peak broadening may be observed as a consequence of defect formation [7] and additional low-intensity peaks and peak broadening have been reported for large *n* values in the $In_2O_3(ZnO)_n$ homologous phases [8]. Thus, the formation of homologous or intergrowth phase compounds may occur in $Zn_{0.98}Sn_{0.01}Al_{0.01}O$. The XRD patterns of $Zn_{0.99}Al_{0.01}O$ and $Zn_{0.99}Sn_{0.01}O$ also contain low-intensity secondary phase peaks that can be indexed according to the $ZnAl_2O_4$ [9] and Zn_2SnO_4 [10] spinel phases respectively. In contrast, no spinel secondary phase peaks are detected in $Zn_{0.98}Sn_{0.01}Al_{0.01}O$.

SEM micrographs of the microstructures of $Zn_{0.98}Sn_{0.01}Al_{0.01}O$, $Zn_{0.99}Sn_{0.01}O$ and $Zn_{0.99}Al_{0.01}O$ are shown in Fig. 4.2 (a), (b) and (c) respectively. The measured densities, average grain sizes and average precipitates sizes for each sample are listed in Table 4.1. Nanometric precipitates are observed both within grains and at grain boundaries in $Zn_{0.99}Sn_{0.01}O$ and $Zn_{0.99}Al_{0.01}O$. SEM-EDS compositional mapping showed an increased concentration of Sn and Al in the precipitates in $Zn_{0.99}Sn_{0.01}O$ and $Zn_{0.99}Al_{0.01}O$ respectively, in agreement with the Zn_2SnO_4 and $ZnAl_2O_4$ phases detected by XRD. Precipitates were not observed in $Zn_{0.98}Sn_{0.01}Al_{0.01}O$.

Table 4.1. Density, Average Grain Size and Average Precipitate Size

Sample Stoichiometry	Density (g/cm^3)	Relative Density (%)[(a)]	Average Grain Size, Range (µm)	Average Precipitate Size, Range (µm)
$Zn_{0.99}Al_{0.01}O$	5.66	99.8	11.1, 1.67-31.8	0.48, 0.094-1.81
$Zn_{0.99}Sn_{0.01}O$	5.44	96.0	4.55, 0.78-12.6	0.65, 0.130-1.83
$Zn_{0.98}Sn_{0.01}Al_{0.01}O$	5.48	96.6	2.95, 0.67-8.53	No Precipitates

(a) Theoretical Density of ZnO: 5.67 g/cm^3

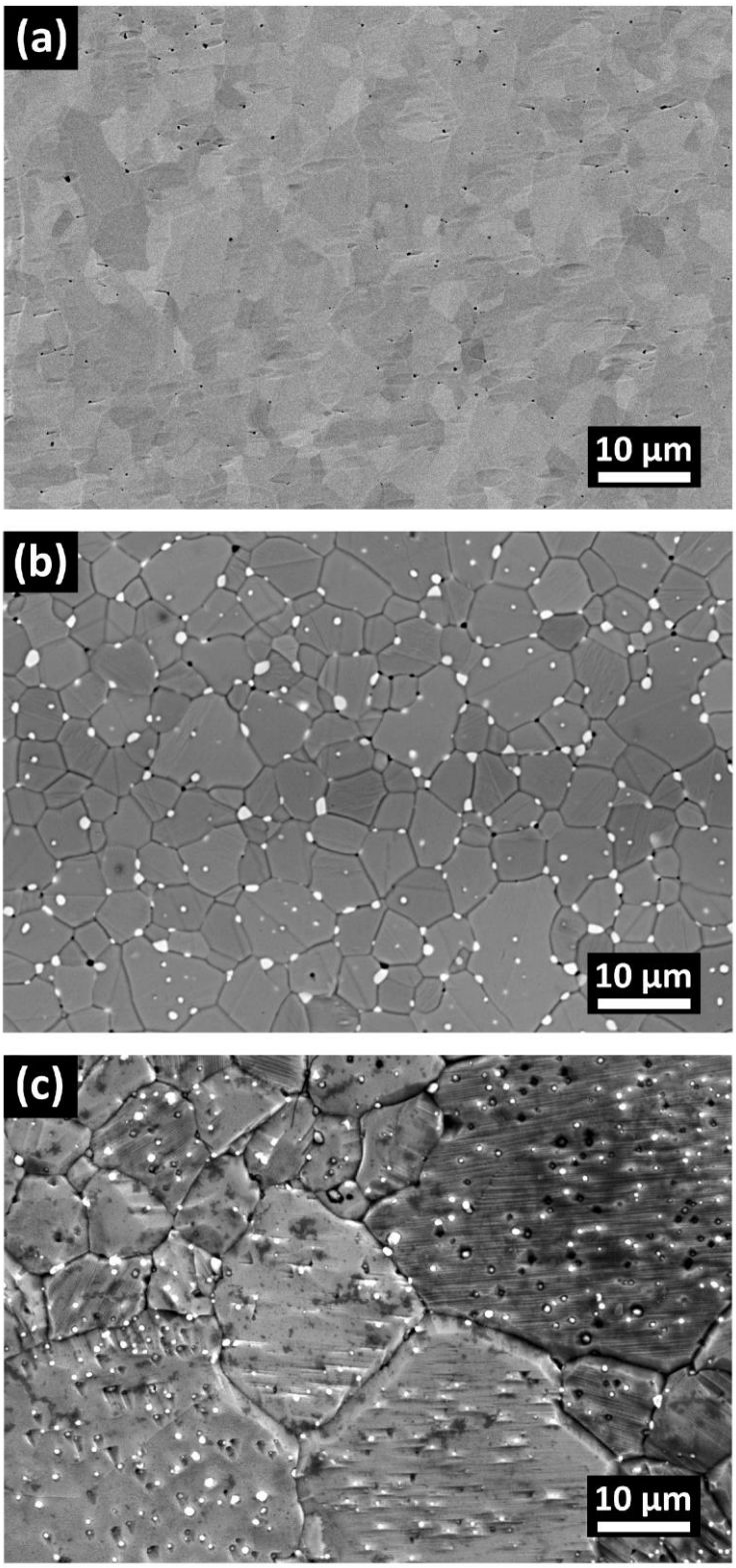

Figure 4.2. SEM images of the microstructures of **(a)** $Zn_{0.98}Sn_{0.01}Al_{0.01}O$ **(b)** $Zn_{0.99}Sn_{0.01}O$ and **(c)** $Zn_{0.99}Al_{0.01}O$. Nanometric precipitates are observed in $Zn_{0.99}Sn_{0.01}O$ and $Zn_{0.99}Al_{0.01}O$, consistent with the Zn_2SnO_4 and $ZnAl_2O_4$ spinel phases detected by XRD. Also in agreement with XRD results, precipitates are not observed in $Zn_{0.98}Sn_{0.01}Al_{0.01}O$.

To determine the origin of the additional peak and peak broadening observed in the XRD profile of $Zn_{0.98}Sn_{0.01}Al_{0.01}O$, TEM observations were carried out. Fig. 4.3 (a) shows a BF-TEM image of $Zn_{0.98}Sn_{0.01}Al_{0.01}O$. Intergrowth-like features are observed within each grain. Extensive microstructural observations of $Zn_{0.98}Sn_{0.01}Al_{0.01}O$ using TEM revealed the formation of intergrowth-like features throughout nearly all grains observed. DF-TEM images acquired at the $[1\bar{2}10]$ zone-axis using the $\mathbf{g} = 0002$ and $\mathbf{g} = 000\bar{2}$ reflections are shown in Fig. 4.3 (b) and (c) respectively. When the DF-TEM reflection is changed from $\mathbf{g} = 0002$ to $\mathbf{g} = 000\bar{2}$, an inversion in contrast similar to that observed in Fig. 3.9 occurs. Thus, it can be concluded that the appearance of the zigzag-like features observed indicates the formation of a network of IDs, with IDB interfaces that form at basal and pyramidal planes corresponding to b-IDBs and p-IDBs respectively. The corresponding EDP is shown in Fig. 4.3 (d). Streaks are observed between reflections in the EDP along the *c*-axis. Similar streaks have been observed in other ZnO samples containing IDBs and arise due to the formation of stacking

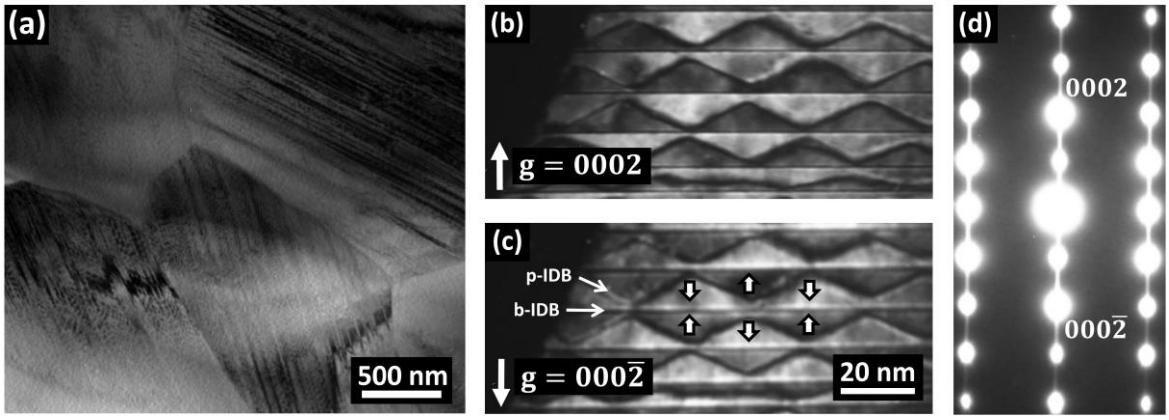

Figure 4.3. (a) BF-TEM image of the microstructure of $Zn_{0.98}Sn_{0.01}Al_{0.01}O$. Intergrowth-like features are observed in individual grains. **(b)/(c)** $[1\bar{2}10]$ zone-axis DF-TEM images of the IDs, recorded using the (b) $\mathbf{g} = 0002$ and (c) $\mathbf{g} = 000\bar{2}$ reflections. Vertical arrows indicate the ZnO *c*-axis polarity in individual domains. The *c*-axis configurations at the b-IDBs and p-IDBs were determined using ABF-STEM (discussed in Section 4.3.3). **(d)** EDP acquired at the edge of the sample area shown in (b)/(c).

faults at the b-IDBs and the distribution of spacings between neighboring b-IDBs [11]. The average spacing between b-IDBs along the *c*-axis in the ID networks was determined to be 14.9 nm (range: 5.0-85.5 nm).

4.3.2 Dopant Localization at Specific IDB Sites: STEM-EDS Analysis of ID Networks

To determine whether the localization of Sn or Al at the b-IDB or p-IDB interfaces occurs, STEM-EDS analysis was carried out. Fig. 4.4 (a) shows a high-magnification HAADF-STEM image viewed at the $[1\bar{1}00]$ zone-axis. Both b-IDBs and p-IDBs are viewed edge-on. In the $RMO_3(ZnO)_n$ phases, p-IDBs can only be viewed edge-on at one of the three *m*-axes (e.g. $[1\bar{1}00]$) [12]. This is shown schematically in Fig. 1.3. The HAADF intensity in Fig. 4.4 (a) increases at the b-IDBs and decreases at the p-IDBs, indicating the possible occupation of the b-IDBs and p-IDBs by the high atomic number Sn (Z = 50) and low atomic number Al (Z = 13) respectively. To confirm this, STEM-EDS net counts maps of an ID network were acquired. Fig. 4.4 (b)-(f) show EDS maps corresponding to the Al *K*, Sn *L*, composite Al *K*/Sn *L*, Zn *K* and O *K* signals respectively. The intensities of the Al *K* and Sn *L* signals increase sharply at the p-IDBs and b-IDBs respectively, in agreement with the HAADF-STEM contrast observed at the positions of the b-IDBs and p-IDBs in Fig. 4.4 (a). This result shows that Al and Sn preferentially occupy the respective sites of the p-IDBs and b-IDBs. A small increase of the Sn *L* signal intensity is also detected at the p-IDBs, indicating some co-occupation of the p-IDB sites by Al and Sn. The observed intensity of the Zn *K* and O *K* signals is uniform within the area imaged.

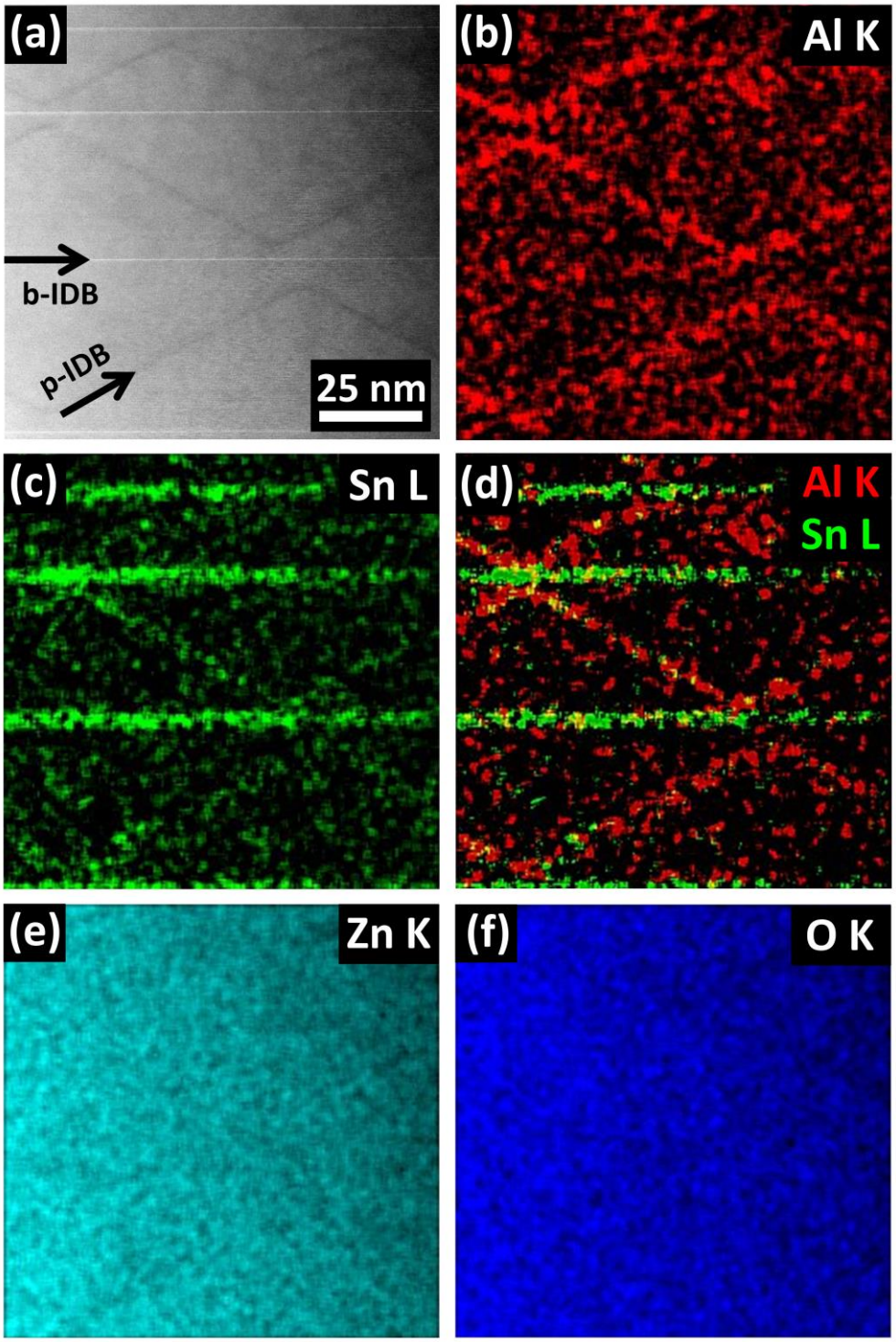

Figure 4.4. (a) HAADF-STEM image of the ID networks in $Zn_{0.98}Sn_{0.01}Al_{0.01}O$. The HAADF intensity increases at b-IDBs and decreases at p-IDBs. STEM-EDS net counts elemental maps are shown in **(b)-(f)**. The Sn *L* and Al *K* signal intensities exhibit sharp increases at the b-IDB and p-IDB interfaces respectively, indicating a clear preference for Sn and Al to occupy the specific sites of the b-IDBs and p-IDBs. A minor increase of the Sn *L* signal intensity also occurs at the p-IDBs, indicating some localization of Sn at the p-IDB sites. The Zn *K* and O *K* signal intensities are uniform within the area analyzed.

4.3.3 Atomic-Scale Structural Analysis of b-IDBs and p-IDBs by HAADF/ABF-STEM and EELS

b-IDB Atomic Structure

HAADF-STEM images of a b-IDB acquired at the $[1\bar{2}10]$ and $[1\bar{1}00]$ zone-axes are shown in Fig. 4.5 (a) and (b) respectively. There is a significant increase of the HAADF intensity at the b-IDB cation plane. The sharp increase in the HAADF Z-contrast intensity exactly at the b-IDB cation plane indicates occupation of the b-IDB octahedral sites by the high atomic number Sn (Z = 50), in agreement with the STEM-EDS result in Section 4.3.2, which shows a significant increase of the Sn *L* signal intensity at the b-IDBs. ABF-STEM images of the b-IDB viewed at the $[1\bar{2}10]$ and $[1\bar{1}00]$ zone-axes are also shown in Fig. 4.5 (c) and (d) respectively. By observing the *c*-axis stacking sequence of cation and anion atomic planes, respectively appearing as rows of large and small dark contrasts in the ABF-STEM images, the H-H configuration of the *c*-axis at the b-IDB is confirmed. The octahedral coordination of the cations occupying the b-IDB layer is also determined based on the cation-anion stacking sequence along the *c*-axis. Structural models of the Sn-doped b-IDB, obtained by DFT calculations (discussed in Chapter 5), are also shown superimposed in Fig. 4.5 (c) and (d). The models, which assume full occupancy of the b-IDB cation plane by Sn, are in general agreement with the b-IDB structural features observed in the STEM images. The *c*-axis cation stacking sequence of αβαβ|α|γβγβ observed at the b-IDB is in agreement with that previously reported for Sn-doped b-IDBs in ZnO [13].

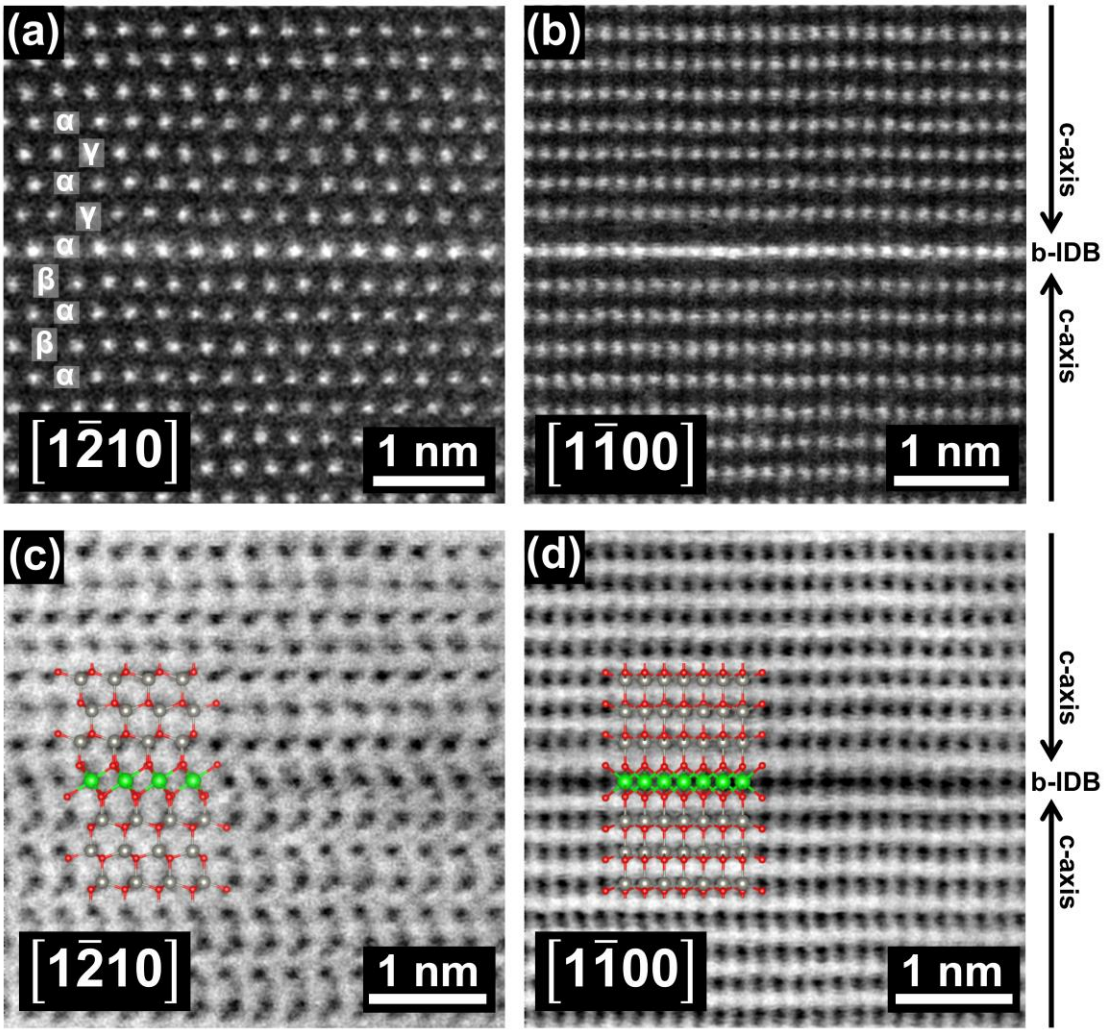

Figure 4.5. (a)/(b) HAADF and **(c)/(d)** ABF-STEM images of the b-IDB viewed at the (a)/(c) [1$\bar{2}$10] and (b)/(d) [1$\bar{1}$00] zone-axes. As shown in (a) and (b), a sharp increase of the HAADF-STEM intensity occurs at the b-IDB cation layer, indicating the localization of the high atomic number Sn at the b-IDB. The *c*-axis cation stacking sequence of αβαβ|α|γαγα is shown in (a). The H-H configuration of the *c*-axis at the b-IDB is confirmed based on the cation-anion stacking sequence along the *c*-axis, which can be observed in (c) and (d). Sections of a slab model refined by DFT calculations (discussed in Chapter 5), which contains a single b-IDB consisting of a monolayer of edge-sharing Sn octahedra, are shown superimposed in (c) and (d). Sn, Zn and O atoms are colored green, grey and red respectively. The b-IDB structure observed in the HAADF and ABF-STEM images is in general agreement with the model.

EELS analysis of the b-IDB was also carried out to confirm the localization of Sn at the b-IDB interface. Fig 4.6 shows the EELS O *K* edges obtained at the b-IDB and within the domain interior. Several differences in the spectra are observed. In comparison to the spectrum

acquired within the domain, the spectrum acquired at the b-IDB exhibits an increase in intensity in the energy-loss region from 510 to 530 eV. The increased intensity in the energy-loss range from 510 to 530 eV can be attributed to the Sn-$M_{4,5}$ edge, while the fine structure observed above 530 eV should be primarily due to the O *K* edges [14,15]. In addition, the O *K* 1 edge at the b-IDB is broadened relative to the O *K* 1 edge acquired within the domain interior. Features of the b-IDB spectrum, including 1) the presence of two Sn *M* peaks in the energy-loss range of 510-530 eV, 2) the separation of the O *K* 1 and O *K* 2 peak maxima at the b-IDB, $\Delta E_{2,1}$, of ~17.5 eV and 3) the position of the O *K* 1 maximum appear to indicate the formation of a tin oxide compound with a valence between that of SnO_2 (Sn^{4+}) and the intermediate tin oxide compound studied in ref. 14. The features of the b-IDB spectrum are clearly inconsistent with SnO (Sn^{2+}) [14].

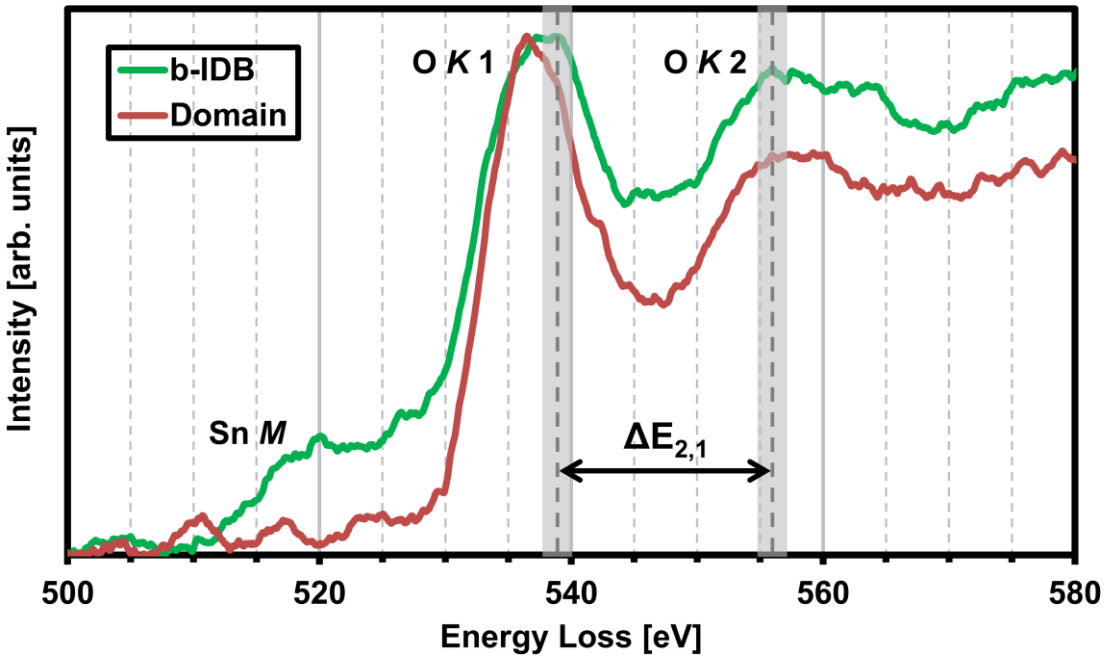

Figure 4.6. EEL spectra acquired at the b-IDB and in the domain interior. In comparison to the domain interior, the b-IDB spectrum exhibits several differences, including: 1) two minor peaks attributed to the Sn $M_{4,5}$ edge in the energy-loss range of 510-530 eV, 2) a broadening of the O *K* 1 edge, 3) a shift of the O *K* 1 edge maximum to a higher energy-loss value and 4) a smaller energy-loss difference between the O *K* 1 and O *K* 2 peak maxima, represented by $\Delta E_{2,1}$, of ~17.5 eV.

Pauling's rule of electroneutrality requires that the average valence of the cations occupying the b-IDB be 3+ [3,6]. Thus, in order to achieve this requirement, the formation of a local structure with an effective cation valence state of 3+ should occur at the b-IDB. It is possible that this can be achieved via the co-occupation of the b-IDB by equal amounts of Zn^{2+} and Sn^{4+}. Indeed, recent studies have determined, based on the results of atomic-resolution STEM and Rietveld refinement of XRD data, that Zn^{2+} and Sn^{4+} co-occupy the b-IDB at a 1:1 ratio [13]. Additional investigations using atomic column-resolved EELS or atomic-resolution quantitative STEM-EDS should lead to a more exact determination of the local composition at the Sn-doped b-IDB in $Zn_{0.98}Sn_{0.01}Al_{0.01}O$.

p-IDB Atomic Structure

High-magnification and atomic-resolution HAADF-STEM images of a p-IDB viewed at the $[1\bar{1}00]$ zone-axis are shown in Fig. 4.7 (a) and (b) respectively. The atomic-resolution HAADF-STEM image of the p-IDB shown in Fig. 4.7 (b) does not exhibit a significant change in intensity at the position of the p-IDB cation columns relative to the domain interior. Thus, unlike the b-IDB, which based on HAADF-STEM observation can be determined to accommodate a significant concentration of Sn, the p-IDB cannot be immediately determined to be occupied by a specific dopant simply based on HAADF-STEM observation. Although STEM-EDS clearly indicates that Al localizes at the p-IDBs, cation columns at the p-IDB could be co-occupied by Al (Z = 13), Sn (Z = 50) and Zn (Z = 30), resulting in HAADF contrast that is largely unchanged in comparison to the domain interior. In order to maintain electroneutrality, the five-fold p-IDB sites should contain cations with an average valence of 2.5+. This can be achieved by equal occupancy of the p-IDB sites by Zn^{2+} and Al^{3+}. Minor

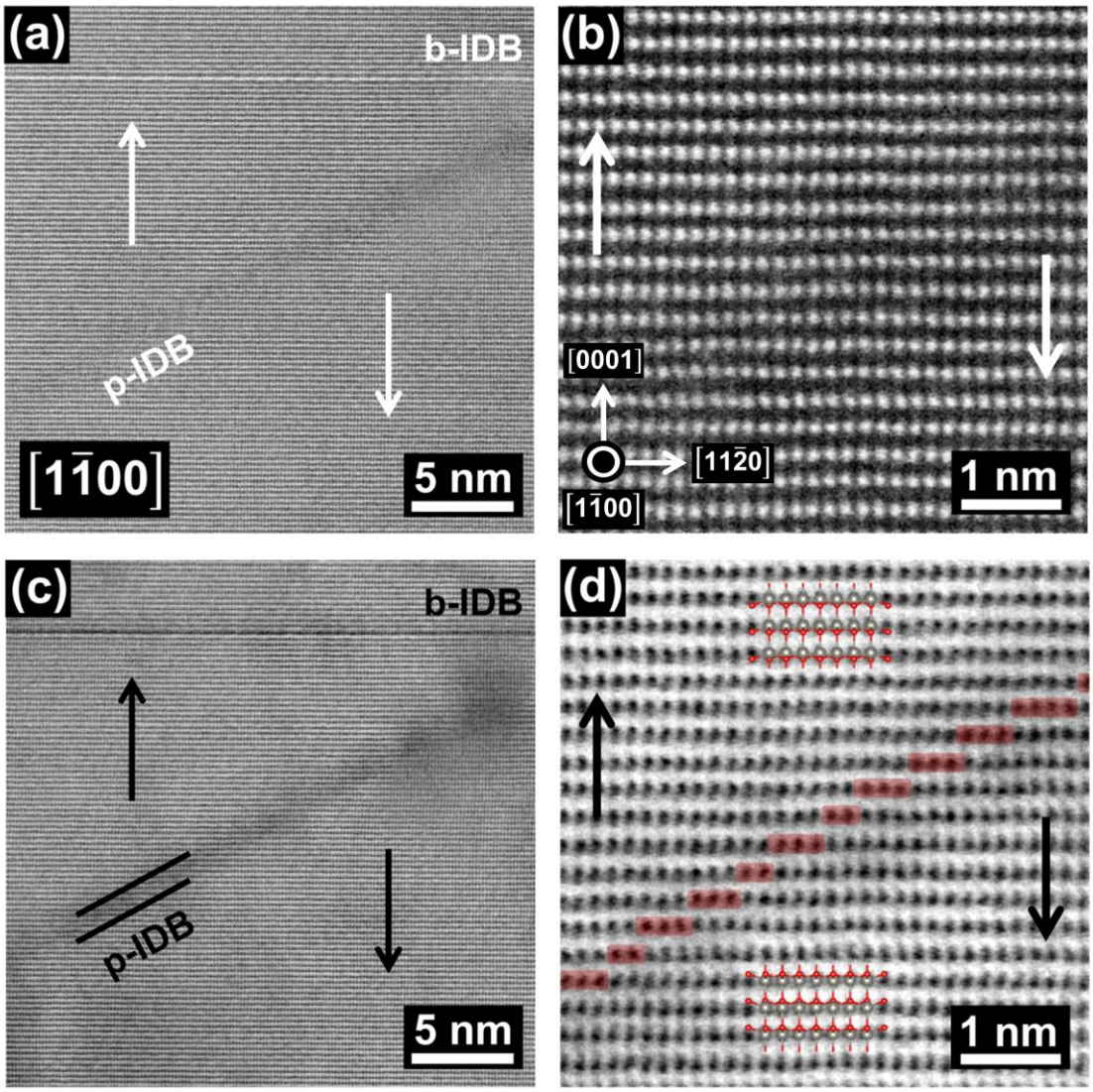

Figure 4.7. (a)/(b) HAADF and **(c)/(d)** ABF-STEM images of a p-IDB viewed at the $[1\bar{1}00]$ zone- axis. Both (a)/(c) high-magnification and (b)/(d) atomic-resolution images are shown. In (a) and (c), a b-IDB is also imaged. The approximate boundaries of the p-IDB are indicated by the solid black lines in (c). As shown in (a) and (c), the p-IDB exhibits reduced contrast in both HAADF and ABF images, indicating that local strain or lattice distortion occurs at the p-IDB interface [17]. The polarity of the *c*-axis at the p-IDB interface is determined based on the cation-anion stacking sequence along the *c*-axis observed in the atomic-resolution ABF-STEM image shown in (d). The polarity of the *c*-axis above and below the p-IDB interface is indicated both by the vertical arrows in each image and by the bulk-like sections of the refined Sn-doped b-IDB slab model that are shown superimposed in (d). In addition, the approximate locations of the five-fold coordinated cation segments that compose the p-IDB, across which the inversion of the *c*-axis occurs, are indicated by the red shading in (d). The position of these segments is determined by observing the inversion of the *c*-axis cation-anion stacking sequence that occurs as the p-IDB is traversed in the $[11\bar{2}0]$ direction.

occupancy of the p-IDB by Sn, indicated by STEM-EDS, may necessitate an increase of either the Zn^{2+} or Al^{3+} content at the p-IDB in order to maintain charge balance, in the case of p-IDB occupation by Sn^{4+} or Sn^{2+} respectively [14-16].

In the high-magnification HAADF-STEM image shown in Fig. 4.7 (a), the p-IDB shows a slight dispersion of dark contrast, relative to the domain interior, and appears to be several atomic columns wide, in comparison to the b-IDB visible at the top of Fig. 4.7 (a), which clearly appears to contain an increased concentration of Sn, based on the increased HAADF image intensity. In Fig. 4.7 (b), the slight reduction in HAADF intensity around the p-IDB indicates either some localization of Al, which could result in a minor reduction of the Z-contrast, or the presence of interfacial strain, which can cause a decrease of the HAADF intensity at defect structures (e.g. interfaces), due to local increases in strain or lattice distortion [17]. High-magnification and atomic-resolution ABF-STEM images of a p-IDB acquired at the $[1\bar{1}00]$ zone-axis are shown in Fig. 4.7 (c) and (d) respectively. The b-IDB and p-IDB imaged in Fig. 4.7 (c) both appear as defects which exhibit a dark contrast. Whereas the reduced contrast of the b-IDB is essentially confined to a $\{0002\}$ basal-plane cation monolayer, the dispersion of dark contrast around the p-IDB is several atomic columns wide. Reduced contrast may be observed at defect structures such as interfaces in both HAADF and ABF-STEM images, due to lattice distortion or strain [17]. Significant strain gradients have been confirmed at p-IDB interfaces using high-resolution TEM [18]. It was proposed that the strain gradients are due to the dilatation and tilting of cation polyhedra at the p-IDB that occur in order to accommodate the shift of the oxygen sublattice along the *c*-axis, which results in *c*-axis inversion at the p-IDB [18].

In Fig. 4.7 (d), the cation and anion columns appear as large and small dark contrasts respectively. Upon observation of the *c*-axis cation-anion stacking sequence across the p-IDB, a T-T *c*-axis configuration is confirmed at the p-IDB. To indicate the *c*-axis polarity, structural models of the ZnO bulk-like domain interior (obtained from DFT calculations of a slab model

containing a single Sn-doped b-IDB, discussed in Chapter 5) are shown superimposed in the regions above and below the p-IDB. When the p-IDB interface, indicated approximately by the red shading in Fig. 4.7 (d), is traversed in the $[11\bar{2}0]$ direction, no significant shift of the cation sublattice along the *c*-axis is observed. In contrast, the oxygen sublattice, clearly resolved in the ABF-STEM image in Fig. 4.7 (d), undergoes a shift in the $[0001]$ direction across the p-IDB interface, resulting in the inversion of the *c*-axis and the formation of a T-T IDB. Depending on the type of dopant occupying the p-IDB, the width of the p-IDB can vary, potentially resulting in the formation of p-IDBs up to several atomic columns wide [12]. The range of p-IDB angles observed in $Zn_{0.98}Sn_{0.01}Al_{0.01}O$ is 25.4°-28.2°, resulting in $\{11\bar{2}l\}$ p-IDB planes with an *l* value range of ~6-7. These *l* values correspond to p-IDBs composed of basal plane segments of five-fold coordinated cations with an average thickness of ~3-3.5 cation columns along the $[11\bar{2}0]$ direction [12]. The approximate positions of these segments are indicated by the red shading in Fig. 4.7 (d).

4.3.4 ID Network Stabilization and Spinel Phase Suppression

After sintering at 1400°C for 12 hr in air, $ZnAl_2O_4$ spinel precipitate formation occurred in $Zn_{0.99}Al_{0.01}O$, although no IDBs were observed. Zn_2SnO_4 spinel precipitates formed and a single b-IDB developed in each grain in $Zn_{0.99}Sn_{0.01}O$. In contrast, in $Zn_{0.98}Sn_{0.01}Al_{0.01}O$ ID networks consisting of b-IDBs and p-IDBs developed throughout most grains and spinel precipitate formation did not occur. Schematics of the microstructures of $Zn_{0.98}Sn_{0.01}Al_{0.01}O$, $Zn_{0.99}Sn_{0.01}O$ and $Zn_{0.99}Al_{0.01}O$ are shown in Fig. 4.8.

Although ID networks developed in $Zn_{0.98}Sn_{0.01}Al_{0.01}O$, spinel phase formation was suppressed, despite spinel phase formation occurring in $Zn_{0.99}Al_{0.01}O$ and $Zn_{0.99}Sn_{0.01}O$. This demonstrates that Sn-Al dual-doping stabilizes the formation of ID networks, which does not

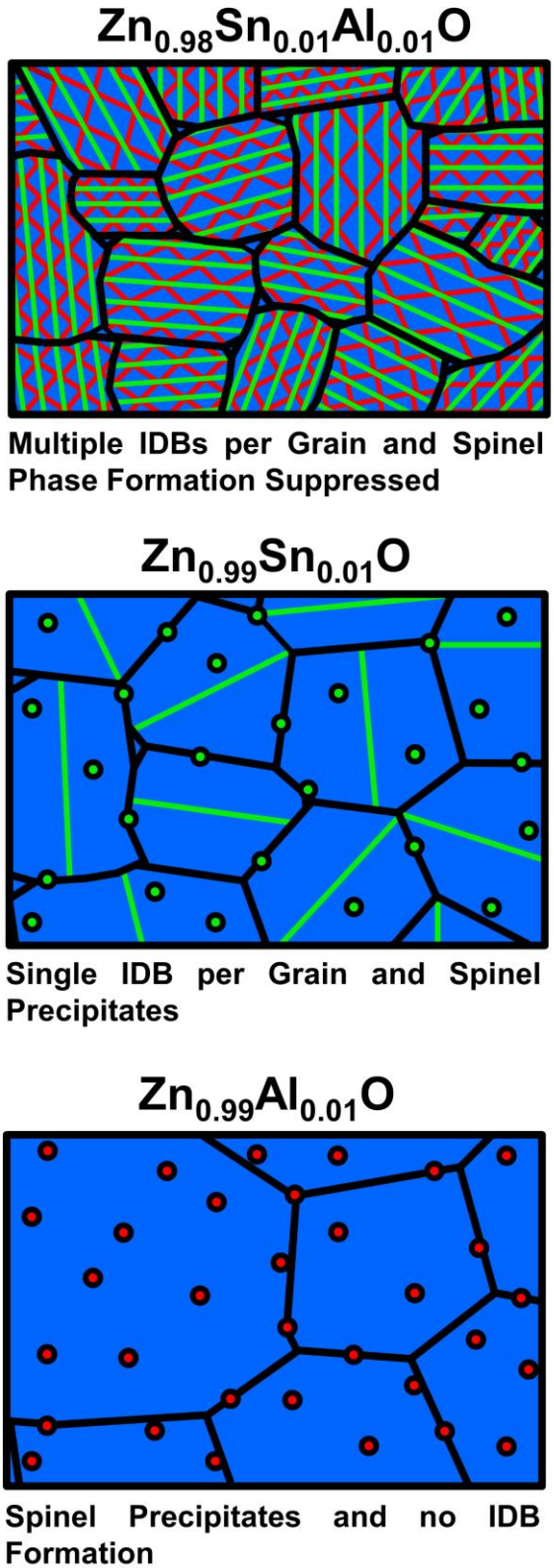

Figure 4.8. Schematics of the microstructures observed in $Zn_{0.98}Sn_{0.01}Al_{0.01}O$, $Zn_{0.99}Sn_{0.01}O$ and $Zn_{0.99}Al_{0.01}O$. Spinel precipitates are observed in $Zn_{0.99}Sn_{0.01}O$ and $Zn_{0.99}Al_{0.01}O$. In contrast, in $Zn_{0.98}Sn_{0.01}Al_{0.01}O$ the formation of ID networks occurs and spinel phase formation is suppressed.

occur when ZnO is doped with either Sn or Al only. Furthermore, the fact that the localization of Sn and Al occurs at the b-IDBs and p-IDBs respectively suggests that the site-specific localization of Sn at the b-IDBs and Al at the p-IDBs is important for stabilizing ID network formation. First principles studies of the InMO$_3$(ZnO)$_n$ homologous phase compounds found that several rules govern homologous phase formation [19]. Specifically, it was determined that maintaining charge neutrality and reducing strain within the ZnO lattice at dopant concentrations exceeding the solubility limit are critical factors governing the development of the InMO$_3$(ZnO)$_n$ homologous phases [19]. Thus, at high dopant concentrations, the formation of intergrowth structures (e.g. b-IDBs and p-IDBs) or RMO$_3$(ZnO)$_n$ homologous phase compounds becomes energetically favorable in order to accommodate excess dopants at distinct IDB sites [19,20].

In RMO$_3$(ZnO)$_n$ homologous phase compounds containing two or more dopants, smaller dopants (e.g. Al) prefer to occupy the p-IDB while larger dopants (e.g. In) prefer to occupy the b-IDB [19]. In considering whether Sn or Al have the potential to occupy either the octahedral b-IDB or five-fold p-IDB sites, the relevant ionic radii are: 48 pm (five-fold) and 53.5 pm (octahedral) for Al^{3+}, while those of Sn^{4+} are: 62 pm (five-fold) and 69 pm (octahedral) [21]. Thus, the stabilization of the ID networks in Sn-Al dual-doped ZnO can be understood in terms of the site-specific occupation of the b-IDBs and p-IDBs by Sn and Al respectively, as a means to minimize strain by having the larger Sn dopant occupy the b-IDB site and the smaller Al dopant occupy the p-IDB site. STEM-EDS analysis indicates that Sn may co-occupy the p-IDB with Al to some degree; however, the localization of Sn at the b-IDB is clearly more significant, in agreement with the prediction by first principles calculations of site-specific occupation of IDB sites based on ionic radius [19].

Spinel phase formation is suppressed in $Zn_{0.98}Sn_{0.01}Al_{0.01}O$, indicating that the occupation of the octahedral b-IDB and five-fold p-IDB sites by Sn and Al respectively is more energetically favorable than Sn-Al co-occupation of the spinel phase octahedral site, the

preferred site for Al and Sn to occupy in $ZnAl_2O_4$ (above 1000°C) [9] and in Zn_2SnO_4 [10] respectively. The significant differences in the octahedral site ionic radii of Al and Sn [21] and the lattice constants of $ZnAl_2O_4$ and Zn_2SnO_4 ($ZnAl_2O_4$: 8.0848 Å [9], Zn_2SnO_4: 8.657 Å [10]) point to the possibility of a structural instability associated with the co-occupation of the spinel phase octahedral site by both Al and Sn. This could contribute to the observed suppression of the spinel phases in favor of ID network formation in $Zn_{0.98}Sn_{0.01}Al_{0.01}O$.

In ZnO doped with only Sn [22,23] or Al [24,25], ID networks do not form even at high sintering temperatures of 1300°C-1400°C. It is likely that Al doping alone cannot stabilize the complete formation of cation monolayers composed of edge-sharing octahedra (i.e. b-IDBs), due to the small ionic radius of Al [21] which precludes the formation of b-IDBs occupied only by Al, possibly due to strong Coulombic repulsion between neighboring Al^{3+} octahedra [26]. This also makes sense based on the consideration of the fact that the b-IDB has been determined to be the favorable site for accommodating larger dopants (e.g. In). In contrast, Sn is known to induce the formation of stable cation monolayers, necessary for b-IDB development, with a single b-IDB in each grain typically being observed in Sn-doped ZnO [1,2]. However, Sn doping alone appears insufficient for stabilizing the formation of p-IDBs, due to both the large ionic radius of Sn^{4+} [21], which could induce considerable strain within the ZnO lattice upon occupation of the p-IDBs [19], and the lower mobility of higher-valence dopants such as Sn^{4+} or Sb^{5+} in comparison to dopants such as Al^{3+}, In^{3+} or Fe^{3+}, which have a lower valence and appear to be able to more readily diffuse within the ZnO lattice [6,27-29].

Two types of diffusion mechanisms leading to the formation of IDBs in ZnO have been identified. They are the internal diffusion mechanism, characteristic of dopants with a 3+ valence (e.g. In^{3+} and Fe^{3+}) and the surface diffusion mechanism, which is the primary diffusion mechanism for dopants with higher valences (e.g. Sn^{4+} and Sb^{5+}) [6]. Since both Al^{3+} and Sn^{4+} are likely to be actively diffusing species in $Zn_{0.98}Sn_{0.01}Al_{0.01}O$, both the internal and surface diffusion mechanisms could contribute to ID network development. Because the formation of

both p-IDBs and b-IDBs is stabilized in Sn-Al co-doped ZnO, the final microstructure resembles that of the $In_2O_3(ZnO)_n$ and $Fe_2O_3(ZnO)_n$ homologous phases, which consist of zigzag-like ID networks composed of p-IDBs and b-IDBs [11,27]. Both internal and surface diffusion have been determined to be active in In and Fe-doped ZnO, although internal diffusion is dominant [6].

Dopants with a valence of 3+ such as Al^{3+} are known to diffuse in ZnO primarily by a V_{Zn}-mediated process [28,29]. As the Fermi level shifts to the conduction band of ZnO, V_{Zn} formation should become increasingly favorable under oxygen-rich conditions [30], while the high sintering temperature (1400°C) should also promote significant V_{Zn} formation [30]. In addition, first principles studies have also found that the diffusion of a higher-valence dopant, As^{5+}, can be facilitated by the formation of dopant-V_{Zn} complexes, which become increasingly mobile under n-type conditions at high temperatures [31]. Thus, both Al^{3+} and Sn^{4+} may attain a high rate of diffusion in ZnO at 1400°C. Overall, the high sintering temperature of 1400°C should promote V_{Zn} formation, which likely facilitates high rates of Al^{3+}, and possibly Sn^{4+}, diffusion, contributing to significant b-IDB and p-IDB development.

As stated in Section 4.3.3, the five-fold sites of the p-IDB should require an average cation valence of 2.5+ in order to maintain electroneutrality. Similar to the likely scenario of Zn^{2+} and Sn^{4+} co-occupation of the b-IDB at a 1:1 ratio, which may occur in order to maintain electroneutrality via an average cation valence of 3+ within the b-IDB octahedral sites, electroneutrality could be achieved at the p-IDB by having Al^{3+} and Zn^{2+} co-occupy the five-fold p-IDB sites at equal concentrations (i.e. at a 1:1 ratio). The stable valence states of Sn are 2+ and 4+ [14-16]. Thus, the occupation of the p-IDBs by Sn could be unfavorable in terms of maintaining charge balance. Overall, the occupation of the p-IDB by Al^{3+} should be more favorable on the basis of both size [19,21] and electroneutrality requirements [3,6]. First principles calculations have also found that the occupation of the five-fold p-IDB site by Sn is unfavorable, with a p-IDB configuration consisting of a single tetrahedral and octahedral site

occupied by Sn and a stacking fault (SF) determined to be more energetically stable than a configuration consisting of two five-fold sites occupied by Sn without a SF [32].

The formation of basal-plane SFs has an associated energetic penalty in ZnO [33]. In addition, based on first principles studies of the InMO$_3$(ZnO)$_n$ homologous phase compounds, it was concluded that the hexagonality of the (MZn$_n$)O$_{n+1}$ layers between neighboring b-IDBs should be maximized in order to reduce the total free energy of the system [19]. If SF formation occurs at p-IDB interfaces, as has been proposed to occur as a result of Sn occupation of the p-IDB sites [32], an increase of the free energy due to the formation of a local cubic *c*-axis cation stacking sequence at the p-IDB could occur, resulting in a reduction of the hexagonality within the (MZn$_n$)O$_{n+1}$ layers. Thus, the occupation of the five-fold p-IDB sites by Al appears to be favorable, due to the reduction of lattice strain, achieved by the small ionic radius of Al, the ability of Al^{3+} to achieve electroneutrality through co-occupation of the p-IDBs with Zn^{2+} and, possibly, due to the ability of Al to stably occupy the p-IDB without causing SF formation, thereby preserving the hexagonality of the bulk ZnO-like regions between b-IDBs. Overall, Sn and Al appear to be essential for stabilizing the formation of the b-IDBs and p-IDBs respectively in $Zn_{0.98}Sn_{0.01}Al_{0.01}O$, and it is the addition of both Sn and Al that enables the formation of ID networks, which do not form in ZnO doped with either Sn or Al only.

4.3.5 Criteria for the Stabilization of IDB Sites by Specific Dopants

It is worthwhile to consider in more detail the specific factors which contribute to the occupation of either the b-IDB or p-IDB sites by the *R* and *M* dopants in the RMO$_3$(ZnO)$_n$ compounds and, also, which types of dopants are most likely to occupy and stabilize IDBs upon addition to ZnO under sintering conditions of high temperatures and long times. Two primary factors which should determine which of the IDB sites, if either, a specific dopant can occupy in ZnO are: 1) the dopant's ionic radius and 2) its stable valence state(s). These factors

can be considered in terms of the rules for determining the stable ionic configurations of crystals put forth by Pauling in his seminal work [34], often referred to generally as Pauling's rules for the prediction of ionic structures. Pauling's first rule is referred to as the radius ratio rule and states that the stable ionic coordination number for a specific cation-anion radius ratio can be predicted generally. The stable ranges of cation-anion ionic radius ratios for different coordination numbers are listed in Table 4.2. These values were calculated by Pauling under the assumption that, for a hard-sphere model, in a given coordination environment, as long as the cation remains in direct contact with each coordinating anion, the coordination number will remain stable. Once the cation ionic radius becomes so small that it can no longer remain in contact with all coordinating anions, a lower coordination number will become stable. Based on Pauling's first rule, the stable coordination for a specific cation (e.g. Zn^{2+} or Al^{3+}) and anion (e.g. O^{2-}) pair can be predicted. Although this method is generally considered to be useful for predicting coordination numbers, some exceptions have been identified [35-38].

Table 4.2. Predicted Ranges of Stability for Different Cation-Anion Ionic Radius Ratios in Specific Coordination Environments, Based on Pauling's First Rule [34]

R_c/R_a	Coord. Number	Coord. Geometry
< 0.155	2	Linear
0.155-0.255	3	Triangular
0.225-0.414	4	Tetrahedral
0.414-0.732	6	Octahedral
0.732-1.0	8	Cubic
1.0	12	Hexagonal or CCP

Equally important to Pauling's first rule is Pauling's second rule, referred to as the electrostatic valence rule, which states that: based on a quantity referred to as the electrostatic bond strength, s, which is defined as: $s = z/\upsilon$, where z is the cation valence state and υ is the cation coordination number, the local electroneutrality within a given ionic configuration can

be preserved by requiring that the anion valence state should equal the sum of the electrostatic bond strengths of each of the coordinating cations. This can be expressed as: $\xi = \sum_i s_i$, where ξ is the anion valence state and s_i is the electrostatic bond strength for one of the cations neighboring a specific anion site in an ionic structure. Conversely, the stable cation valence required for maintaining electroneutrality within a given ionic crystal structure can be determined, assuming the anion valence state and cation and anion coordination numbers are known. Thus, considering the crystallographic structure of the $RMO_3(ZnO)_n$ compounds, specifically the local coordination environment at the octahedral b-IDB and five-fold p-IDB sites, the average cation valence states should be 3+ and 2.5+ at the octahedral b-IDB and five-fold p-IDB sites respectively.

Coordination numbers of 5, 7, 9 and 10 have been observed by experiment [35-38], depsite not being originally included within the framework of Pauling's rules, which are applicable primarily to crystals which are strongly ionic [34]. In crystals such as ZnO which possess a significant covalent bonding component [39], there will be an overlap between neighboring atoms due to electron sharing, making possible the stabilization of other coordination environments, e.g. five-fold coordination, as in the case of the p-IDB, and reducing the applicability of Pauling's rules to some degree. Thus, Pauling's rules should be considered only as a general guideline for determining whether specific dopants can occupy either IDB site in the $RMO_3(ZnO)_n$ compounds and should not be assumed to be absolutely predictive. Indeed, recent studies have determined rules for the formation of $RMO_3(ZnO)_n$ compounds which are less general than Pauling's rules [19]. In parallel to Pauling's first and second rules respectively, they determined that: (1) smaller dopants should occupy the p-IDB sites and larger dopants should occupy the b-IDB sites and (2) the electronic octet rule should be obeyed for the $RMO_3(ZnO)_n$ compounds [19]. The results described in this chapter directly support (1), with the larger Sn and smaller Al dopants clearly appearing to prefer to occupy the respective sites of the b-IDBs and p-IDBs.

Listed in Table 4.3 are the cation-anion ionic radius ratios (R_c/R_a) for the dopants that have been determined to occupy the b-IDB and p-IDB sites in the $RMO_3(ZnO)_n$ homologous phase compounds. Table 4.4 lists which of the IDB sites these dopants have been found to stably occupy. All of the calculated octahedral site R_c/R_a values are within the range of stability (0.414-0.732) predicted based on Pauling's first rule, with the exception of Al^{3+}. This is consistent with the fact that Al doping alone does not stabilize b-IDB formation in ZnO [24,25]; however, Al co-occupation of the b-IDB with both Mn (Chapter 3, Fig. 3.13) and In [40] has been observed. Although a five-fold coordination is not predicted within the framework of Pauling's rules, the calculated R_c/R_a values for the five-fold coordination are near the boundary of stability between tetrahedral (0.225-0.414) and octahedral (0.414-0.732) coordination, which is to be expected. The range of ionic radius values observed for dopants found to stably occupy the octahedral b-IDB site is between 64.5 pm (Fe^{3+} and Mn^{3+}, HS) and 80 pm (In^{3+}) [21] (it should be noted that Ga doping does not result in the formation of a monolayer of edge-sharing octahedra, representing a b-IDB, but instead causes the formation of inversion twin boundaries with a somewhat different structure [41]). Additionally, Sb^{5+} doping also has not been found to result in the formation of a monolayer of edge-sharing Sb octahedra; instead, Sb occupies the b-IDB in a 1:2 ratio with Zn^{2+} [42], in order to maintain electroneutrality, i.e. an average cation charge of 3+ at the b-IDB. It appears reasonable to assume that cation dopants with a valence state of 3+ should be able to stably occupy the octahedral b-IDB sites if their ionic radius is within the range of 64.5-80 pm, although the lower and, in particular, the upper limits may actually be respectively less than and greater than this, considering the known limits of stability of the octahedral coordination environment according to Pauling's first rule (R_c/R_a: 0.414-0.732). For cation dopants with a valence state greater than 3+, e.g. Sn^{4+} and Sb^{5+}, the co-occupation of the b-IDB with lower valence cations (e.g. Zn^{2+}) will likely be necessary in order to maintain electroneutrality. Similarly, dopants with lower valences, e.g. Li^{+} (octahedral ionic radius: 76 pm) and Mg^{2+} (octahedral ionic radius: 72 pm) may also be found to stably

occupy the b-IDB, provided that they co-occupy the b-IDB with other dopants of an appropriate higher valence (e.g. Sn^{4+} or Sb^{5+}) [21].

In the case of the p-IDB, as shown in Table 4.3, the range of cation ionic radii that can be determined to stably occupy the five-fold p-IDB sites appears to be between 48 pm (Al^{3+}) and 62 pm (In^{3+}); although both the lower and upper limit may actually be respectively somewhat smaller and larger than this. In particular, it is expected that the upper limit is greater than 62 pm, since the value listed in Table 4.3 is for tetrahedrally coordinated In^{3+}, with In^{3+} being known to stably occupy both the b-IDB and p-IDB sites without the addition of other dopants [11,12]. In the case of the p-IDB, it should be noted that Zn^{2+} likely co-occupies the five-fold p-IDB sites with dopants having a valence of 3+ in a 1:1 ratio, in order to maintain electroneutrality via an average cation valence of 2.5+ within the five-fold sites of the p-IDBs. As to the question of whether or not the occupation of the p-IDB sites by other dopants, with valences either larger than 3+ or smaller than 2+ occurs, there appears to be a distinct possibility due to the fact that Sn co-occupation of the b-IDB with Al appears to occur, based on the result of STEM-EDS analysis (Fig. 4.4); however the valence state of Sn at the p-IDB interface was not investigated by EELS. Thus, there is also the possibility that the Sn dopants occupying the p-IDB are, at least partially, in a valence state of 2+ [14-16] and substitute primarily for the five-fold coordinated Zn^{2+} cations (ionic radius: 68 pm [21]). Previous investigations into the diffusion mechanisms of dopants with different valence states in ZnO found that dopants with higher valences (e.g. Sn^{4+} and Sb^{5+}) diffuse primarily by a surface diffusion mechanism [6], resulting in the formation of microstructure with a single b-IDB in each grain [1-5]. This indicates that higher-valence dopants may not readily diffuse to occupy the five-fold sites of the p-IDBs, possibly due to a lower rate of diffusion in ZnO than dopants with lower valences (e.g. 2+ or 3+). This may be a result of the fact that higher-valence dopants require a higher V_{Zn} concentration to diffuse at a high enough rate to stabilize p-IDB formation and movement than is required for the lower valence dopants [6,12,28,29,31,43]. However, this remains an

open question. Similarly, it remains undetermined whether or not dopants with valences either less than 2+, e.g. Li^{+} (tetrahedral ionic radius: 59 pm, octahedral ionic radius: 76 pm), or greater than 3+, e.g. Zr^{4+} (five-fold ionic radius: 66 pm), can stably occupy the five-fold p-IDB sites [21]. Important questions for future studies to explore should include the determination of what the exact upper and lower limits are for the cation ionic radii that can stably occupy either the b-IDB or p-IDB sites as well as whether or not dopants, such as Li^{+} or Zr^{4+}, with nominal valences either less than or greater than those of the dopants determined thus far to stably occupy the b-IDB and p-IDB sites can in fact occupy these sites, either independently or via co-occupation with other dopants.

Table 4.3. Ionic Radii and Cation-Anion Ionic Radius Ratios for Dopants Known to Occupy b-IDB or p-IDB Sites [21]

Dopant	Five-Fold Ionic Radius [21]	Octahedral Ionic Radius [21]	R_c/R_a,[(a)] Five-Fold p-IDB Site	R_c/R_a,[(a)] Octahedral b-IDB Site
Al^{3+}	48 pm	53.5 pm	0.348	0.388
Ga^{3+}	55 pm	62 pm	0.399	0.449
In^{3+}	62 pm[(b)]	80 pm	0.449	0.580
Fe^{3+}	58 pm	64.5 pm (HS)	0.420	0.467
Mn^{3+}	58 pm	64.5 pm (HS)	0.420	0.467
Ti^{4+}[(c)]	51 pm	60.5 pm	0.370	0.438
Sn^{4+}	62 pm	69 pm	0.449	0.507
Sb^{5+}	-	60 pm	-	0.435

(a) O^{2-} Tetrahedral Ionic Radius: 138 pm [21]; **(b)** Tetrahedral Ionic Radius [21]

(c) Grains containing a single, meandering IDB were observed in Ti-doped ZnO [44]; however, the valence state(s) of Ti at the IDB(s) and the exact IDB sites it occupies were not determined conclusively.

(d) Zn^{2+} Ionic Radii: 60 pm (tetrahedral), 68 pm (five-fold), 74 pm (octahedral) [21]

Table 4.4. Occupation of b-IDB and p-IDB Sites by Specific Dopants in Inversion Domain Networks			
	Stable Occupation of:		IDB Occupation Reported in (Reference):
Dopant	p-IDBs	b-IDBs	
Al^{3+}	Yes	No **(a)**	This work
Ga^{3+}	**(b)**		[41]
In^{3+}	Yes	Yes	[6,11,12]
Fe^{3+}	Yes	Yes	[27]
Mn^{3+}	**(c)**	Yes	This work
Sn^{4+}	No **(d)**	Yes	This work, [1,2,13,32] **(e)**
Sb^{5+}	No	Yes	[3-5,42] **(e)**

(a) Al^{3+} co-occupation of b-IDBs with In^{3+} was reported in ref. 40; however, Al^{3+} single dopant addition to ZnO is not considered to be able to induce the formation of b-IDBs due to the small ionic radius of Al^{3+} [21]. **(b)** Although Ga^{3+} doping of ZnO can induce the formation of homologous phase compounds, these compounds are composed of inversion twins, and thus lack distinct b-IDB and p-IDB interfaces [41], in contrast to the case of In^{3+} or Fe^{3+} doping of ZnO. **(c)** Although the occupation of p-IDB sites by Mn^{3+} has not been confirmed, it is likely that Mn^{3+} can induce the formation of both b-IDBs and p-IDBs, due to the similar ionic radii of Mn^{3+} and Fe^{3+}, another dopant known to induce the formation of ID networks composed of both b-IDBs and p-IDBs in ZnO [27]. **(d)** As shown in Fig. 4.4, Sn appears to co-occupy the p-IDBs with Al to some extent. However, single-dopant addition of Sn to ZnO has not been found to induce the formation of p-IDBs [1,2]. **(e)** In ref. 1-5, a microstructure consisting of grains containing a single b-IDB was reported for either Sn or Sb-doped ZnO. However, ID network formation has not been reported to occur in ZnO ceramics doped with only a single higher-valence (i.e. valence state $\geq$ 4+) cation dopant. In ref. 32 and 42 respectively, the occupation of b-IDBs by Sn and Sb was reported in ZnO nanowires. Ref. 13 contains observations of Sn localization at the b-IDBs in Sn-Ga co-doped ZnO polycrystals and single crystals. However, the concept of ID network stabilization via multiple-dopant addition cannot be said to be demonstrated in ref. 13 due to the fact that Ga single-dopant addition is known to induce homologous phase formation in ZnO, which precludes the clear determination of the specific roles of Sn and Ga in terms of stabilizing the formation of the specific b-IDB and p-IDB sites.

Although, primarily, dopants with a valence of 3+ have been found to occupy both the b-IDB and p-IDB sites, likely due to the fact that, as can be understood based on Pauling's second rule, the b-IDB should be occupied by dopants with an average valence of 3+ and the p-IDB should be occupied by dopants with an average valence of 2.5+, which can likely be

achieved by equal occupancy of the five-fold p-IDB sites by Zn^{2+} and dopants with a 3+ valence (e.g. In^{3+} and Al^{3+}), it is possible that dopants with lower or higher valences may occupy either site. As shown in Fig. 4.9, previous investigations of the atomic-scale structure of the b-IDBs in Sb-doped ZnO nanowires have found that Zn^{2+} and Sb^{5+} form an ordered structure within the b-IDB cation plane, resulting in the appearance of atomic columns with the periodicity of $Zn^{2+}|Zn^{2+}|Sb^{5+}$ along one of the *a*-axes of ZnO, in order to maintain an average cation charge of 3+ at the octahedral sites of the b-IDB [3,42]. Thus, it is possible that other combinations of cation dopants may form ordered structures at the b-IDBs or p-IDBs in order to maintain a local cation charge of 3+ and 2.5+ at the respective IDB sites and that these dopants may have lower valences (e.g. 1+ or 2+) or higher valences (e.g. 4+ or 5+) than the 3+ valence which meets the requirement for electroneutrality at the b-IDB cation sites. Specific combinations of dopants with different valence states, e.g. 1+/5+ and 2+/4+, may be most likely to form ordered

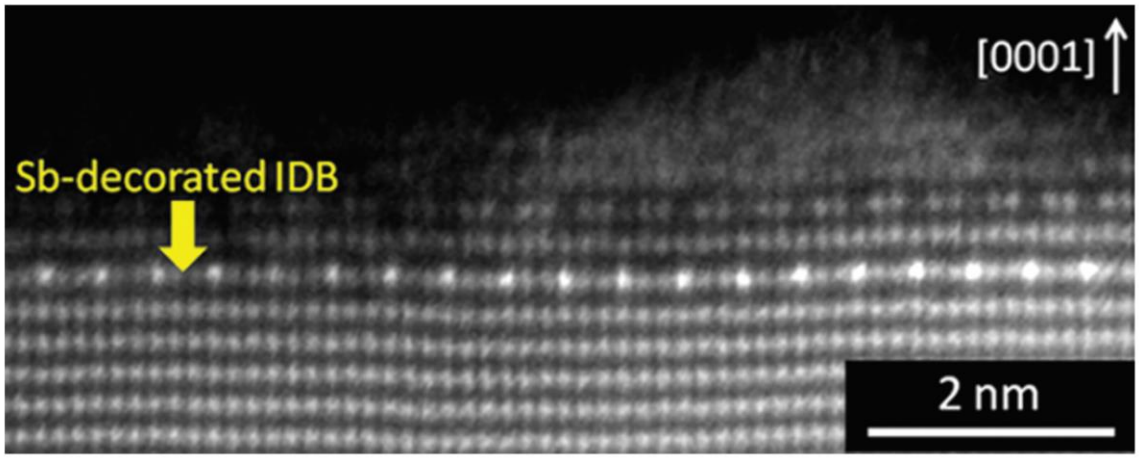

Figure. 4.9. HAADF-STEM image of the modulated b-IDB structure observed to form in Sb-doped ZnO nanowires, viewed along one of the *m*-axes of ZnO. The b-IDB consists of both Zn^{2+} and Sb^{5+} cations, in a 2:1 ratio. Thus, at the {0002} plane of the b-IDB, nearest neighbor Sb atomic columns, which exhibit increased HAADF intensity due to the high atomic number of Sb (Z = 51), are separated by two Zn atomic columns along the direction of the *a*-axis perpendicular to the zone-axis of the image. This ordering occurs in order to achieve electroneutrality within the b-IDB cation layer by maintaining an average cation valence of 3+. The image shown is adapted from ref. 42 and reprinted with the permission of the American Chemical Society.

structures at the b-IDB due to the fact that they can maintain electroneutrality while also reducing the electrostatic repulsion that may be associated with dopants having the same or nearly the same valence states. It should also be noted that the relative ionic radii of the dopants occupying either IDB site is also likely to be a determining factor influencing whether a specific ordering scheme, or any degree of co-occupation, can be stabilized or not. In addition, the shape assumed by the b-IDB octahedra is likely to be distorted from that of an ideal octahedron, for example due to compression of the b-IDB octahedra along the *c*-axis, with the extent of this deviation from the ideal octahedron shape expected to be influenced by the ionic radius of the dopant or dopants occupying the b-IDB. Thus, the possibility of polyhedral distortion should also be taken into consideration when evaluating the likelihood that a specific dopant or combination of dopants can stably occupy the IDB sites.

In addition to the specific ionic radii and valence states of the dopants, *R* and *M*, which occupy the respective sites of the b-IDBs and p-IDBs in the $RMO_3(ZnO)_n$ compounds, other factors may also determine whether or not the addition of specific dopants or dopant oxides to ZnO can cause the formation of IDBs or result in the occupation of the IDBs by specific dopants. For example, certain dopants may have a higher intrinsic diffusivity in ZnO than others. A higher rate of diffusivity should promote IDB formation; however, the rate of diffusivity will be significantly influenced by the temperature and, possibly, by the defect (i.e. V_{Zn}) concentration, in the case of some dopants [6,12,27-31,43]. Alternatively, some other dopants (e.g. Li^+ or Na^+) may not diffuse by a V_{Zn}-mediated mechanism in ZnO, instead diffusing via interstitial diffusion [45,46]. Thus, the specific diffusion mechanism and intrinsic diffusivity of the dopants added to ZnO should be considered in determining whether or not doping can induce IDB formation. In addition, not only the diffusivity of specific dopants but also the reactivity of the dopant oxide powders with ZnO is likely to play a role in determining whether IDB formation can occur, regardless of the dopant ionic radius and valence state. If no reaction between ZnO and the dopant oxide powder occurs, IDB formation may not occur. It is possible

that sintering with dopant oxide powders which undergo a reaction to form a ZnO-based spinel phase may be particularly conducive to the formation of IDBs in ZnO, due to the structural similarities between the b-IDBs and the spinel phases and the fact that IDB formation has been proposed to be a precursor step which occurs before complete spinel phase development [1,2,6,20]. Lastly, the characteristics of the dopant oxide powders used may also influence the ease by which IDB formation occurs; for example, due to the facts that nanopowders may have a high rate of reactivity and the use of nanometric oxides may promote surface diffusion and interdiffusion, enabling more extensive and homogeneous IDB development. Overall, based on the significant number of dopants and combinations of dopants that are yet to be considered in terms of their potential for IDB stabilization, it is clear that the research field for the investigation of IDB formation in ZnO and the stabilization of $RMO_3(ZnO)_n$ homologous phase compounds is vast. However, as stated above, not only should the ionic radii and valence states of the dopants added to ZnO be considered in determining their potential for inducing IDB formation, but, in addition, the dopant diffusion mechanism and diffusion rate in ZnO, the reactivity of the dopant oxide powders with ZnO and the particle characteristics (e.g. average particle size, purity) should also be taken into account. The sample preparation methods and sintering temperature and time must also be determined carefully, particularly by considering how they may influence IDB formation.

4.4 Conclusion

ID networks consisting of b-IDBs and p-IDBs have been observed in Sn-Al co-doped ZnO. In contrast to Al-doped ZnO, in which IDB formation does not occur, and Sn-doped ZnO, in which only a single b-IDB develops in each grain, the development of ID networks in Sn-Al co-doped ZnO is extensive, with ID networks developing thoughout essentially all grains observed. STEM-EDS analysis of the ID networks revealed that the localization of Sn and Al occurs at the b-IDB and p-IDB interfaces respectively. The localization of Sn at the b-IDB was also confirmed by HAADF-STEM and EELS analysis. The b-IDB appears to be composed of a monolayer of edge-sharing cation octahedra, containing a significant concentration of Sn. In contrast, based on HAADF and ABF-STEM observations, the p-IDB has been determined to be a more diffuse defect than the b-IDB, with p-IDBs forming at $\{11\bar{2}l\}$ planes with l values of ~6-7, corresponding to a p-IDB width of ~3-3.5 cation columns.

The critical factor influencing the formation of ID networks in Sn-Al co-doped ZnO is the difference in the ionic radii of Sn and Al. The larger Sn dopant prefers to occupy the octahedral b-IDB site while the smaller Al dopant prefers to occupy the five-fold p-IDB site [19,21]. The distinct diffusion mechanisms of Al^{3+} and Sn^{4+} may also contribute to ID network formation. While the higher-valence Sn^{4+} is less mobile and may cause b-IDB formation primarily by a surface diffusion mechanism, Al^{3+}, with a lower valence, should be more mobile and can readily diffuse within the ZnO grain interior in order to stabilize p-IDB nucleation and growth [6,12], which is necessary for ID network development. The ionic radius mismatch of Sn and Al and the stable occupation of the respective sites of the b-IDBs and p-IDBs by these dopants also appears to contribute to the suppression of the spinel phases, which contain only a single octahedral site at which to accommodate both the Sn and Al dopants.

The results of this chapter have implications for the synthesis of $RMO_3(ZnO)_n$ materials based on the specific characteristics (e.g. ionic radius and valence state) of the *R* and

M dopants occupying the b-IDBs and p-IDBs respectively. As observed in $Zn_{0.98}Sn_{0.01}Al_{0.01}O$, by controlling the concentration and/or the type of the *R* and *M* dopants, it should be possible to stabilize ID network or homologous phase compound formation even in systems containing *R* and *M* dopants that are both considered to be ineffective for inducing ID network development in the case of single-dopant addition. Thus, the synthesis of new $RMO_3(ZnO)_n$ compounds could allow for the development of materials with properties (e.g. electrical conductivity, optical transparency or thermal conductivity) that can be tuned based on the value of *n* and the fractional occupancy of the b-IDBs and p-IDBs by the *R* and *M* dopants respectively, with the potential for the co-occupation of b-IDB and/or p-IDB sites by multiple dopants, particularly via the addition of dopants with average valence states meeting the specific criteria for electroneutrality at either IDB. The suppression of the spinel phases through multi-dopant addition for the preferential stabilization of ID network and homologous phase compound formation should also aid in obtaining monophasic materials with properties unaffected by spinel secondary phase development.

4.5 References

[1] N. Daneu, A. Rečnik, S. Bernik, and D. Kolar, J. Am. Ceram. Soc., **83**, 3165 (2000)

[2] N. Daneu, A. Rečnik, and S. Bernik, J. Am. Ceram. Soc., **94**, 1619 (2011)

[3] A. Rečnik, N. Daneu, T. Walther, and W. Mader, J. Am. Ceram. Soc., **84**, 2657 (2001)

[4] N. Daneu, A. Rečnik, and S. Bernik, J. Am. Ceram. Soc., **86**, 1379 (2003)

[5] S. Bernik, J. Bernard, N. Daneu, and A. Rečnik, J. Am. Ceram. Soc., **90**, 3239 (2007)

[6] A. Rečnik, N. Daneu, and S. Bernik, J. Eur. Ceram. Soc., **27**, 1999 (2007)

[7] T. Ungár, Scr. Mater., **51**, 777 (2004)

[8] T. Moriga, D.D. Edwards, T.O. Mason, G.B. Palmer, K.R. Poeppelmeier, J.L. Schindler, C.R. Kannewurf, and I. Nakabayashi, J. Am. Ceram. Soc., **81**, 1310 (1998)

[9] S. Mathur, M. Veith, M. Haas, H. Shen, N. Lecerf, V. Huch, S. Hüfner, R. Haberkorn, H.P. Beck, and M. Jilavi, J. Am. Ceram. Soc., **84**, 1921 (2001)

[10] M.A. Alpuche-Aviles, and Y. Wu, J. Am. Chem. Soc. **131**, 3216 (2009)

[11] T. Hörlin, G. Svensson, and E. Olsson, J. Mater. Chem., **8**, 2465 (1998)

[12] A.P. Goldstein, S.C. Andrews, R.F. Berger, V.R. Radmilovic, J.B. Neaton, and P. Yang, ACS Nano, **7**, 10747 (2013)

[13] S. Eichhorn, H. Schmid, W. Assenmacher, and W. Mader, J. Solid State Chem., **246**, 214 (2017)

[14] M.S. Moreno, R.F. Egerton, and P.A. Midgley, Phys. Rev. B, **69**, 233304 (2004)

[15] M.S. Moreno, R.F. Egerton, J.J. Rehr, and P.A. Midgley, Phys. Rev. B, **71**, 035103 (2005)

[16] M.S. Moreno, R.C. Mercador, and A.G. Biblioni, J. Phys.: Condens. Matter, **4**, 351 (1992)

[17] S.D. Findlay, S. Azuma, N. Shibata, N. Okunishi, and Y. Ikuhara, Ultramicroscopy, **111**, 285 (2011)

[18] W. Yu, and W. Mader, Ultramicroscopy, **110**, 411 (2010)

[19] J.L.F. Da Silva, Y. Yan, and S.H. Wei, Phys. Rev. Lett., **100**, 255501 (2008)

[20] A. Rečnik, M. Čeh, and D. Kolar, J. Eur. Ceram. Soc., **21**, 2117 (2001)

[21] R.D. Shannon, Acta Cryst. Sec. A, **32**, 751 (1976)

[22] M. Peiteado, Y. Iglesias, J.F. Fernández, J. De Frutos, and A.C. Caballero, Mater. Chem. Phys., **101**, 1 (2007)

[23] K. Park, J.K. Seong, Y. Kwon, S. Nahm, and W.S. Cho, Mater. Res. Bull., **43**, 54 (2008)

[24] K. Shirouzu, T. Ohkusa, M. Hotta, N. Enomoto and J. Hojo, J. Ceram. Soc. Jpn., **115**, 254 (2007)

[25] J.P. Han, P.Q. Mantas, and A.M.R. Senos, J. Mater. Res., **16**, 459 (2001)

[26] J. Wen, L. Wu, and X. Zhang, J. Appl. Phys., **111**, 113716 (2012)

[27] O. Köster-Scherger, H. Schmid, N. Vanderschaeghe, F. Wolf, and W. Mader, J. Am. Ceram. Soc., **90**, 3984 (2007)

[28] K.M. Johansen, L. Vines, T.S. Bjørheim, R. Schifano, and B.G. Svensson, Phys. Rev. Appl., **3**, 024003 (2015)

[29] D. Steiauf, J.L. Lyons, A. Janotti, and C.G. Van de Walle, APL Materials, **2**, 096101 (2014)

[30] A. Janotti, and C.G. Van de Walle, Phys. Rev. B, **76**, 165202 (2007)

[31] B. Puchala, and D. Morgan, Phys. Rev. B, **85**, 064106 (2012)

[32] B. Cao, T. Shi, S. Zheng, Y.H. Ikuhara, W. Zhou, D. Wood, M.M. Al-Jassim, and Y. Yan, J. Phys. Chem. C, **116**, 5009 (2012)

[33] Y. Yan, G.M. Dalpian, M.M. Al-Jassim, and S.H. Wei. Phys. Rev. B, **70**, 193206 (2004)

[34] L. Pauling, J. Am. Chem. Soc., **51**, 1010 (1929)

[35] M.K. Kelly, P. Barboux, J.M. Tarascon, and D.E. Aspnes, Phys. Rev. B, **40**, 6797 (1989)

[36] E. Fernández López, V. Sánchez Escribano, M. Panizza, M.M. Carnasciali, and G. Busca, J. Mater. Chem., **7**, 1891 (2001)

[37] C. Boudaren, J.P. Auffrédic, M. Louër, and D. Louër, Chem. Mater., **12**, 2324 (2000)

[38] U. Schwarz, K. Takemura, M. Hanfland, and K. Syassen, Phys. Rev. Lett., **81**, 2711 (1998)

[39] Ü. Özgur, Y.I. Alivov, C. Liu, A. Teke, M.A. Reschikov, S. Doğan, V. Avrutin, S.J. Cho, and H. Morkoç, J. Appl. Phys., **98**, 041301 (2005)

[40] M. Košir, M. Čeh, C.W. Ow-Yang, E. Guilmeau, and S. Bernik, J. Am. Ceram. Soc., **100**, 3712 (2017)

[41] E. Guilmeau, P. Díaz-Chao, O.I. Lebedev, A. Rečnik, M.C. Schäfer, F. Delorme, F. Giovanelli, M. Košir, and S. Bernik, Inorg. Chem., **56**, 480 (2016)

[42] A.B. Yankovich, B. Puchala, F. Wang, J.H. Seo, D. Morgan, X. Wang, Z. Ma, A.V. Kvit, and P.M. Voyles, Nano Lett., **12**, 1311 (2012)

[43] G. Petretto, and F. Bruneval, Phys. Rev. Appl., **1**, 024005 (2014)

[44] S. Bernik, N. Daneu, and A. Recnik, J. Eur. Ceram. Soc., **24**, 3703 (2004)

[45] K.E. Knutsen, K.M. Johansen, P.T. Neuvonen, B.G. Svensson, and A.Y. Kuznetsov, J. Appl. Phys., **113**, 023702 (2013)

[46] G.Y. Huang, C.Y. Wang, and J.T. Wang, J. Phys.: Cond. Matter, **21**, 345802 (2009)

Chapter 5. Atomistic and Electronic Properties of Mn and Sn-Doped b-IDBs: First Principles Calculations

5.1 Introduction

In chapters 3 and 4, the localization of Mn and Sn at the b-IDB interfaces was observed in Mn-Al and Sn-Al co-doped ZnO materials respectively. In this chapter, the atomistic properties and local electronic structures at the Mn and Sn-doped b-IDBs have been investigated by first principles calculations using the density functional theory (DFT) as implemented in the Vienna Ab Initio Simulation Package (VASP). Slab models containing a single b-IDB interface were constructed and structural relaxation was carried out to determine the stable interface structure. The relaxed structural models are in general agreement with the b-IDB atomic structures observed by HAADF and ABF-STEM. The local electronic density of states (DOS) at the Mn and Sn-doped b-IDBs has also been calculated and the local b-IDB electronic structure has been compared with that of bulk ZnO. The implications of the results for the design of $RMO_3(ZnO)_n$ materials with interfaces having electronic structures which can be modified based on the specific dopants substituting at IDB sites are discussed.

5.2 Methods

Mn-Doped b-IDB

Calculations were carried out using the density functional theory (DFT) [1] as implemented in the Vienna Ab Initio Simulation Package (VASP) [2]. The projector augmented-wave (PAW) method (plane wave cutoff: 520 eV) [3] and generalized gradient approximation (GGA) [4] were used. The slab models studied contained a monolayer of edge-sharing Mn octahedra, representing the b-IDB interface. The b-IDB was bounded by 11 Zn-O

cation-anion planes both above and below the b-IDB cation plane. The model also contained two oxygen-terminated $(000\bar{1})$ surfaces and 98 atoms total (44 Zn, 48 O, 2 Mn and 4 H). 12, 6 and 7 valence electrons were included for the Zn, O and Mn atoms respectively. A pseudo-hydrogen atom with a charge of 0.5 e was placed above each surface oxygen atom to maintain charge balance. Surface passivation using pseudo-hydrogen atoms is also useful for removing dangling bonds, which can result in spurious localized mid-gap electronic states [5]. A vacuum layer of ~12-13 Å was included between the surfaces to avoid interactions between periodic images of the slab model [5].

The slab model volume, shape and atomic coordinates were relaxed subject to the convergence criteria that the residual forces on all ions be $\leq$ 0.02 eV/Å. Γ-point centered k-points meshes of size 5x8x1 and 10x16x2 were used for the structural relaxation and calculation of the density of states (DOS) respectively. For comparison, a calculation was also carried out for bulk ZnO, with k-points meshes of size 9x9x5 and 36x36x20 used for the structural relaxation and DOS calculation respectively. The electronic on-site Coulombic interaction was also incorporated in the calculation by including the effective Hubbard interaction parameter, U_{eff} [6]. For Mn, U_d = 6 eV was used [7]. The use of GGA alone results in a significant underestimation of the band gap, E_g, of ZnO (GGA E_g: 0.78 eV, experimental E_g: 3.3-3.44 eV); thus, U_{eff} values of U_d = 10 eV and U_p = 7 eV were included for the Zn and O atoms respectively [6], resulting in an increase of the calculated band gap value to 2.23 eV for bulk ZnO.

Sn-Doped b-IDB

Slab model calculations for the Sn-doped b-IDB were carried out using essentially the same methods and parameters as used for the Mn-doped b-IDB calculation. Edge-sharing Sn octahedra were substituted in place of Mn octahedra to represent the b-IDB cation layer. It should be noted that the b-IDB sites in Sn-doped ZnO may, alternatively, actually consist of

Zn^{2+} and Sn^{4+} in a 1:1 ratio, which fulfills the condition for electrostatic neutrality at the b-IDB by maintaining an average cation valence of 3+. The model studied contained a total of 98 atoms (44 O, 48 Zn, 2 Sn and 4 H) and 12, 6 and 14 valence electrons were included for the Zn, O and Sn atoms respectively. Oxygen surfaces were passivated by hydrogen atoms with a charge of 0.5 e and a vacuum layer of ~15-16 Å was included between surfaces. A k-points mesh of size 5x8x1 was used for both the structural relaxation and DOS calculations.

5.3 Results and Discussion

5.3.1 b-IDB Structural Models

Mn-Doped b-IDB

Based on the results of HAADF/ABF-STEM, STEM-EDS and EELS analysis, a slab model containing a single Mn-doped b-IDB was constructed. Although minor localization of Al was detected at the b-IDB in $Zn_{0.89}Mn_{0.1}Al_{0.01}O$, Al doping was not included in the model due to the significantly higher Mn concentration detected at the b-IDB. Al doping alone does not induce IDB formation, with only spinel precipitates being observed in ZnO doped with 1 at. % Al and sintered in air at 1400°C for 12 hr. Views of the refined slab model, which was visualized using VESTA [8], at several different zone-axes are shown in Fig. 5.1. The slab model dimensions (including vacuum layer) are: 5.38 Å, 3.11 Å and 72.29 Å in the $[\bar{1}010]$, $[1\bar{2}10]$ and $[0001]$ directions respectively. The stable *c*-axis cation stacking sequence of αβαβ|γ|αβαβ, observed across the b-IDB, is in agreement with that observed in HAADF/ABF-STEM images of $Zn_{0.89}Mn_{0.1}Al_{0.01}O$.

The $\{0002\}$ cation interplanar spacing of the slab model is 2.527 Å and 2.835 Å within the bulk-like domain interior and at the b-IDB respectively. Thus, there is an expansion of the $\{0002\}$ cation interplanar spacing by 12.2 % at the b-IDB. This is larger than the value

of 8.5 % measured in the HAADF-STEM image shown in Fig. 3.11 (a). The presence of Al in addition to Mn at the b-IDB and the substitution of Mn at Zn tetrahedral sites within the domain interior, features not accounted for in the slab model, should respectively result in additional lattice contraction at the b-IDB and lattice expansion within the domain interior of the $Zn_{0.89}Mn_{0.1}Al_{0.01}O$ samples synthesized. This may contribute to the discrepancy observed between the values of the $\{0002\}$ cation interplanar spacing of the slab model and the experimental images. The $\{0002\}$ cation interplanar spacing of the bulk-like domain interior in the model, 2.527 Å, is noticeably smaller than the experimental value for undoped ZnO, 2.6 Å [9]. The inclusion of the U_{eff} parameter can cause increased localization of the Zn *d* and O *p* states, resulting in a reduction of the lattice constants of ZnO [6]. However, the difference of ~3 % observed between the calculated and experimental lattice constant values is reasonable considering that LDA and GGA typically result in a deviation of up to ± 3 % from the experimental lattice constant values [10]. Overall, the features of the slab model Mn-doped b-IDB are in general agreement with those observed experimentally.

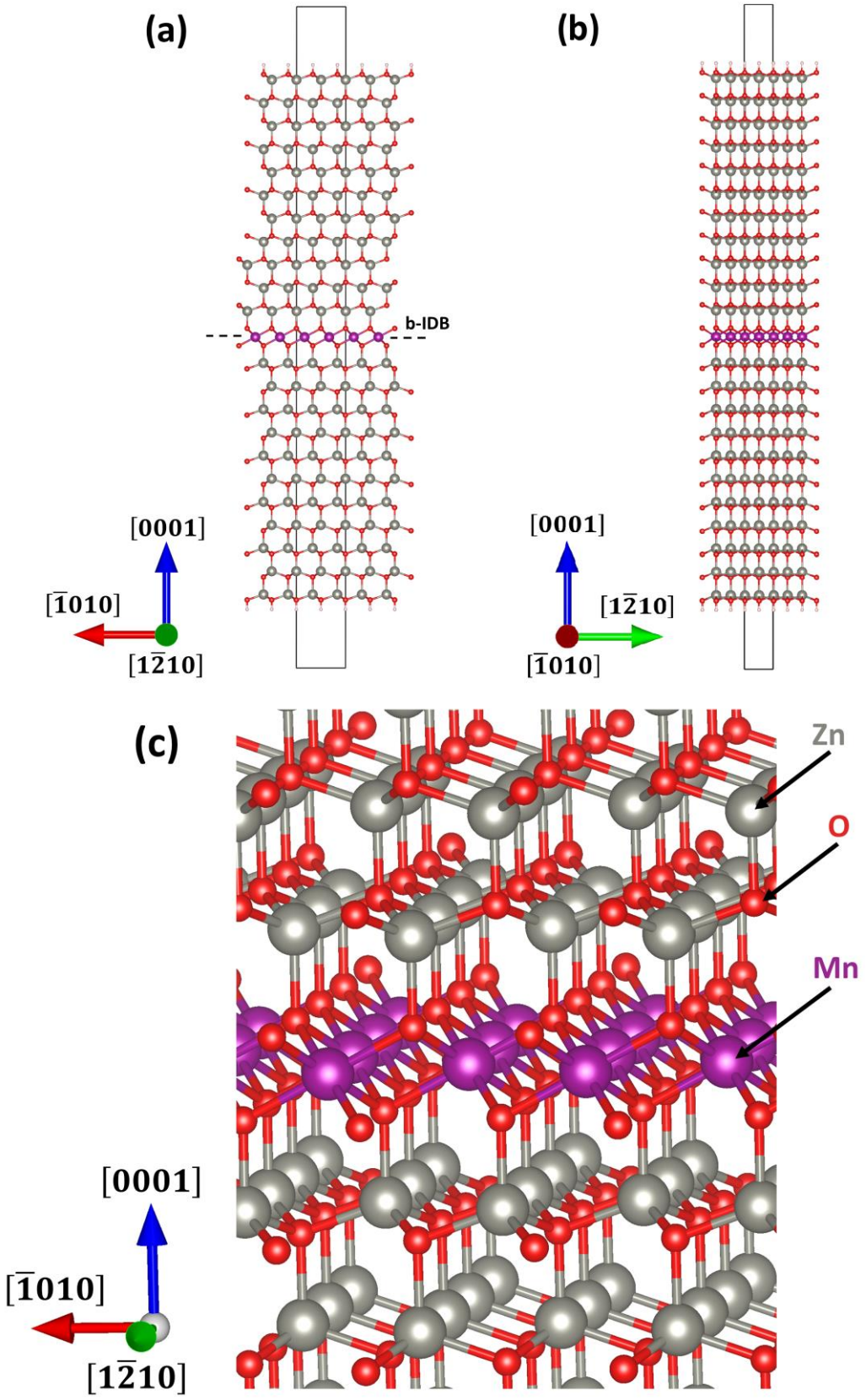

Figure 5.1. (a) [1$\bar{2}$10] **(b)** [$\bar{1}$010] and **(c)** enlarged inclined views of the Mn-doped b-IDB slab model. The b-IDB cation layer is indicated by the dashed lines in (a).

Sn-Doped b-IDB

Views of the Sn-doped b-IDB at several zone-axes are shown in Fig. 5.2. The structures were visualized using VESTA [8]. Substitution of Zn at the b-IDB octahedral sites was not considered in order to investigate only the influence of Sn doping; although the co-occupation of the b-IDBs by both Zn^{2+} and Sn^{4+} at a ratio of 1:1 may occur in actual samples in order to maintain an average cation valence of 3+ at the b-IDB. The *c*-axis cation stacking sequence of αβαβ|α|γαγα observed at the b-IDB is in agreement with that observed in the HAADF/ABF-STEM images shown in Chapter 4. Two different Sn sites are observed at the b-IDB and are labeled as Sn1 and Sn2 in Fig. 5.3. The average Sn-O bond lengths of Sn1 and Sn2 are 2.33 Å and 2.09 Å respectively. These values resemble the Sn-O bond lengths of the Sn^{2+} and Sn^{4+} cations in SnO (2.22 Å) and SnO_2 (2.06 Å) respectively [11]. As described in Chapters 3 and 4, in order to maintain electroneutrality, the average cation valence should be 3+ at the octahedral sites of the b-IDB [12]. Thus, to maintain charge balance, different octahedral sites with Sn-O bond lengths resembling those of Sn^{2+} and Sn^{4+}, in SnO and SnO_2 respectively, could be stabilized at the b-IDB interface in the model, effectively resulting in an average cation valence of 3+ within the b-IDB cation plane.

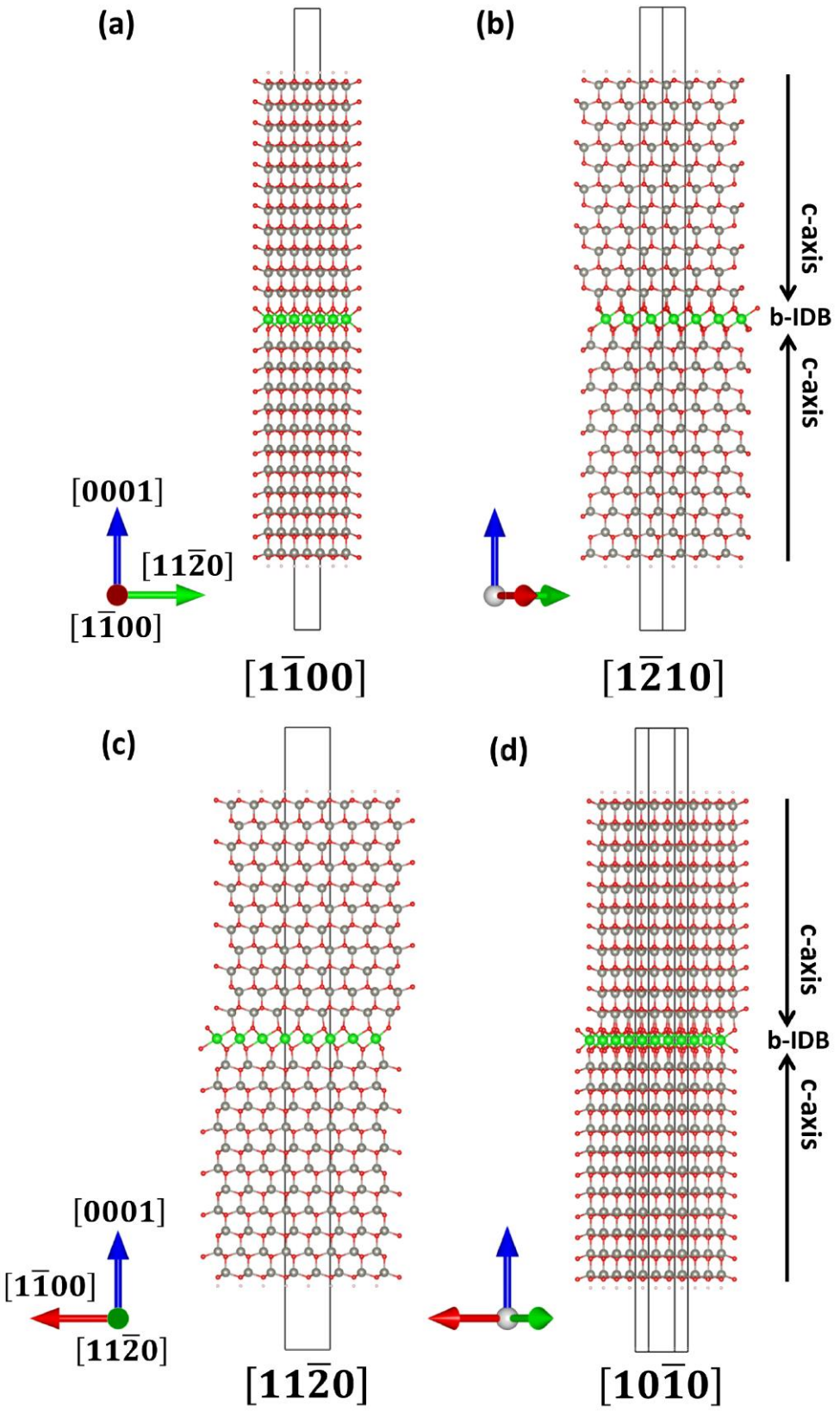

Figure 5.2. (a) [1$\bar{1}$00] **(b)** [1$\bar{2}$10] **(c)** [11$\bar{2}$0] and **(d)** [10$\bar{1}$0] zone-axis views of the Sn-doped b-IDB slab model. The *c*-axis configuration at the b-IDB is indicated by the vertical arrows.

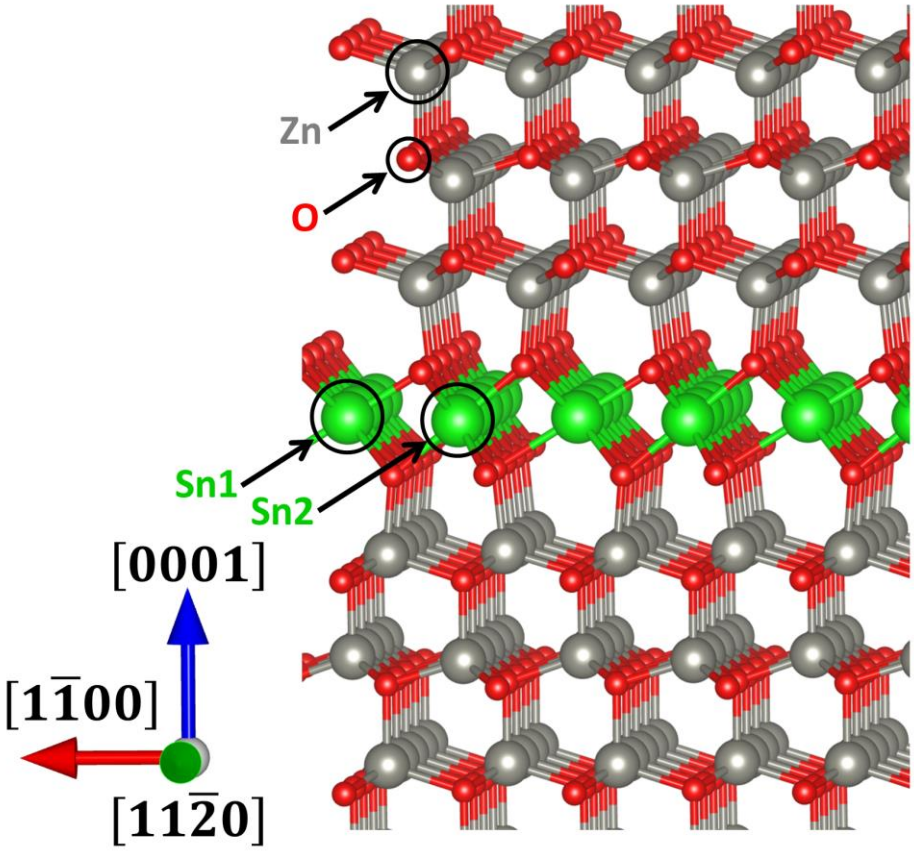

Figure 5.3. Enlarged inclined view of the b-IDB interface in the Sn-doped b-IDB slab model. The distinct Sn sites (Sn1 and Sn2) at the b-IDB are shown. These sites can be distringuished at the $[11\bar{2}0]$ zone-axis in the model.

5.3.2 Electronic Density of States

Mn-Doped b-IDB

The local electronic density of states (LDOS) at the Mn-doped b-IDB is shown in Fig. 5.4 (a). The electronic DOS of bulk ZnO is also shown for comparison in Fig. 5.4 (b). There are several important differences between the DOS of the Mn-doped b-IDB and bulk ZnO. As shown in Fig. 5.4 (a), the Mn-doped b-IDB LDOS contains a valence band exhibiting significant hybridization between the Mn *d* and O *p* states over the energy range from -5.5 eV to just below the Fermi level at 0.0 eV. In contrast, the Mn *d* states that occupy the bottom of the conduction band, from just above 2.0 eV to ~4.5 eV, exhibit a highly localized character,

with a smaller degree of hybridization with the O *p* states. As observed in the Mn_3O_4 Hausmannite compound, the equatorial Mn-O bonds of octahedrally-coordinated Mn, Mn_{oct}, possess a more covalent character than and correspond to electronic states located lower in energy than the electronic states associated with the apical Mn-O bonds, which are more ionic in character and are, thus, expected to correspond to electronic states located higher in energy [13]. Contributions to the DOS from the Zn *s*, *p* and *d* states and O *s* and *p* states exhibit similar features in the LDOS at the b-IDB and in bulk ZnO, with the primary difference being a reduced contribution of these states relative to the Mn *d* states at the b-IDB.

In contrast to the previous studies of Mn-doped ZnO, in which the DOS of tetrahedrally-coordinated Mn, Mn_{tet}, was studied [14], the LDOS at the b-IDB shows different features due to the local octahedral coordination of Mn. The partial DOS (PDOS) of Mn_{tet} in ZnO exhibits mid-gap Mn *d* states [14], which are not observed in the LDOS of Mn_{oct}. The mid-gap Mn *d* states due to Mn_{tet} cause the band gap of ZnO to increase due to repulsive interactions with the O *p* states in the valence band [14]. The hybridization of the Mn *d* states of Mn_{oct} and the O *p* states within the valence band, observed in the LDOS at the Mn-doped b-IDB, could result in band gap reduction due to a shift upward in energy of the valence band maximum (VBM) [14]. The Hausmannite Mn_3O_4 compound contains both Mn_{tet} and Mn_{oct} sites and the calculated DOS of this compound clearly indicates that the contributions of the Mn_{oct} atoms to the DOS are located lower in energy than those due to the Mn_{tet} atoms [13], which is to be expected based on the relatively covalent and ionic bonding character of the Mn_{oct} and Mn_{tet} sites respectively. The band gap at the Mn-doped b-IDB, determined via the LDOS, is 2.17 eV, in comparison to the value of 2.23 eV for bulk ZnO. Although Mn_{oct} does not induce the formation of mid-gap states, which are known to act as electron traps, a quantum well could form at the b-IDB, due to the local zinc-blende cation stacking sequence within the wurtzite matrix [15], potentially resulting in electron localization at the b-IDB.

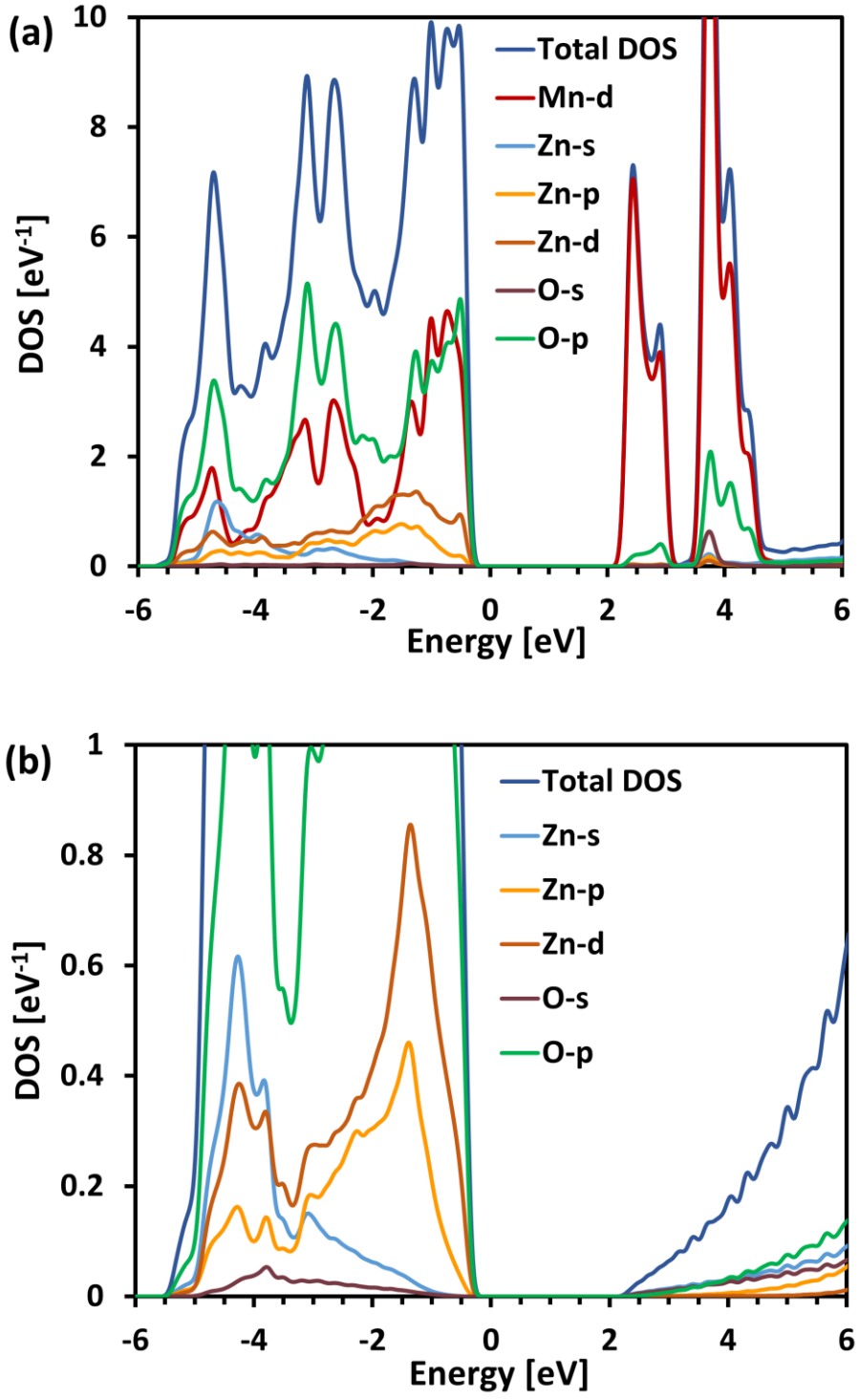

Figure 5.4. (a) LDOS at the Mn-doped b-IDB. The Mn, Zn and O states correspond to the two Mn at the b-IDB, the four Zn directly neighboring the b-IDB and the four O coordinated to the Mn at the b-IDB. **(b)** Bulk ZnO DOS. The Fermi level (E_f) is set to the zero on the abscissa and, in the case of the slab model, represents the E_f value for the entire model.

The thickness of the Zn-O bulk-like regions of the slab model is ~2.5 nm, which is considerably less than the average spacing between b-IDBs along the *c*-axis of 50.6 nm (range: 17-206 nm) observed in $Zn_{0.89}Mn_{0.1}Al_{0.01}O$ by TEM observation. This thickness was chosen as a compromise between achieving convergence of the DFT calculation and maintaining a sufficient separation between the Mn-doped b-IDB interface and the slab model surfaces, in order to avoid the occurrence of spurious results due to interactions between the interface and the surfaces. Calculations were also carried out for a smaller slab model containing only 50 total atoms and a total of 5 Zn-O cation-anion layers both above and below the b-IDB plane. The Zn-O, Mn-O and H-O bond distances were found to change by less than 1 % upon increasing the number of Zn-O cation-anion layers to 11. In future experiments, increasing the concentration of Mn or Al, in order to synthesize other $Mn_2O_3(ZnO)_n$ or $Mn_xAl_yO_3(ZnO)_n$ compounds, could result in the formation of intergrowth or homologous phase compounds with smaller b-IDB spacings. Similar to the $In_2O_3(ZnO)_n$ homologous phases, these compounds could exhibit optoelectronic properties that are dependent on the relative concentration of Mn to Al, as well as on the concentration of these elements relative to Zn (i.e. properties dependent on the values of Mn:Al and *n*) [16-18].

Sn-Doped b-IDB

The LDOS at the Sn-doped b-IDB is shown in Fig. 5.5 (a). The LDOS of the ZnO bulk-like region of the slab model is also shown in Fig. 5.5 (b). There is a considerable decrease of the fundamental band gap magnitude at the b-IDB, to a value of 0.72 eV in comparison to 2.06 eV in the bulk-like region consisting of Zn tetrahedra (bulk ZnO: 2.23 eV). In ZnO doped with group III elements (e.g. Al^{3+}, Ga^{3+} and In^{3+}), the ZnO fundamental band gap can undergo a renormalization depending on the energy position of the group-III element *s* states. Al is considered an ideal n-type dopant for ZnO because the Al *s* states are located high enough in

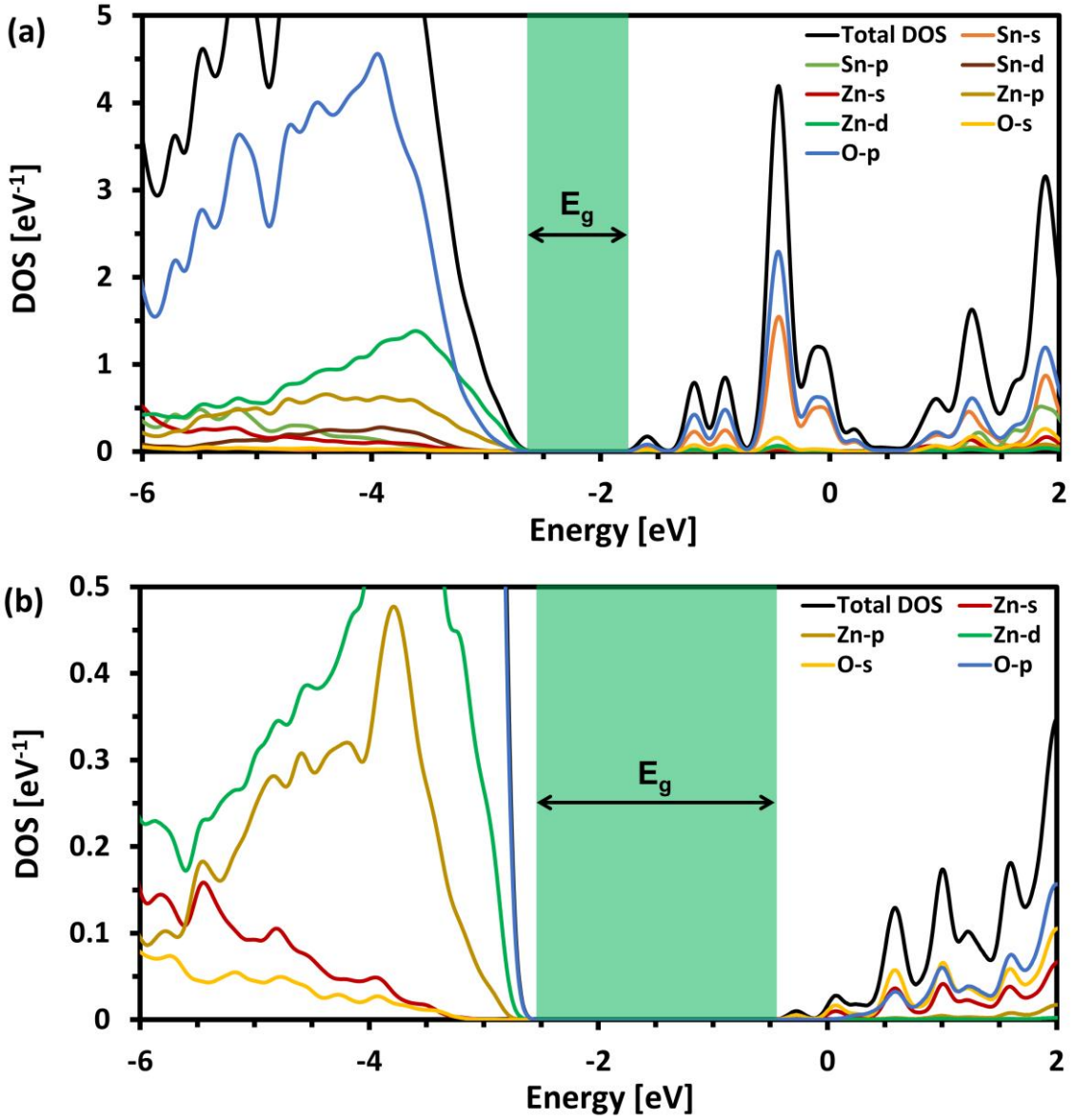

Figure 5.5. (a) LDOS at the Sn-doped b-IDB. The Sn, Zn and O states correspond to the two Sn at the b-IDB, the four Zn directly neighboring the b-IDB and the four O coordinated to the Sn atoms at the b-IDB. **(b)** LDOS in the domain interior. The Zn and O states correspond to the two Zn in the sixth basal-plane cation layer above the b-IDB and the four coordinating O atoms. Relative to the domain interior, a large renormalization of the fundamental band gap (indicated by the green shading) occurs at the b-IDB, causing a local decrease of the band gap. The Fermi level of the entire slab model is set to the zero on the abscissa.

energy relative to the conduction band minimum (CBM) of ZnO that they do not cause a renormalization of the ZnO band gap [19,20]. This is a result of the large band gap of Al_2O_3 (Al_2O_3 E_g: 8.8 eV [21], ZnO E_g: 3.3-3.44 [6]). In contrast, the *s* states of In and Ga are located

lower in energy and, thus, cause a considerable renormalization of the ZnO band gap [19,20], due to the fact that the band gap magnitudes of In_2O_3 and Ga_2O_3 are closer to that of ZnO (In_2O_3 E_g: 3.75 eV [18], Ga_2O_3 E_g: 5.2 eV [22]). The band gap renormalization is thus due to the close proximity of the In *s* and Ga *s* states to the ZnO CBM. As in the case of In, the *s* states of Sn are located close to the CBM of ZnO, since the band gap of SnO_2 is similar in magnitude to that of ZnO (SnO_2 E_g: 3.25-4.1 eV [23,24]). This is considered to be the primary factor contributing to the large renormalization of the fundamental band gap at the Sn-doped b-IDB.

In addition, the Fermi level is shifted to the conduction band at the b-IDB, indicating that Sn acts as a donor dopant. The shift of the Fermi level to the conduction band should result in an increase of the optical band gap (measured from the energy level of the VBM, E_{VBM}, to the Fermi level, E_f) to a value of: E_f-E_{VBM} = 2.57 eV, due to the Burstein-Moss effect [19,20]. Based on the average Sn-O bond lengths at the b-IDB, the Sn2 site clearly bears a resemblance to Sn^{4+} in SnO_2 (Sn2: 2.09 Å, Sn^{4+}: 2.06) [11]. In contrast, the average Sn-O bond length of the Sn1 site is closer to that of Sn^{2+} in SnO, but exhibits a greater deviation than Sn2 does from Sn^{4+} in SnO_2 (Sn1: 2.33 Å, Sn^{2+}: 2.22 Å) [11]. It is thus possible, assuming a valence of 2- for each coordinating oxygen atom, that Sn2, which appears to possess a Sn^{4+}-like character, could act as a donor dopan at the b-IDB octahedral site and cause the Fermi level to shift to the conduction band.

The PDOS of the Sn1 and Sn2 sites at the Sn-doped b-IDB are shown in Fig. 5.6 (a) and (b) respectively. A number of distinctive features are observed in the PDOS for the two sites. The PDOS for both Sn1 and Sn2 exhibit a sharp peak due to the Sn *s* states located near -9 eV. Throughout the energy range from -8 eV to -3 eV, the PDOS of both sites contains a lower-intensity broadened feature due to the Sn *p* states. However, the intensity of this feature is lower at the Sn1 site. From -3 eV to 0.5 eV, an energy gap in which the Fermi level, which is set to 0.0 eV, is located is observed within the Sn2 PDOS. In contrast, the Sn1 site exhibits a smaller energy gap located between -3 eV and -2 eV. These PDOS features of the Sn1 and Sn2

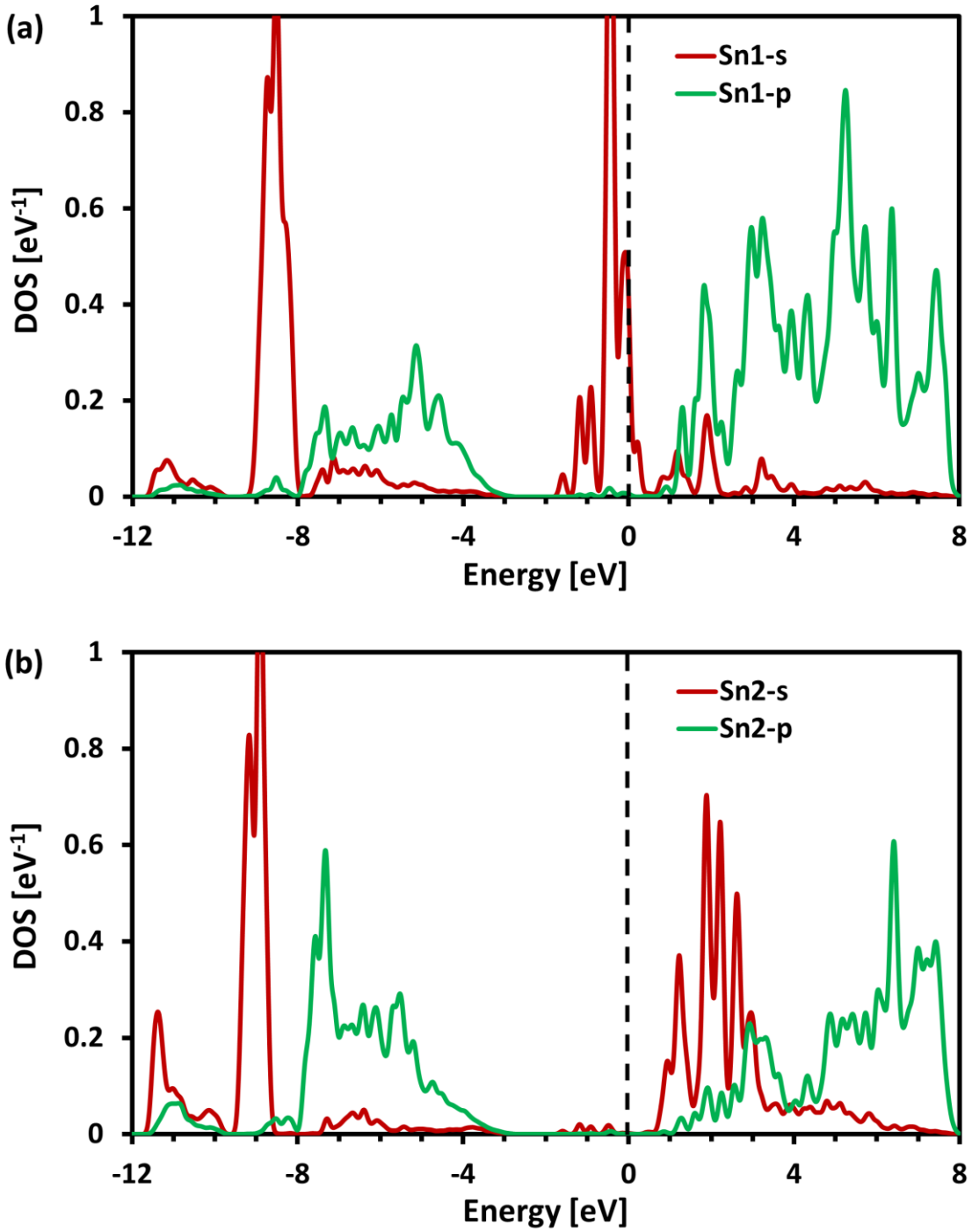

Figure 5.6. PDOS of the **(a)** Sn1 and **(b)** Sn2 sites at the Sn-doped b-IDB. The Fermi level of the entire slab model is set to the zero on the abscissa and is indicated by the dashed lines.

sites closely resemble those of the respective Sn(b) and Sn(a) sites that are found within the proposed Sn_2O_3 tin oxide homologous phase compound that has been studied by first principles calculations [25]. The Sn(a) and Sn(b) PDOS respectively correspond to octahedrally

coordinated (SnO_2-like) and four-fold coordinated (SnO-like) Sn sites in the Sn_2O_3 compound [25]. In addition to the similarity of the bond lengths of Sn1 and Sn2 sites to those reported for SnO and SnO_2 respectively [11], the relative sizes of the band gaps observed for the Sn1 and Sn2 sites are also in general agreement with the experimental band gaps reported for SnO and and SnO2 (SnO E_g: 2.5-3.0 eV, SnO_2 E_g: 3.25-4.1 eV [23,24]).

The PDOS of Sn1 contains a sharp peak due to the Sn *s* states that is approximately located between -2 eV and 0.5 eV, with an intensity maximum located at ~ -0.5 eV. This feature is in agreement with the PDOS of the Sn(b) site in the Sn_2O_3 compound; however, it is inconsistent with the PDOS of SnO, which, instead of a sharp peak located near the Fermi level, exhibits a broader PDOS feature due to the Sn *s* states near E_f [25]. At higher energy levels, within the energy range starting at ~1 eV, the Sn *p* states dominate the PDOS of Sn1. This is consistent with the PDOS of both the Sn(b) site in Sn_2O_3 and SnO [25]. For the Sn2 site, above the Fermi level, which is located within the energy gap region, sharp PDOS features due the Sn *s* states are dominant within the energy range from 1 eV to 3 eV. This is in agreement with the PDOS of the Sn(a) site in Sn_2O_3 but inconsistent with the PDOS of SnO_2, which exhibits Sn *s* states that are lower in intensity and increase gradually in intensity within the energy range from 1 eV to 3 eV [25].

Overall, the PDOS of the Sn1 and Sn2 sites of the Sn-doped b-IDB resemble the PDOS of the SnO and SnO_2 compounds respectively [25]. However, several incongruities between the PDOS of the Sn1 and Sn2 sites and the SnO and SnO_2 compounds are observed. A better agreement is observed between the PDOS of the Sn1 and Sn2 sites located at the b-IDB and the respective Sn(b) and Sn(a) sites in the Sn_2O_3 homologous phase compound that has been studied by first principles calculations [25]. Similar to the Sn1 and Sn2 sites located at the Sn-doped b-IDB, the Sn(b) and Sn(a) sites are directly bonded and exhibit distinct average Sn-O bond lengths. In order to maintain electroneutrality, the b-IDB should possess an average cation charge of 3+ [12,26]. The Sn_2O_3 compound also possesses an average cation valence of 3+.

Thus, the similarities between the PDOS of the Sn1 and Sn2 sites at the Sn-doped b-IDB and those of the respective Sn(b) and Sn(a) sites in the Sn_2O_3 compound may reflect the similarity of the local atomic bonding environments of the Sn-doped b-IDB and the Sn_2O_3 compound.

5.4 Conclusion

First principles calculations were carried out using the density functional theory as implemented in the VASP software in order to determine the stable atomistic and electronic structures of the Mn-doped and Sn-doped b-IDBs. The structural features of the relaxed models are in general agreement with those observed using HAADF and ABF-STEM in the $Zn_{0.89}Mn_{0.1}Al_{0.01}O$ and $Zn_{0.98}Sn_{0.01}Al_{0.01}O$ samples synthesized. The local electronic density of states at the Mn-doped b-IDB exhibits a hybridization of the Mn *d* and O *p* states within the valence band and localized Mn *d* states within the conduction band. This is attributed to the octahedral coordination of Mn at the b-IDB, with equatorial and apical Mn-O bonds possessing a relatively covalent and ionic bonding character respectively. In contrast to tetrahedrally coordinated Mn in bulk ZnO, the octahedrally coordinated Mn at the b-IDB does not introduce localized mid-gap electronic states.

At the Sn-doped b-IDB, two different Sn sites, Sn1 and Sn2, are observed. The two sites have Sn-O bond lengths resembling those of Sn^{2+} and Sn^{4+} in SnO and SnO_2 respectively. This charge disproportionation between b-IDB sites, which results in the stabilization of Sn sites with bond lengths resembling those associated with Sn^{2+} and Sn^{4+}, could occur in order to maintain electroneutrality at the b-IDB. The PDOS of the Sn1 and Sn2 sites at the Sn-doped b-IDB also exhibit a clear resemblance to the PDOS of the Sn(b) (SnO-like) and Sn(a) (SnO_2-like) sites of the Sn_2O_3 homologous phase compound, suggesting a similarity between the local atomic structure of the Sn-doped b-IDB in the model and the Sn_2O_3 compound. Sn^{4+} sites at the b-IDB may act as electron donors, since the Sn-doped b-IDB LDOS exhibits an n-type

character, with the Fermi level shifted to the conduction band. The fundamental band gap at the Sn-doped b-IDB also undergoes a large renormalization to a value of 0.72 eV (bulk ZnO: 2.23 eV) due to the close proximity of the Sn *s* states to the CBM of ZnO.

The Mn-doped b-IDB and Sn-doped b-IDB exhibit very different atomistic and electronic properties due to the differences in the Mn and Sn elements, which can both occupy the b-IDB octahedral site. Similar to the $In_2O_3(ZnO)_n$ homologous phase compounds [16-18], the optoelectronic properties of other $RMO_3(ZnO)_n$ homologous phase compounds (where *R* = Sn, Mn, In, Fe, and Sb etc.; *M* = In, Fe, Ga or Al etc.) could be systematically modified by varying the value of *n* and, additionally, the ratio *R*:*M*. By studying the effects on the properties of ZnO due to doping with different elements, in particular the influence of different dopants on IDB formation in ZnO, additional *R* and *M* dopants, which localize at the respective interfaces of the b-IDBs and p-IDBs, could be identified. The structural and electronic properties of ZnO could also be tuned locally at the nanoscale level by varying the type and also the relative concentrations of the dopant species, *R* and *M*, that substitute at the octahedral b-IDB and five-fold p-IDB sites respectively.

5.5 References

[1] W. Kohn, and L.J. Sham, Phys. Rev., **140**, A1133 (1965)

[2] G. Kresse, and J. Furthmüller, Phys. Rev. B, **54**, 11169 (1996)

[3] P.E. Blöchl, Phys. Rev. B, **50**, 17953 (1994)

[4] J.P. Perdew, K. Burke, and M. Ernzerhof, Phys. Rev. Lett., **77**, 3865 (1996)

[5] R. Puthenkovilakam, E.A. Carter, and J.P. Chang, Phys. Rev. B, **69**, 155329 (2004)

[6] X. Ma, Y. Wu, Y. Lu, and Y. Zhu, J. Phys. Chem. C, **117**, 26029, (2013)

[7] T. Chanier, M. Sargolzaei, I. Opahle, R. Hayn, and K. Koepernik, Phys. Rev. B, **73**, 134418 (2006)

[8] K. Momma, and F. Izumi, J. Appl. Crystallogr., **44**, 1272 (2011)

[9] Ü. Özgur, Y.I. Alivov, C. Liu, A. Teke, M.A. Reschikov, S. Doğan, V. Avrutin, S.J. Cho, and H. Morkoç, J. Appl. Phys., **98**, 041301 (2005)

[10] P. Haas, F. Tran, and P. Blaha, Phys. Rev. B, **79**, 085104 (2009)

[11] M.S. Moreno, R.F. Egerton, and P.A. Midgley, Phys. Rev. B, **69**, 233304 (2004)

[12] A. Rečnik, N. Daneu, and S. Bernik, J. Eur. Ceram. Soc., **27**, 1999 (2007)

[13] A. Chartier, P. D'Arco, R. Dovesi, and V.R. Saunders, Phys. Rev. B, **60**, 14042 (1999)

[14] S.J. Gilliland, J.A. Sans, J.F. Sánchez-Royo, G. Almonacid, B. García-Domene, A. Segura, G. Tobias, and E. Canadell, Phys. Rev. B, **86**, 155203 (2012)

[15] Y. Yan, G.M. Dalpian, M.M. Al-Jassim, and S.H. Wei, Phys. Rev. B, **70**, 193206 (2004)

[16] T. Moriga, D.D. Edwards, T.O. Mason, G.B. Palmer, K.R. Poeppelmeier, J.L. Schindler, C.R. Kannewurf, and I. Nakabayashi, J. Am. Ceram. Soc., **81**, 1310 (1998)

[17] X. Liang, and D.R. Clarke, Acta Mater., **63**, 191 (2014)

[18] A. Walsh, J.L.F. Da Silva, Y. Yan, M.M. Al-Jassim, and S.H. Wei, Phys. Rev. B, **79**, 073105 (2009)

[19] A. Walsh, J.L.F Da Silva, and S.H. Wei, Phys. Rev. B, **78**, 075211 (2008)

[20] J.A. Sans, J.F. Sánchez-Royo, A. Segura, G. Tobias, and E. Canadell, Phys. Rev. B, **79**, 95105 (2009)

[21] R.H. French, J. Am. Ceram. Soc., **73**, 477 (1990)

[22] J.L.F. Da Silva, A. Walsh, and S.H. Wei, Phys. Rev. B, **80**, 214118 (2009)

[23] M.S. Moreno, R.C. Mercador, and A.G. Biblioni, J. Phys.: Condens. Matter., **4**, 351 (1992)

[24] M.A. Alpuche-Aviles, and Y. Wu, J. Am. Chem. Soc., **131**, 3216 (2009)

[25] A. Seko, A. Togo, F. Oba, and I. Tanaka, Phys. Rev. Lett., **100**, 045702 (2008)

[26] A. Rečnik, N. Daneu, T. Walther, and W. Mader, J. Am. Ceram. Soc., **84**, 2657 (2001)

Chapter 6. Thermoelectric Properties of Mn-Al and Sn-Al Dual-Doped ZnO

6.1 Introduction

In this chapter, the results of thermoelectric property measurements of Mn-Al and Sn-Al dual-doped ZnO ceramics from RT to 750°C are described and the findings are discussed by separately considering the influence of substitutional doping and defect (IDB) formation on the thermoelectric properties. Substitutional dopants, at levels below the solubility limit, are found to have a significant impact on the thermoelectric properties, with the addition of Al and Sn, which act as donors, causing the carrier concentration of ZnO to increase. Increases in the concentration of Mn are found to result in thermal conductivity reduction due to the scattering of phonons by Mn point defects. At high doping levels, above the solubility limit, the formation of ID networks occurs. ID networks also significantly influence the thermoelectric properties, with IDBs acting as interfaces that can affect both electron and phonon transport. The effects of both point defects and IDBs on the thermoelectric properties, specifically the electrical conductivity, Seebeck coefficient, thermal conductivity and figure of merit, are analyzed and discussed in detail. Comparisons are also made with previous studies of the thermoelectric properties of both conventionally doped ZnO ceramics and ZnO ceramics doped with IDB-forming elements. Potential strategies for improving the thermoelectric properties of ZnO ceramics containing IDBs are suggested. Optimization of phonon and electron transport should be acheivable through a combination of nanostructuring by ID network formation and the modification of IDB interfaces by controlling the type and concentration of dopants that occupy the IDBs.

6.2 Methods

Electrical Conductivity and Seebeck Coefficient Measurement

The electrical conductivity (σ) and Seebeck coefficient (S) were measured using the Ulvac-Riko ZEM-2 from 50°C to 730°C. Samples with a typical cross-section of ~2-3 mm^2 and length of ~8-11 mm were cut from sintered pellets using a diamond isometric cutter, sample surfaces were polished using SiC paper and the samples were cleaned in an ultrasonic bath. The ZEM-2 measures σ and S simultaneously. σ is measured using the four-probe method. A pressure contact is made with the top and bottom sample faces in order to apply a current through the sample at each measurement temperature. The resulting voltage difference between the central contacts is then measured to determine the resistivity, from which the conductivity is determined. The Seebeck coefficient is measured by using a heater to apply a temperature difference, ΔT, of 10, 20 and 30 K at each measurement temperature. The Seebeck coefficient is determined from a ΔV/ΔT plot, with ΔV values determined by the voltage difference measured between the two central contacts to the sample at each ΔT. Measurements were made along the direction perpendicular to the axis of uniaxial pressing during sample pelletizing prior to sintering (i.e. along the direction within the plane of the sintered pellet).

Thermal Conductivity Measurement

The thermal conductivity (κ) was determined via measurements of the thermal diffusivity of pellet-shaped samples with a typical thickness of ~1-2 mm and diameter of ~10-11 mm. The thermal diffusivity was measured from room temperature (RT) to 750°C using the laser flash method (Ulvac-Riko, TC-7000). Sample surfaces were polished and covered with a black carbon spray coating to reduce thermal losses due to increasing emissivity at high temperatures. To measure the thermal diffusivity, a laser pulse is applied to one face of the pellet at each measurement temperature and the profile of temperature increase is measured by

an infrared (IR) detector at the other face. This process is carried out a total of three times at each measurement temperature and the thermal diffusivity is calculated as the average of the three measurements. The thermal diffusivity is then used to calculate the thermal conductivity, according to the following equation: $\kappa = \alpha * C_p * \rho$, where α, C_p and ρ are the thermal diffusivity, specific heat and density respectively. The C_p values of undoped ZnO were used [1]. This approximation is reasonable since the dopant concentration is low ($\leq$ 10 at. %) [2]. ρ values were determined by Archimedes' method or by measuring the sample weight and dimensions.

6.3 Results and Discussion

6.3.1 Electrical Conductivity, σ

Mn-Al Co-Doped ZnO

The electrical conductivity of ZnO doped with 1 at. % Al and 0, 1, 2, 5 and 10 at. % Mn measured from 50°C to 730°C is plotted in Fig. 6.1. $Zn_{0.99}Al_{0.01}O$ attains the highest σ over the entire temperature range and exhibits a metallic behavior, i.e. as the temperature increases the electrical conductivity is reduced. Al^{3+} is known to act as a donor dopant in ZnO and can generate electrons by substituting on the Zn sublattice according to the following reaction:

$$Al_2O_3 \xrightarrow{ZnO} 2Al_{Zn}^{\bullet} + 2e' + 2O_O^X + \frac{1}{2}O_2 \uparrow \quad [3]$$

Al doping can increase the σ value of ZnO by up to three orders of magnitude [4]. The electrical conductivity of Al-doped ZnO will continue to increase up to the solubility limit of Al in ZnO, beyond which the less conductive $ZnAl_2O_4$ spinel secondary phase will form, resulting in increasing reduction of σ as the volume fraction of $ZnAl_2O_4$ increases [4]. In 1 at. % Al-doped ZnO, the volume fraction of $ZnAl_2O_4$ is low, thus σ remains high. Because Al^{3+} acts as a donor dopant in ZnO, causing a significant increase in the carrier density, the Fermi level will shift to the conduction band of ZnO. Thus, as the temperature increases, electron-electron scattering

will occur at an increasing rate within the conduction band, resulting in σ reduction, characteristic of a metal or degenerate semiconductor [5].

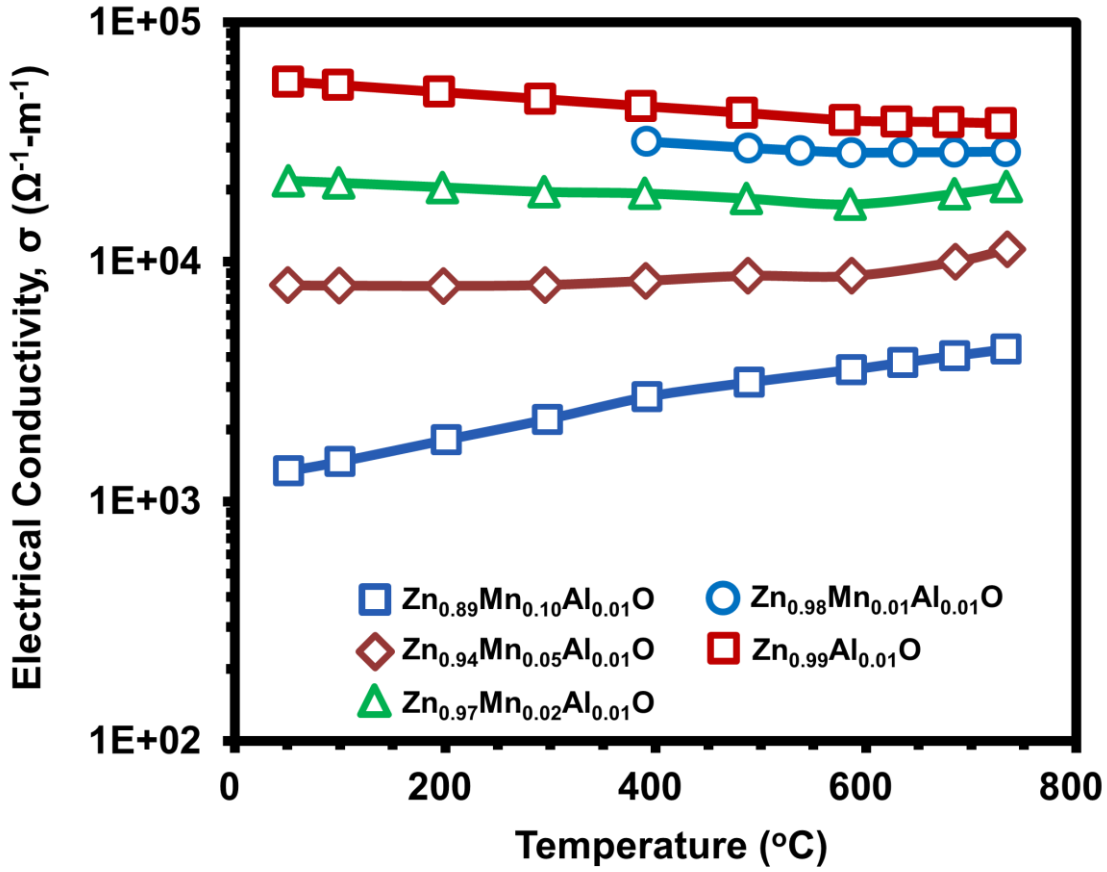

Figure 6.1. Plot of the electrical conductivity measured from RT to 730°C for $Zn_{0.99-x}Mn_xAl_{0.01}O$ samples.

As the concentration of Mn in $Zn_{0.99-x}Mn_xAl_{0.01}O$ increases, the temperature dependence of σ exhibits an increasingly semiconducting or activated electronic transport behavior, i.e. σ increases as the temperature increases. In contrast to Al^{3+}, Mn substitutes on the Zn sublattice in the Mn^{2+} state [6]. Thus, Mn doping of ZnO will not result in an increase of the carrier density. Mn^{2+} can, however, act as a deep acceptor in ZnO, causing the formation of mid-gap states within the band gap of ZnO [7,8]. A schematic of the band structure of ZnO, including the position of the $Mn^{2+/3+}$ mid-gap states is shown in Fig. 6.2 [9]. As the concentration of Mn mid-gap states increases, the carrier density will decrease, because the

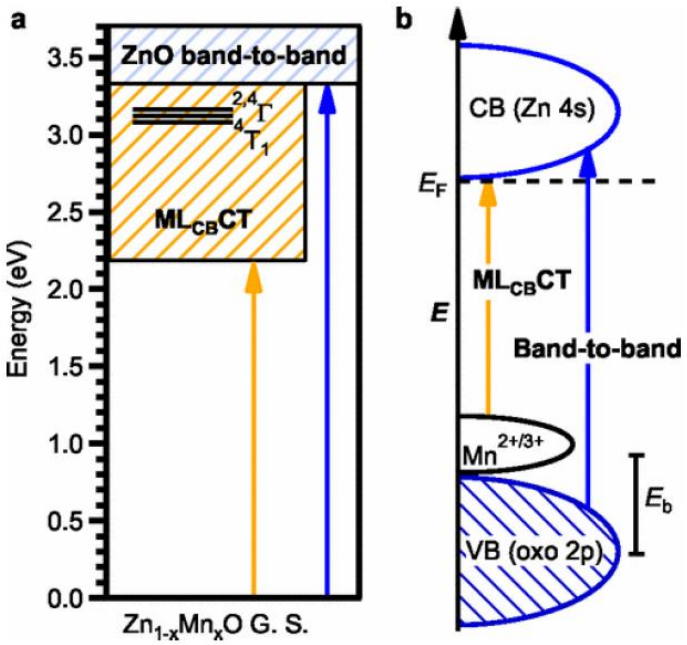

Figure 6.2. Schematics showing **(a)** the magnitude of the energy of 1) the transition from the VBM to the CBM and 2) the transition from the localized $Mn^{2+/3+}$ mid-gap energy levels to the CBM in ZnO and **(b)** the location of the localized $Mn^{2+/3+}$ deep acceptor levels which form within the band gap of ZnO upon substitution of Mn^{2+} for Zn^{2+} on the Zn sublattice. Significant formation of $Mn^{2+/3+}$ deep acceptor levels will lead to an increase of the resistivity due to the depletion of conducting electrons and the shift of E_f to lower energy values. Images shown are adapted from [9] and reprinted with permission from the American Physical Society.

impurity levels can act as traps for the electrons that would normally occupy the shallow donor levels located higher in energy. Electrons trapped in these levels will be increasingly excited with increasing temperature, resulting in the activated character of the electrical conductivity. As the concentration of Mn increases, the mobility may also be reduced due to alloy scattering caused by the substitution of Mn at Zn sites. When the solubility limit of Mn in ZnO (~3-8 at. % at 1400°C [10-12]) is exceeded, the formation of $Zn_xMn_{3-x}O_4$ spinel phases can occur [10-13]. When the volume fraction of these phases is high, σ will be degraded due to the low σ values of the $Zn_xMn_{3-x}O_4$ phases [14]. However, instead of the formation of a high volume fraction of $Zn_xMn_{3-x}O4$ spinel phase precipitates, the extensive development of IDBs was found to occur at a Mn concentration of 10 at. %.

Networks of IDs, consisting of b-IDBs and p-IDBs, formed throughout most grains in

$Zn_{0.89}Mn_{0.1}Al_{0.01}O$. The average b-IDB spacing along the *c*-axis is ~50 nm, thus IDB formation is expected to exert a stronger influence on the electrical conductivity than the presence of spinel precipitates or grain boundaries, which are spaced at intervals ranging from several μm to tens of μm, significantly larger than the electron mean free path and, thus, resulting in less electron scattering. The combination of substitutional Mn^{2+} dopants and a high density of IDB interfaces in $Zn_{0.89}Mn_{0.1}Al_{0.01}O$ causes significant electron scattering, resulting in the lowest σ values measured for all $Zn_{0.99-x}Mn_xAl_{0.01}O$ samples. IDB interfaces can act as potential barriers, influencing electron transport and contributing to the activated character of σ with respect to temperature [15]. Indeed, $Zn_{0.89}Mn_{0.1}Al_{0.01}O$ clearly exhibits the most strongly activated conductivity. Variation in the electrical conductivity values observed in ZnO systems containing IDBs, e.g. $In_2O_3(ZnO)_n$ [16] and $Ga_2O_3(ZnO)_n$ [17], indicates that the transparency of the ID networks to electron transport may be dependent on the type of dopant occupying the IDB interfaces [15]. Thus, by controlling both the type and fractional occupancy of the dopants substituting at the IDB interfaces, it may be possible to modify the electronic potential energy barrier height at the IDB interfaces, in order to optimize the value of σ.

Sn-Al Co-Doped ZnO

The values of σ measured from 50°C to 730°C for $Zn_{0.99}Al_{0.01}O$, $Zn_{0.99}Sn_{0.01}O$ and $Zn_{0.98}Sn_{0.01}Al_{0.0}1O$ are shown in Fig. 6.3. $Zn_{0.99}Al_{0.01}O$ exhibits the highest σ values due to the significant increase in carrier density caused by Al doping [3,4]. The σ values of $Zn_{0.99}Sn_{0.01}O$ and $Zn_{0.98}Sn_{0.01}Al_{0.01}O$ are lower than $Zn_{0.99}Al_{0.01}O$ over the measured temperature range. Sn^{4+} can act as a donor dopant in ZnO by substituting on the Zn sublattice [18]. However, the solubility limit of Sn in ZnO (< 0.1 at. % [19]) is lower than that of Al (~0.3 at. % [20]), resulting in a smaller increase in the carrier density in the case of Sn doping. As discussed in Chapter 4, extensive IDB formation was observed in $Zn_{0.98}Sn_{0.01}Al_{0.01}O$. This accounts for the reduction in σ in comparison to $Zn_{0.99}Al_{0.01}O$. Although the average IDB spacing along the *c*-

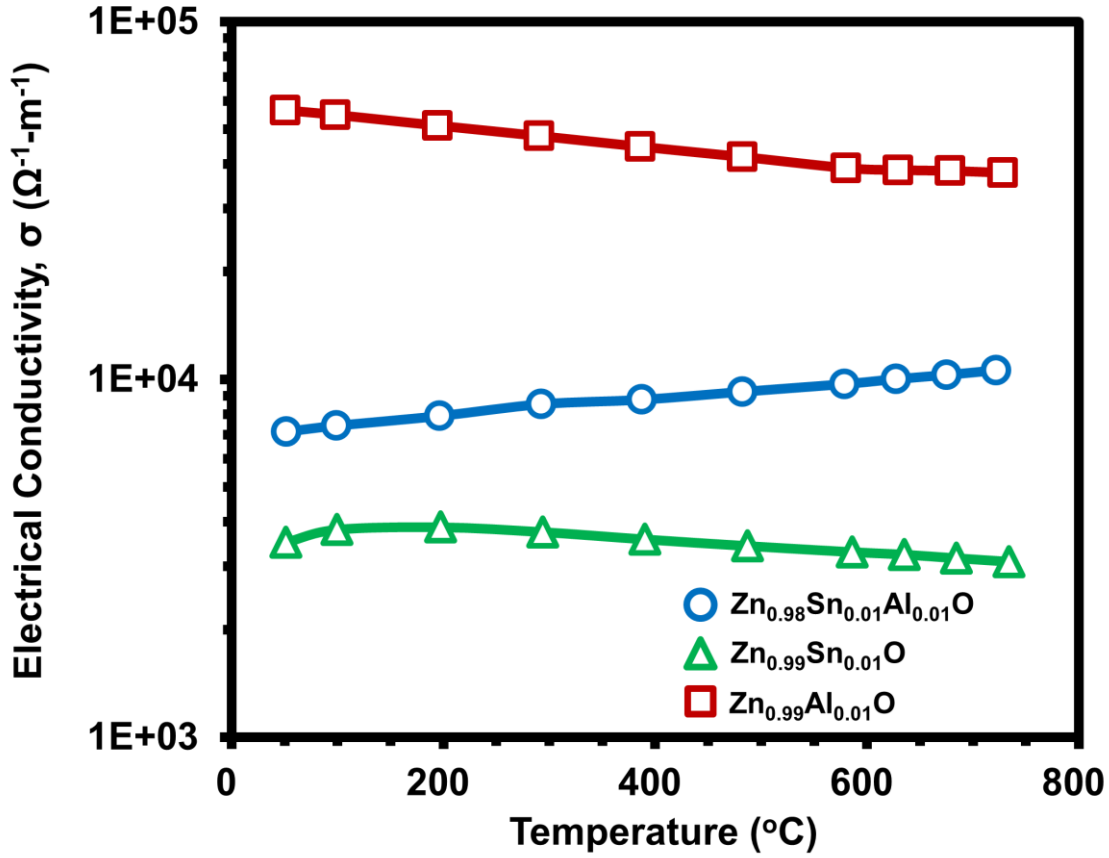

Figure 6.3. Plot of the electrical conductivity measured from RT to 730°C for $Zn_{0.98}Sn_{0.01}Al_{0.01}O$ (●), $Zn_{0.99}Sn_{0.01}O$ (▲) and $Zn_{0.99}Al_{0.01}O$ (■).

axis in $Zn_{0.98}Sn_{0.01}Al_{0.01}O$ is ~15 nm, smaller than the value of ~50 nm in $Zn_{0.89}Mn_{0.1}Al_{0.01}O$, the σ values of $Zn_{0.98}Sn_{0.01}Al_{0.01}O$ are considerably higher. This suggests that alloy scattering due to the substitution of Mn^{2+} on the Zn sublattice contributes significantly to the reduction of σ. This makes sense because the grain size of $Zn_{0.98}Sn_{0.01}Al_{0.01}O$ is smaller than $Zn_{0.89}Mn_{0.1}Al_{0.01}O$ and the volume fraction of the spinel phases in $Zn_{0.89}Mn_{0.1}Al_{0.01}O$ is low. At higher concentrations of Sn or Al, i.e. in $Sn_xAl_yO_3(ZnO)_n$ compounds, an optimum σ value could be achieved due to increased carrier transport isotropy, as observed in the $In_2O_3(ZnO)_n$ homologous phase compounds [16,21].

6.3.2 Seebeck Coefficient, S

Mn-Al Co-Doped ZnO

The values of the Seebeck coefficient for $Zn_{0.99-x}Mn_xAl_{0.01}O$ samples, measured over the temperature range from 50°C to 730°C, are shown in Fig. 6.4. All Seebeck coefficient values are negative, indicating that the samples are n-type semiconductors. The absolute value of the Seebeck coefficient, **|S|**, is known to exhibit an inverse relationship with respect to the carrier density, n, scaling as $S \propto n^{-2/3}$ [22]. Thus, because Al doping of ZnO results in a significant increase of the carrier density, **|S|** is significantly reduced in comparison to undoped ZnO. As the concentration of Mn increases, there is little change in the value of **|S|** throughout the measured temperature range. Because Mn^{2+}, which is isovalent with Zn^{2+},

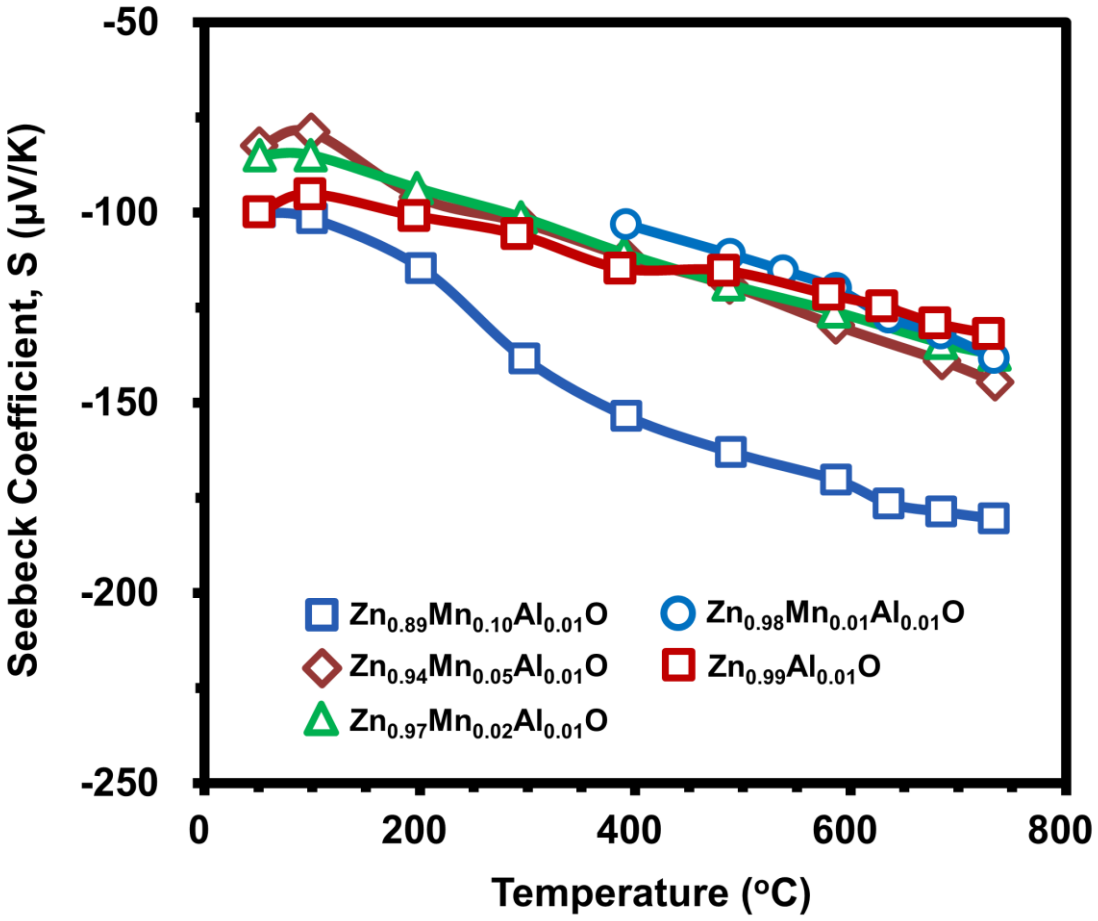

Figure 6.4. Plot of the Seebeck coefficient measured from RT to 730°C for $Zn_{0.99-x}Mn_xAl_{0.01}O$ samples.

substitutes on the Zn sublattice [6], there is expected to be little change in the carrier density. Previous studies have found that the Seebeck coefficient increases when ZnO is doped with Mn, due to spin polarization caused by the Mn *d* states and a shift of the Fermi level downward in energy toward the localized Mn^{2+} mid-gap states [7,8]. However, these effects do not appear to be significant at low ($\leq$ 5 at. %) Mn doping levels in Al-doped ZnO. At a high Mn concentration of 10 at. %, there is a larger increase in $|\mathbf{S}|$ observed throughout the entire temperature range. The extensive ID networks that form in $Zn_{0.89}Mn_{0.1}Al_{0.01}O$ could result in an increase of the Seebeck coefficient. Possible sources for the increase in $|\mathbf{S}|$ include: 1) electron filtering at electronic potential energy barriers that may form at the IDB interfaces, resulting in an asymmetry of the DOS near the Fermi level [23,24], 2) quantum confinement at IDB interfaces [25,26], which could arise due to the local zinc-blende cation stacking sequence at the b-IDB [27], or 3) an increase of the DOS near the Fermi level due to localized transition metal (TM) *d* states at IDB interfaces [26].

Sn-Al Co-Doped ZnO

The values of the Seebeck coefficient measured from 50°C to 730°C for $Zn_{0.99}Al_{0.01}O$, $Zn_{0.99}Sn_{0.01}O$ and $Zn_{0.98}Sn_{0.01}Al_{0.01}O$ are shown in Fig. 6.5. All values are negative, indicating an n-type semiconducting character. In comparison to the $|\mathbf{S}|$ values of $Zn_{0.99}Al_{0.01}O$, the $|\mathbf{S}|$ values of $Zn_{0.99}Sn_{0.01}O$ are considerably larger throughout the measured temperature range, although lower than reported for undoped ZnO [4]. This is due to the higher carrier density of $Zn_{0.99}Al_{0.01}O$ in comparison to $Zn_{0.99}Sn_{0.01}O$, which is a result of the higher solubility of Al in ZnO. In $Zn_{0.98}Sn_{0.01}Al_{0.01}O$, $|\mathbf{S}|$ is increased in comparison to $Zn_{0.99}Al_{0.01}O$. This is attributed to the formation of ID networks with a high density of IDB interfaces, which may cause increased electron filtering [23,24] or quantum confinement [25,26] at IDB interfaces, leading to increases in $|\mathbf{S}|$. A significant increase of the Seebeck coefficient, in comparison to In-doped ZnO, has been observed in In-Al co-doped ZnO [15]. The increase may be due to a modification

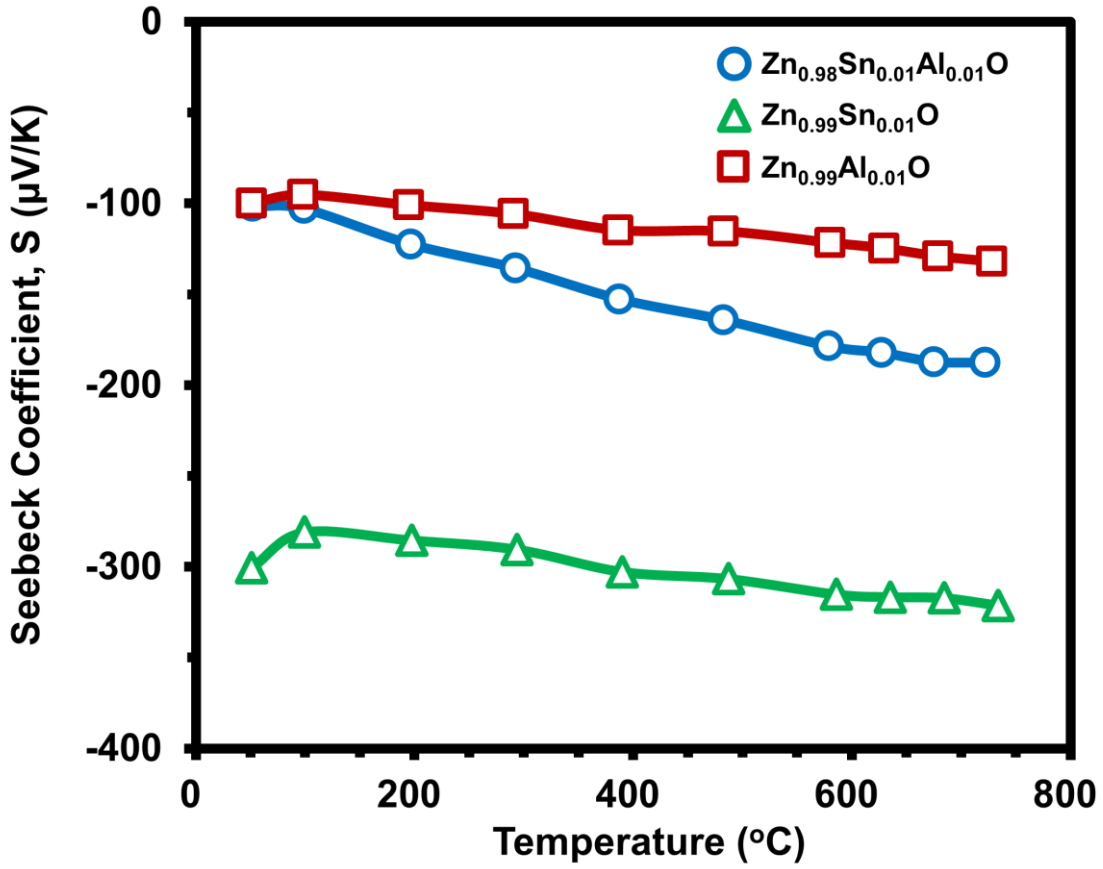

Figure 6.5 Plot of the Seebeck coefficient measured from RT to 730ºC for $Zn_{0.98}Sn_{0.01}Al_{0.01}O$ (●), $Zn_{0.99}Sn_{0.01}O$ (▲) and $Zn_{0.99}Al_{0.01}O$ (■).

of the IDB electronic potential energy barrier height, due to the substitution of In by Al at IDB sites [15]. This modification has been suggested to increase electron filtering, resulting in increases in $|\mathbf{S}|$. Thus, by controlling the type and also the fractional occupancy of different dopants within the b-IDB and/or p-IDB sites, it may be possible to tune the IDB electronic potential energy barrier height, in order to optimize both $|\mathbf{S}|$ and σ.

6.3.3 Power Factor, σS^2

The power factor, σS^2, of $Zn_{0.99-x}Mn_xAl_{0.01}O$ samples, measured within the temperature range from 50°C to 730°C, is shown in Fig. 6.6. As the concentration of Mn increases, the power factor is reduced as a result of the decrease of σ caused by increasing electron scattering due to Mn^{2+} points defects and, at the doping level of 10 at. % Mn, a high

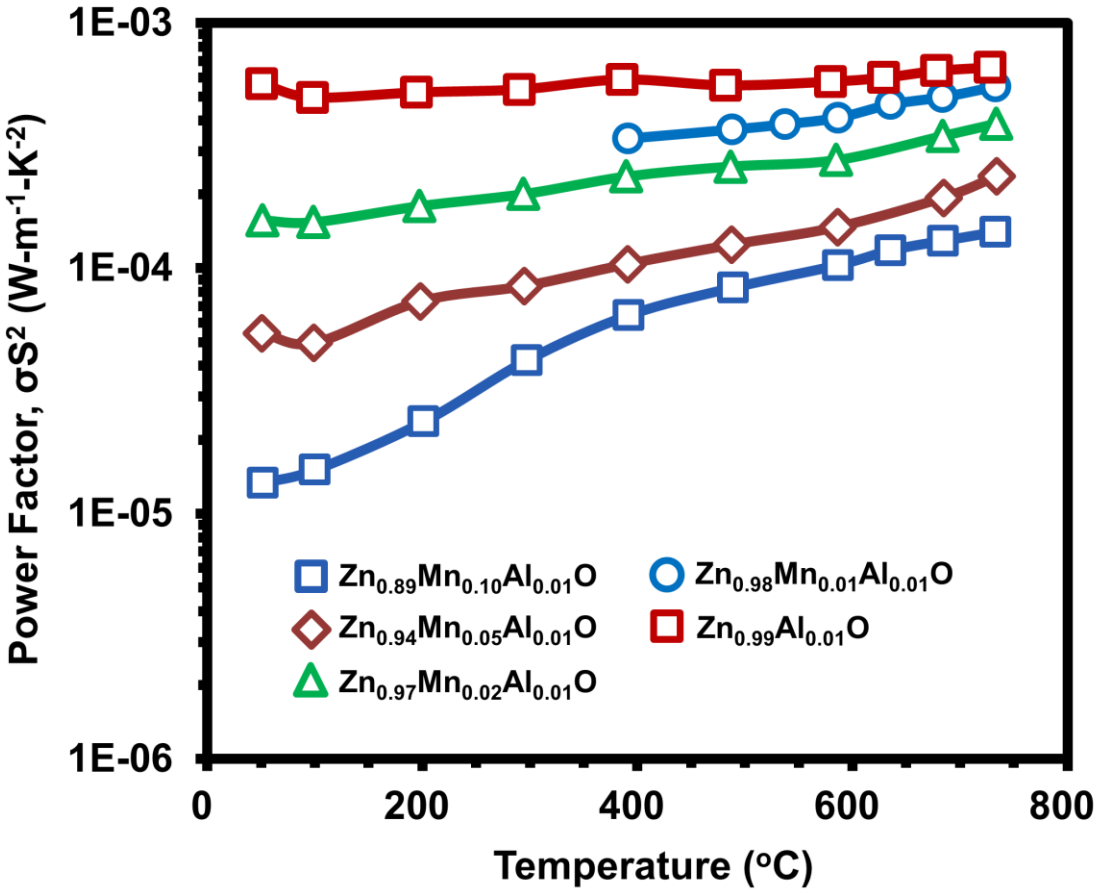

Figure 6.6. Plot of the Power Factor (σS^2) measured from RT to 730°C for $Zn_{0.99-x}Mn_xAl_{0.01}O$ samples.

density of IDB interfaces. The power factor values measured from RT to 730°C for $Zn_{0.99}Al_{0.01}O$, $Zn_{0.99}Sn_{0.01}O$ and $Zn_{0.98}Sn_{0.01}Al_{0.01}O$ are shown in Fig. 6.7. $Zn_{0.99}Al_{0.01}O$ exhibits the highest values of the power factor, which are in agreement with those previously reported for 1 at. % Al doped ZnO ceramics sintered under similar conditions [4]. The values of the power factor for $Zn_{0.99}Sn_{0.01}O$ are lower than those of $Zn_{0.99}Al_{0.01}O$, but also somewhat lower than previously reported for $Zn_{0.99}Sn_{0.01}O$ ceramics (PF = 1.2E-3 W/(m-K^2) at ~750°C [18]). This discrepancy may be attributed to differences in the oxide powders or sample preparation methods used during synthesis. The power factor of $Zn_{0.98}Sn_{0.01}Al_{0.01}O$ is lower than $Zn_{0.99}Al_{0.01}O$, due to increased electron scattering at IDB interfaces, which causes the reduction of σ. However, it is possible that, at higher concentrations of Sn and/or Al, σ, $|\mathbf{S}|$ and, correspondingly, σS^2 could be increased by reducing the b-IDB spacing along the *c*-axis, as

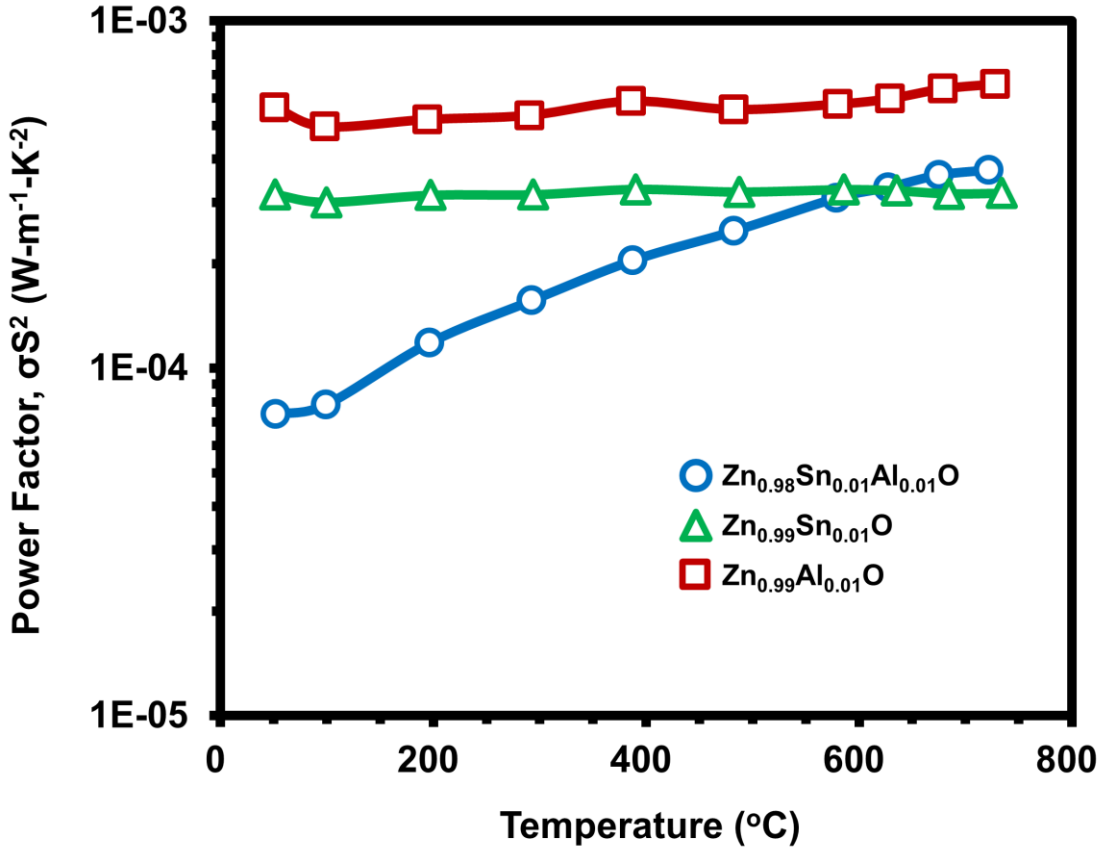

Figure 6.7. Plot of the Power Factor (σS^2) measured from RT to 730°C for $Zn_{0.98}Sn_{0.01}Al_{0.01}O$ (●), $Zn_{0.99}Sn_{0.01}O$ (▲) and $Zn_{0.99}Al_{0.01}O$ (■).

has been observed to occur in the $In_2O_3(ZnO)_n$ homologous phase compounds at specific values of n (e.g. n = 4 in $In_2O_3(ZnO)_n$ [16]). This optimization is due to a reversal of the trend of decreasing σ with decreasing b-IDB spacing at the point where the b-IDB spacing becomes sufficiently small that increases in the carrier transport isotropy occur, causing σ to increase [16,21]. Additionally, even at somewhat small values of n (e.g. n = 4-5 [16]), it should be possible to maintain sufficiently large values of $|\mathbf{S}|$, e.g. due to significant carrier filtering at the IDB interfaces [15,16,23,24], allowing the power factor to be maximized.

6.3.4 Thermal Conductivity, κ

Mn-Al Co-Doped ZnO

The thermal conductivity, κ, of $Zn_{0.99-x}Mn_xAl_{0.01}O$ samples, measured from RT to 750°C, is shown in Fig. 6.8. As the concentration of Mn increases, a drop in the thermal conductivity is observed over the entire temperature range. κ values also become less strongly dependent on temperature as the concentration of Mn increases. The thermal conductivity can be described generally according to the following expression:

$$\kappa = \frac{k_B}{2\pi^2 v_s}\left(\frac{k_B T}{\hbar}\right)^3 \int_0^{\frac{\theta_D}{T}} \tau_c(x) \frac{x^4 e^x}{(e^x-1)^2} dx, \quad \text{eqn. 6.1} \quad [28]$$

where T is the temperature, v_s is the speed of sound, $\hbar$ is Planck's constant divided by 2π, θ_D is the Debye temperature, τ_c is the total relaxation time for all phonon scattering processes and x is defined as: $x = (\hbar\omega)/(k_B T)$, where ω is the phonon frequency [28]. The inverse of the total relaxation time can be expressed as the sum of several terms according to the following equation:

$$\tau_c^{-1} = \tau_P^{-1} + \tau_D^{-1} + \tau_B^{-1}, \quad \text{eqn. 6.2} \quad [28]$$

where τ_P^{-1}, τ_D^{-1} and τ_B^{-1} are the inverses of the relaxation times due to phonon-phonon scattering, the scattering of phonons by point defects and the scattering of phonons by boundaries respectively [28]. The solubility limit of Mn in ZnO is rather high (~3-8 at. % [10-12]); thus, for the samples containing Mn concentrations $\leq$ 5 at. % that were studied in this work, the τ_D^{-1} term due to scattering by Mn substitutional point defects will be significant. τ_D^{-1} generally takes the form: $\tau_D^{-1} = A\omega^4$, where A is the defect scattering coefficient, expressed as: $A = \Omega_0\Gamma/(4\pi v_s^3)$ [28]. Ω_0 is the unit cell volume and Γ is the scattering parameter, which describes the strength that a specific type of point defect has to scatter phonons [28]. Γ can be written generally as:

$$\Gamma_i = x_i\left[\left(\frac{M_i - \bar{M}}{\bar{M}}\right)^2 + \varepsilon\left(\frac{\delta_i - \bar{\delta}}{\bar{\delta}}\right)^2\right], \quad \text{eqn. 6.3} \quad [29]$$

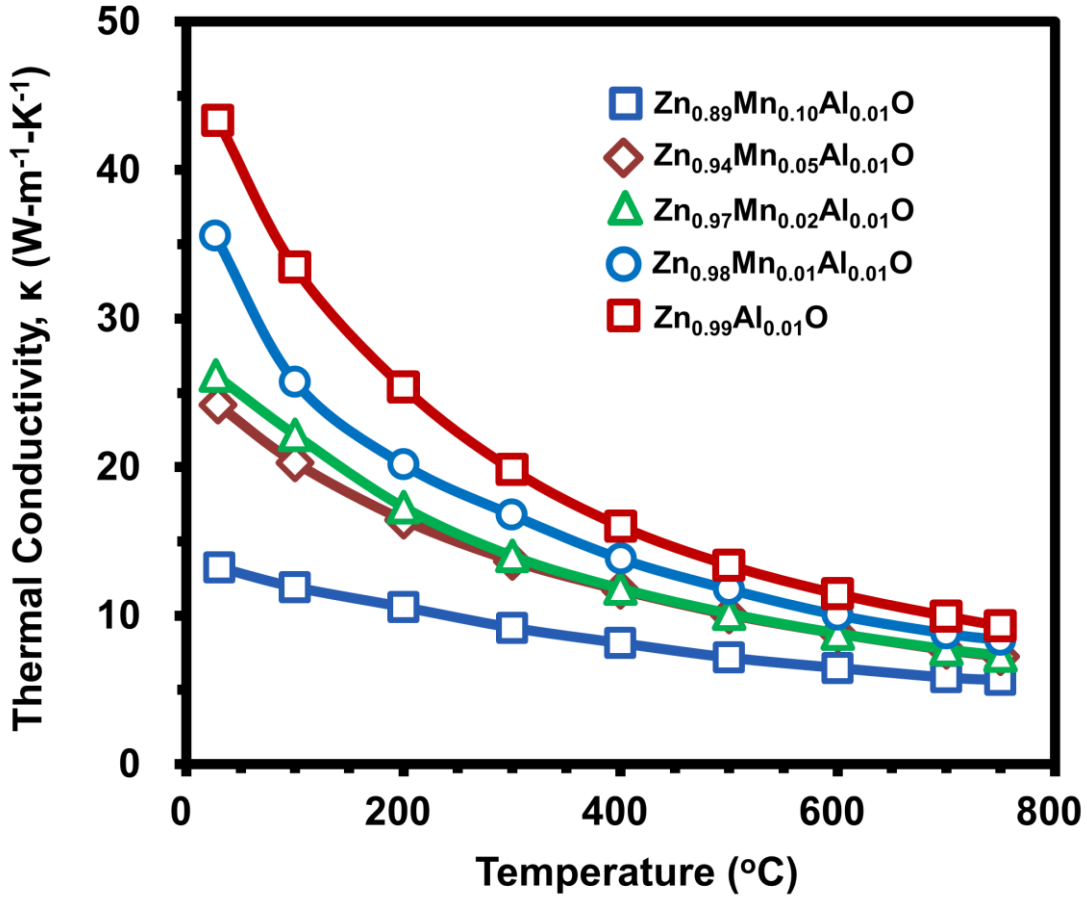

Figure 6.8. Plot of the thermal conductivity measured from RT to 750°C for $Zn_{0.99-x}Mn_xAl_{0.01}O$ samples.

where x_i is the concentration of a specific type of impurity or defect, M_i is the impurity or defect mass, $\bar{M}$ is the average mass of all atoms in the solid, ε is a parameter describing size misfit, δ_i is the size of the defect and $\bar{\delta}$ is the average size of all atoms in the solid [29]. The complete expression for the contribution to Γ due to the mass contrast caused by Mn substitution on the Zn sublattice is expressed as:

$$\Gamma = \frac{1}{2}x\left[\frac{M_{Mn} - \overline{M_{Zn}}}{\bar{M}}\right]^2, \qquad \text{eqn. 6.4} \quad [29]$$

where M_{Mn} is the mass of Mn and $\overline{M_{Zn}}$ is the average mass of the atoms (and vacancies) composing the Zn sublattice [29]. A plot of the κ (T = 300 K) and Γ gamma values determined using the above equation for Mn concentrations up to 10 at. % is shown in Fig. 6.9. An additional term for Al doping is included, in order to take into account the substitution of up to

0.3 at. % Al on the Zn sublattice [20]. An inverse relationship between κ and Γ is observed, indicating that increasing phonon scattering due to impurities leads to an increasing reduction in κ as the concentration of Mn increases.

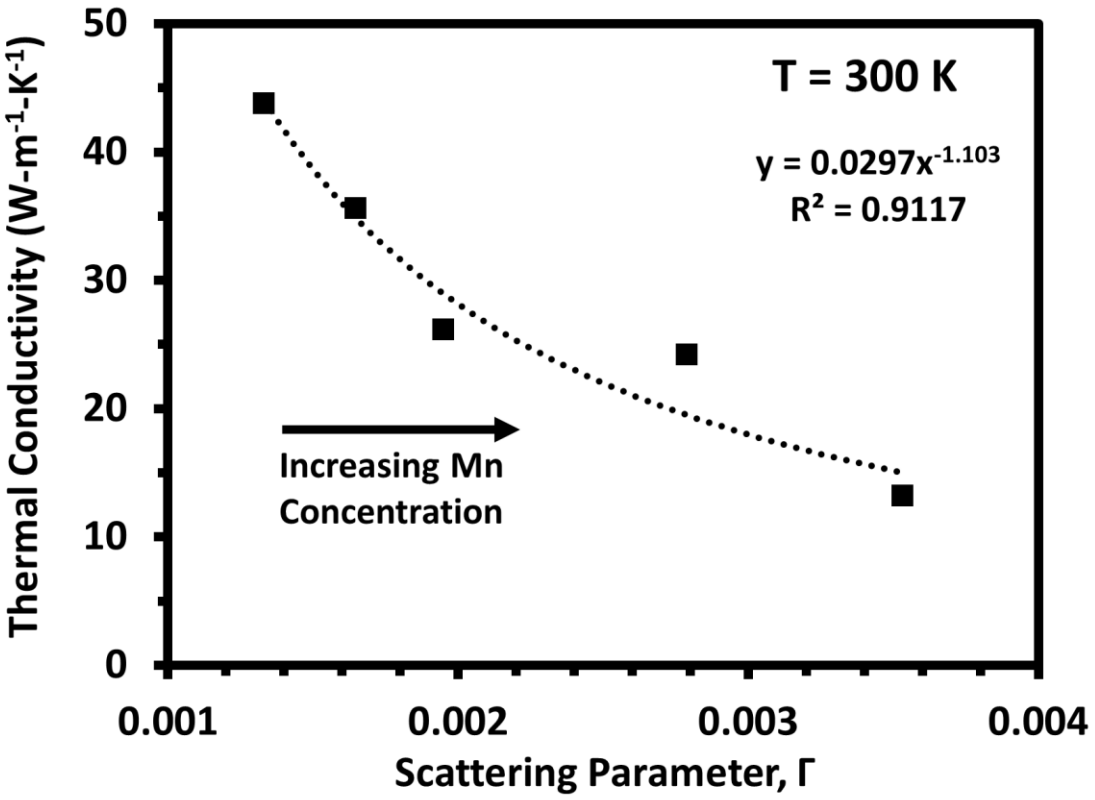

Figure 6.9. Plot of the thermal conductivity values for $Zn_{0.99-x}Mn_xAl_{0.01}O$ samples measured at RT vs. the scattering parameter, Γ. An inverse relationship is observed.

At a high Mn concentration of 10 at. %, in $Zn_{0.89}Mn_{0.1}Al_{0.01}O$, the solubility limit of Mn in bulk ZnO is exceeded, resulting in ID network formation. The formation of the ID networks in $Zn_{0.89}Mn_{0.1}Al_{0.01}O$, discussed in Chapter 3, should result in increased phonon scattering due to the high density of IDB interfaces [15-17,30,31]. Thus, the term τ_B^{-1}, representing grain boundary or interface scattering, will become significant. Indeed, by observing the trend of decreasing κ values that occurs as the concentration of Mn increases, as shown in Fig. 6.9, it appears that an additional drop in the thermal conductivity which cannot be accounted for by considering only point defect scattering occurs between the Mn doping levels of 5 and 10 at. %. The additional phonon scattering due to IDB interfaces in

$Zn_{0.89}Mn_{0.1}Al_{0.01}O$ thus appears to result in a significant decrease of κ beyond that due to point defect scattering. This effect is particularly pronounced at RT, as observed in Fig. 6.8, and the κ values of $Zn_{0.89}Mn_{0.10}Al_{0.01}O$ exhibit the weakest dependence on temperature, due to the combined influence of both point defects and IDBs on phonon scattering. As the temperature increases, the difference in the κ values for samples with different Mn concentrations becomes less significant, as a result of the increasing impact of phonon-phonon scattering on the thermal conductivity [32]. Although spinel precipitates are observed in $Zn_{0.89}Mn_{0.10}Al_{0.01}O$, they likely have a minimal impact on κ in comparison to IDBs, since the size of the spinel precipitates (~2 μm) is considerably greater than the b-IDB spacing of ~50 nm along the *c*-axis and the volume fraction of the spinel precipitates is low, based on the results of XRD, SEM and TEM analysis, described in Chapter 3.

Sn-Al Co-Doped ZnO

The κ values of $Zn_{0.99}Al_{0.01}O$, $Zn_{0.99}Sn_{0.01}O$ and $Zn_{0.98}Sn_{0.01}Al_{0.01}O$, measured from RT to 750°C, are shown in Fig. 6.10. The κ values of $Zn_{0.99}Al_{0.01}O$ are in general agreement with those previously reported for ZnO doped with 1 at. % Al and sintered under similar conditions [4]. There is not a significant difference between the thermal conductivities of $Zn_{0.99}Al_{0.01}O$ and $Zn_{0.99}Sn_{0.01}O$ due to the fact that: 1) the solubility limits of Al and Sn in ZnO are both low, resulting in minimal scattering of phonons due to point defects, 2) the average grain sizes of $Zn_{0.99}Al_{0.01}O$ and $Zn_{0.99}Sn_{0.01}O$ differ only by a factor of ~2 and 3) the volume fractions and average sizes of the $ZnAl_2O_4$ and Zn_2SnO_4 spinel precipitates are similar in their respective samples (see Table 4.1). In contrast to $Zn_{0.99}Al_{0.01}O$ and $Zn_{0.99}Sn_{0.01}O$, the thermal conductivity of $Zn_{0.98}Sn_{0.01}Al_{0.01}O$ is significantly reduced over the entire temperature range, with the κ values of $Zn_{0.98}Sn_{0.01}Al_{0.01}O$ exhibiting a weaker dependence on temperature than the other samples from RT to 750°C. This is primarily attributed to the high density of b-IDB and p-IDB interfaces in $Zn_{0.98}Sn_{0.01}Al_{0.01}O$, since the grain sizes of

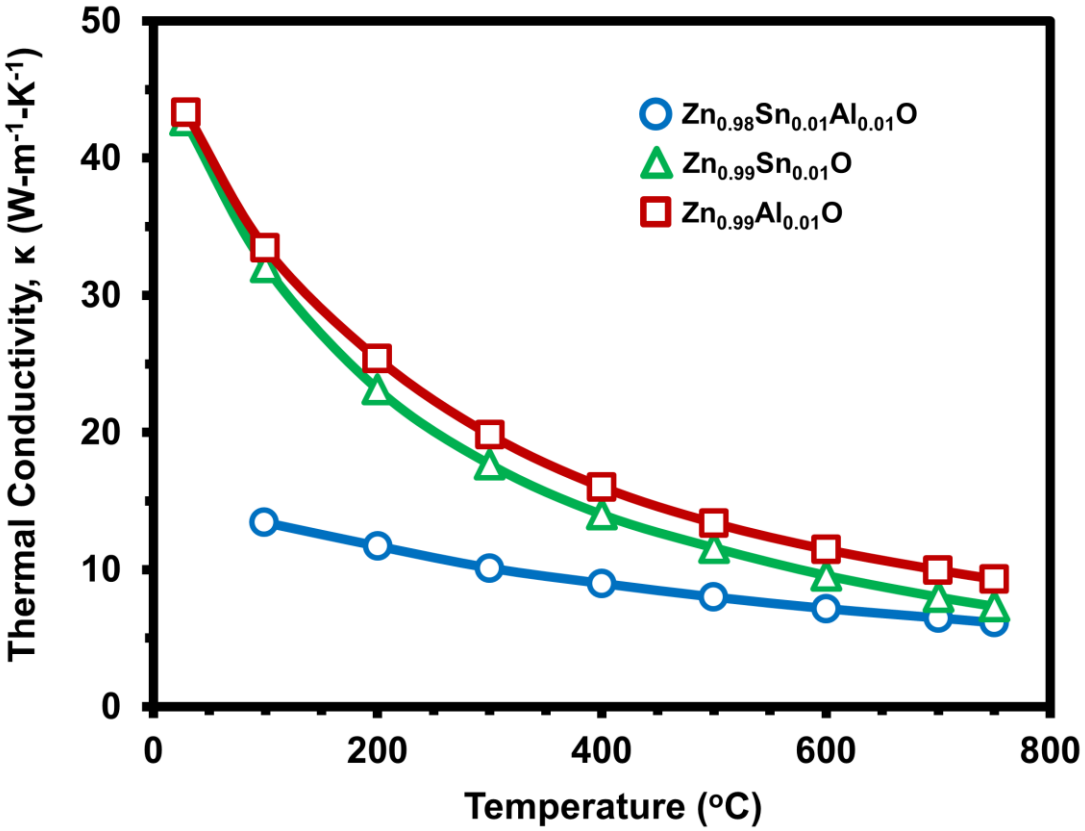

Figure 6.10. Plot of the thermal conductivity measured from RT to 750°C for $Zn_{0.98}Sn_{0.01}Al_{0.01}O$ (●), $Zn_{0.99}Sn_{0.01}O$ (▲) and $Zn_{0.99}Al_{0.01}O$ (■).

$Zn_{0.99}Sn_{0.01}O$ and $Zn_{0.98}Sn_{0.01}Al_{0.01}O$ differ only by a factor of ~2 and spinel precipitates do not form in $Zn_{0.98}Sn_{0.01}Al_{0.01}O$. The small b-IDB spacing along the *c*-axis (~15 nm) in $Zn_{0.98}Sn_{0.01}Al_{0.01}O$ should also result in increased boundary scattering of phonons in comparison to $Zn_{0.89}Mn_{0.1}Al_{0.01}O$ (b-IDB spacing: ~50 nm). However, the additional contribution to the reduction of κ, due to point defect scattering caused by Mn^{2+} substitution on the Zn sublattice, likely results in the similar κ values observed for $Zn_{0.98}Sn_{0.01}Al_{0.01}O$ and $Zn_{0.89}Mn_{0.1}Al_{0.01}O$.

Networks consisting of two types of IDBs: b-IDBs and p-IDBs, form in both $Zn_{0.89}Mn_{0.1}Al_{0.01}O$ and $Zn_{0.98}Sn_{0.01}Al_{0.01}O$. Since the b-IDBs and p-IDBs have different *c*-axis cation stacking sequences, contain dopants at different densities and are occupied by different types of cations, they likely exert a different degree of influence on the scattering of phonons. Previous studies of Fe-doped ZnO have found that the b-IDB consists of a complete monolayer

of Fe, while the p-IDB has an Fe occupancy of ~2/3 [33]. The b-IDB is also considered to be the favorable site for accommodating larger dopants (e.g. In and Sn), in comparison to the p-IDB which is the favorable site for accommodating smaller dopants (e.g. Fe and Al) [34,35], particularly in systems containing multiple IDB-forming dopants. Larger dopants such as In and Sn that can stably occupy the b-IDB are also heavier than the smaller dopants (e.g. Fe or Al) that prefer to occupy the p-IDB. Heavy dopants are known to scatter phonons effectively [22,36]. b-IDBs should, thus, be able to accommodate larger dopants at higher densities and, based on HAADF/ABF-STEM observations (e.g. Fig. 4.7), appear to form a sharper discontinuity in the ZnO lattice than the p-IDBs. Consequently, b-IDBs may scatter phonons more effectively than p-IDBs. Both b-IDBs and p-IDBs have been found to accomodate co-occupation by several different types of dopants (e.g. In/Fe co-doped b-IDBs [35], Sb/Zn co-doped b-IDBs [37], Mn/Al co-doped b-IDBs (Chapter 3), Sb/Bi co-doped b-IDBs [38], Sn/Al co-doped p-IDBs (Chapter 4) and In/Ga co-doped p-IDBs [31]). Depending on the extent of intermixing, the degree of phonon scattering at the b-IDBs and/or p-IDBs could be increased via the co-occupation of the IDB sites by multiple dopants, which could result in increased disorder and mass contrast at the IDB interfaces, leading to thermal conductivity reduction [15].

6.3.5 Thermoelectric Figure of Merit, ZT
Mn-Al Co-Doped ZnO

The thermoelectric figure of merit, ZT ($Z = \sigma S^2/\kappa$, T: temperature), calculated using the σ, S and κ values measured from 50°C to 730°C (σ and S) and RT to 750°C (κ) for the $Zn_{0.99-x}Mn_xAl_{0.01}O$ samples, is shown in Fig. 6.11. As the temperature increases, the ZT values of all samples increase. Also, as the concentration of Mn increases, a decrease in the ZT values is observed. Although $|\mathbf{S}|$ either remains approximately constant or increases and κ is reduced as the concentration of Mn increases, ZT is ultimately reduced due to decreasing σ values. The specific influence of several different dopants with high solubility limits in ZnO (e.g. Mn [10-

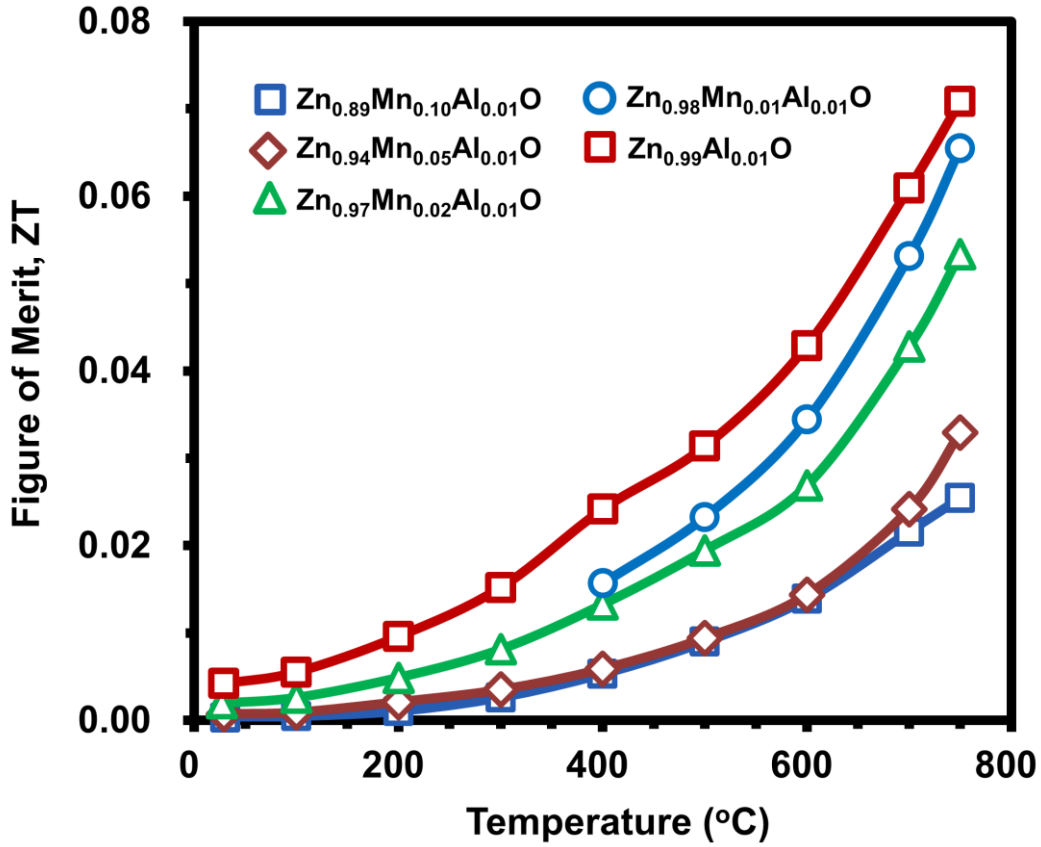

Figure 6.11. Plot of the Figure of Merit (ZT) determined using thermoelectric parameter measurements from RT to ~750°C for $Zn_{0.99-x}Mn_xAl_{0.01}O$ samples.

12], Mg [39]) on the thermoelectric properties of ZnO has been investigated both in this thesis and in previous works [39]; however, an increase of ZT due to the reduction of κ caused by the alloying of ZnO has not been observed. This contrasts with the behavior of some systems (e.g. $Si_{1-x}Ge_x$ [40]) in which alloying has been demonstrated to result in the improvement of ZT. According to equation 6.3, the scattering parameter, Γ, is linearly proportional to the impurity concentration and proportional to the square of the mass contrast between the impurity element and the matrix element for which it substitutes. Thus, in order to improve ZT, it is best to choose an alloying element with a high solubility limit and a large mass contrast. Alternatively, dopants with a large size mismatch could also be beneficial for reducing κ in order to increase ZT. However, a large size misfit may result in a low solubility limit. The $Si_{1-x}Ge_x$ systems exhibits a complete solid solubility between Si and Ge [41] and the mass contrast of Si and Ge is ~61 %. In contrast, the solubility limit of Mn in ZnO is between 3 and 8 at. % [10-12] and the mass

contrast of Mn and Zn is ~16 %. Thus, κ reduction will not be as significant as in the $Si_{1-x}Ge_x$ system. However, in comparison to $Zn_{0.99}Al_{0.01}O$, a 40 % reduction in κ is observed at RT for a doping level of 2 at. % Mn (see Fig. 6.8), indicating that a substantial reduction of κ is achieved by alloying ZnO with Mn.

There is a tradeoff between the reduction of κ and the reduction of σ associated with solid solution alloying of thermoelectric materials [40]. Thus, in addition to the importance of choosing a dopant with a high solubility limit in the host lattice and a large mass contrast with the matrix element to be substituted for, the influence of the dopant on alloy scattering, which can result in σ reduction, must also be considered. The difference in the electronegativity, U, between Mn and Zn is small [42], indicating that the reduction of σ due to Mn alloying of ZnO may be minimal. However, a significant decrease in σ occurs as the Mn concentration increases, indicating that the difference in the U values of Mn and Zn is not insignificant enough to acheive ZT increase simply via the reduction of κ by point defect scattering. Other dopants with U values similar to Zn, as well as a high solubility limit in ZnO and a large mass contrast with Zn could potentially result in ZT increase through κ reduction by point defect scattering. However, given the limited number of dopants with a solubility limit exceeding even 5 at. % in ZnO (e.g. Mn [10-12], Mg [39] and Co [43]), the prospects for increasing the ZT values of ZnO through solid solution alloying could be limited.

Alternatively, nanostructuring, for example via the formation of defects such as IDBs, may be a more promising pathway to acheiving significant increases in the ZT values of ZnO. Although the ZT values of $Zn_{0.89}Mn_{0.1}Al_{0.01}O$ are the lowest among all the $Zn_{0.99-x}Mn_xAl_{0.01}O$ samples studied, due to significant σ reduction caused by the combination of alloy scattering of electrons by Mn point defects and interface scattering of electrons by IDBs, the thermoelectric properties of other systems containing IDBs, e.g. $In_2O_3(ZnO)_n$ [16], have been investigated systematically and it was found that at specific values of *n*, both the power factor and ZT values can be optimized. Optimization occurs at low values of *n* (e.g. *n* = 4 [16]) and

has been determined to be a consequence of the increasing isotropy of the carrier transport that occurs as the b-IDB spacing is reduced and the fraction of the In_2O_3 b-IDB layers increases [21]. The increase in carrier transport isotropy is accompanied by a significant reduction in κ due to a high density of IDB interfaces and an increase of the Seebeck coefficient, possibly due to significant electron filtering, also caused by the formation of dense ID networks [15,23,24]. Thus, at higher concentrations of Mn or Al, i.e. in other $Mn_xAl_yO_3(ZnO)_n$ compounds, the ZT values could be improved and even surpass the values obtained for $Zn_{0.99}Al_{0.01}O$, as a consequence of the combination of a low κ, high $|\mathbf{S}|$ and improved values of σ due to the increased carrier isotropy at small values of *n*. Additional modifications of the IDB interfaces could also be beneficial for improving ZT. As observed in In-Al co-doped ZnO [15] and In-Ga co-doped ZnO [31], the co-occupation of IDBs by different dopants leads to increased disorder and mass contrast at the IDB interfaces, which likely contributes to the reduction of κ. The co-doping of other homologous phase compounds, e.g. $In_2O_3(ZnO)_n$, with TM dopants (e.g. Mn, Ni or Ti) could also lead to improved ZT values due to increases in $|\mathbf{S}|$ caused by an increased DOS near the Fermi level, resulting from the formation of localized TM *d* states [26].

Sn-Al Co-Doped ZnO

The ZT values determined for $Zn_{0.99}Al_{0.01}O$, $Zn_{0.99}Sn_{0.01}O$ and $Zn_{0.98}Sn_{0.01}Al_{0.01}O$ are plotted in Fig. 6.12. $Zn_{0.99}Al_{0.01}O$ exhibits the highest values of ZT as a result of its high σ values. $Zn_{0.99}Sn_{0.01}O$ exhibits lower ZT values, likely due to decreased σ values caused by a lower carrier density relative to $Zn_{0.99}Al_{0.01}O$. The ZT values of $Zn_{0.98}Sn_{0.01}Al_{0.01}O$ are between those of $Zn_{0.99}Al_{0.01}O$ and $Zn_{0.99}Sn_{0.01}O$, though closer to $Zn_{0.99}Al_{0.01}O$ above 500°C, the primary temperature range of interest for the thermoelectric operation of ZnO. In contrast to $Zn_{0.99}Al_{0.01}O$ and $Zn_{0.99}Sn_{0.01}O$, spinel precipitates do not form in $Zn_{0.98}Sn_{0.01}Al_{0.01}O$. Instead, a dense network of IDs, consisting of b-IDBs and p-IDBs, with a b-IDB spacing of ~15 nm is observed. The ID networks significantly reduce κ due to phonon scattering at b-IDB and p-IDB

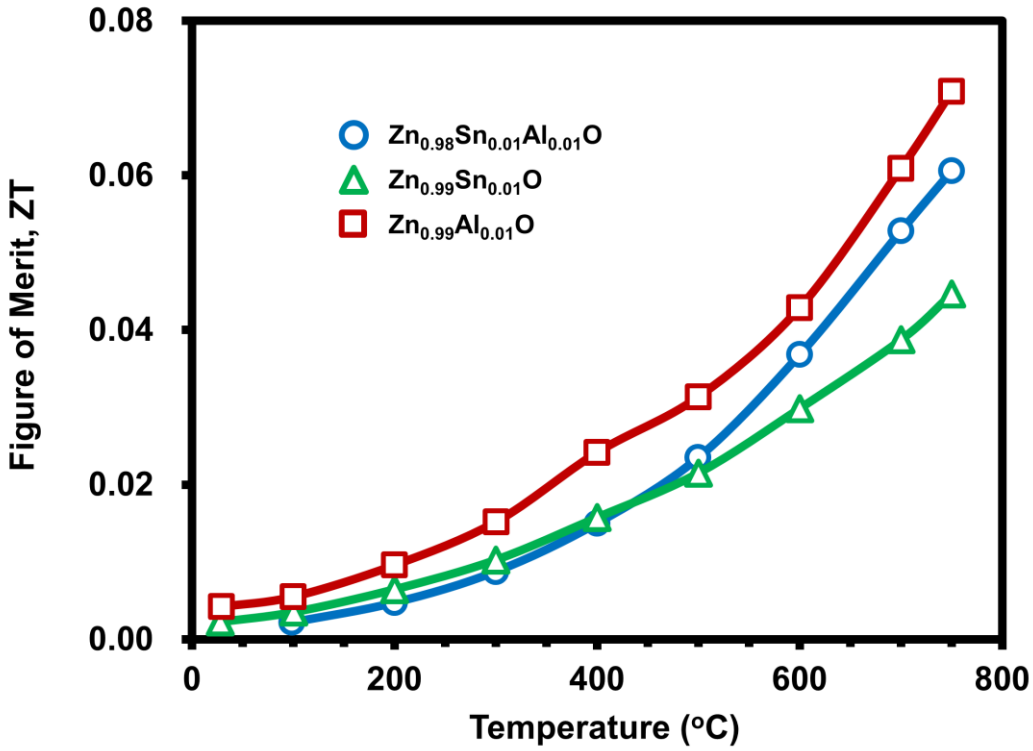

Figure 6.12. Plot of the Figure of Merit (ZT) determined using thermoelectric parameter measurements from RT to ~750°C for $Zn_{0.98}Sn_{0.01}Al_{0.01}O$ (●), $Zn_{0.99}Sn_{0.01}O$ (▲) and $Zn_{0.99}Al_{0.01}O$ (■).

interfaces. However, they also cause electron scattering, resulting in σ values reduced in comparison to $Zn_{0.99}Al_{0.01}O$. Despite the smaller b-IDB spacing of $Zn_{0.98}Sn_{0.01}Al_{0.01}O$ (~15 nm) relative to $Zn_{0.89}Mn_{0.1}Al_{0.01}O$ (~50 nm), the κ values of the two samples are similar. This is likely due to the high concentration of Mn point defects in $Zn_{0.89}Mn_{0.1}Al_{0.01}O$, which also contribute to the reduction of κ. However, the σ values of $Zn_{0.98}Sn_{0.01}Al_{0.01}O$ are higher than those of $Zn_{0.89}Mn_{0.1}Al_{0.01}O$. This indicates that the ID networks in $Zn_{0.98}Sn_{0.01}Al_{0.01}O$ cause less total electron scattering than the combination of both the Mn point defects and IDBs in $Zn_{0.89}Mn_{0.1}Al_{0.01}O$, despite the smaller b-IDB spacing in $Zn_{0.98}Sn_{0.01}Al_{0.01}O$. The smaller b-IDB spacing observed in $Zn_{0.98}Sn_{0.01}Al_{0.01}O$ indicates that a higher total dopant amount, likely very nearly 1 at. % Sn and 1 at. % Al, contributes to IDB formation in this sample, whereas in $Zn_{0.89}Mn_{0.1}Al_{0.01}O$ the spinel secondary phases appear to be able to accommodate a significant fraction of the total dopant content, supported by the appearance of spinel precipitates

exhibiting twinned bands, indicative of a significant Mn^{3+} content, at the doping level of 10 at. % Mn. This indicates that a lower total dopant amount may contribute to the formation of the ID networks in $Zn_{0.89}Mn_{0.1}Al_{0.01}O$, in comparison to $Zn_{0.98}Sn_{0.01}Al_{0.01}O$.

There is the potential for increasing the ZT values of $Sn_xAl_yO_3(ZnO)_n$ compounds at higher Sn or Al concentrations. As observed in the $In_2O_3(ZnO)_n$ homologous phases [16], the carrier transport isotropy of the $Sn_xAl_yO_3(ZnO)_n$ compounds could increase as the b-IDB spacing decreases and the fraction of the Sn and Al doped IDB layers increases [21]. The use of texturing has also been shown to significantly improve the thermoelectric performance of In-doped ZnO ceramics containing IDBs by increasing the in-plane electrical conductivity [44-46]. The introduction of texture in the $Sn_xAl_yO_3(ZnO)_n$ compounds could potentially result in a significant increase of the power factor, especially if a 2D electron gas (2DEG) is determined to form at the Sn-doped b-IDB interfaces. The shift of the Fermi level to the conduction band and the high density of Sn *s* states near the Fermi level observed in Fig. 5.5 suggest that 2DEG formation could occur at the Sn-doped b-IDB interface. 2DEG formation can increase σ and $|\mathbf{S}|$ simultaneously through the combined effects of 2D carrier density increase and carrier localization at the b-IDB [26]. Co-doping of the $In_2O_3(ZnO)_n$ homologous phases with Sn or Al could also improve the thermoelectric performance of these phases, since co-doping has been found to improve the ZT values of the $In_2O_3(ZnO)_n$ homologous phase compounds (e.g. In-Ga co-doped ZnO [31], In-Ca co-doped ZnO [45], In-Y co-doped ZnO [46,47] and In-M (M = Y, Mg or Co) co-doped ZnO [48]), due to the reduction of κ, likely caused by increased disorder and mass contrast at the IDB interfaces. Co-doping could also be useful for modifying the electronic potential energy barrier height at the IDB interfaces, in order to optimize carrier transport [15].

6.4 Conclusion

The thermoelectric properties of Mn-Al and Sn-Al dual-doped ZnO ceramics have been measured from RT to ~750℃. The addition of Al resulted in a significant increase of the carrier density of ZnO, increasing the electrical conductivity. As the concentration of Mn increased, the electrical conductivity decreased due to alloy scattering of electrons by Mn point defects. The increasing concentration of Mn point defects also caused thermal conductivity reduction due to phonon scattering. When the solubility limit of Mn in ZnO was exceeded (in $Zn_{0.89}Mn_{0.1}Al_{0.01}O$), IDBs formed. IDB formation caused an additional reduction of both the electrical and thermal conductivity due to the scattering of electrons and phonons at IDB interfaces. The Seebeck coefficient also increased in $Zn_{0.89}Mn_{0.1}Al_{0.01}O$, possibly due to effects occurring at IDB interfaces, including electron filtering, quantum confinement or an increased DOS near the Fermi level caused by localized Mn *d* states. In $Zn_{0.98}Sn_{0.01}Al_{0.01}O$, a smaller b-IDB spacing along the *c*-axis of ~15 nm, in comparison to ~50 nm in $Zn_{0.89}Mn_{0.1}Al_{0.01}O$, resulted in a similar thermal conductivity to $Zn_{0.89}Mn_{0.1}Al_{0.01}O$ likely because of the absence of Mn point effects, which also contribute to thermal conductivity reduction. The lack of Mn point defects also enabled a larger electrical conductivity in $Zn_{0.98}Sn_{0.01}Al_{0.01}O$, despite its smaller b-IDB spacing.

The ZT values obtained for the $Zn_{0.89}Mn_{0.1}Al_{0.01}O$ and $Zn_{0.98}Sn_{0.01}Al_{0.01}O$ ceramics containing IDBs are lower than the maximum values previously reported for In-doped ZnO [16], Ga-doped ZnO [30] and In-Ga co-doped ZnO [31] ceramics containing IDBs. By the investigation of other $Mn_xAl_yO_3(ZnO)_n$ and $Sn_xAl_yO_3(ZnO)_n$ ceramics with higher concentrations of Sn, Al and/or Mn, it may be possible to acheive higher ZT values, due to the potential increase in the carrier transport isotropy and reduction in the thermal conductivity which can occur when the b-IDB spacing is reduced sufficiently. Additionally, the modification of the IDB interfaces via co-doping with multiple dopants that can substitute at the IDB sites

should be beneficial for further optimizing the ZT values of $RMO_3(ZnO)_n$ compounds. This can be achieved by increased interface disorder and mass contrast due to the co-occupation of IDBs by different dopants, which can reduce the thermal conductivity, and by the modification of the IDB electronic potential energy barrier height, which can be optimized to improve carrier transport and increase the power factor, σS^2. Co-doping of other homologous phase systems such as $In_2O_3(ZnO)_n$ and $Ga_2O_3(ZnO)_n$ with heavy dopants (e.g. Sn), which are effective phonon scatterers, and TM dopants (e.g. Mn), which can introduce localized *d* states at IDB interfaces, thereby increasing the DOS, could also enable further optimization and improvement of the thermoelectric performance of these compounds. Investigations focusing on the identification of additional IDB-forming dopants and $RMO_3(ZnO)_n$ homologous phase compounds will be useful for the systematic optimization of bulk properties ranging from the thermoelectric properties, such as the electrical and thermal conductivity, to other properties such as the optical transmission or quantum efficiency, for LED applications. It should be possible to optimize the bulk properties not only by controlling the formation of specific nanoscale ID features (e.g. the b-IDB spacing and p-IDB angle) but also via the control of sub-nanometer features, for example by selecting specific dopant elements to occupy the b-IDB and/or p-IDB sites and by controlling the fractional occupancy of these IDB sites by one or more dopants.

6.5 References

[1] A. Seko, F. Oba, A. Kuwabara, and I. Tanaka, Phys. Rev. B, **72**, 024107 (2005)

[2] W.N. Lawless, and T.K. Gupta, J. Appl. Phys., **60**, 607 (1986)

[3] D. Berardan, C. Byl, and N. Dragoe, J. Am. Ceram. Soc., **93**, 2352 (2010)

[4] T. Tsubota, M. Ohtaki, K. Eguchi, and H. Arai, J. Mater. Chem., **7**, 8590 (1997)

[5] P.V. Chinta, O. Lozano, P.V. Wadekar, W.C. Hsieh, H.W. Seo, S.W. Yeh, C.H. Liao, L.W. Tu, N.J. Ho, Y.S. Zhang, and W.Y. Pang, J. Elect. Mater., **46**, 2030 (2017)

[6] H.K. Schmid, and W. Mader, Micron, **37**, 426 (2006)

[7] J. Han, P.Q. Mantas, and A.M.R Senos, J. Eur. Ceram. Soc., **21**, 1883 (2001)

[8] G.K. Ghosh, S. Das, and K.K. Chattopadhyay, Physica B, **399**, 38 (2007)

[9] C.A. Johnson, K.R. Kittilstved, T.C. Kaspar, T.C. Droubay, S.A. Chambers, G. Mackay Salley, and D.R. Gamelin, Phys. Rev. B, **82**, 115202 (2010)

[10] M. Kakazey, M. Vlasova, M. Dominguez-Patiño, J. Kliava, and T. Tomila, J. Am. Ceram. Soc., **89**, 1458 (2006)

[11] L. Nádherný, O. Jankovský, Z. Sofer, J. Leitner, C. Martin, and D. Sedmidubský, J. Eur. Ceram. Soc., **35**, 555 (2015)

[12] F.C.M. Driessens, and G.D. Rieck, J. Inorg. Nucl. Chem., **28**, 1593 (1966)

[13] M. Peiteado, S. Sturm, A.C. Caballero, and D. Makovec, Acta Mater., **56**, 4028 (2008)

[14] S. Guillemet-Fritsch, C. Chanel, J. Sarrias, S. Bayonne, A. Rousset, X. Alcobe, and M.L. Martinez Sarrioin, Solid State Ionics, **128,** 233 (2000)

[15] X. Liang, Phys. Chem. Chem. Phys., **17**, 29655 (2015)

[16] X. Liang, and D.R. Clarke, Acta Mater., **63**, 191 (2014)

[17] E. Guilmeau, P. Díaz-Chao, O.I. Lebedev, A. Rečnik, M.C. Schäfer, F. Delorme, F. Giovanelli, M. Košir, and S. Bernik, Inorg. Chem., **56**, 480 (2017)

[18] K. Park, J.K. Seong, Y. Kwon, S. Nahm, and W.S. Cho, Mater. Res. Bull., **43**, 54 (2008)

[19] M. Peiteado, Y. Iglesias, J.F. Fernández, J. De Frutos, and A.C. Caballero, Mater. Chem. Phys., **101**, 1 (2007)

[20] K. Shirouzu, T. Ohkusa, M. Hotta, N. Enomoto and J. Hojo, J. Ceram. Soc. Jpn., **115**, 254 (2007)

[21] A. Walsh, J.L.F. Da Silva, Y. Yan, M.M. Al-Jassim, and S.H. Wei, Phys. Rev. B., **79**, 073105 (2009)

[22] G. J. Snyder, and E. S. Toberer, Nat. Mater., **7**, 105114 (2008).

[23] J. Martin, L. Wang, L. Chen and G. S. Nolas, Phys. Rev. B, **79**, 115311 (2009)

[24] J.M.O. Zide, D. Vashaee, Z.X. Bian, G. Zeng, J.E. Bowers, A. Shakouri, and A.C. Gossard, Phys. Rev. B, **74**, 205335 (2006)

[25] L.D. Hicks, and M.S. Dresselhaus, Phys. Rev. B, **47**, 12727 (1993)

[26] H. Ohta, S. Kim, Y. Mune, T. Mizoguchi, K. Nomura, S. Ohta, T. Nomura, Y. Nakanishi, Y. Ikuhara, M. Hirano, H. Hosono, and K. Koumoto, Nat. Mater., **6**, 129 (2007)

[27] Y. Yan, G.M. Dalpian, M.M. Al-Jassim, and S.H. Wei, Phys Rev B, **70**, 193206 (2004)

[28] J. Callaway, and H. C. von Baeyer, Phys. Rev., **120**, 1149 (1960)

[29] Z. Qu, T. D. Sparks, W. Pan, and D. R. Clarke, Acta Mater., **59**, 3841 (2011)

[30] X. Liang, J. Eur. Ceram. Soc., **36**, 1643 (2016)

[31] H. Takemoto, K. Fugane, P. Yan, J. Drennan, M. Saito, T. Mori, and H. Yamamura, RSC Adv., **4**, 2661 (2014)

[32] Ü. Özgur, Y.I. Alivov, C. Liu, A. Teke, M.A. Reschikov, S. Doğan, V. Avrutin, S.J. Cho, and H. Morkoç, J. Appl. Phys., **98**, 041301 (2005)

[33] O. Köster-Scherger, H. Schmid, N. Vanderschaeghe, F. Wolf, and W. Mader, J. Am. Ceram. Soc., **90**, 3984 (2007)

[34] J.L.F. Da Silva, Y. Yan, and S.H. Wei, Phys. Rev. Lett., **100**, 255501 (2008)

[35] A.P. Goldstein, S.C. Andrews, R.F. Berger, V.R. Radmilovic, J.B. Neaton, and P. Yang, ACS Nano, **7**, 10747 (2013)

[36] E.S. Toberer, A. Zevalkink, and G.J. Snyder, J. Mater. Chem., **21**, 15843 (2011)

[37] A. Rečnik, N. Daneu, T. Walther, and W. Mader, J. Am. Ceram. Soc., **84**, 2657 (2001)

[38] M.A. McCoy, R.W. Grimes, and W.E. Lee, J. Mater. Res., **11**, 2009 (1996)

[39] T. Tsubota, M. Ohtaki, K. Eguchi, and H. Arai, J. Mater. Chem., **8**, 409 (1998)

[40] H. Wang, A.D. LaLonde, Y. Pei, and G.J. Snyder, Adv. Funct. Mater., **23**, 1586 (2013)

[41] J.P. Dismukes, L. Ekstrom, and R.J. Paff, J. Phys. Chem., **68**, 3021 (1964)

[42] K.S. Lackner, and G. Zweig, Phys. Rev. D, **28**, 1671 (1983)

[43] N.H. Perry, and T.O. Mason, J. Am. Ceram. Soc., **96**, 966 (2013)

[44] T. Tani, S. Isobe, W.S. Seo, and K. Koumoto, J. Mater. Chem., **11**, 2324 (2001)

[45] H. Kaga, R. Asahi, and T. Tani, Jpn. J. Appl. Phys., **43**, 7133 (2004)

[46] S. Isobe, T. Tani, Y. Masuda, W.S. Seo, and K. Koumoto, Jpn. J. Appl. Phys., **41**, 731 (2002)

[47] M. Kazeoka, H. Hiramatsu, W.S. Seo, and K. Koumoto, J. Mater. Res., **13**, 523 (1998)

[48] Y. Masuda, M. Ohta, W.S. Seo, W. Pitschke, and K. Koumoto, J. Solid State Chem., **150**, 221 (2000)

Chapter 7. Summary and Outlook

In this thesis, the atomic and electronic structures of inversion domain boundaries in Mn-Al and Sn-Al dual-doped ZnO ceramics have been investigated by atomic-resolution scanning transmission electron microscopy, energy-dispersive X-ray spectroscopy, electron energy-loss spectroscopy and density functional theory calculations. The influence of inversion domain boundaries on the thermoelectric properties of these compounds has also been investigated in the temperature range from room temperature to ~750℃.

Inversion domain networks consisting of basal-plane and pyramidal-plane inversion domain boundaries formed when the solubility limit of Mn in ZnO was exceeded in $Zn_{0.89}Mn_{0.1}Al_{0.01}O$ ceramics sintered at 1400°C in air. Inversion domain networks exhibited a basal-plane inversion domain boundary spacing of ~50 nm along the *c*-axis axis and consisted of pyramidal-plane inversion domain boundaries that form shallow angles of ~8.8°-22.3° with the basal-plane inversion domain boundaries and form at $\{11\bar{2}l\}$ pyramidal planes with l values of ~8-21. Atomic-scale observation of basal-plane inversion domain boundaries revealed a head-to-head configuration of the *c*-axis and a cation stacking sequence along the *c*-axis of $\alpha\beta\alpha\beta|\gamma|\alpha\beta\alpha\beta$ at the basal-plane inversion domain boundary interface. Elemental analysis revealed significant localization of Mn and minor localization of Al at the basal-plane inversion domain boundary. The results of STEM-EELS suggested the valence of Mn at the basal-plane inversion domain boundary octahedral site to be 3+, as expected based on Pauling's rule of electrostatic neutrality. Inversion domain boundaries are considered to develop in $Zn_{0.89}Mn_{0.1}Al_{0.01}O$ due to the high concentration of Mn, which exceeds the solubility limit of Mn in ZnO, allowing for the formation of polytypic structures such as inversion domain boundaries. The 3+ valence of Mn^{3+} and Al^{3+} should facilitate the formation of inversion domain boundaries by an internal diffusion mechanism. Based on their respective ionic radii,

the larger Mn^{3+} and smaller Al^{3+} dopants may be more likely to assist in stabilizing the formation of the basal-plane and pyramidal-plane inversion domain boundaries respectively.

The formation of inversion domains also occurred in $Zn_{0.98}Sn_{0.01}Al_{0.01}O$ ceramics sintered at 1400°C in air. However, unlike in $Zn_{0.89}Mn_{0.1}Al_{0.01}O$, spinel secondary phases did not form. A spacing between the basal-plane inversion domain boundaries of ~15 nm and pyramidal-plane inversion domain boundaries with angles of ~25.4°-28.2° which form at $\{11\bar{2}l\}$ planes with l values of ~6-7 were observed in $Zn_{0.98}Sn_{0.01}Al_{0.01}O$. Elemental analysis revealed that Sn and Al primarily localize at the basal-plane and pyramidal-plane inversion domain boundaries respectively. Atomic-resolution observations of both the basal-plane and pyramidal-plane inversion domain boundaries in $Zn_{0.98}Sn_{0.01}Al_{0.01}O$ were carried out. HAADF-STEM imaging and EELS analysis also confirmed that the b-IDBs contain significant concentrations of Sn, which appears to occupy the b-IDB sites uniformly. Using ABF-STEM imaging, H-H and T-T *c*-axis configurations were determined to form at the b-IDBs and p-IDBs respectively. The development of ID networks in $Zn_{0.98}Sn_{0.01}Al_{0.01}O$, which does not occur in $Zn_{0.99}Al_{0.01}O$ or $Zn_{0.99}Sn_{0.01}O$, is attributed to the stabilization of b-IDB and p-IDB formation via the addition of the Sn and Al dopants respectively. This occurs due to the ionic radius mismatch of Sn and Al, with the large Sn and small Al dopants preferentially occupying the b-IDB and p-IDB sites in order to minimize lattice strain. The stabilization of inversion domain network formation in $Zn_{0.98}Sn_{0.01}Al_{0.01}O$ also results in the suppression of the formation of the $ZnAl_2O_4$ and Zn_2SnO_4 spinel phases. Although Sn and Al can only occupy a single octahedral site in the spinel phases, the separate b-IDB and p-IDB sites in the inversion domain networks allow for the site-specific localization of Sn and Al based on their distinct ionic radii. This avoids unfavorable co-occupation of the spinel octahedral site by Sn and Al, which could potentially result in a large lattice distortion due to ionic radius mismatch.

The differences in the features of the IDs and IDBs determined, by TEM, HAADF/ABF-STEM, EDS and EELS analysis, to develop in $Zn_{0.89}Mn_{0.1}Al_{0.01}O$ and

$Zn_{0.98}Sn_{0.01}Al_{0.01}O$ demonstrates the importance of the characteristics of the specific IDB-forming dopant element in terms of influencing the exact microstructural features that develop upon sintering, e.g. the b-IDB spacing, p-IDB angle and the cation stacking sequence at the b-IDB interface. The co-occupation of the b-IDB by Mn and Al has been confirmed in $Zn_{0.89}Mn_{0.1}Al_{0.01}O$ and the stabilization of ID networks due to the site-specific localization of Sn and Al at the b-IDBs and p-IDBs has been observed in $Zn_{0.98}Sn_{0.01}Al_{0.01}O$. These results prove that, by selecting specific types of dopant elements, not only can the occupancy of the specific IDB sites be controlled but also that the formation of yet unidentified intergrowth and $RMO_3(ZnO)_n$ homologous phase compounds can be acheived. Future investigations of other $RMO_3(ZnO)_n$ compounds should take into consideration the potential for different dopants and dopant combinations to stabilize inversion domain network formation based on the ionic radii and stable valence states of the specific types of dopants, as these factors will likely influence which of the IDB sites, if either, a particular dopant can occupy. This can be understood generally by considering Pauling's first and second rules for the formation of ionic crystal structures. In systems doped with multiple dopants, these factors will be very important, as the relative ionic radii of the dopants will likely dictate which of the IDB sites specific dopants will occupy and since the addition of multiple dopants with distinct valence states may make possible the formation of ordered structures, due to the specific requirements for elecroneutrality at the b-IDB and p-IDB sites. In addition to the ionic radii and valence states, other factors to be considered in investigating IDB formation and $RMO_3(ZnO)_n$ homologous phase compound stabilization include the dopant diffusion mechanism and diffusion rate of specific elements in ZnO, the reactivity of the dopant oxide with ZnO and also the characteristics of the dopant oxide powder (e.g. particle size and impurity concentration). The suppression of the spinel phases in $Zn_{0.98}Sn_{0.01}Al_{0.01}O$ also demonstrates that dopant-controlled ID network stabilization can be utilized to maintain phase purity by suppressing the formation of unfavorable secondary phases, with potential implications for improving functional

properties such as the electrical conductivity and optical transmission.

The local atomistic and electronic properties of the Mn-doped b-IDBs and Sn-doped b-IDBs observed experimentally have been investigated using DFT calculations. Slab models containing a single b-IDB interface were constructed and structural relaxation was carried out. The stable b-IDB structural features of the refined models were found to be in general agreement with those of the experimentally observed b-IDB structures. The local electronic structure of the b-IDB model containing a monolayer of octahedrally coordinated Mn exhibited LDOS features showing significant hybridization of the Mn *d* and O *p* states within the valence band and localized Mn *d* states in the conduction band. The equatorial Mn-O bonds, which should exhibit a significant covalent bonding character, likely make the primary contribution to the lower-energy hybridized valence band states, while the apical Mn-O bonds, which should exhibit a significant ionic bonding character, are expected to make the primary contribution to the higher-energy localized conduction band states. The Fermi level of the Mn-doped b-IDB model remained near the VBM, similar to the DOS of undoped bulk ZnO. In contrast, the LDOS of the Sn-doped b-IDB exhibited a significant renormalization of the fundamental band gap in comparison to undoped bulk ZnO. The Fermi level of the Sn-doped b-IDB shifted to the conduction band, indicating that the octahedrally coordinated Sn at the b-IDB acts as an electron donor dopant. The shift of the Fermi level to the conduction band at the Sn-doped b-IDB is expected to result in an increase of the optical band gap due to the Burstein-Moss effect. The appearance of significant Sn *s* states near the Fermi level at the Sn-doped b-IDB also suggests that 2DEG formation could occur at the b-IDB interface.

The thermoelectric properties of the Mn-Al and Sn-Al dual-doped ZnO ceramics were also investigated in the temperature range from RT to ~750°C. The addition of Al to ZnO resulted in a significant increase of the carrier density of ZnO. In Mn-Al dual-doped ZnO, as the concentration of Mn increased, the electrical and thermal conductivity decreased due to the scattering of electrons and phonons by Mn substitutional point defects. When the solubility

limit of Mn in ZnO was exceeded, in $Zn_{0.89}Mn_{0.1}Al_{0.01}O$, the formation of IDBs occurred. The high density of b-IDB and p-IDB interfaces caused additional electron and phonon scattering, further decreasing the electrical and thermal conductivity. The Seebeck coefficient of $Zn_{0.89}Mn_{0.1}Al_{0.01}O$ also increased relative to $Zn_{0.99-x}Mn_xAl_{0.01}O$ samples with lower Mn concentrations, possibly due to electron filtering or quantum confinement at the IDB interfaces. The presence of ID networks with a small b-IDB spacing of ~15 nm in $Zn_{0.98}Sn_{0.01}Al_{0.01}O$ resulted in a drop in the magnitude of the thermal conductivity in comparison to $Zn_{0.99}Al_{0.01}O$ and $Zn_{0.99}Sn_{0.01}O$. The IDB interfaces in $Zn_{0.98}Sn_{0.01}Al_{0.01}O$ also caused the electrical conductivity to decrease relative to $Zn_{0.99}Al_{0.01}O$, likely due to electron scattering at IDB interfaces, while the Seebeck coefficient increased, suggesting the filtering of low-energy electrons by IDB potential barriers or the quantum confinement of electrons at the IDBs.

The results of both first principles calcualations, that demonstrate that the local atomistic and electronic properties of the IDBs can be modified based on the specific type of dopant occupying the IDB sites, and also of thermoelectric property measurements, which show a significant influence of IDB formation on the thermoelectric properties, prove, respectively, that the local properties at the nanoscale level as well as the bulk properties at the macroscopic level can be controlled not only by nanostructuring via ID formation but also by selecting specific dopant elements with distinct characteristics. Future research focusing on the study of ZnO materials containing IDBs, in particular $RMO_3(ZnO)_n$ homologous phase systems, should include a systematic investigation of the influence of changing both the type and concentration of the specific dopants occupying the b-IDB and p-IDB sites on the nanoscale and atomic-scale properties, e.g. b-IDB spacing, p-IDB angle and cation stacking sequences at the b-IDB, using atomic-resolution methods for structural and elemental analysis, such as HAADF/ABF-STEM and STEM-EDS/EELS. Atomic-resolution EDS will be useful for evaluating the site-specific occupancy of both the b-IDBs and p-IDBs by different dopants, particularly in the case where multiple dopants co-occupy either of the IDB sites. The use of

image simulation methods should also assist in determining the origin of the distinct features observed in the HAADF or ABF-STEM images. For example, to more definitively determine the precise origin of the reduced HAADF contrast that has been previously observed around the b-IDB interfaces in Fe-doped ZnO and also in the Mn-doped ZnO samples analyzed in this thesis.

As new IDB-forming dopants and $RMO_3(ZnO)_n$ systems are identified, additional first principles studies should be useful for understanding how specific dopants modify the local properties at the IDBs in the materials observed experimentally. First principles studies comparing the cases of dopant substitution in the bulk vs. dopant occupation of the IDB interfaces should assist in determining the stability of IDB formation for different dopants, as well as the IDB formation energy. Systematic studies focusing on the effects of changing the value of n in a diverse range of $RMO_3(ZnO)_n$ homologous phase systems should enable the optimization of bulk properties such as the electrical conductivity, thermal conductivity and optical transmission, in order to improve device functionality. Control of the microstructural properties to the Ångström level may be achieved via the selection of different combinations of dopants, R and M, and by changing the ratio R:M. As has been demonstrated in $Zn_{0.98}Sn_{0.01}Al_{0.01}O$, the suppression of spinel secondary phase formation in favor of the formation of monophasic $RMO_3(ZnO)_n$ homologous phase systems should also be beneficial for the optimization of the the bulk properties.

Appendix

The following experimental findings and results of DFT calculations are provided as additional support for the primary findings discussed within the main body of this thesis.

Mn-Al Dual-Doped ZnO

As shown in Fig. A1, an additional orientation relationship, OR2, was identified between the spinel precipitates and the surrounding ZnO grains observed in $Zn_{0.94}Mn_{0.05}Al_{0.01}O$. OR2 exhibited an alignment between the $[1\bar{1}\bar{2}]$ zone-axis of the spinel precipitate and the $[\bar{1}2\bar{1}0]$ zone-axis, i.e. the *a*-axis, of the ZnO grain. Based on the indexing of the reciprocal lattice reflections in the corresponding EDPs, shown in Fig. A1 (b) and (c), the alignment of the $[220]$ direction of the spinel precipitate with the $[0002]$ direction of the ZnO grain was also confirmed, with an approximate misalignment of ~3.4°. Based on the relationships between the crystallographic directions described above, OR2 can be expressed generally according to the following expressions: $[\bar{1}2\bar{1}0]_{ZnO}//[1\bar{1}\bar{2}]_{SP}$, $(0002)_{ZnO}//(220)_{SP}$.

Chapter 3 focuses on the analysis of the basal-plane inversion domain boundary in $Zn_{0.89}Mn_{0.1}Al_{0.01}O$ as observed primarily at the *a*-axis. As shown in Fig. A2, images of the b-IDB were also collected at the *m*-axis. Fig. A2 (a) and (b) respectively show atomic-resolution HAADF and ABF-STEM images of the b-IDB interface. In agreement with HAADF-STEM observations of the b-IDB at the *a*-axis, there is a reduction in HAADF intensity within the cation planes of the b-IDB and the neighboring $\{0002\}$ cation planes. However, the individual cation columns at the b-IDB cation plane are not clearly resolved, possibly due to the combination of the smaller spacing between cation columns within the basal plane that is observed when the ZnO lattice is viewed at the *m*-axis and the presence of increased strain at the b-IDB interface, relative to the domain interior. In addition, a modulation of bright and dark cation columns, several atomic columns wide, is observed along the direction

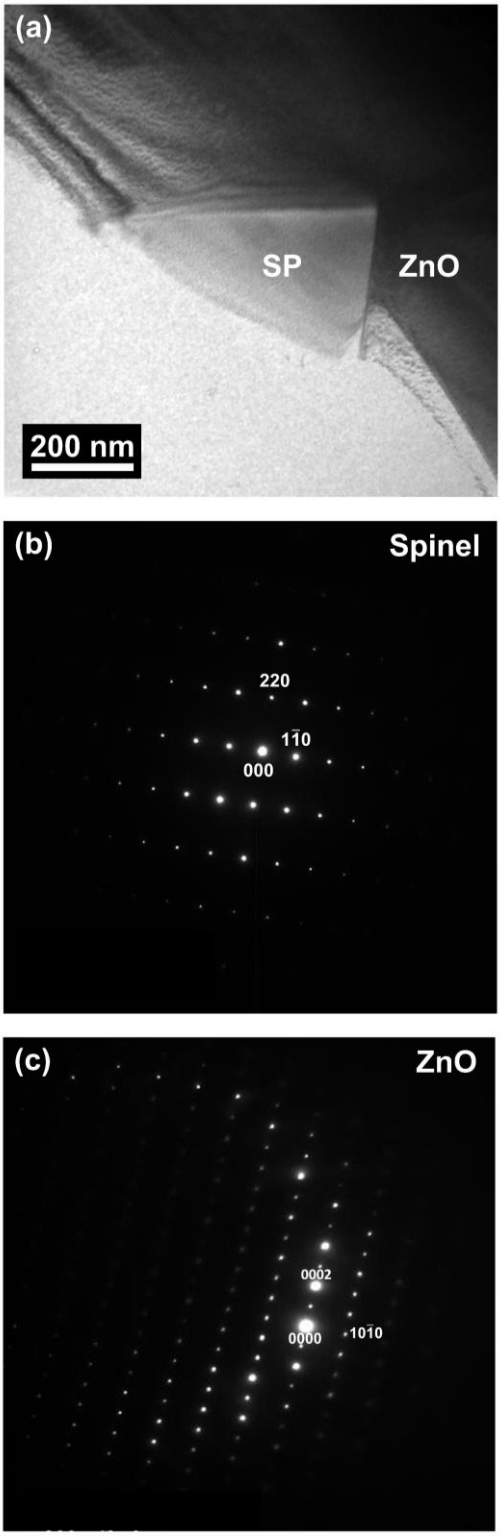

Figure A1. (a) BF-TEM image of a spinel precipitate (SP) and ZnO grain (ZnO) in $Zn_{0.94}Mn_{0.05}Al_{0.01}O$. **(b)** EDP of the spinel precipitate, aligned to the $[1\bar{1}\bar{2}]$ zone-axis. **(c)** EDP of the ZnO grain, aligned to the $[\bar{1}2\bar{1}0]$ zone-axis. Based on the EDPs, a second orientation relationship (OR2) of: $[\bar{1}2\bar{1}0]_{ZnO} // [1\bar{1}\bar{2}]_{SP}$, $(0002)_{ZnO} // (220)_{SP}$, with a misorientation angle of ~3.4° along the $[0002]_{ZnO}$ direction, is observed between the spinel precipitates and ZnO grains.

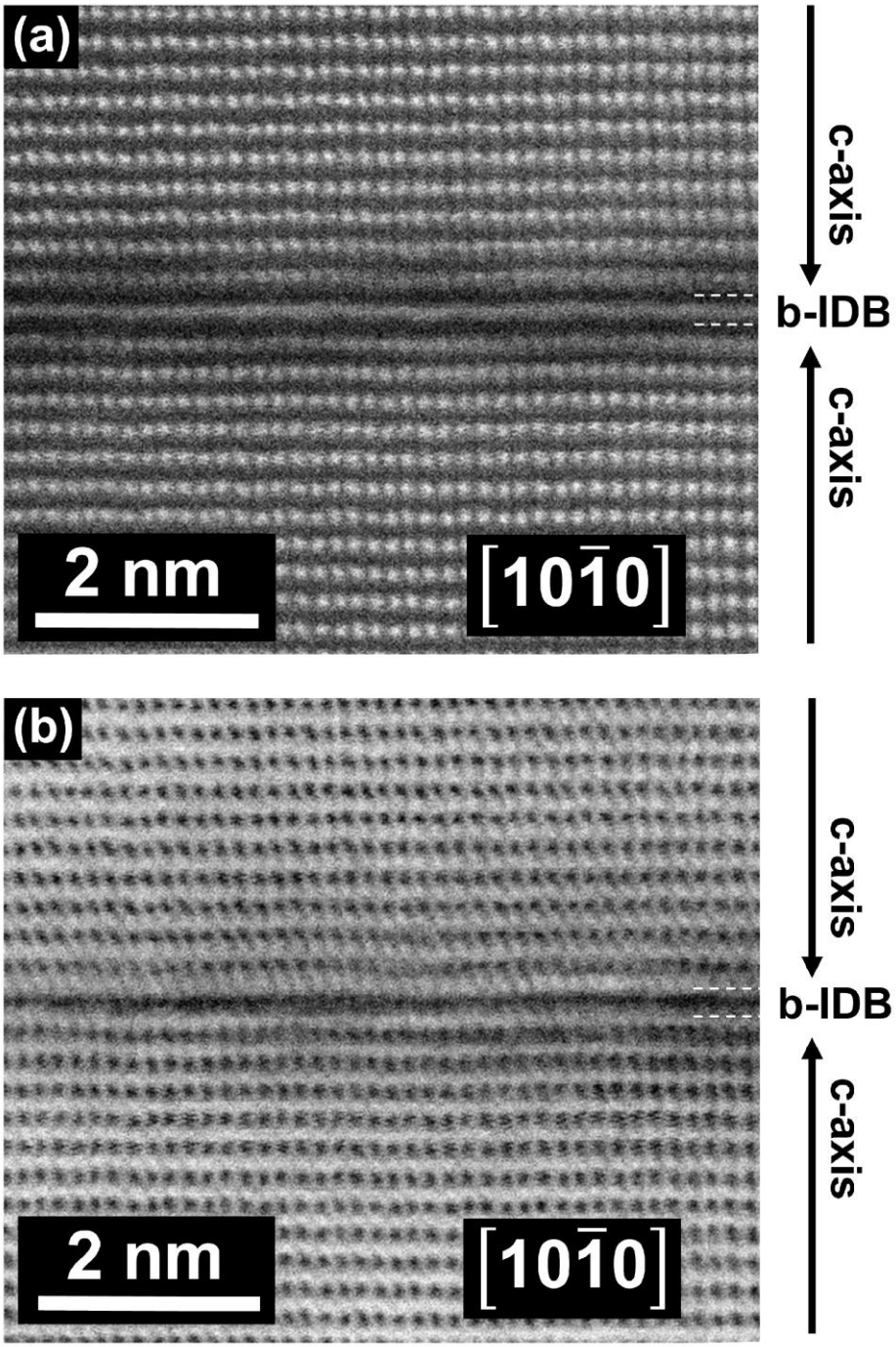

Figure A2. Atomic-resolution $[10\bar{1}0]$ zone-axis **(a)** HAADF and **(b)** ABF-STEM images of the b-IDB in $Zn_{0.89}Mn_{0.10}Al_{0.01}O$. Similar to the $[\bar{1}2\bar{1}0]$ zone-axis atomic-resolution HAADF-STEM image of the b-IDB shown in Fig. 3.11, a reduction in contrast is observed at the b-IDB cation layer and within the two cation layers directly neighboring the b-IDB.The approximate boundaries of the b-IDB cation layer are indicated by the dashed white lines in (a) and (b).

perpendicular to the zone-axis in the cation layers directly neighboring the b-IDB. This modulation may be due to lattice distortion around the b-IDB interface or, possibly, an ordering of the Mn and/or Al dopants within these layers. Additional studies using atomic-resolution STEM-EDS may assist in clarifying whether cation ordering actually occurs within these layers.

In order to clearly illustrate the polyhedral connectivity between the Zn tetrahedra, which form the bulk-like inversion domain interior, and the cation dopant-occupied octahedra at the b-IDB interface, additional visualizations of the refined slab model containing a single Mn-doped b-IDB are shown in Fig. A3. The edge-sharing between Mn octahedra within the basal-plane cation layer as well as the corner-sharing between the Zn tetrahedra and Mn octahedra can clearly be observed. In addition, as shown in Fig. A3 (b), when the b-IDB is observed at the *a*-axis, the *c*-axis cation stacking sequence can be determined to be αβαβ|γ| αβαβ, in agreement with the experimentally observed b-IDB structure, described in Chapter 3.

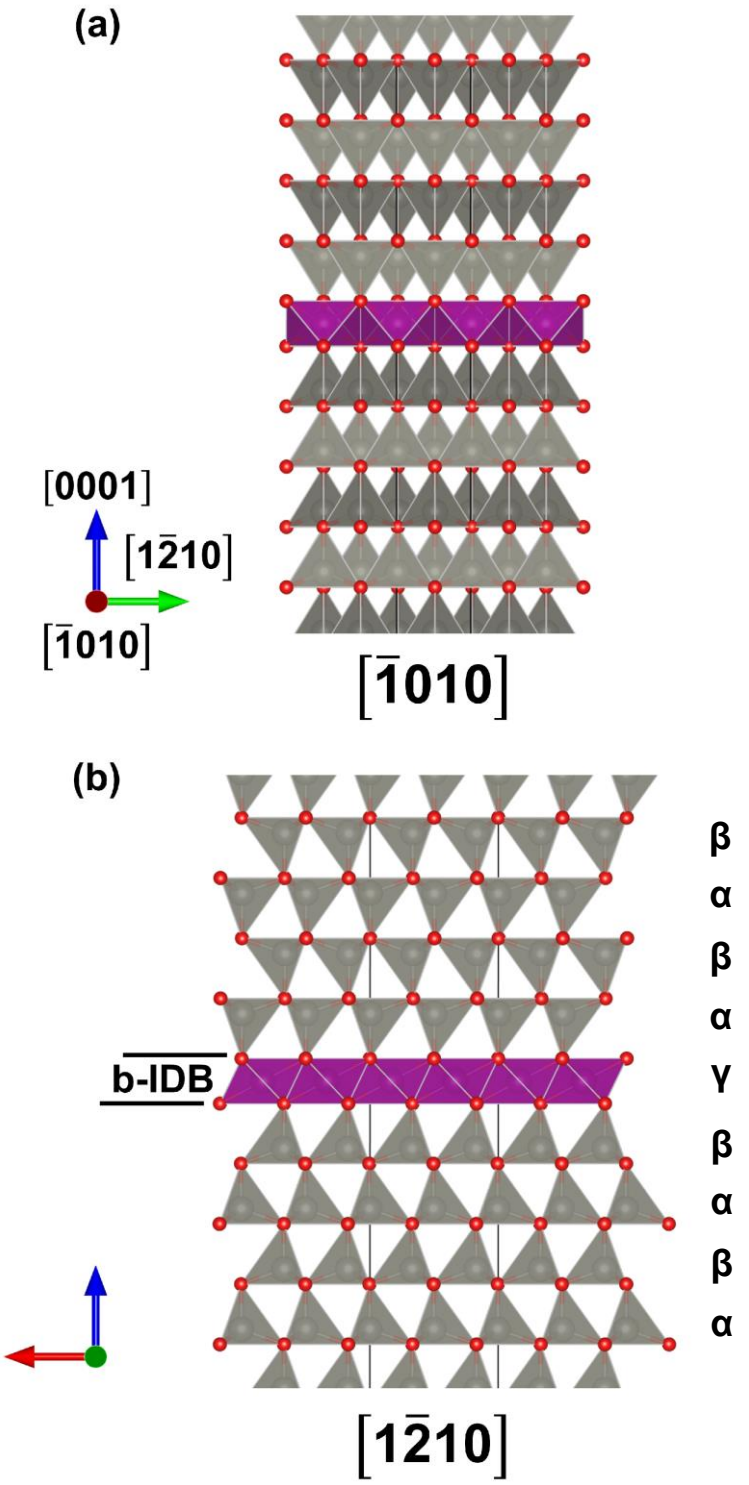

Figure A3. (a) [$\bar{1}$010] and **(b)** [1$\bar{2}$10] zone-axis views of the b-IDB interface within the Mn-doped b-IDB slab model, showing the polyhedral connectivity of the Mn octahedra (purple) and the Zn tetrahedra (grey). The b-IDB is composed of a {0002} plane monolayer of edge-sharing Mn octahedra.

Sn-Al Dual-Doped ZnO

Although STEM-EDS analysis of the inversion domain networks (Fig. 4.4) clearly shows that Sn and Al localize at the respective interfaces of the b-IDBs and p-IDBs, additional information can be obtained by the determination of the exact extent of the localization at a higher spatial resolution. As shown in Fig. A4, high-resolution STEM-EDS analysis clearly indicates that the Sn dopant localizes primarily within $\leq$ 1 nm of the b-IDB interface. This

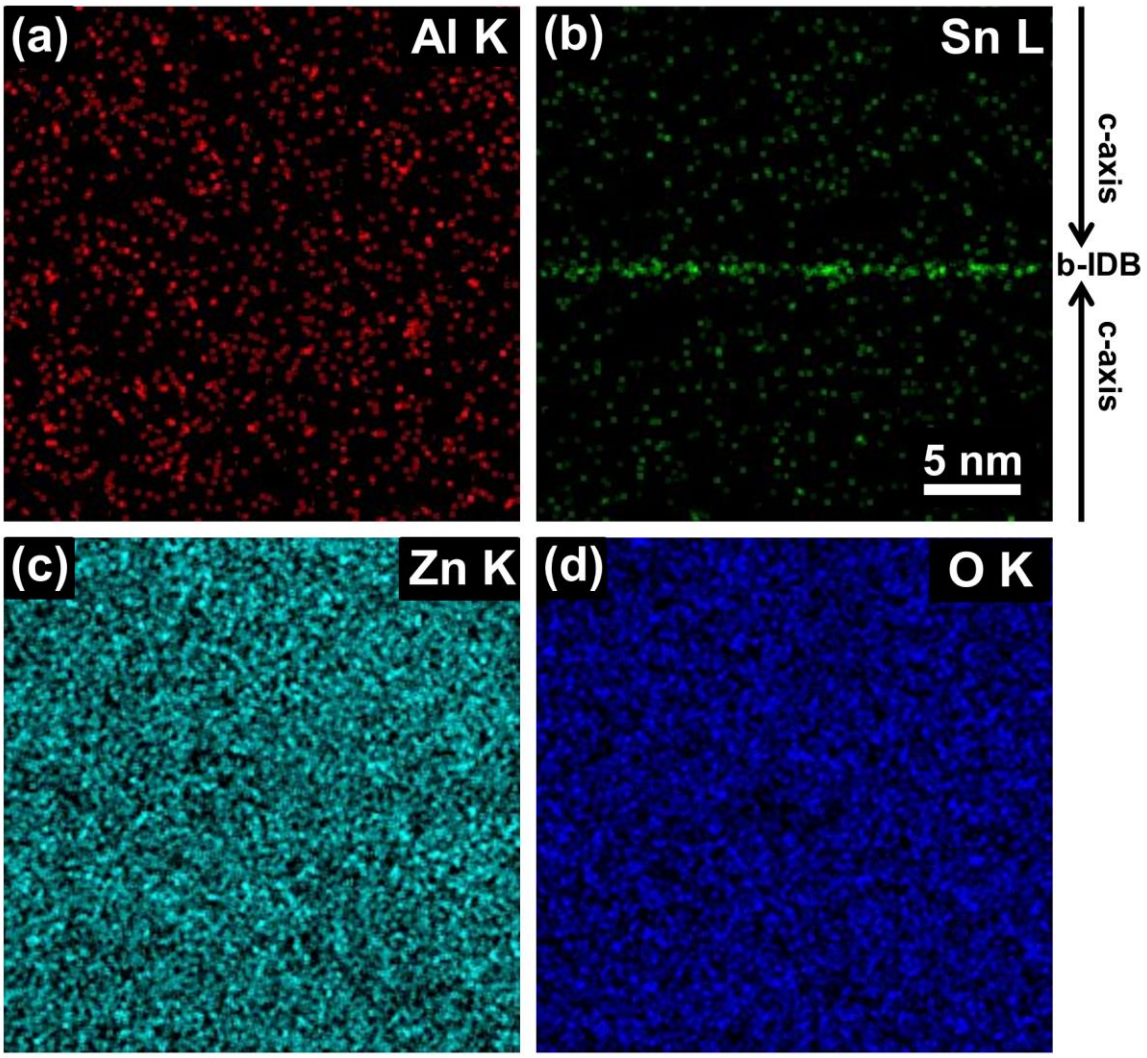

Figure A4. High-resolution STEM-EDS net counts elemental maps acquired at a b-IDB in $Zn_{0.98}Sn_{0.01}Al_{0.01}O$. A local increase of the Sn *L* signal is detected within $\leq$ 1 nm of the b-IDB, indicating significant Sn localization at the b-IDB cation layer. In contrast, the Al *K* signal exhibits no local increase at the b-IDB, indicating the absence of significant localization of Al at the b-IDB.

result directly confirms the finding of HAADF-STEM analysis of the b-IDBs in $Zn_{0.98}Sn_{0.01}Al_{0.01}O$, shown in Fig. 4.5, that indicates that the b-IDB cation plane contains significant concentrations of the high atomic number Sn dopant. Also in agreement with STEM-EDS analysis of the inversion domain networks at a lower magnification (Fig. 4.4) and the results of HAADF-STEM analysis of the b-IDBs (Fig. 4.5), high-resolution STEM-EDS analysis indicates that significant localization of Al does not occur at the b-IDB interface.

Although Chapter 4 contains a detailed analysis of the b-IDB and p-IDB interfaces that form within the inversion domain networks in $Zn_{0.98}Sn_{0.01}Al_{0.01}O$, additional observations of both the b-IDBs and p-IDBs were also carried out using HAADF/ABF-STEM to analyze the inversion domain networks in greater detail. Fig. A5 shows high-magnification HAADF-STEM images of an ID network in $Zn_{0.98}Sn_{0.01}Al_{0.01}O$, as viewed along the *m*-axis. Both b-IDBs and p-IDBs can be viewed edge-on. The b-IDBs exhibit increased HAADF-STEM contrast, in agreement with other STEM-EDS/EELS and HAADF-STEM results discussed in Chapter 4, which indicate that Sn localizes within the $\{0002\}$ b-IDB cation plane. This is particularly evident in Fig. A5 (b), in which $\{0002\}$ cation monolayers with increased HAADF contrast are observed at the positions of the b-IDBs. In contrast, the p-IDBs appear to form at $\{11\bar{2}l\}$ pyramidal planes that form an angle, θ, with respect to the b-IDBs, as indicated in Fig. A5 (b), and consist of segments exhibiting reduced HAADF contrast that are several atomic columns wide and stack along the *c*-axis, with consecutive segments shifted in the direction of the *a*-axis perpendicular to the $[1\bar{1}00]$ zone-axis. The reduced HAADF intensity observed at the p-IDBs may be attributed to a combination of increased concentrations of the low atomic number Al dopant and the presence of increased local strain gradients, which can contribute to reduced HAADF intensity at defect structures such as the p-IDB interface.

Fig. A6-A9 show HAADF and ABF-STEM images of the inversion domain networks as viewed along the *a*-axis, i.e. along the $[1\bar{2}10]$ zone-axis, at different magnifications and positions with respect to the IDB interfaces. Figure A6 (a) and (b) respectively show ABF and

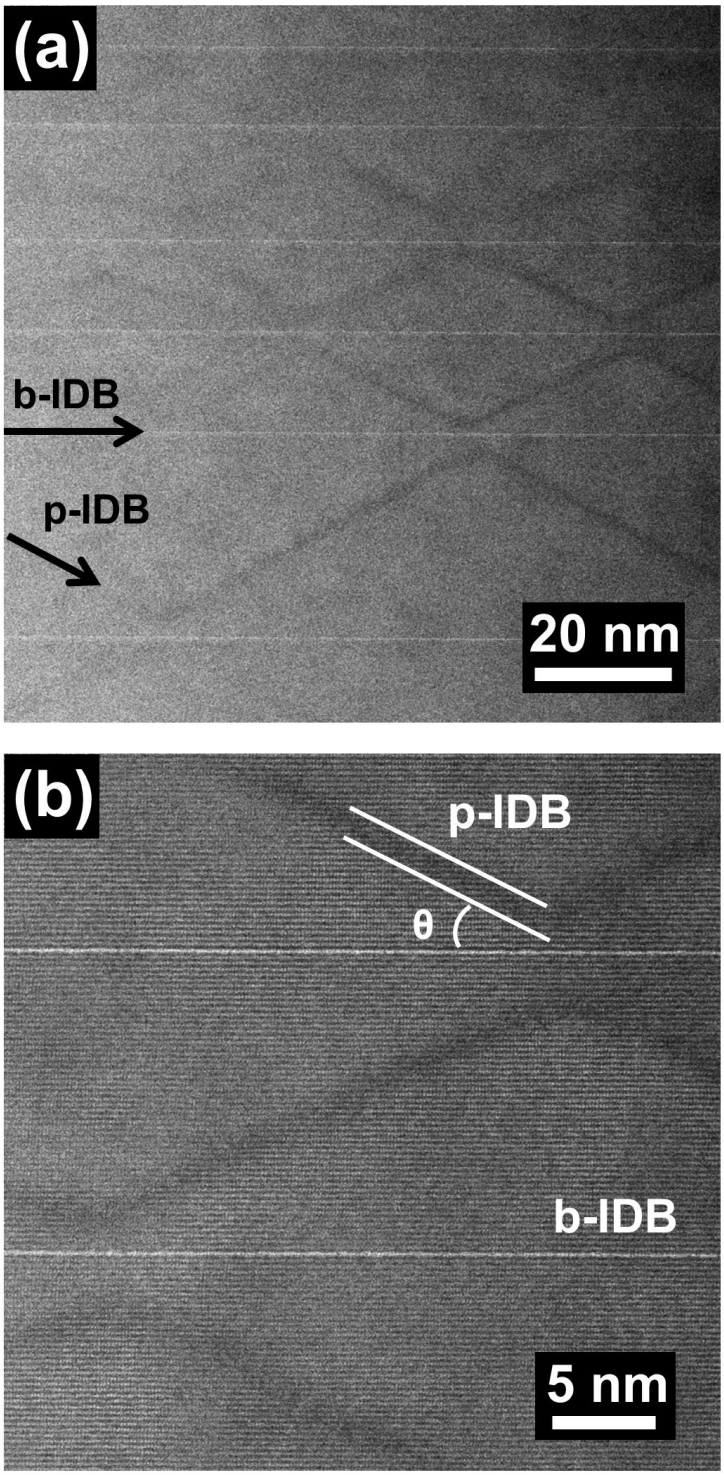

Figure A5. (a) Medium and **(b)** high-magnification HAADF-STEM images of an area within an ID network in $Zn_{0.98}Sn_{0.01}Al_{0.01}O$, viewed at the $[1\bar{1}00]$ zone-axis. Both b-IDBs and p-IDBs are viewed edge-on. The HAADF intensity increases and decreases at the b-IDBs and p-IDBs respectively. The solid lines in (b) indicate the approximate boundaries of the p-IDB and the angle, θ, formed between the p-IDBs and b-IDBs.

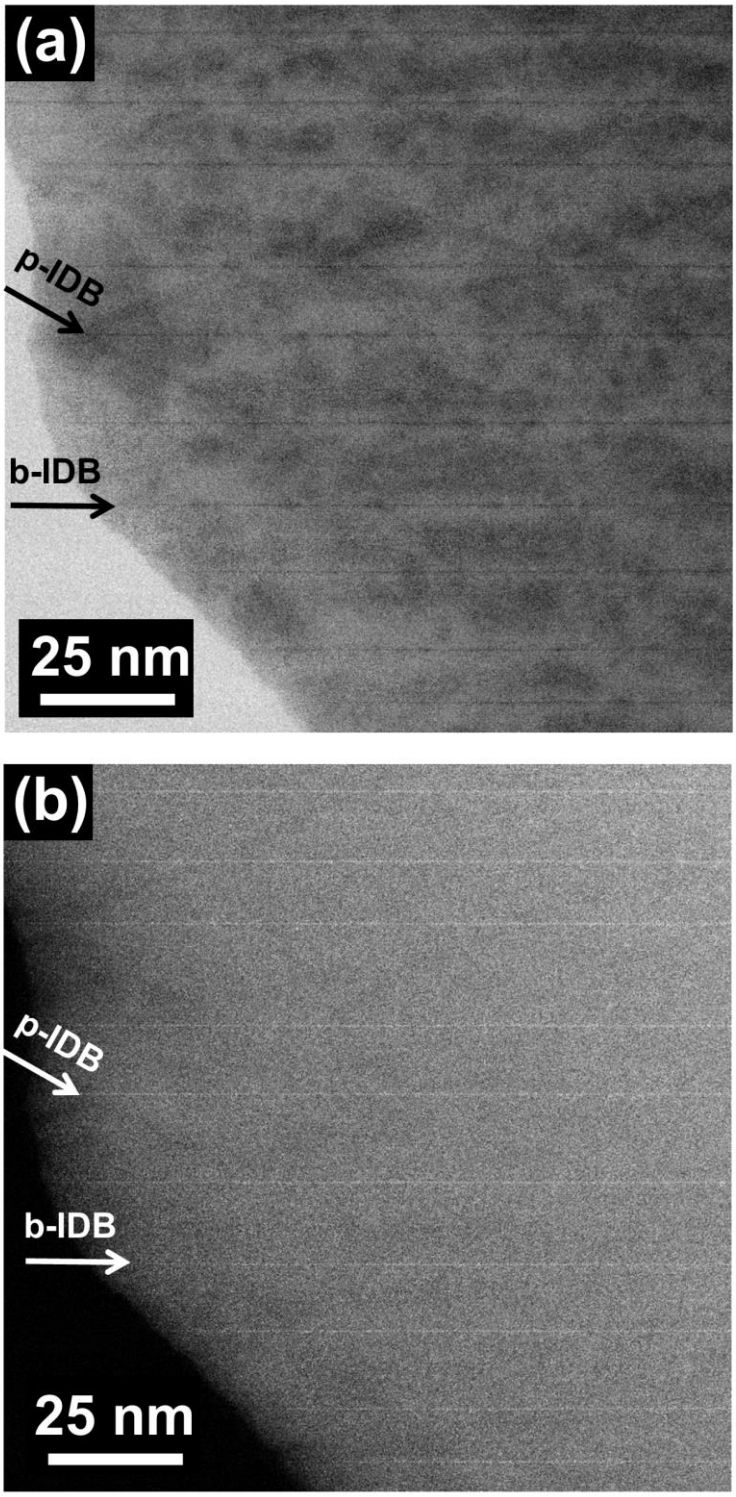

Figure A6. Medium-magnification **(a)** ABF and **(b)** HAADF-STEM images of an ID network in $Zn_{0.98}Sn_{0.01}Al_{0.01}O$, viewed at the $[1\bar{2}10]$ zone-axis. b-IDBs are viewed edge-on, while p-IDBs are inclined with respect to the zone-axis.

HAADF-STEM images of the general microstructure of an ID network, viewed along the *a*-axis. At this orientation, the b-IDBs can be viewed edge-on; however, the p-IDBs are inclined with respect to the zone-axis and, thus, cannot be imaged clearly. Fig. A7 (a)/(c) and (b)/(d) respectively show atomic-resolution ABF and HAADF-STEM images of a single b-IDB and p-IDB. The meeting point between the b-IDB and p-IDB is shown in Fig. A7 (a) and (b), while Fig. A7 (c) and (d) show the b-IDB and p-IDB interfaces at a higher magnification. The vertical arrows indicate the polarity of the *c*-axis in individual domains, which can be confirmed based on the stacking sequence of the cation-anion planes observed in Fig. A7 (a)/(c). The solid lines in (b) and (d) indicate the approximate position and orientation of the p-IDB plane, which is, however, inclined with respect to the zone-axis. The b-IDB interface exhibits reduced intensity in the ABF images and increased intensity in the HAADF images, in agreement with other HAADF/ABF-STEM and STEM-EDS/EELS results, discussed in Chapter 4, which confirmed the localization of the high atomic number Sn at the b-IDB interface. The reduced intensity observed at the p-IDB in Fig. A7 (a)-(d) may be due to local strain or lattice distortion.

Fig. A8 shows atomic-resolution ABF-STEM images of the meeting point of a single b-IDB and two p-IDBs. Fig. A8 (a) and (b) respectively show lower and higher magnification views of the ID network structure at the meeting point. The vertical arrows indicate the *c*-axis polarity in individual domains, determined based on the stacking sequence of the cation and anion planes long the *c*-axis that can be observed in Fig. A8 (a) and (b). The p-IDB appears as a diffuse defect, several atomic columns wide, as a result of both the diffuse nature of the defect itself and the fact that the p-IDB interface is inclined with respect to the zone-axis. Sections of the Sn-doped b-IDB slab model corresponding to both the region including the Sn-doped b-IDB and the bulk-like regions of the domain interior, with either a +*c* or –*c* polarity, are shown superimposed in (b), in order to indicate the polarity of the *c*-axis in the different regions of the

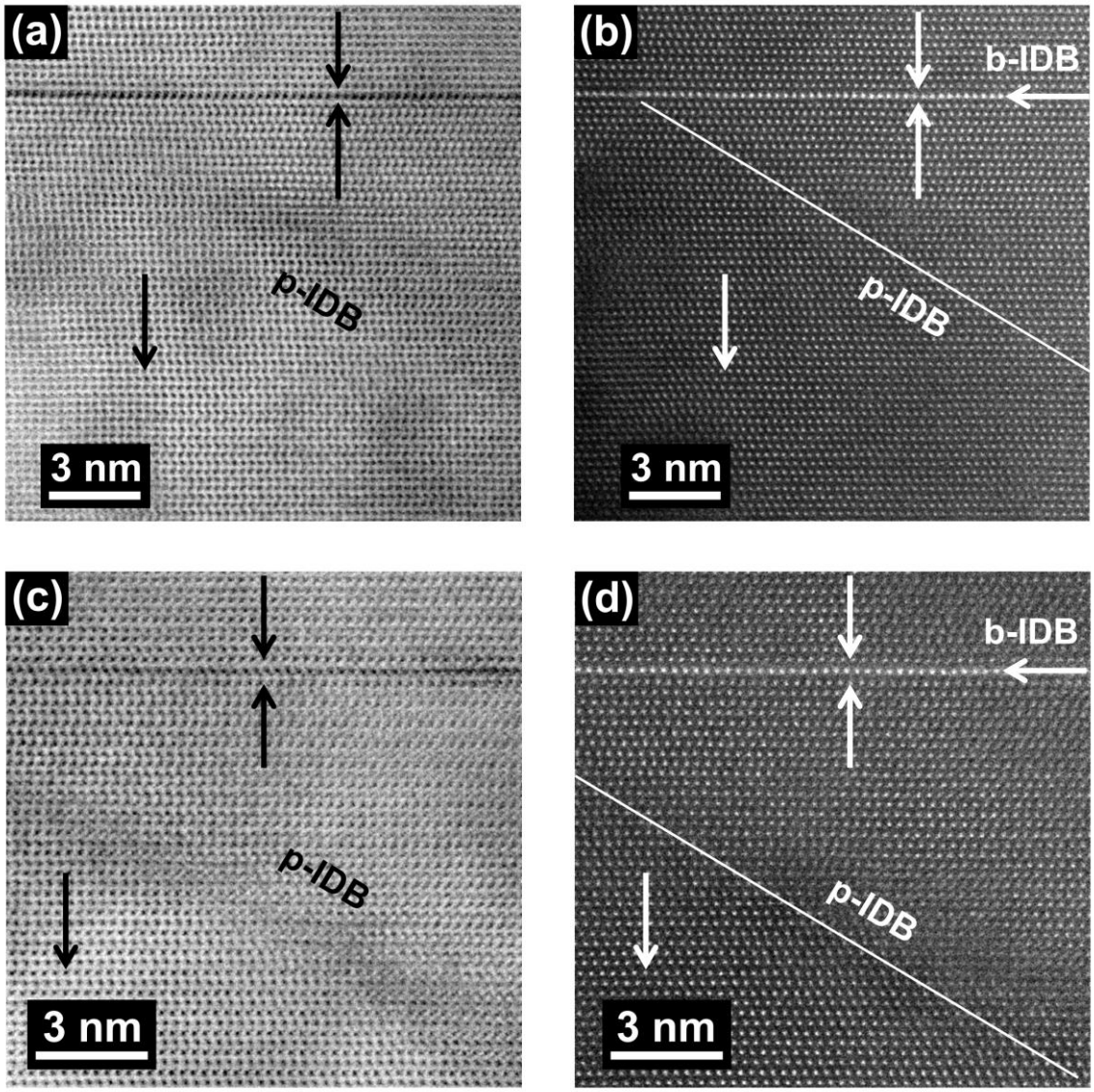

Figure A7. Atomic-resolution $[1\bar{2}10]$ zone-axis **(a)/(c)** ABF and **(b)/(d)** HAADF-STEM images of a single b-IDB and p-IDB in $Zn_{0.98}Sn_{0.01}Al_{0.01}O$. Vertical arrows indicate the polarity of the *c*-axis in individual domains.

IDs that are bounded by the b-IDBs and the p-IDBs. Based on Fig. A8 (a) and (b), it can be observed that the dispersion of dark contrast around the p-IDB interface appears to extend very close to the b-IDB interface. However, based on images of the b-IDBs and p-IDBs, as simultaneously viewed edge-on in Fig. A5, the apices of the p-IDBs actually appear to form several (~2-7) basal-plane cation layers away from the b-IDB interfaces. This may occur in order to avoid the formation of localized regions of high strain by increasing the separation between the b-IDB octahedra and the five-fold p-IDB sites, due to the fact that both interfaces

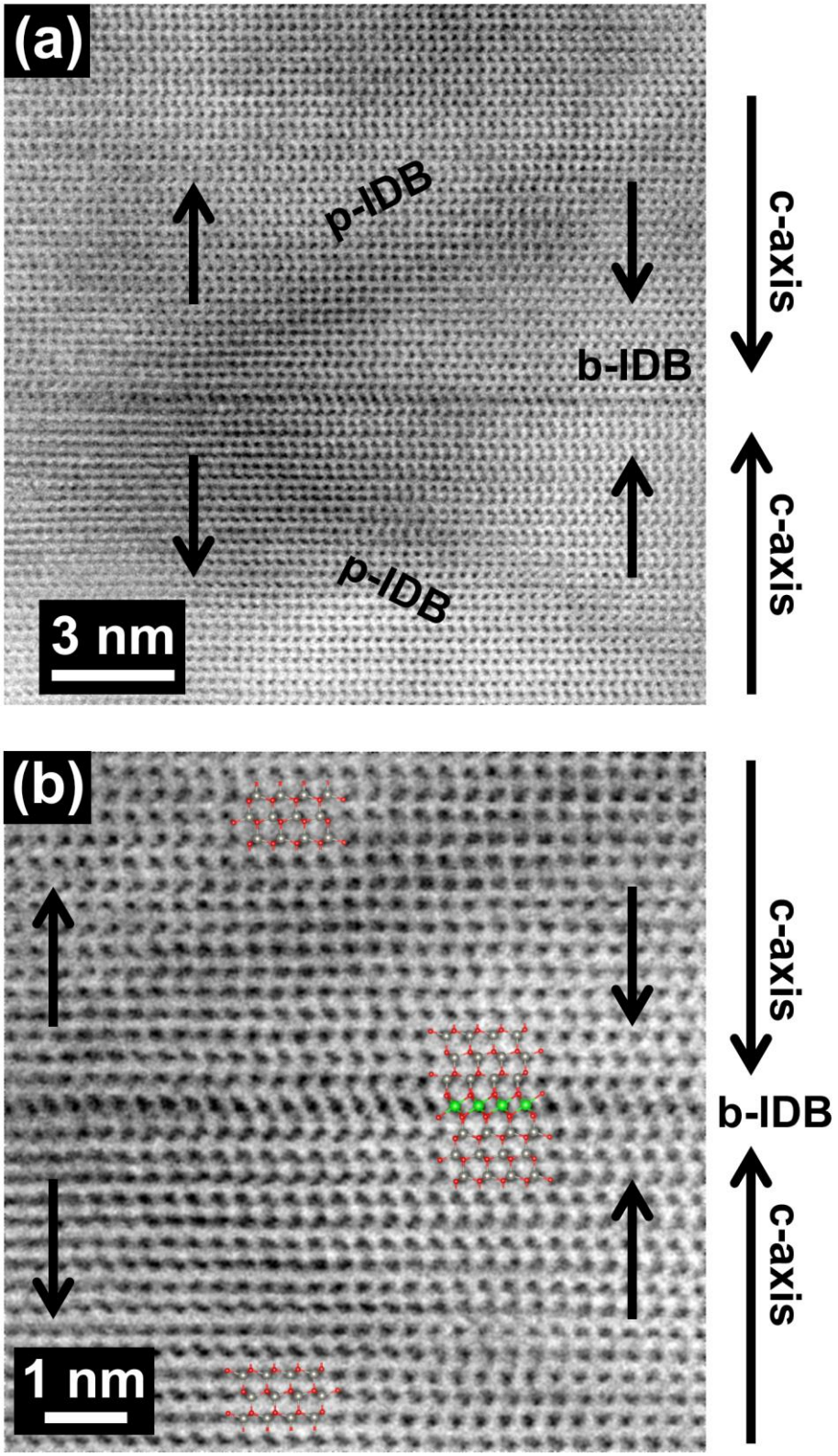

Figure A8. (a)/(b) Atomic-resolution [1$\bar{2}$10] zone-axis ABF-STEM images of the meeting point of two p-IDBs with a b-IDB in $Zn_{0.98}Sn_{0.01}Al_{0.01}O$.

have an associated built-in strain as a result of the local lattice expansion caused by the accommodation of the cation dopants. Local inhomogeneities in the chemical composition and local variations in the spacing between neighboring b-IDBs may result in local variations in the spacing between the p-IDB apex and the neighboring b-IDB interface.

Fig. A9 shows the HAADF-STEM images corresponding to the ABF-STEM images shown in Fig. A8. The b-IDB cation layer is clearly imaged based on the increased HAADF intensity observed at the {0002} plane corresponding to the octahedrally coordinated cation layer at which the inversion of the *c*-axis can be observed in Fig. A8. The vertical arrows indicate the *c*-axis polarity in individual IDs. The solid lines in (a) indicate the approximate location and orientation of the p-IDB, which is inclined with respect to the zone-axis. The *c*-axis cation stacking sequence of αβαβ|α|γαγα at the b-IDB is shown. As shown in Fig. A9 (b), the cation stacking sequences of γαγα and αβαβ are unaltered across the p-IDBs located both above and below the b-IDB respectively, suggesting that SF formation does not occur at the p–IDB interfaces. However, only a limited number of p-IDB interfaces and, thus, areas within the $Zn_{0.98}Sn_{0.01}Al_{0.01}O$ sample were observed. Thus, the formation of SFs at p-IDB interfaces located at other areas in the sample cannot be precluded based on the results shown in Fig. A9.

The polyhedral connectivity of the edge-sharing b-IDB octahedra and corner-sharing Zn tetrahedra, respectively located at the b-IDB interface and within the ID interior respectively, is shown in Fig. A10, in which the slab model containing a single Sn-doped b-IDB, discussed in Chapter 5, is visualized at several zone-axis orientations. The Sn, Zn and O atoms are colored green, grey and red respectively. The model b-IDB is composed of a {0002} plane monolayer of edge-sharing Sn octahedra that share corners with the neighboring Zn tetrahedra. As shown in Fig. A10 (c), in contrast to the b-IDB interface in the Mn-doped b-IDB slab model, which only contains a single Mn-doped octahedral b-IDB site, the Sn-doped b-IDB contains two distinct Sn sites, Sn1 and Sn2, which can be distinguished at one of the *a*-axes, e.g. the

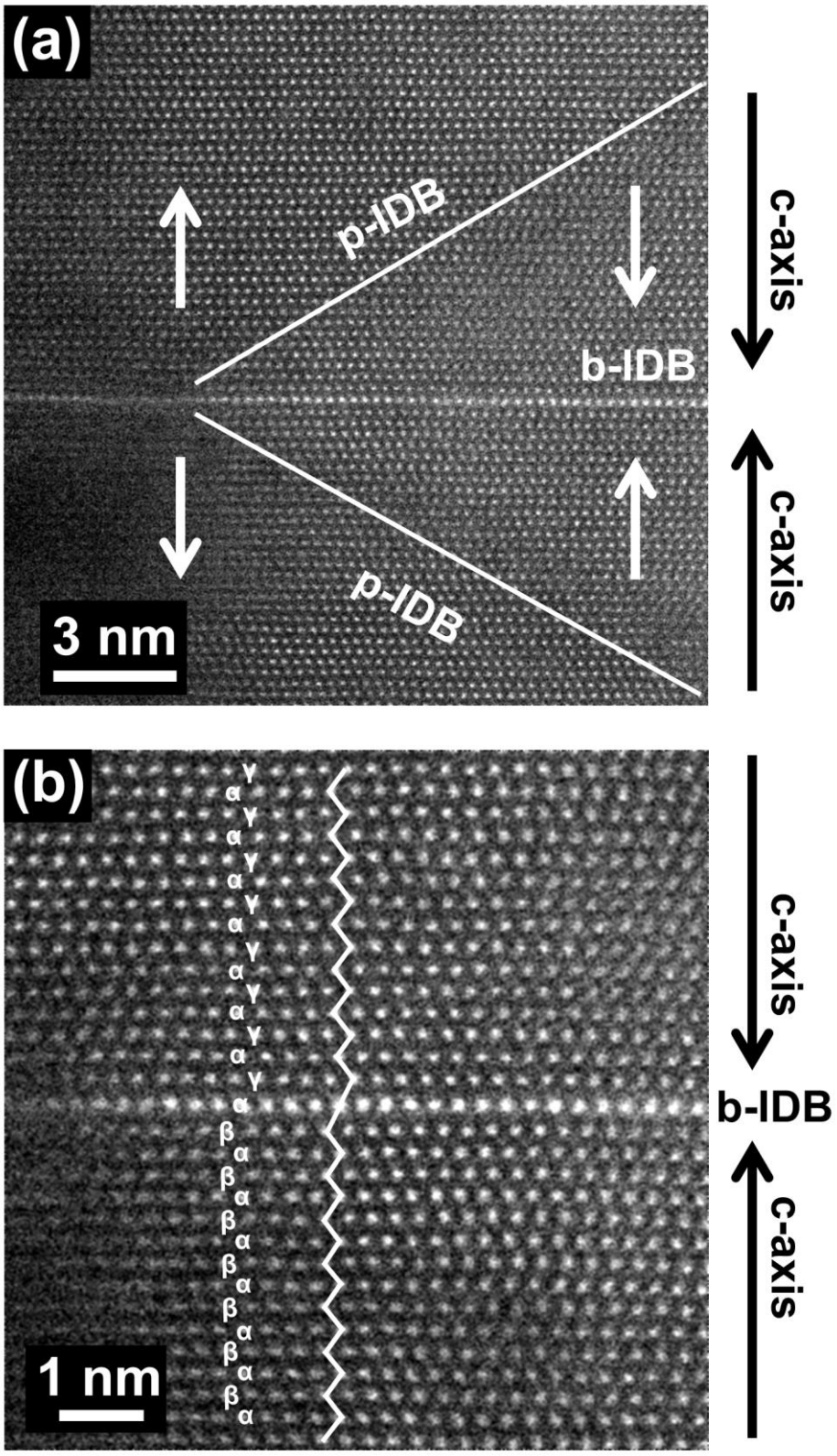

Figure A9. (a)/(b) Atomic-resolution $[1\bar{2}10]$ zone-axis HAADF-STEM images of the meeting point of two p-IDBs and a b-IDB in $Zn_{0.98}Sn_{0.01}Al_{0.01}O$.

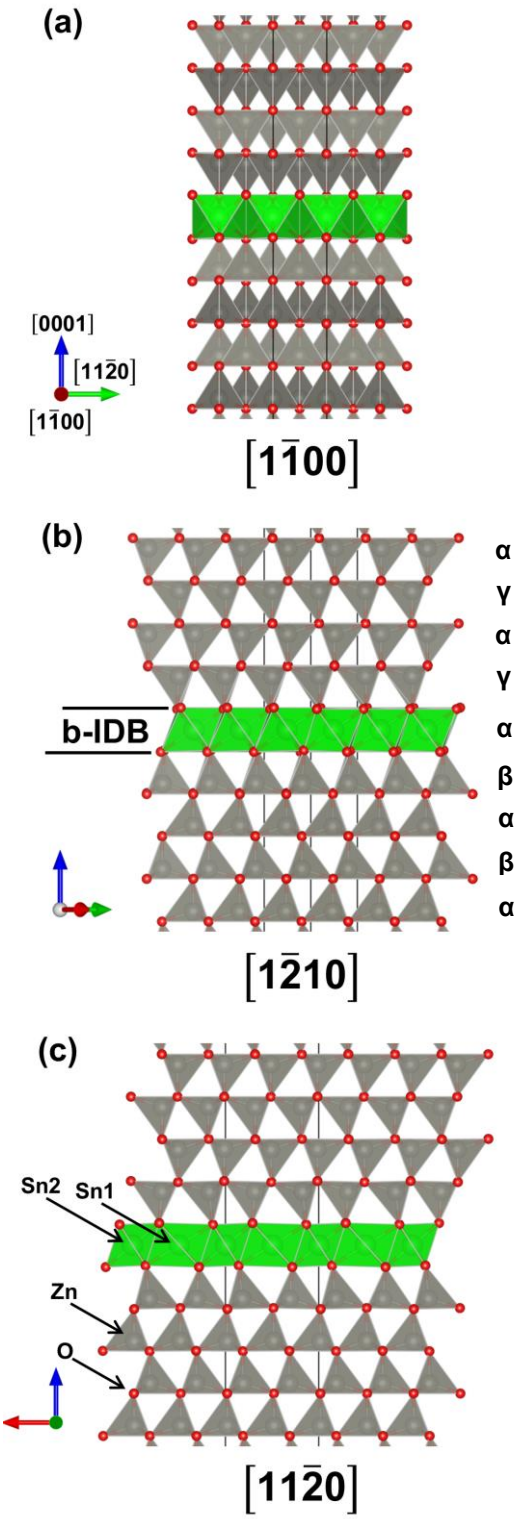

Figure A10. (a) [1$\bar{1}$00] **(b)** [1$\bar{2}$10] and **(c)** [11$\bar{2}$0] zone-axis views of the b-IDB interface within the Sn-doped b-IDB slab model, showing the polyhedral connectivity of the Sn octahedra (green) and Zn tetrahedra (grey).

$[11\bar{2}0]$ zone-axis. As shown in Fig. A10 (a) and (b), when the slab model b-IDB interface is viewed along the *m*-axis or either one of the other *a*-axes, the Sn1 and Sn2 sites cannot be distinguished.

As discussed in Chapter 5, the Sn1 and Sn2 sites exhibit different average bond lengths, resulting in some distortion of the polyhedral connectivity between the Sn-doped b-IDB octahedra and the Zn tetrahedra with which they share corners. This can be observed at the $[11\bar{2}0]$ zone-axis, as shown in Fig. A10 (c). The formation of distinct Sn sites may be a consequence of charge disproportionation between different Sn sites with bond lengths similar to those of the Sn^{2+} and Sn^{4+} sites in SnO and SnO_2 respectively, resulting in a local average cation valence state of 3+ at the b-IDB, which is expected to be a requirement for maintaining electroneutrality based on the local cation and anion coordination environments and the polyhedral connectivity at the b-IDB interface. The *c*-axis cation stacking sequence of αβαβ|α|γαγα at the Sn-doped b-IDB is shown in Fig. A10 (b) and is in agreement with the stacking sequence observed in HAADF/ABF-STEM images of the Sn-doped b-IDB interface (Fig. 4.5, Fig. A7-A9). It should be noted that although the model studied assumes the occupation of the b-IDB octahedra entirely by Sn, an alternative b-IDB configuration consisting of octahedra occupied by Zn^{2+} and Sn^{4+} in a 1:1 ratio may be observed in actual samples.

Acknowledgments

I would like to thank all the people that helped me complete the work contained in this thesis. First, I am grateful to Prof. Ikuhara and Prof. Shibata of the University of Tokyo for inviting me to join their laboratory and for providing guidance throughout the work toward the completion of my doctoral thesis. I also thank Prof. Ikuhara and Prof. Shibata, as well as Assoc. Prof. Mizoguchi and Prof. Inoue of the University of Tokyo and Dr. Yoshida of the National Institute for Materials Science (NIMS) in Tsukuba, Japan for reviewing this thesis and acting as the committee for my dissertation. In addition, I am grateful to the Ministry of Education, Culture, Sports and Technology (MEXT) in Japan, for providing me with a scholarship over the course of my studies toward the completion of this thesis.

Thanks to Dr. Tochigi of the University of Tokyo for his aid in learning the fundamentals of TEM operation, for collecting STEM data, which was vital to the completion of this thesis, and also for providing direction throughout the course of my doctoral thesis work. I also thank Dr. Tohei of the University of Tokyo for providing guidance over the course of my doctoral thesis work and for useful discussions regarding first principles calculations.

I am grateful to Dr. Yoshida and Prof. Sakka of NIMS for inviting me to work at their institution and providing me with guidance throughout my research work at NIMS. Also, I thank Prof. Mori of NIMS for allowing to me work in his laboratory and Dr. Atta Ullah Khan of NIMS for his help carrying out thermoelectric property measurements, which was crucial to the completion of this thesis.

Thanks to the other assistant professors, postdoctoral researchers and doctoral, masters and undergraduate students at the University of Tokyo and NIMS who were good friends throughout the course of my doctoral work for any assistance they may have provided toward the completion of this thesis.

Curriculum Vitae

Education

Bachelor of Science in Engineering, Materials Science and Engineering, University of Michigan, Ann Arbor 2007-2011

Master of Science in Engineering, Materials Science and Engineering, University of California, San Diego 2011-2012

Ph.D. in Engineering, Materials Science and Engineering, University of Tokyo 2013-2017

Peer-Reviewed Articles

1) Joshua Hoemke, Eita Tochigi, Tetsuya Tohei, Hidehiro Yoshida, Naoya Shibata, Yuichi Ikuhara and Yoshio Sakka, "Inversion Domain Boundaries in Mn and Al Dual-Doped ZnO: Atomic Structure and Electronic Properties", J. Am. Ceram. Soc., **100**, 4252 (2017)

2) Joshua Hoemke, Eita Tochigi, Tetsuya Tohei, Hidehiro Yoshida, Naoya Shibata, Yuichi Ikuhara and Yoshio Sakka, "Inversion Domain Network Stabilization and Spinel Phase Suppression in ZnO" Under Review in J. Am. Ceram. Soc.

3) Joshua Hoemke, Atta Ullah Khan, Hidehiro Yoshida, Takao Mori, Eita Tochigi, Naoya Shibata, Yuichi Ikuhara and Yoshio Sakka, "Sintering Characteristics and Thermoelectric Proprties of Mn-Al Co-Doped ZnO Ceramics" J. Ceram. Soc. Jpn., **124**, 515 (2016)

Conference Proceedings

Joshua Hoemke, Atta Ullah Khan, Hidehiro Yoshida, Takao Mori, Eita Tochigi, Naoya Shibata, Yuichi Ikuhara and Yoshio Sakka, "Microstructural Analysis and Thermoelectric Properties of Sn-Al Co-Doped ZnO Ceramics" AIP Conf. Proc., **1763**, 050004 (2016)

Conference Presentations

1) Joshua Hoemke, Atta Ullah Khan, Hidehiro Yoshida, Takao Mori, Eita Tochigi, Naoya Shibata, Yuichi Ikuhara and Yoshio Sakka, "Sintering of ZnO Ceramics for Thermoelectric Applications by Conventional Sintering and Spark Plasma Sintering" (Talk) Sept. 16-18, 2015: The Ceramic Society of Japan Fall Symposium, Toyama, Japan

2) Joshua Hoemke, Atta Ullah Khan, Hidehiro Yoshida, Eita Tochigi, Takao Mori, Naoya Shibata, Yuichi Ikuhara and Yoshio Sakka "Investigation of Thermoelectric Properties and Microstructure in Mn and Al co-doped ZnO Ceramics" (Poster) Oct. 19-21, 2015: The 9th International Conference on the Science and Technology of Advanced Ceramics (STAC-9), Tsukuba, Japan

3) Joshua Hoemke, Atta Ullah Khan, Hidehiro Yoshida, Eita Tochigi, Takao Mori, Naoya Shibata, Yuichi Ikuhara and Yoshio Sakka "Preparation of Mn-Al Co-Doped ZnO Thermoelectric Ceramics by Conventional Sintering and Spark Plasma Sintering (SPS)" (Poster) Nov. 19-21, 2015: 2nd International Symposium on Frontiers in Materials Science, Waseda University, Tokyo, Japan

4) Joshua Hoemke, Atta Ullah Khan, Hidehiro Yoshida, Takao Mori, Eita Tochigi, Naoya Shibata, Yuichi Ikuhara and Yoshio Sakka "Characterization of the Microstructure and Thermoelectric Properties of Doped ZnO Ceramics" (Poster) May 11-13, 2016: The 5th International Symposium on Advanced Microscopy and Theoretical Calculations (AMTC-5), Nagoya, Japan